

Advances in Mathematical Physics

Theoretical and Computational Advances in Nonlinear Dynamical Systems 2018

Lead Guest Editor: Zhi-Yuan Sun

Guest Editors: Kaliyaperumal Nakkeeran, Christos Volos, and Xin Yu





**Theoretical and Computational Advances in
Nonlinear Dynamical Systems 2018**

Advances in Mathematical Physics

**Theoretical and Computational Advances in
Nonlinear Dynamical Systems 2018**

Lead Guest Editor: Zhi-Yuan Sun

Guest Editors: Kaliyaperumal Nakkeeran, Christos Volos,
and Xin Yu



Copyright © 2018 Hindawi. All rights reserved.

This is a special issue published in “Advances in Mathematical Physics.” All articles are open access articles distributed under the Creative Commons Attribution License, which permits unrestricted use, distribution, and reproduction in any medium, provided the original work is properly cited.

Editorial Board

Giovanni Amelino-Camelia, Italy
Stephen C. Anco, Canada
P. Areias, Portugal
Matteo Beccaria, Italy
Jacopo Bellazzini, Italy
Luigi C. Berselli, Italy
Carlo Bianca, France
Giovanna Bonfanti, Italy
Tinh Q. Bui, Japan
Manuel Calixto, Spain
José F Cariñena, Spain
Zengtao Chen, Canada
John D. Clayton, USA
Pierluigi Contucci, Italy
Giampaolo Cristadoro, Italy
Claudio Dappiaggi, Italy
Prabir Daripa, USA
Pietro d'Avenia, Italy
Manuel De León, Spain
Tiziana Di Matteo, UK
Yannis Dimakopoulos, Greece
Zine El Abidine Fellah, France
Ciprian G. Gal, USA
Maria L. Gandarias, Spain
Mergen H. Ghayesh, Australia

Ivan Giorgio, Italy
Irina A. Graur, France
Sebastien Guenneau, France
Alexander Iomin, Israel
Giorgio Kaniadakis, Italy
Boris G. Konopelchenko, Italy
Pavel Kurasov, Sweden
Remi Léandre, France
Ping Li, Hong Kong
Emmanuel Lorin, Canada
Guozhen Lu, USA
Wen-Xiu Ma, USA
Jorge E. Macias-Diaz, Mexico
Marin Marin, Romania
Juan C. Marrero, Spain
Nikos E. Mastorakis, Bulgaria
Ming Mei, Canada
Yuki Minamoto, Japan
Andrei D. Mironov, Russia
Takayuki Miyadera, Japan
Merced Montesinos, Mexico
Hagen Neidhardt, Germany
André Nicolet, France
Anatol Odziejewicz, Poland
Mikhail Panfilov, France

Phuc Phung-Van, Belgium
Angelo Plastino, Argentina
Ziemowit Popowicz, Poland
Alkesh Punjabi, USA
Zhijun Qiao, USA
Eugen Radu, Portugal
Laurent Raymond, France
Nicola L. Rizzi, Italy
Soheil Salahshour, Iran
Antonio Scarfone, Italy
Artur Sergyeyev, Czech Republic
Sergey Shmarev, Spain
Diogo O. Soares-Pinto, Brazil
Ruben Specogna, Italy
Francesco Toppan, Brazil
Dimitrios Tsimpis, France
Emilio Turco, Italy
Ricardo Weder, Mexico
Sandro Wimberger, Italy
Jiahong Wu, USA
Agnieszka Wylomanska, Poland
Su Yan, USA
Shuo Yin, Ireland
Yao-Zhong Zhang, Australia
Qin Zhou, China

Contents

Theoretical and Computational Advances in Nonlinear Dynamical Systems 2018

Zhi-Yuan Sun , K. Nakkeeran, Christos Volos, and Xin Yu
Editorial (3 pages), Article ID 4732167, Volume 2018 (2018)

Dynamic Characteristics of Deeply Buried Spherical Biogas Digesters in Viscoelastic Soils

Hongwei Hou, Shihu Gao , Qianqian Guo, Long Chen, Bing Wu , and Lei Wang
Research Article (9 pages), Article ID 9349175, Volume 2018 (2018)

A Study of the Transport of Marine Pollutants Using Adjoint Method of Data Assimilation with Method of Characteristics

Xiaona Li, Minjie Xu, Xianqing Lv , and Kai Fu 
Research Article (14 pages), Article ID 7408263, Volume 2018 (2018)

On the Convergence Ball and Error Analysis of the Modified Secant Method

Rongfei Lin , Qingbiao Wu , Minhong Chen, and Xuemin Lei
Research Article (5 pages), Article ID 2704876, Volume 2018 (2018)

CIP Method of Characteristics for the Solution of Tide Wave Equations

Yafei Nie, Kai Fu , and Xianqing Lv 
Research Article (10 pages), Article ID 3469534, Volume 2018 (2018)

The Global Existence and Uniqueness of the Classical Solution with the Periodic Initial Value Problem for One-Dimension Klein-Gordon-Zakharov Equations

Cong Sun  and Lixia Li
Research Article (10 pages), Article ID 4820601, Volume 2018 (2018)

Nonlinear Green's Functions for Wave Equation with Quadratic and Hyperbolic Potentials

Asatur Zh. Khurshudyan 
Research Article (9 pages), Article ID 7179160, Volume 2018 (2018)

Adaptive Fuzzy Synchronization of Fractional-Order Chaotic Neural Networks with Backlash-Like Hysteresis

Wenqing Fu  and Heng Liu 
Research Article (13 pages), Article ID 7535628, Volume 2018 (2018)

Motion of a Spot in a Reaction Diffusion System under the Influence of Chemotaxis

Satoshi Kawaguchi 
Research Article (24 pages), Article ID 6152961, Volume 2018 (2018)

Reachable Set Bounding for a Class of Nonlinear Time-Varying Systems with Delay

Xingao Zhu, Yuangong Sun , and Fanwei Meng
Research Article (7 pages), Article ID 7308476, Volume 2018 (2018)

Traveling Wave Solutions of Two Nonlinear Wave Equations by (G'/G) -Expansion Method

Yazhou Shi, Xiangpeng Li, and Ben-gong Zhang 
Research Article (8 pages), Article ID 8583418, Volume 2018 (2018)

Chaos in a System with an Absolute Nonlinearity and Chaos Synchronization

Victor Kamdoum Tamba, Karthikeyan Rajagopal , Viet-Thanh Pham , and Duy Vo Hoang
Research Article (12 pages), Article ID 5985489, Volume 2018 (2018)

Fractional-Order Sliding Mode Synchronization for Fractional-Order Chaotic Systems

Chenhui Wang 
Research Article (9 pages), Article ID 3545083, Volume 2018 (2018)

Editorial

Theoretical and Computational Advances in Nonlinear Dynamical Systems 2018

Zhi-Yuan Sun ^{1,2}, K. Nakkeeran,³ Christos Volos,⁴ and Xin Yu⁵

¹*Institute of Fluid Mechanics, Beihang University, Beijing 100191, China*

²*International Research Institute for Multidisciplinary Science, Beihang University, Beijing 100191, China*

³*School of Engineering, University of Aberdeen, Aberdeen AB24 3UE, UK*

⁴*Department of Physics, Aristotle University of Thessaloniki, 54124 Thessaloniki, Greece*

⁵*School of Aeronautic Science and Engineering, Beihang University, Beijing 100191, China*

Correspondence should be addressed to Zhi-Yuan Sun; sunzhiyuan137@aliyun.com

Received 25 September 2018; Accepted 25 September 2018; Published 18 October 2018

Copyright © 2018 Zhi-Yuan Sun et al. This is an open access article distributed under the Creative Commons Attribution License, which permits unrestricted use, distribution, and reproduction in any medium, provided the original work is properly cited.

After the success of last year's special issue, we have received more than 30 submissions for TCAN 2018. Twelve articles, containing the studies in chaos and synchronization, nonlinear evolution equations, and applied dynamical systems, are accepted after strict review process. A new Guest Editor, Christos Volos, from Aristotle University of Thessaloniki, was invited to serve in the areas of chaotic systems and synchronization. We believe these articles, including their bibliographic resources, will substantially improve the quality of our special issue and show wide interest to the readers in nonlinear communities.

Chaos belongs to the field of "Nonlinear Oscillations Theory," which was initiated in the previous century. The experiment that boosted the consideration of chaotic behavior was due to Lorenz [1]. In 1961, working in a simplified model of atmospheric transfer with three nonlinear differential equations, he observed numerically that when making very small changes in the initial conditions he got a huge effect on their solutions. It was one evidence of the main properties of chaotic dynamics which was later known as sensitive dependence on initial conditions, also known as "Butterfly Effect." This property in fact had already been investigated from the topological point of view by Poincaré who described it in his monograph "Science and Method" [2].

For many years the property of chaos became undesirable, since it reduced the predictability of the chaotic system over long time periods. However, the scientific community was gradually becoming aware of this type of dynamical behavior. Some experiments, where abnormal results had

been previously explained in terms of experimental error or additional noise, were evaluated for an explanation in terms of chaos. In the mid-70s, the term deterministic chaos was introduced by Li and Yorke in a famous paper entitled "Period Three Implies Chaos" [3]. Since then, a huge number of studies in chaotic phenomena and dynamical systems that produce chaos have been published.

The dynamics of a system displays chaotic behavior; when it never repeats itself, and even if initial conditions are correlated by proximity, the corresponding trajectories quickly become uncorrelated. As such, the possibility of two (or more) chaotic systems oscillating in a coherent and synchronized way seems to be not an obvious phenomenon. However, there are sets of coupled chaotic oscillators in which the attractive effect of a sufficiently strong coupling can counterbalance the trend of the trajectories to diverge. As a result, it is possible to reach full synchronization in chaotic systems since they are coupled by a suitable dissipative coupling. Chaos synchronization began in the mid-80s about coupling of discrete and continuous identical systems, evolving from different initial conditions [4–8]. These works immediately received a great deal of attention from the scientific community and opened up a wide range of applications outside the traditional scope of chaos and nonlinear dynamics research. Since then, various synchronization methods and several new concepts necessary for analyzing synchronization have been developed.

In this special issue, three articles are dedicated to the investigation of chaotic systems and their synchronization.

In “Fractional-Order Sliding Mode Synchronization for Fractional-Order Chaotic Systems,” by C. Wang, some sufficient conditions, which are valid for the stability check of fractional-order nonlinear systems, are presented. Based on the aforementioned conditions, the synchronization of two fractional-order chaotic systems is investigated. The asymptotical stability of the synchronization error can be guaranteed by a proposed fractional-order sliding mode controller. The numerical examples show the feasibility of the proposed method.

In “Adaptive Fuzzy Synchronization of Fractional-Order Chaotic Neural Networks with Backlash-Like Hysteresis,” by W. Fu and H. Liu, an adaptive fuzzy synchronization controller is designed for a class of fractional-order neural networks subjected to backlash-like hysteresis input. The stability of the closed-loop system, under the influence of the adaptive fuzzy controller, is rigorously analyzed based on the fractional Lyapunov stability criterion. Furthermore, fractional adaptation laws are established to update the fuzzy parameters. The simulation examples indicate the effectiveness and the robustness of the proposed control method.

In “Chaos in a System with an Absolute Nonlinearity and Chaos Synchronization,” by V. K. Tamba et al., a system with an absolute nonlinearity is studied. The system is shown to be chaotic and has an adjustable amplitude variable, which is suitable for practical uses. Circuit design of such a system has been realized without any multiplier, and experimental measurements have been reported. In addition, an adaptive control has been applied to reach the synchronization of the system.

Nonlinear evolution equations (NEEs) play important roles in simulating the real dynamical behaviors that appear in various scientific and engineering fields. Analysis of the NEEs, especially for finding their solutions, is one of the main tasks in nonlinear communities. For integrable NEEs, there exist several effective methods, such as the inverse scattering transformation and the Hirota method, in deriving certain types of localized wave solutions, e.g., the soliton and breather solutions [9, 10]. For nonintegrable NEEs, multiple tools are employed to analyze their properties, among which the numerical methods are becoming powerful with the rapid development of computational resources.

In this special issue, six articles are included to demonstrate advances relating to the NEEs, from both of the analytic and numerical aspects.

In “Traveling Wave Solutions of Two Nonlinear Wave Equations by (G'/G) -Expansion Method,” by Y. Shi et al., the (G'/G) -expansion method is employed to seek exact traveling wave solutions of two nonlinear wave equations: Padé-II equation and Drinfeld-Sokolov-Wilson equation. Hyperbolic function solution, trigonometric function solution, and rational solution with general parameters are obtained. The solitary wave solutions and new traveling wave solutions can be derived when special values of the parameters are taken.

The advantageous Green's function method that originally has been developed for nonhomogeneous linear equations has been recently extended to nonlinear equations by Frasca. In “Nonlinear Green's Functions for Wave Equation with Quadratic and Hyperbolic Potentials,” the author A.

Zh. Khurshudyan developed a rigorous numerical analysis of some second order one-dimensional wave differential equations with quadratic and hyperbolic nonlinearities by means of Frasca's method. Numerical error analysis in both cases of nonlinearity is carried out for various source functions supporting the advantage of the method.

In “The Global Existence and Uniqueness of the Classical Solution with the Periodic Initial Value Problem for One-Dimension Klein-Gordon-Zakharov Equations,” by C. Sun and L. Li, the Galerkin method is applied to establish the approximate solutions for the one-dimension Klein-Gordon-Zakharov (KGZ) equations, and the local classical solutions are obtained. The authors also derive the existence and uniqueness of the global classical solutions of the KGZ equations by integral estimates.

In “CIP Method of Characteristics for the Solution of Tide Wave Equations,” by Y. Nie et al., the Constrained Interpolation Profile/Method of Characteristics (CIP-MOC) is proposed to solve the tide wave equations with large time step size. The bottom topography and bottom friction are included to the equation of Riemann invariants as the source term. Numerical experiments demonstrate the good performance of the scheme. In addition, numerical tests with reflective boundary conditions are carried out by CIP-MOC with large time step size, and good results are obtained as well.

In “Reachable Set Bounding for a Class of Nonlinear Time-Varying Systems with Delay,” by X. Zhu et al., the authors investigate the problem of reachable set bounding for a class of continuous-time and discrete-time nonlinear time-varying systems with time-varying delay. They use an approach which does not involve the conventional Lyapunov-Krasovskii functional, and propose new conditions such that all the state trajectories of the system converge asymptotically within a ball.

In “On the Convergence Ball and Error Analysis of the Modified Secant Method,” by R. Lin et al., the authors have studied the convergence properties of a modification of secant iteration methods. This work introduced the convergence ball and error estimate of the modified secant method using a technique based on Fibonacci series.

In this special issue, we also include three articles focusing on application of the nonlinear dynamical systems in diffusion behavior, fluid, and solid mechanics.

In “Motion of a Spot in a Reaction Diffusion System under the Influence of Chemotaxis,” by S. Kawaguchi, the motion of a spot under the influence of chemotaxis is considered. For this reason, a two-component reaction diffusion system, with a global coupling term and a Keller Segel type chemotaxis term, is presented. The existence of an upper limit for the velocity and a critical intensity for the chemotaxis, over which there is no circular motion, is proved. As a consequence the chemotaxis suppresses the range of velocity for the circular motion. This braking effect on velocity originates from the refractory period behind the rear interface of the spot and the negative chemotactic velocity.

In “A Study of the Transport of Marine Pollutants Using Adjoint Method of Data Assimilation with Method of Characteristics,” by X. Li et al., the authors apply an adjoint method of data assimilation with the characteristic finite

difference scheme to marine pollutant transport problems and simulate the temporal and spatial distribution of marine pollutants. They show that their method can not only reduce simulation error to get a good inversion, but also enable larger time step size to decrease computation time and improve the calculation efficiency.

In “Dynamic Characteristics of Deeply-Buried Spherical Biogas Digesters in Viscoelastic Soil,” by H. Hou et al., the vibration characteristics of a deeply-buried spherical methane tank in viscoelastic soil subjected to cyclic loading in the frequency domain are investigated. By introducing potential functions, the closed-form expressions for the displacement and the stress of the soil surrounding the tank are obtained. In addition, the effects of relative physical properties and geometrical parameters on the dynamics of the system are discussed.

Conflicts of Interest

The authors declare that there are no conflicts of interest regarding the publication of this article.

Acknowledgments

We would like to express our sincere thanks to all the authors and reviewers for their contributions to this special issue.

Zhi-Yuan Sun
K. Nakkeeran
Christos Volos
Xin Yu

References

- [1] E. N. Lorenz, “Deterministic nonperiodic flow,” *Journal of the Atmospheric Sciences*, vol. 20, no. 2, pp. 130–141, 1963.
- [2] H. Poincaré and F. Maitland, *Science and method*, Courier Corporation, 2003.
- [3] T. Y. Li and J. A. Yorke, “Period three implies chaos,” *The American Mathematical Monthly*, vol. 82, no. 10, pp. 985–992, 1975.
- [4] K. Kaneko, “Lyapunov analysis and information flow in coupled map lattices,” *Physica D: Nonlinear Phenomena*, vol. 23, no. 1-3, pp. 436–447, 1986.
- [5] V. S. Afraimovichh, N. N. Verichev, and M. I. Rabinovich, “Stochastic synchronization of oscillations in dissipative systems,” *Izvestiya Vysshikh Uchebnykh Zavedeniui. Radiofizika*, vol. 29, no. 9, pp. 1050–1060, 1986.
- [6] H. Fujisaka and T. Yamada, “Stability theory of synchronized motion in coupled-oscillator systems,” *Progress of Theoretical and Experimental Physics*, vol. 69, no. 1, pp. 32–47, 1983.
- [7] T. Yamada and H. Fujisaka, “Stability theory of synchronized motion in coupled-oscillator systems. II. The mapping approach,” *Progress of Theoretical and Experimental Physics*, vol. 70, no. 5, pp. 1240–1248, 1983.
- [8] A. S. Pikovsky, “Synchronization and stochastization of the ensemble of autogenerators by external noise,” *Radiophysics and Quantum Electronics*, vol. 27, pp. 576–581, 1984.
- [9] M. J. Ablowitz and P. A. Clarkson, *Solitons, Nonlinear Evolution Equations and Inverse Scattering*, Cambridge University Press, New York, NY, USA, 1991.
- [10] R. Hirota, *The Direct Method in Soliton Theory*, Cambridge University Press, Cambridge, UK, 2004.

Research Article

Dynamic Characteristics of Deeply Buried Spherical Biogas Digesters in Viscoelastic Soils

Hongwei Hou,^{1,2} Shihu Gao ,³ Qianqian Guo,⁴ Long Chen,⁴ Bing Wu ,⁴ and Lei Wang⁵

¹Zhejiang Academy of Building Research and Design Co. Ltd., Hangzhou, Zhejiang 310000, China

²College of Civil Engineering and Architecture, Zhejiang University, Hangzhou, Zhejiang 310000, China

³College of Civil Engineering and Architecture, Wenzhou University, Wenzhou, Zhejiang 325035, China

⁴Key Laboratory of Ministry of Education for Geomechanics and Embankment Engineering, Hohai University, Nanjing 210098, China

⁵Shanghai City Construction and Design Research Institute, No. 1170 Tibet South Road, Huangpu District, Shanghai, China

Correspondence should be addressed to Shihu Gao; lzccgsh@163.com

Received 10 January 2018; Revised 2 May 2018; Accepted 10 May 2018; Published 18 October 2018

Academic Editor: Zhi-Yuan Sun

Copyright © 2018 Hongwei Hou et al. This is an open access article distributed under the Creative Commons Attribution License, which permits unrestricted use, distribution, and reproduction in any medium, provided the original work is properly cited.

The harmonic vibration characteristics of a deeply buried spherical methane tank in viscoelastic soil subjected to cyclic loading in the frequency domain are investigated. The dynamic behavior of the soil is described based on the theory of fractional derivatives. By introducing potential functions, the closed-form expressions for the displacement and the stress of the viscoelastic soil surrounding the deeply buried spherical methane tank are obtained. Two die structures are considered: a homogeneous elastic medium and a shell structure. Based on the theory of elastic motion and the Flügge theory, analytic solutions for the dynamic responses of the spherical methane tank in a fractional-derivative viscoelastic soil are derived explicitly. Analytic solution expressions of the undetermined coefficients are determined by using the continuum boundary conditions. The system dynamic responses to the homogeneous elastic medium and the shell structure and the influences of the parameters of the fractional derivative, soil, and die on the dynamic characteristic of the system are compared and analyzed. The results indicate a significant difference between the dynamic responses of the die structures for the two models.

1. Introduction

Not only has an underground, deeply buried spherical digester the advantages of a small spherical mouth, good airtightness, and high gas production but also the fermentation of biogas slurry does not produce a crust and the structure is not affected by the external ambient temperature [1]. Therefore, spherical underground digesters are widely used and are promoted in China's rural areas.

The vibration response of biogas digesters has wide applications in the fields of seismic resistance, explosion-resistant design, and structural stability of the die. Forrestal and Sagartz studied the dynamic responses of thin-walled spherical shells and cylindrical shells in homogeneous elastic soil under the action of heavy loads [2]. Duffey obtained the transient dynamic response of viscoelastic and viscous-plastic spherical die structures under impulsive loading by using a Laplace transform technique [3]. Glenn regarded the soil as

a linear elastic medium and deduced the vibration response of a deeply buried spherical digester under heavy loads and pulse loads [4]. The transient response of a spherical cavity has been studied under explosive loading by using displacement as an unknown quantity [5].

Many experimental studies have been carried out to investigate the clay behavior under dynamic loading; Lin Guo studied the deformation behavior of saturated soft soil under long-term cyclic loading and established two equations for the prediction of long-term resilient modulus and permanent strain [6, 7]. Strain and pore pressure development on soft marine soil have been studied under dynamic loadings and an empirical formula is established to predict the long-term permanent strain [8]. Chuan Gu studied the influence of cyclic loading history on small strain shear modulus of saturated soils by triaxial test; test results show that both cyclic strain history and cyclic stress history will induce reduction of G_{max} compared to the corresponding G_{max} values with

noncyclic loading effects at the same effective stress [9]. Dynamic modulus characteristics of saturated soils under variable confining pressure have been studied by cyclic triaxial tests; tests results shows that both the phase differences and ratios between the cyclic deviatoric stress and cyclic confining pressure exerted a constant and pronounced influence on dynamic modulus [10–12].

Studies of the viscoelastic properties of soils have shown that a fractional-derivative constitutive model is well suited for the characterization of the soil's creep properties [13]. However, based on the fractional-derivative model, the dynamic equation is a singular integral-partial differential equation and its theoretical analysis and numerical calculation present many difficulties [14] and there have been few reports on the use of this approach for the study of soil dynamic characteristics [15]. What is more, the above studies ignore the thickness of the mold structure. In this paper, the soil element is regarded as a viscoelastic element with fractional-derivative properties and the exact expression of the displacement and stress of the infinite fractional-derivative viscoelastic soil surrounding the biogas digester is deduced based on the viscoelastic theory. In our research, the thickness of the mold structure also can be considered.

The gas fermentation and user consumption cause repeated changes in pressure in the pool and this pressure is uniformly applied to the inner side of the pool wall and is equivalent to the periodic load [16]. In this study, the soil body is regarded as a viscoelastic body with fractional-derivative properties and the exact expression of the displacement and stress of the infinite fractional-derivative viscoelastic soil surrounding the biogas digester is deduced based on the viscoelastic theory. Secondly, the die structure is considered a homogeneous elastic medium and thin-walled shell structure and the analytics solution for the vibration response of the die structure is obtained based on the theory of elastic motion [17] and the Flügge theory [18]. Finally, the concrete expression of the relevant undetermined coefficients is obtained according to the boundary conditions of displacement and stress in the mold structure and the contact surface of the soil body. A comparison of the results of this study and existing data demonstrates the correctness of the assumptions of this study. Finally, the influences of the parameters of the fractional derivative on the vibration response of the system are investigated, providing a theoretical basis for the design and construction of underground spherical digesters.

2. Mathematical Model

Because the spherical digester is deeply embedded in the soil, it is assumed that there is a spherical digester with an inner radius R_1 and an outer radius R_2 , as shown in Figure 1; the distance from the center to the middle surface is a . The spherical digester has a circular frequency ω of a uniform radial harmony excitation load ($q_0 e^{i\omega t}$), where i is the imaginary unit. The shear modulus parameters of the soil and die structure are G^S and G^L , respectively, the material density parameters are ρ^S and ρ^L , respectively, and the Poisson's ratios of the soil and the model are ν^S and ν^L , respectively. The mold

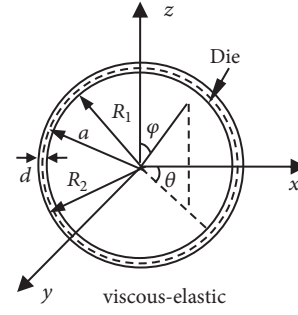


FIGURE 1: A spherical biogas digester in viscoelastic soil.

and the soil interface are in complete and close contact to meet the stress and displacement continuity.

3. Establish and Solution of the Soil Control Equation

In the case of spherical symmetry, the stress-displacement constitutive relationship of the constitutive model with the fractional derivative is [11]

$$\begin{aligned}
 & (1 + \tau_\epsilon^\alpha D^\alpha) \sigma_r^S \\
 &= (1 + \tau_\sigma^\alpha D^\alpha) \left[\lambda^S \left(\frac{\partial u_r^S}{\partial r} + \frac{2u_r^S}{r} \right) + 2\mu^S \frac{\partial u_r^S}{\partial r} \right] \\
 & (1 + \tau_\epsilon^\alpha D^\alpha) \sigma_\theta^S \\
 &= (1 + \tau_\sigma^\alpha D^\alpha) \left[\lambda^S \left(\frac{\partial u_r^S}{\partial r} + \frac{2u_r^S}{r} \right) + 2\mu^S \frac{u_r^S}{r} \right] \\
 & (1 + \tau_\epsilon^\alpha D^\alpha) \sigma_\phi^S \\
 &= (1 + \tau_\sigma^\alpha D^\alpha) \left[\lambda^S \left(\frac{\partial u_r^S}{\partial r} + \frac{2u_r^S}{r} \right) + 2\mu^S \frac{u_r^S}{r} \right]
 \end{aligned} \quad (1)$$

Where σ_r is radial stress of soil layer, σ_θ is circumferential stress of soil layer, σ_ϕ is shear stress of soil layer, σ is stress tensor of soil, ϵ is strain tensor of soil, τ_ϵ and τ_σ are constitutive model parameters, λ^S and μ^S are Lamé constant of soil skeleton and $\lambda^S = 2\nu^S/(1-2\nu^S)$, and ν is Poisson's ratio. $D^\alpha = d^\alpha/dt^\alpha$ is α -step Riemann-Liouville fractional derivative, which is defined as

$$D^\alpha [x(t)] = \frac{1}{\Gamma(1-\alpha)} \frac{d}{dt} \int_0^t \frac{x(\tau)}{(t-\tau)^\alpha} d\tau \quad (2)$$

in which $\Gamma(u) = \int_0^\infty t^{u-1} e^{-t} dt$ is Gamma Function.

Under the action of dynamic load, according to the theory of elasticity, the dynamic equation [16] of soil is as follows.

$$\frac{\partial \sigma_r^S}{\partial r} + \frac{2\sigma_r^S - \sigma_\theta^S - \sigma_\phi^S}{r} = \rho^S \frac{\partial^2 u_r^S}{\partial t^2} \quad (3)$$

Substituting (1) into (3), we obtain

$$\left(\lambda^S + 2\mu^S \right) \frac{1 + \tau_\sigma^\alpha D^\alpha}{1 + \tau_\epsilon^\alpha D^\alpha} \frac{\partial}{\partial r} \left(\frac{\partial u_r^S}{\partial r} + \frac{2u_r^S}{r} \right) = \rho^S \frac{\partial^2 u_r^S}{\partial t^2} \quad (4)$$

Introduce potential function

$$u_r^S = \frac{\partial}{\partial r} \left(\frac{\varphi^S(r, t)}{r} \right) \quad (5)$$

For steady-state vibration, let

$$\begin{aligned} u_r^S &= R_2 U_\eta^S e^{i\omega t}, \\ \varphi^S &= R_2^3 \bar{\varphi}^S e^{i\omega t} \end{aligned} \quad (6)$$

Introduce dimensionless quantity and constant as follows:

$$\begin{aligned} \eta &= \frac{r}{R_2}, \\ \lambda &= \frac{\omega R_2}{V^S}, \\ T_\sigma &= \frac{\tau_\sigma V^S}{R_2}, \\ T_\varepsilon &= \frac{\tau_\varepsilon V^S}{R_2}, \\ \eta_0 &= 1 - \delta, \\ \delta &= \frac{d}{R_2}. \end{aligned} \quad (7)$$

Substituting (5), (6), and (7) into (4), we obtain (8) as follows:

$$\frac{d^2 \bar{\varphi}^S}{d\eta^2} - \beta^2 \bar{\varphi}^S = 0 \quad (8)$$

where

$$\beta^2 = -\frac{1 + T_\varepsilon^\alpha (i\lambda)^\alpha (1 - 2\nu^S) \lambda^2}{1 + T_\sigma^\alpha (i\lambda)^\alpha 2(1 - \nu^S)} \quad (9)$$

According to (8), we obtain

$$\bar{\varphi}^S = A e^{-\beta\eta} + B e^{\beta\eta} \quad (10)$$

where A and B are undetermined coefficient; they are determined by boundary conditions. According to boundary conditions $r \rightarrow \infty$, $u_r^S = 0$, we obtain B=0,

$$\bar{\varphi}^S = A e^{-\beta\eta} \quad (11)$$

Substituting (5) into (11), we obtain (12) as follows:

$$U_\eta^S = -\left(\frac{1}{\eta^2} + \frac{\beta}{\eta} \right) e^{-\beta\eta} A \quad (12)$$

Substituting (12) into (1), we obtain (13) as follows:

$$\begin{aligned} \sigma_r^S &= \mu^S \frac{1 + T_\sigma^\alpha (i\lambda)}{1 + T_\varepsilon^\alpha (i\lambda)} \\ &\cdot e^{i\omega t} \left[\frac{2\nu^S}{1 - 2\nu^S} \frac{\beta^2}{\eta} + 2 \left(\frac{2}{\eta^3} + \frac{2\beta}{\eta^2} + \frac{\beta^2}{\eta} \right) \right] e^{-\beta\eta} A \\ \sigma_\theta^S &= \mu^S \frac{1 + T_\sigma^\alpha (i\lambda)}{1 + T_\varepsilon^\alpha (i\lambda)} e^{i\omega t} \left[\frac{2\nu^S}{1 - 2\nu^S} \frac{\beta^2}{\eta} - 2 \left(\frac{1}{\eta^3} + \frac{\beta}{\eta^2} \right) \right] \\ &\cdot e^{-\beta\eta} A \end{aligned} \quad (13)$$

4. Establishment and Solution of Die Structure Motion Equation

4.1. Die Structure Equation of Type 1. We considered the mold structure of the spherical digester as a homogeneous elastic medium and assumed that the mold structure and soil interface are in complete and close contact with no relative slip to satisfy the stress and displacement continuity. Under the action of a dynamic load, the motion equation of the die junction is as follows [16].

$$\frac{\partial \sigma_r^L}{\partial r} + \frac{2\sigma_r^L - \sigma_\theta^L - \sigma_\varphi^L}{r} = \rho^L \frac{\partial^2 u_r^L}{\partial t^2} \quad (14)$$

Constitutive model is

$$\begin{aligned} \sigma_r^L &= \lambda^L \left(\frac{\partial u_r^L}{\partial r} + \frac{2u_r^L}{r} \right) + 2\mu^L \frac{\partial u_r^L}{\partial r} \\ \sigma_\theta^L &= \lambda^L \left(\frac{\partial u_r^L}{\partial r} + \frac{2u_r^L}{r} \right) + 2\mu^L \frac{u_r^L}{r} \\ \sigma_\varphi^L &= \lambda^L \left(\frac{\partial u_r^L}{\partial r} + \frac{2u_r^L}{r} \right) + 2\mu^L \frac{u_r^L}{r} \end{aligned} \quad (15)$$

Substituting (15) into (14), we obtain (16) as follows:

$$(\lambda^L + 2\mu^L) \frac{\partial}{\partial r} \left(\frac{\partial u_r^L}{\partial r} + \frac{2u_r^L}{r} \right) = \rho^L \frac{\partial^2 u_r^L}{\partial t^2} \quad (16)$$

For steady-state vibration, let $u_r^L = R_2 U_\eta^L e^{i\omega t}$, $\varphi^L = R_2^3 \bar{\varphi}^L e^{i\omega t}$. Introduce displacement potential function

$$u_r^L = \frac{\partial}{\partial r} \left(\frac{\varphi^L(r, t)}{r} \right) \quad (17)$$

Substituting (17) into (16), we obtain

$$\frac{d^2 \bar{\varphi}^L}{d\eta^2} - q^2 \bar{\varphi}^L = 0 \quad (18)$$

where

$$\begin{aligned} G^{SL} &= \frac{G^S}{G^L}, \\ \rho^{LS} &= \frac{\rho^L}{\rho^S}, \\ q^2 &= -\frac{(1-2\nu^L)\lambda^2\rho^{LS}G^{SL}}{2(1-\nu^L)} \end{aligned} \quad (19)$$

According to (18), we obtain

$$\bar{\varphi}^L = C_5 e^{-q\eta} + C_6 e^{q\eta} \quad (20)$$

where C_5 and C_6 are undetermined coefficient; they are determined by boundary conditions. Substituting (20) into (17), we obtain

$$U_\eta^L = -\left(\frac{1}{\eta^2} + \frac{q}{\eta}\right) e^{-q\eta} C_5 - \left(\frac{1}{\eta^2} - \frac{q}{\eta}\right) e^{q\eta} C_6 \quad (21)$$

According to (15), we obtain radial stress amplitude

$$\begin{aligned} \sigma_r^L &= \left(\frac{2\nu^L G^L}{1-2\nu^L} \frac{q^2}{\eta} + 2G^L \vartheta_1\right) e^{-q\eta} e^{i\omega t} C_5 \\ &+ \left(\frac{2\nu^L G^L}{1-2\nu^L} \frac{q^2}{\eta} + 2G^L \vartheta_2\right) e^{q\eta} e^{i\omega t} C_6 \end{aligned} \quad (22)$$

where

$$\begin{aligned} \vartheta_1 &= \frac{2}{\eta^3} + \frac{2q}{\eta^2} + \frac{q^2}{\eta}, \\ \vartheta_2 &= \frac{2}{\eta^3} - \frac{2q}{\eta^2} + \frac{q^2}{\eta} \end{aligned} \quad (23)$$

Satisfy the boundary conditions as follows:

(1) Displacement continuous in the mold structure and soil interface ($r = R_2, \eta = 1$); that is,

$$u_r^S = u_r^L \quad r = R_2 \quad (24)$$

(2) Stress continuity in the mold structure and soil interface ($r = R_2, \eta = 1$); that is,

$$\sigma_r^S = \sigma_r^L \quad r = R_2 \quad (25)$$

(3) Internal hemorrhage loading equal to the radial stress in the mold structure and soil interface ($r = R_1, \eta = 1$) of the die structure; that is,

$$\sigma_r^L = q_0 e^{i\omega t} \quad r = R_1 \quad (26)$$

According to (24)~(26), we obtain the actual formulas of the undetermined coefficients A, C_5, C_6 ,

$$\begin{aligned} C_6 &= \frac{a_2 b_1 - a_1 b_2}{e_1 (a_1 b_3 - a_3 b_1) + e_2 (a_2 b_1 - a_1 b_2)} Q \\ C_5 &= \frac{Q}{e_1} - \frac{e_2}{e_1} C_6 \\ A &= -\frac{a_2}{a_1} C_5 - \frac{a_3}{a_1} C_6, \end{aligned} \quad (27)$$

where

$$\begin{aligned} a_1 &= -(1+\beta) e^{-\beta}, \\ a_2 &= (1+q) e^{-q}, \\ a_3 &= (1-q) e^q, \\ b_1 &= G^{SL} \\ &\cdot \frac{1 + T_\sigma^\alpha(i\lambda)^\alpha}{1 + T_\varepsilon^\alpha(i\lambda)^\alpha} \left[\frac{2\nu^S \beta^2 e^{-\beta}}{1-2\nu^S} + 2e^{-\beta} (2 + 2\beta + \beta^2) \right], \\ b_2 &= -\left[\frac{2\nu^L q^2}{1-2\nu^L} + 2(2+2q+q^2) \right] e^{-q}, \\ b_3 &= -\left[\frac{2\nu^L q^2}{1-2\nu^L} + 2(2-2q+q^2) \right] e^q, \\ e_1 &= \left[\frac{2\nu^L q^2}{(1-2\nu^L)\eta_0} + 2\left(\frac{2}{\eta_0^3} + \frac{2q}{\eta_0^2} + \frac{q^2}{\eta_0}\right) \right] e^{-q\eta_0}, \\ e_2 &= \left[\frac{2\nu^L q^2}{(1-2\nu^L)\eta_0} + 2\left(\frac{2}{\eta_0^3} - \frac{2q}{\eta_0^2} + \frac{q^2}{\eta_0}\right) \right] e^{q\eta_0}. \end{aligned} \quad (28)$$

4.2. Die Structure Equation of Type 2. Since the thickness of the die structure is much smaller than the radius of the spherical digester, it can be assumed that the mold structure has little effect on the interface $r = R_2$ of the soil and the middle surface radius [6] $r = a$. According to the Hamilton principle, the motion equation of the die structure [7] is as follows:

$$u_r^L \frac{2G^L d}{(1-\nu^L)R_2^2} + \rho^L d \frac{\partial^2 u_r^L}{\partial t^2} = Q_a \quad (29)$$

where Q_a is net pressure.

For steady-state vibration, we assumed

$$\begin{aligned} u_r^L &= R_2 U_\eta^L e^{i\omega t}, \\ Q_a &= G^S \bar{Q}_a e^{i\omega t} \\ G^{SL} &= \frac{G^S}{G^L}, \\ \rho^{LS} &= \frac{\rho^L}{\rho^S} \end{aligned} \quad (30)$$

Meanwhile, satisfy the boundary conditions as follows:

(1) Stress compatibility in the mold structure and soil interface ($r = R_2, \eta = 1$); that is,

$$G^{SL} \bar{Q}_a e^{i\omega t} = Q e^{i\omega t} - \frac{\sigma_r^S}{G^L} \quad (31)$$

(2) Displacement continuous in the mold structure and soil interface ($r = R_2, \eta = 1$); that is,

$$u_r^S = u_r^L \quad r = R_2 \quad (32)$$

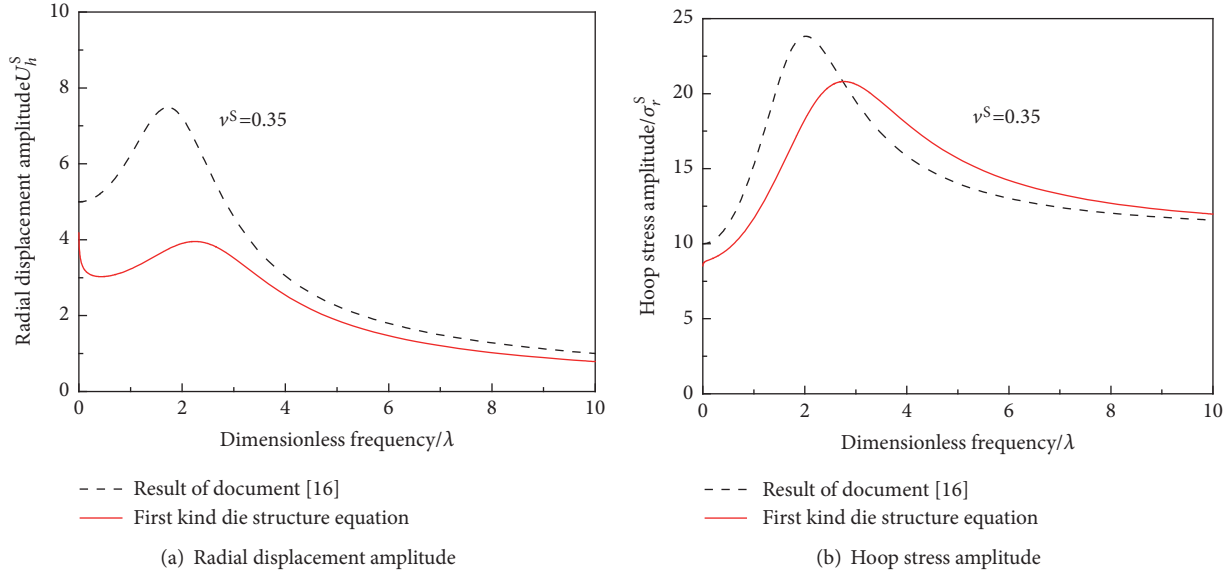


FIGURE 2: Comparison between present results and [16] results.

Substituting (29) and (13) into (31) and (32), we obtain

$$A = \frac{Q}{G^{\text{SL}} \left((1 + T_\sigma^\alpha (i\lambda)^\alpha) / (1 + T_\varepsilon^\alpha (i\lambda)^\alpha) \right) \vartheta_3 - \vartheta_4 (1 + \beta) e^{-\beta}} \quad (33)$$

where

$$\begin{aligned} \vartheta_3 &= \frac{2\nu^S \beta^2}{1 - 2\nu^S} e^{-\beta} + 2e^{-\beta} (2 + 2\beta + \beta^2) \\ \vartheta_4 &= \frac{2\delta}{1 - 2\nu^L} - \rho^{\text{LS}} G^{\text{SL}} \delta \lambda^2 \end{aligned} \quad (34)$$

5. Comparison with Existing Results

In order to verify the correctness of the calculation, we compared the results with existing results, which include the ideal elastic model of [16], the classical elastic constitutive model [17], and classical viscoelastic constitutive model [18].

The ideal elastic model of [16] ignores the influence of the die structure firstly. Besides, it establishes the dynamic characteristics of the spherical digester in a general and ideal elastic soil. Substituting the equation for the classical elastic constitutive method into (3) and assuming that the material parameters of the soil are the same as in the die structure, we determined that the results of this study were in agreement with other published solutions [16]. The parameter values were as follows: $\eta=1$, $\nu^S=0.35$, $\rho^{\text{LS}}=1.5$, $G^{\text{SL}}=0.05$, $\nu^L=0.25$, $\delta=0.005$, $T_\sigma/T_\varepsilon=3$, $T_\varepsilon=10$, and $\alpha=0.5$. Figure 2 shows a curve for the radial displacement and hoop stress amplitude with a dimensionless frequency for the two models of a uniform elastic medium. It can be seen that, in [16], the resonance effect is significantly greater for the model than for the homogeneous elastic dielectric model and that the base frequency is also higher than the base frequency of the resonance effect of the system. There are two main reasons

for this: firstly, the author uses the fractional-derivative constitutive model to describe the soil viscosity and [16] uses a general and ideal elastic soil body; secondly, the author considers the influence of the die structure which has a greater stiffness than the soil body.

Thirdly, the fractional-derivative constitutive model used in this study is compared with the classical elastic model [17] and the classical viscoelastic constitutive model [18]. Substituting the classical elastic constitutive model and classical viscoelastic constitutive model used in the literature [19] into the soil equation of motion (3), respectively, changes the results of [19, 20]. Figure 3 shows the changes in the curves of the radial displacement amplitude and circumference displacement amplitude as a result of the changing frequency of the three models. It can be seen that, for the elastic model in [20], the peak value of the displacement amplitude of the soil is maximum; the resonance effect is clear and the resonance phenomenon decreases with increasing. The peak value of the classical viscoelastic model used in [19] is the minimum, while, for the fractional-derivative viscoelastic model, it is in the middle.

6. Analysis of Example and Graphic Analysis

The effects of the shear modulus ratio G^{SL} of the soil and die, the Poisson ratio ν^S of the soil material, the fractional-derivative order α , the material parameter ratio T_σ/T_ε on the radial displacement, and the hoop stress amplitude were investigated.

Figure 4 shows that the values of the radial displacement and circumferential stress amplitude change with the frequency f as the shear modulus ratio G^{SL} of the soil body and die structure variation change. It is evident that when the modulus ratio G^{SL} is comparatively small, the displacement amplitudes are very different for the model and the second type of mold model and the resonance effect produced by the

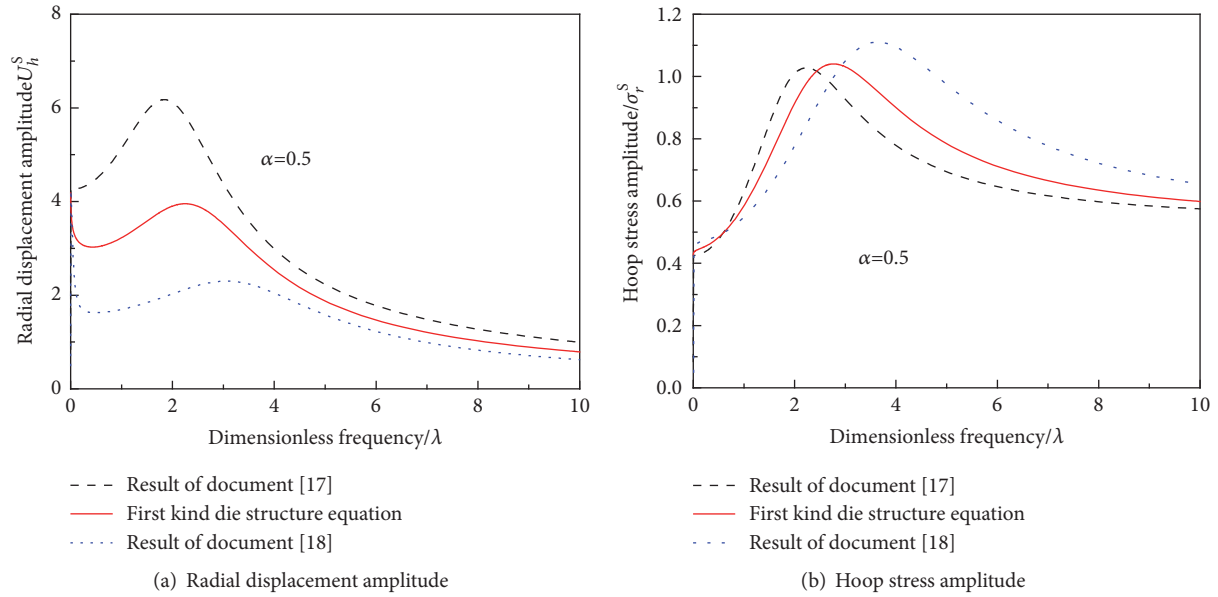


FIGURE 3: Comparison analysis of three models.

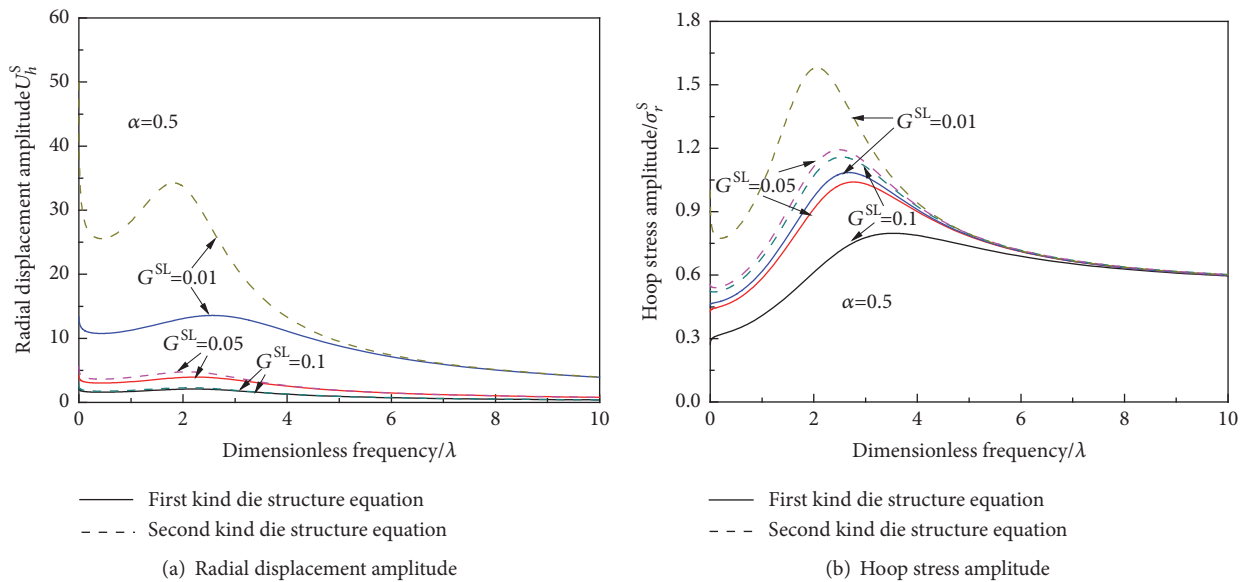


FIGURE 4: Influence of modulus ratio on radial displacement and hoop stress amplitude.

latter system is significant. With the increase in the modulus ratio λ , the difference in the displacement amplitude for the two models is small. The stress amplitude is clearly greater for the spherical shell die structure than for the uniform elastic medium. As the frequency increases, the difference between the two models decreases and the displacement and the stress amplitude decrease with an increase in the modulus ratio.

Figure 5 shows the effect of the changes in Poisson's ratio ν^s on the radial displacement and the amplitude of the circumferential stress. As Poisson's ratio ν^s increases, the radial displacement and amplitude of the hoop stress

increase gradually. The difference in the displacement and stress amplitude between the two types of die structures at high frequency is very small.

Figure 6 shows the influence of the fractional-derivative order α on the radial displacement and circumferential stress amplitude. It is evident that the amplitude of radial displacement decreases with an increase in the order number α in genera; with the increase in the frequency λ , the difference in the displacement amplitude for the two models is small. The hoop stress changed with the fractional-derivative order number α being interesting. Its change has a certain

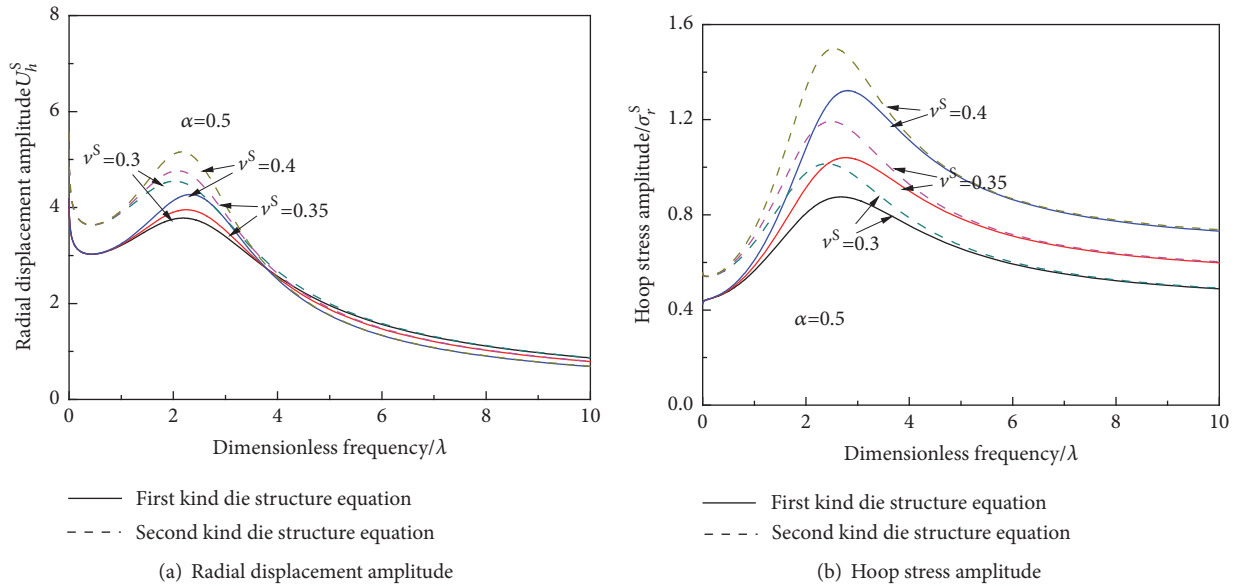


FIGURE 5: Influence of Poisson's ratio on radial displacement and hoop stress amplitude.

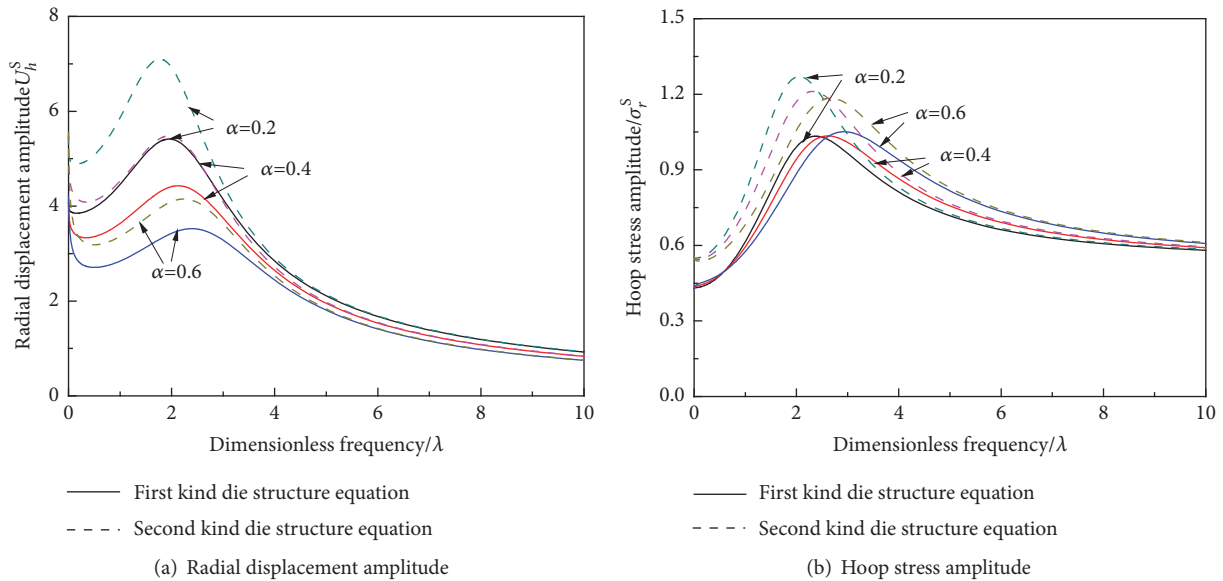


FIGURE 6: Influence of order on radial displacement and hoop stress amplitude.

relationship with the frequency λ : when the frequency λ is between 0 and 3, the hoop stress amplitude decreases with an increase in the order number α ; when the frequency λ is greater than 3, the circumferential stress amplitude increases with an increase in the order number α .

Figure 7 shows the changes in the radial displacement and circumferential stress amplitude as a result of changes in the frequency λ when the material parameter ratio T_σ/T_ϵ of the constitutive model is changed. The data indicate that the radial displacement and circumferential stress amplitude decrease as the material parameter ratio T_σ/T_ϵ increases; this is caused by the increase in the impedance of the soil body.

7. Conclusions

In this paper, the simplified vibration characteristics of a deeply buried spherical digester in viscoelastic soil under uniform internal pressure in the frequency domain are studied using an analytics method; the effects of relative physical properties and geometrical parameters on the dynamic characteristics of the system are considered. The main conclusions are summarized as follows:

- (1) Under the condition of $T_\sigma/T_\epsilon = 3$, the steady-state response of the viscoelastic soil is greater for the fractional-derivative viscoelastic soil than for the classical viscoelastic soil but less than for the classical elastic soil

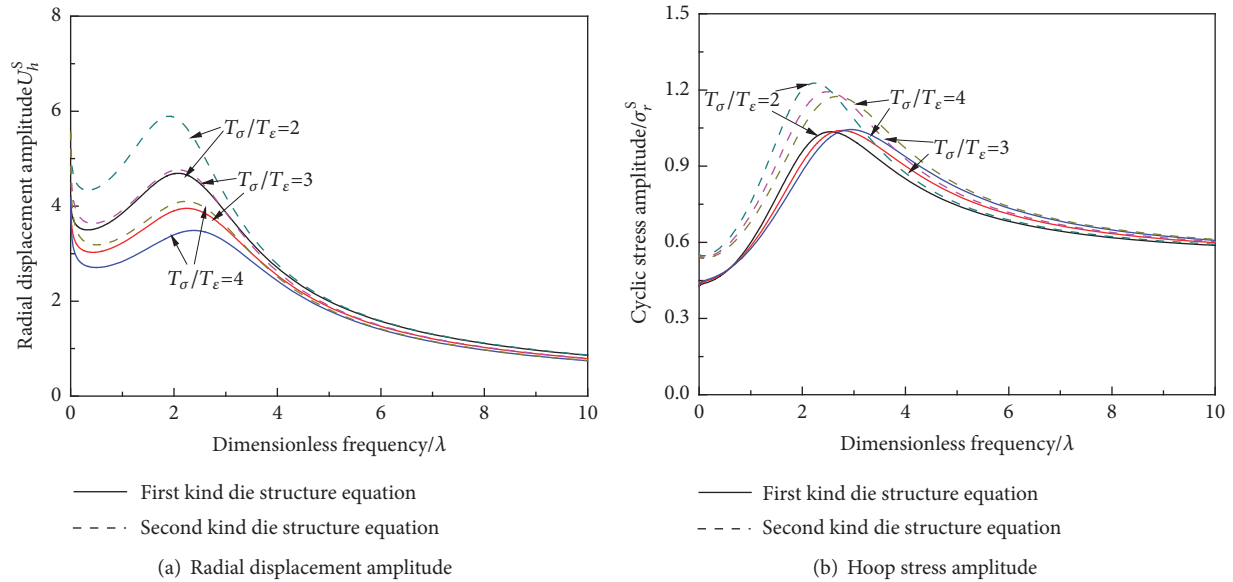


FIGURE 7: Influence of material parameter ratio on radial displacement and hoop stress amplitude.

(2) The steady-state response of the spherical digester is clearly greater for the spherical shell mold structure model than for the homogeneous elastic medium model

(3) When the modulus is comparatively small, the displacement amplitude is very different for the two types of mold type models and the difference between them decreases with increases in G^{SL}

(4) With the increase in Poisson's ratio ν^S of the soil material, the displacement amplitude and the hoop stress amplitude increases gradually

(5) With the increase in the order number α , the radial displacement and the hoop stress amplitude decrease and the system resonance effect weakens

(6) With the increase in the material parameter ratio T_σ/T_ϵ , the radial displacement and the hoop stress amplitude decrease

Data Availability

No data were used to support this study.

Conflicts of Interest

The authors declare that they have no conflicts of interest.

Acknowledgments

The work presented in this paper was supported by the Department of Construction of Zhejiang Province Science and Technology Project (no. 2015K31), National Natural Science Foundation of China under (Grant no. 51708175), and Business Funds of Central Colleges and Universities (Grant no. 2018B00814).

References

- [1] W. Gong, M. Ding, Q. Xu, and X. Jiang, "Earth pressure on pool wall and stress analysis on pool cover of underground biogas digester," *Nongye Gongcheng Xuebao*, vol. 27, no. 4, pp. 270–276, 2011.
- [2] M. J. Forrestal and M. J. Sagartz, "Radiated pressure in an acoustic medium produced by pulsed cylindrical and spherical shells," *Journal of Applied Mechanics*, vol. 38, no. 4, pp. 1057–1060, 1971.
- [3] T. A. Duffey, "Transient response of viscous-elastic and viscous-elastic shells submerged in fluid media," *AMSE Journal of Applied Mechanics*, vol. 98, pp. 137–143, 1976.
- [4] A. L. Glenn and R. E. Kidder, "Blast loading of a spherical container surrounded by an infinite elastic medium," *Journal of Impact Engineering*, vol. 22, pp. 984–992, 2000.
- [5] Z. Qingyuan and Z. Renrui, "The dynamic response of spherical hollow chamber under explosive loading," *Explosion and Shock Waves*, vol. 14, no. 2, pp. 182–185, 1994.
- [6] C. Gu, J. Wang, Y. Cai, L. Sun, P. Wang, and Q. Dong, "Deformation characteristics of overconsolidated clay sheared under constant and variable confining pressure," *Soils and Foundations*, vol. 56, no. 3, pp. 427–439, 2016.
- [7] L. Guo, J. Wang, Y. Cai, H. Liu, Y. Gao, and H. Sun, "Undrained deformation behavior of saturated soft clay under long-term cyclic loading," *Soil Dynamics and Earthquake Engineering*, vol. 50, pp. 28–37, 2013.
- [8] J. Wang, L. Guo, Y. Cai, C. Xu, and C. Gu, "Strain and pore pressure development on soft marine clay in triaxial tests with a large number of cycles," *Ocean Engineering*, vol. 74, pp. 125–132, 2013.
- [9] C. Gu, J. Wang, Y. Cai, and L. Guo, "Influence of cyclic loading history on small strain shear modulus of saturated clays," *Soil Dynamics and Earthquake Engineering*, vol. 66, pp. 1–12, 2014.

- [10] C. Gu, Z. Gu, Y. Cai, J. Wang, and D. Ling, "Dynamic modulus characteristics of saturated clays under variable confining pressure," *Canadian Geotechnical Journal*, vol. 54, no. 5, pp. 729–735, 2017.
- [11] Y. Cai, T. Wu, L. Guo, and J. Wang, "Stiffness degradation and plastic strain accumulation of clay under cyclic load with principal stress rotation and deviatoric stress variation," *Journal of Geotechnical and Geoenvironmental Engineering*, vol. 144, no. 5, Article ID 04018021, 2018.
- [12] T. Wu, Y. Cai, L. Guo, D. Ling, and J. Wang, "Influence of shear stress level on cyclic deformation behaviour of intact Wenzhou soft clay under traffic loading," *Engineering Geology*, vol. 228, pp. 61–70, 2017.
- [13] H. X. Gao and M. J. Wen, "Dynamic characteristics of a spherical cavity in nearly saturated viscoelastic soil," *Chinese Journal of Theoretical and Applied Mechanics*, vol. 44, no. 4, pp. 753–761, 2012.
- [14] L.-C. Liu and X. Yang, "Analysis of vertical vibrations of a pile in saturated soil described by fractional derivative model," *Rock and Soil Mechanics*, vol. 32, no. 2, pp. 526–532, 2011.
- [15] H. Lijun, K. Lingwei, W. Wenjun et al., "A description of creep model for soft soil with fractional derivative," *Rock and Soil Mechanics*, vol. 32, supplement 2, pp. 239–244, 2011.
- [16] P. Weiland, "Biogas production: current state and perspectives," *Applied Microbiology and Biotechnology*, vol. 85, no. 4, pp. 849–860, 2010.
- [17] X. Changjie and W. Shiming, "Spherical wave propagation in saturated soils," *Applied Mathematics and Mechanics*, vol. 19, no. 3, pp. 243–252, 1998.
- [18] X. Changjie and C. Yuanqiang, "Dynamic response of spherical cavity in viscous-elastic saturated soils," *China Civil Engineering Journal*, vol. 34, no. 4, pp. 88–92, 2001.
- [19] U. Zakout and N. Akkas, "Transient response of a cylindrical cavity with and without a bonded shell in an infinite elastic medium," *International Journal of Engineering Science*, vol. 35, no. 13-12, pp. 1203–1220, 1997.
- [20] S. P. Timoshenko and J. N. Goodier, *Theory of Elasticity*, McGraw-Hill, New York, NY, USA, 1977.

Research Article

A Study of the Transport of Marine Pollutants Using Adjoint Method of Data Assimilation with Method of Characteristics

Xiaona Li,¹ Minjie Xu,¹ Xianqing Lv ,¹ and Kai Fu ²

¹Physical Oceanography Laboratory, Ocean University of China, Qingdao 266100, China

²School of Mathematical Sciences, Ocean University of China, Qingdao 266100, China

Correspondence should be addressed to Kai Fu; kfu@ouc.edu.cn

Received 2 February 2018; Accepted 9 July 2018; Published 2 August 2018

Academic Editor: Xin Yu

Copyright © 2018 Xiaona Li et al. This is an open access article distributed under the Creative Commons Attribution License, which permits unrestricted use, distribution, and reproduction in any medium, provided the original work is properly cited.

An adjoint method of data assimilation with the characteristic finite difference (CFD) scheme is applied to marine pollutant transport problems and the temporal and spatial distribution of marine pollutants are simulated. Numerical tests of two-dimensional problems of pollutant transport with two different schemes indicate that the error of CFD is smaller than that of central difference scheme (CDS). Then the inversion experiments of the initial field and the source and sink terms of pollutants are carried out. Applying CFD in the adjoint method of data assimilation cannot only reduce simulation error to get a good inversion but can also enable larger time step size to decrease computation time and improve the calculation efficiency.

1. Introduction

With the rapid development of the coastal economy, offshore waters have suffered severe pollution damage and the ecological environment is gradually deteriorated, which is an important topic that attracted the attention all over the world, especially countries with long coastlines.

Many scholars have used mathematical models and methods to make numerical analysis in various areas. Gupta et al. [1] applied a two-dimensional model considering organized wastewater discharges to determine the waste water assimilative capacity of Tane creek; Harms et al. [2] applied a three-dimensional coupled ice-ocean-models of different horizontal resolution to simulate the dispersion of water from these rivers; Grell et al. [3] built the WRF/Chem model to simulate the distribution of atmospheric pollutants in the northeastern United States; Guo et al. [4] used the surface spline interpolation in the inversion of bottom friction coefficients in a two-dimensional tidal model to get a smoother surface; Liu et al. [5] presented a modified Cressman interpolation method for the simulation of routine monitoring data of total nitrogen in the Bohai Sea, which reduces interpolation errors by decreasing the influence radius and introducing background value.

The variational adjoint data assimilation can be applied to assimilate observations data into model by optimizing initial values and other parameters, which improves the model performance remarkably. Elbern et al. [6] used the adjoint method of data assimilation in the European air pollution dispersion model system and found the method allows them to analyze initial data even when sparse observations are available only; Peng and Xie [7] studied the inversion of the initial conditions of storm surge disaster and discovered that using the adjoint method of data assimilation can reduce error caused by uncertain initial condition; Zhang et al. [8] studied the space varying bottom friction coefficient using the adjoint method of data assimilation and get simulation result which is much better than that of traditional methods; Lv and Fan [9] applied the adjoint method of data assimilation in the inversion of spatially varying parameters of a marine ecosystem model and validated the efficiency of the method; Wang et al. [10] used the adjoint method of data assimilation to study the process of pollutant transport in Bohai Sea and studied the inversion of initial field using the assimilated routine monitoring data of pollutants. In the study of Fan and Lv [11], SeaWiFS chlorophyll-a data were assimilated into a NPZD (Nutrient-Phytoplankton-Zooplankton-Detritus) model by the adjoint method; Pan et

al. [12] studied the open boundary condition of the M_2 tidal constituent using the adjoint method of data assimilation with spline interpolation; Zhang et al. [13] applied this method to study the similarities and the differences between the Ekman (linear) and the Quadratic (nonlinear) bottom friction parameters of a two-dimensional tidal model; and many other researches (Yu and O'Brien [14], Lawson et al. [15], Zhao et al. [16], Zhao and Lu [17], and Qi et al. [18]) have also proven the validity and rationality of the adjoint method.

Method of characteristics and the schemes it derives have been used to solve problems in several areas for its high accuracy and ability to use large time step size. Douglas Jr. and Russell [19] proposed characteristic method to solve convection-diffusion equations; Shen et al. [20] presented a characteristic finite difference method and its stability and convergence were analyzed; Fu and Liang [21] developed a conservative characteristic finite difference method to predict the distribution of atmospheric aerosols; Xu et al. [22] used the adjoint assimilation method with the characteristic finite difference scheme to solve aerosol transport problems.

In this paper, we construct an adjoint data assimilation model using the characteristic finite difference (CFD) scheme which has high accuracy and enables large time steps. Numerical experiments show that CFD can get more accurate results than central difference scheme (CDS) [10]. Ideal experiments of inverse problems for model variables are carried out. Applying CFD in the adjoint data assimilation model, simulation errors are reduced and time step sizes can be increased, which improves the calculation efficiency a lot.

The paper is structured as follows. Section 2 introduces the pollutant transport model, the adjoint model, and the CFD. In Section 3, numerical experiments are carried out and results are analyzed. Finally, conclusions are given in Section 4.

2. Model and Method

2.1. Three-Dimensional Marine Pollutant Transport Model. For the simulation of the pollutant transport in Bohai Sea, the initial field and the source and sink terms of pollutants have significant influences on the results. In this paper, we mainly consider the convection and diffusion processes, while other chemical and biological changes are included in the source and sink terms. The three-dimensional marine pollutant transport model [10] is given as below:

$$\begin{aligned} & \frac{\partial C}{\partial t} + u \frac{\partial C}{\partial x} + v \frac{\partial C}{\partial y} + w \frac{\partial C}{\partial z} \\ &= \frac{\partial}{\partial x} \left(A_H \frac{\partial C}{\partial x} \right) + \frac{\partial}{\partial y} \left(A_H \frac{\partial C}{\partial y} \right) + \frac{\partial}{\partial z} \left(K_H \frac{\partial C}{\partial z} \right) \quad (1) \\ &+ \theta, \end{aligned}$$

meanings of symbols in (1) are presented in Table 1.

TABLE 1: The symbols in the pollutant transport model (1).

Symbol	Meaning
C	Pollutant concentration
u	Convection velocity in the east-west direction
v	Convection velocity in the north-south direction
w	Convection velocity in vertical direction
A_H	Horizontal diffusion coefficient
K_H	Vertical diffusion coefficient
θ	The source and sink terms of pollutants

The boundary conditions of the above model are set to

$$\begin{aligned} \frac{\partial C}{\partial t} &= 0, \quad V_n \leq 0, \\ \frac{\partial C}{\partial n} &= 0, \quad V_n > 0, \end{aligned} \quad (2)$$

where \vec{n} is the outward normal to the boundary and V_n is the normal velocity of the boundary.

Assuming the pollutant concentrations at the grid points are known at $t = t^n$, in order to obtain the pollutant concentration at $t = t^{n+1}$, characteristic method is used here. Following the characteristic curve from a point (x_i, y_j, z_k) at $t = t^{n+1}$, the intersection point $(\bar{x}_i, \bar{y}_j, \bar{z}_k)$ of the curve with time level $t = t^n$ can be obtained. We approximate the point by $\bar{x}_i \approx x_i - u_{i,j,k}^n \cdot \Delta t$, $\bar{y}_j \approx y_j - v_{i,j,k}^n \cdot \Delta t$, and $\bar{z}_k \approx z_k - w_{i,j,k}^n \cdot \Delta t$.

The characteristic finite difference (CFD) scheme of the pollutant transport model (1) is given as

$$\begin{aligned} & \frac{C1_{i,j,k} - \bar{C}_{i,j,k}^n}{\Delta t} \\ &= A_H \frac{C1_{i+1,j,k} - 2C1_{i,j,k} + C1_{i-1,j,k}}{(\Delta x_j)^2} + \theta_{i,j,k}^n, \end{aligned} \quad (3)$$

$$\frac{C2_{i,j,k} - \bar{C}_{i,j,k}^n}{\Delta t} = A_H \frac{C2_{i,j+1,k} - 2C2_{i,j,k} + C2_{i,j-1,k}}{(\Delta y)^2}, \quad (4)$$

$$\begin{aligned} & \frac{C_{i,j,k}^{n+1} - \bar{C}_{i,j,k}^n}{\Delta t} \\ &= K_H \left(\frac{C_{i,j,k+1}^{n+1} - C_{i,j,k}^{n+1}}{\Delta z_k \cdot \Delta z_{k+1/2}} - \frac{C_{i,j,k}^{n+1} - C_{i,j,k-1}^{n+1}}{\Delta z_k \cdot \Delta z_{k-1/2}} \right), \end{aligned} \quad (5)$$

where $\bar{C}_{i,j,k}^n$, $\bar{C}_{i,j,k}^n$, and $\bar{C}_{i,j,k}^n$ are obtained from the following schemes:

$$\bar{C}_{i,j,k}^n = \frac{x_{r+1} - \bar{x}_i}{\Delta x_j} C_{r,j,k}^n + \frac{\bar{x}_i - x_r}{\Delta x_j} C_{r+1,j,k}^n, \quad (6)$$

$$\bar{C}_{i,j,k}^n = \frac{y_{m+1} - \bar{y}_j}{\Delta y} C_{i,m,k}^n + \frac{\bar{y}_j - y_m}{\Delta y} C_{i,m+1,k}^n, \quad (7)$$

$$\bar{C}_{i,j,k}^n = \frac{z_{l+1} - \bar{z}_k}{\Delta z_l} C_{i,j,l}^n + \frac{\bar{z}_k - z_l}{\Delta z_{l+1}} C_{i,j,l+1}^n. \quad (8)$$

The CFD of the adjoint (15) is

$$\frac{\lambda 1_{i,j,k} - \bar{\lambda}_{i,j,k}^{n+1}}{\Delta t} = A_H \frac{\lambda 1_{i+1,j,k} - 2\lambda 1_{i,j,k} + \lambda 1_{i-1,j,k}}{(\Delta x_j)^2} + K \left(C_{i,j,k}^{n+1} - C_{i,j,k}^{n+1} \right), \quad (17)$$

$$\frac{\lambda 2_{i,j,k} - \bar{\lambda}_{i,j,k}}{\Delta t} = A_H \frac{\lambda 2_{i,j+1,k} - 2\lambda 2_{i,j,k} + \lambda 2_{i,j-1,k}}{(\Delta y)^2}, \quad (18)$$

$$\frac{\lambda_{i,j,k}^n - \bar{\lambda}_{i,j,k}^n}{\Delta t} = K_H \left(\frac{\lambda_{i,j,k+1}^n - \lambda_{i,j,k}^n}{\Delta z_k \cdot \Delta z_{k+1/2}} - \frac{\lambda_{i,j,k}^n - \lambda_{i,j,k-1}^n}{\Delta z_k \cdot \Delta z_{k-1/2}} \right), \quad (19)$$

where $\bar{\lambda}_{i,j,k}^{n+1}$, $\bar{\lambda}_{i,j,k}$, and $\bar{\lambda}_{i,j,k}^n$ are obtained from the following schemes:

$$\bar{\lambda}_{i,j,k}^{n+1} = \frac{x_{r+1} - \bar{x}_i}{\Delta x_j} \lambda_{r,j,k}^{n+1} + \frac{\bar{x}_i - x_r}{\Delta x_j} \lambda_{r+1,j,k}^{n+1}, \quad (20)$$

$$\bar{\lambda}_{i,j,k} = \frac{y_{m+1} - \bar{y}_j}{\Delta y} \lambda_{i,m,k} + \frac{\bar{y}_j - y_m}{\Delta y} \lambda_{i,m+1,k}, \quad (21)$$

$$\bar{\lambda}_{i,j,k}^n = \frac{z_{l+1} - \bar{z}_k}{\Delta z_l} \lambda_{i,j,l} + \frac{\bar{z}_k - z_l}{\Delta z_{l+1}} \lambda_{i,j,l+1}. \quad (22)$$

Based on (13), we can get the gradient of the cost function on the initial conditions of pollutant concentration $C_{i,j,k}^0$ [22]

$$\frac{\partial J}{\partial C^0} = \left[\frac{\partial \lambda}{\partial t} + u \frac{\partial \lambda}{\partial x} + v \frac{\partial \lambda}{\partial y} + w \frac{\partial \lambda}{\partial z} - \frac{\partial}{\partial x} \left(A_H \frac{\partial \lambda}{\partial x} \right) - \frac{\partial}{\partial x} \left(A_H \frac{\partial \lambda}{\partial y} \right) - \frac{\partial}{\partial x} \left(K_H \frac{\partial \lambda}{\partial z} \right) \right]^0, \quad (23)$$

Then the optimization of the initial condition can be obtained using the steepest descent method. The relationship between C^0 and the gradient is as follows:

$$C_{new}^0 = C_{old}^0 - \alpha \frac{\partial J}{\partial C^0}, \quad (24)$$

where α is the step size of the steepest descent method.

With the initial condition obtained using the adjoint method, we can get more accurate simulation results of the pollutant transport model.

3. Numerical Experiments

In this section, we will first carry out numerical tests to observe the performance of the characteristic finite difference (CFD) scheme. Two-dimensional problems of pollutant

transport are solved and results obtained from CFD and a first order in time central difference scheme (CDS) [10] are compared. Then we analyze the inversion of the initial field and the source and sink terms of pollutants to further explain the advantages of CFD.

3.1. Comparison of Different Schemes. We consider the two-dimensional pollutant transport model:

$$\frac{\partial C}{\partial t} + u \frac{\partial C}{\partial x} + v \frac{\partial C}{\partial y} = \frac{\partial}{\partial x} \left(A_H \frac{\partial C}{\partial x} \right) + \frac{\partial}{\partial y} \left(A_H \frac{\partial C}{\partial y} \right) + \theta. \quad (25)$$

The characteristic finite difference (CFD) scheme of the two-dimensional model is

$$\frac{C_{i,j}^{n+1} - \bar{C}_{i,j}^n}{\Delta t} = A_H \frac{C_{i+1,j}^{n+1} - 2C_{i,j}^{n+1} + C_{i-1,j}^{n+1}}{(\Delta x_j)^2} + A_H \frac{C_{i,j+1}^{n+1} - 2C_{i,j}^{n+1} + C_{i,j-1}^{n+1}}{(\Delta y)^2} + \theta_{i,j}^n, \quad (26)$$

where $\bar{C}_{i,j}^n$ is the pollutant concentration at the point (\bar{x}_i, \bar{y}_j) , which is obtained from the following scheme:

$$\bar{C}_{i,j}^n = a_{00} C_{r,m}^n + a_{01} C_{r,m+1}^n + a_{10} C_{r+1,m}^n + a_{11} C_{r+1,m+1}^n, \quad (27)$$

with

$$\begin{aligned} a_{00} &= \frac{x_{r+1} - \bar{x}_i}{\Delta x} \cdot \frac{y_{m+1} - \bar{y}_j}{\Delta y}, \\ a_{01} &= \frac{x_{r+1} - \bar{x}_i}{\Delta x} \cdot \frac{\bar{y}_j - y_m}{\Delta y}, \\ a_{10} &= \frac{\bar{x}_i - x_r}{\Delta x} \cdot \frac{y_{m+1} - \bar{y}_j}{\Delta y}, \\ a_{11} &= \frac{\bar{x}_i - x_r}{\Delta x} \cdot \frac{\bar{y}_j - y_m}{\Delta y}. \end{aligned} \quad (28)$$

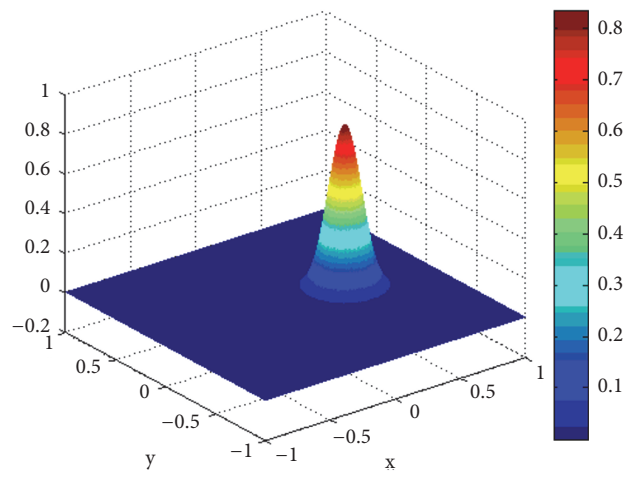
And the central difference scheme (CDS) [10] is

$$\begin{aligned} \frac{C_{i,j}^{n+1} - C_{i,j}^n}{\Delta t} &= -u_{i,j}^n \frac{C_{i+1,j}^n - C_{i-1,j}^n}{2\Delta x_j} - v_{i,j}^n \frac{C_{i,j+1}^n - C_{i,j-1}^n}{2\Delta y} \\ &+ A_H \frac{C_{i+1,j}^n - 2C_{i,j}^n + C_{i-1,j}^n}{(\Delta x_j)^2} \\ &+ A_H \frac{C_{i,j+1}^n - 2C_{i,j}^n + C_{i,j-1}^n}{(\Delta y)^2} + \theta_{i,j}^n. \end{aligned} \quad (29)$$

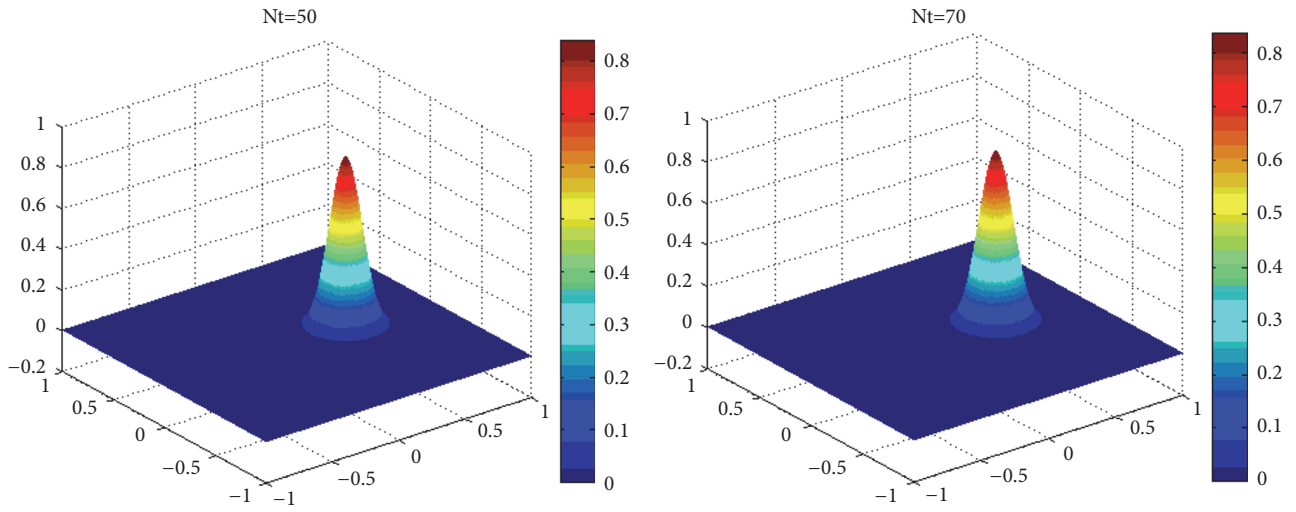
Consider model (25) with the initial condition:

$$C(x, y, 0) = \exp \left(-\frac{(x - x_0)^2 + (y - y_0)^2}{2\sigma_0^2} \right), \quad (30)$$

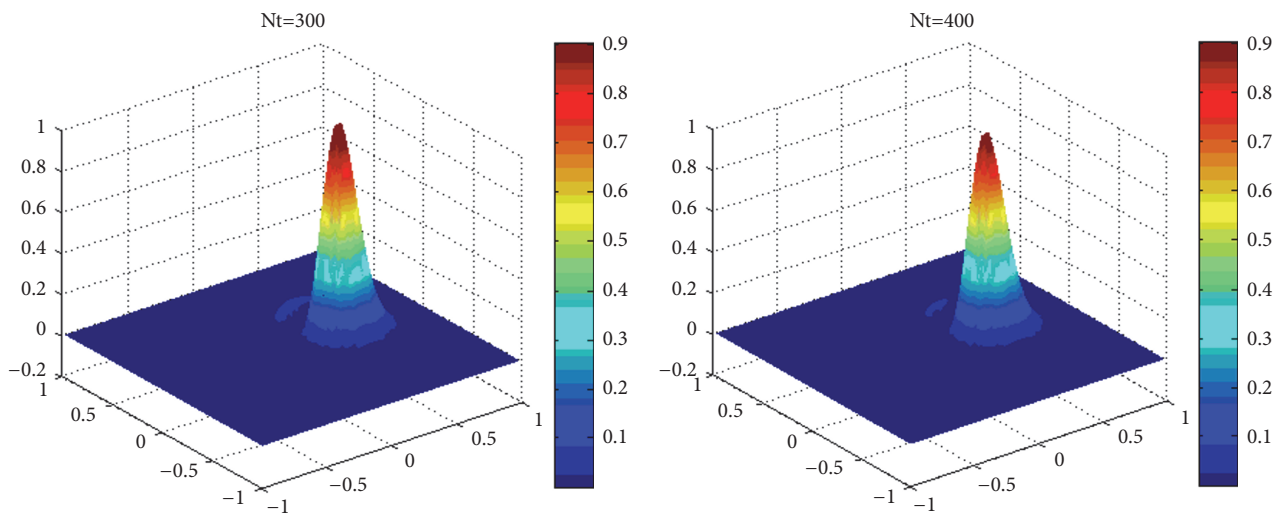
$(x, y) \in \Omega,$



(a) The exact solution



(b) Solution of the CFD



(c) Solution of the CDS

FIGURE 2: The exact solution and approximate solutions of different schemes with different time steps.

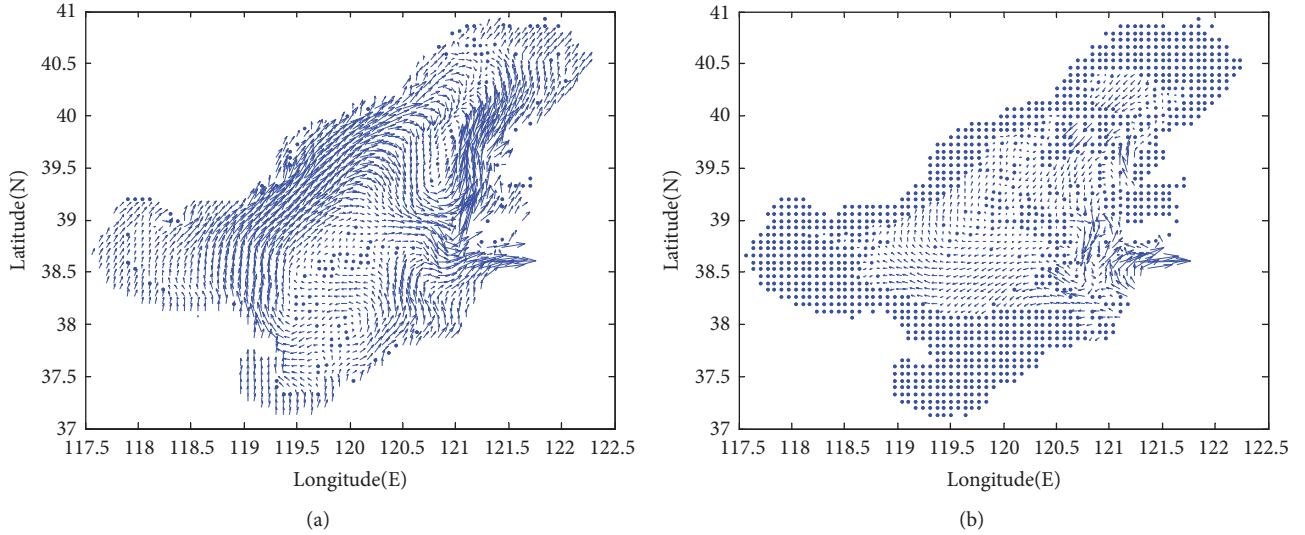


FIGURE 3: The average flow field of Bohai Sea in May 209. Figures (a) and (b) are the average flow field of the first and third layers.

in domain $\Omega = [-1, 1] \times [-1, 1]$ and on $[0, T] = [0, \pi/4]$. The initial center is $(x_0, y_0) = (-0.4, 0)$ and $\sigma_0^2 = 0.01$. Besides, the diffusion coefficient A_H and the source and sink terms of pollutants θ are set to 0.0001 and 0, respectively. The variable velocity field is $u = -4y, v = 4x$.

The exact solution of the problem with the given initial condition is

$$C(x, y, t) = \exp\left(-\frac{(x-x_0)^2 + (y-y_0)^2}{2\sigma_0^2 + 4Kt}\right), \quad (31)$$

where $x = x \cos(4t) + y \sin(4t)$, $y = -x \sin(4t) + y \cos(4t)$.

Let $C^n(x, y)$ be the numerical solution. The errors in L_∞ -norm and L_2 -norm are calculated by

$$E_\infty = \max_i \max_j \{|C(x_i, y_j, t^n) - C^n(x_i, y_j)|\},$$

$$E_2 = \sqrt{\sum_i \sum_j \Delta x \Delta y (C(x_i, y_j, t^n) - C^n(x_i, y_j))^2}. \quad (32)$$

We now compute the errors and ratios in time. In order to eliminate the effect of the error in space, a small space step size $\Delta x = \Delta y = 1/30$ is used. $\Delta t = T/N_t$ denotes the time step size, where N_t means the time step number. By choosing different $N_t = 40, 50, 60, 70$, and 80 , we compute the errors and ratios of the CFD in time, while we compute the errors and ratios of the CDS by choosing $N_t = 250, 300, 350, 400$, and 450 in order to ensure stability.

The exact solution, the solution of the CFD with $N_t = 50$ and 70 , and the solution of CDS with $N_t = 300$ and 400 are shown in Figure 2. Tables 2 and 3 present the results of the L_∞ and L_2 error of the characteristic finite difference (CFD) scheme and the central difference scheme (CDS). It is clearly shown that both two different schemes have first-order accuracy in time. However, the numerical simulation errors of CFD are smaller, even though the time step sizes of the CFD are much larger than those of the CDS. For example,

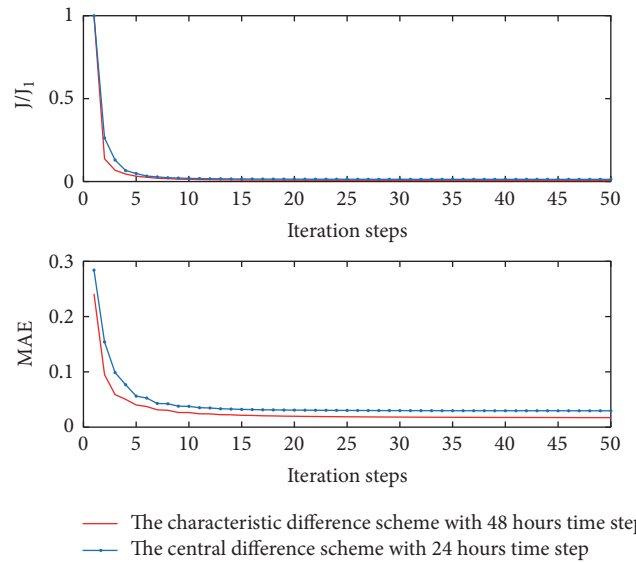


FIGURE 4: The descending curves of the relative magnitude of the cost function J/J_1 and the mean absolute error (MAE) of observation points using CFD and CDS with different time steps.

when $N_t = 300$, the E_∞ error and the E_2 error of CDS are 3.8256×10^{-1} and 6.6713×10^{-2} , while the E_∞ error and the E_2 error of CFD are 2.4370×10^{-1} and 4.5245×10^{-2} when $N_t = 50$.

The results show that the characteristic finite difference scheme can use large time step sizes to get better solutions of the pollutant transport model (25) than the central difference scheme.

3.2. The Inversion of the Initial Field and the Source and Sink Terms. In this section, we study the inversion of the initial field and the source and sink terms of pollutants through ideal experiments; the ‘‘observation data’’ used in the

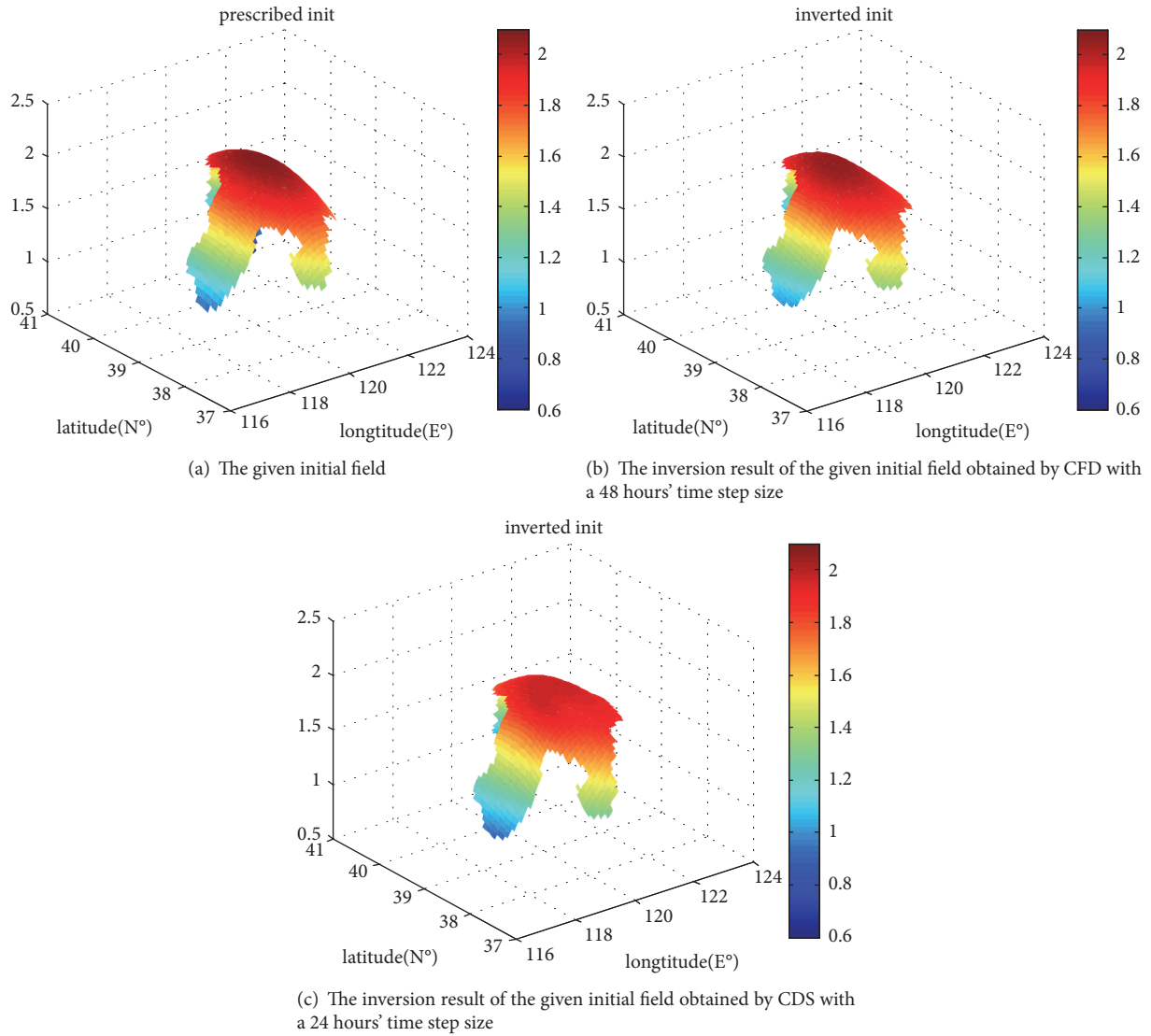


FIGURE 5: Figures of the initial distribution inverted by the adjoint method of data assimilation with CFD and CDS.

TABLE 2: Errors and ratios in time of the characteristic finite difference scheme (CFD).

N_t	40	50	60	70	80
E_∞	3.0017E-01	2.4370E-01	2.0544E-01	1.7835E-01	1.5751E-01
Ratio	-	0.93394	0.93686	0.91736	0.93042
E_2	5.5471E-02	4.5245E-02	3.8185E-02	3.3043E-02	2.9150E-02
Ratio	-	0.91318	0.93054	0.93812	0.93893

TABLE 3: Errors and ratios in time of the central difference scheme (CDS).

N_t	250	300	350	400	450
E_∞	4.3826E-01	3.8256E-01	3.4791E-01	3.2436E-01	3.0875E-01
Ratio	-	0.74551	0.61569	0.52489	0.41870
E_2	7.8419E-02	6.6713E-02	5.9804E-02	5.5299E-02	5.2169E-02
Ratio	-	0.88673	0.70920	0.58651	0.49468

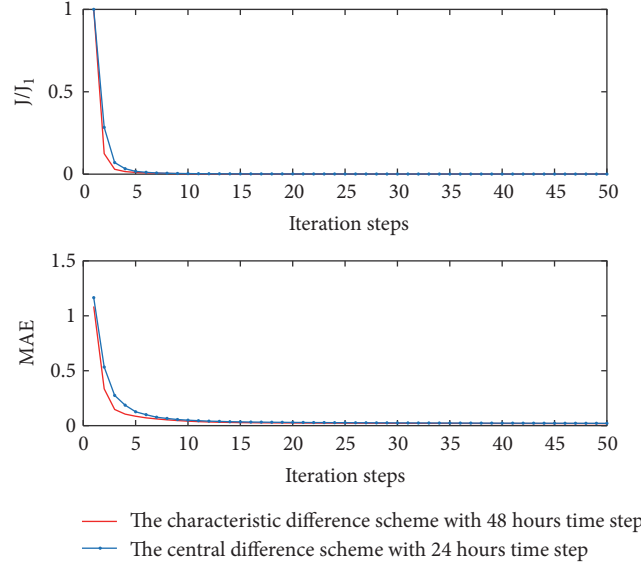


FIGURE 6: The descending curves of the relative magnitude of the cost function J/J_1 and the mean absolute error (MAE) of observation points using CFD and CDS with different time steps.

assimilation process is the simulation result obtained from pollutant transport model.

The experiments are carried out in the following steps.

Step 1. Give an initial field of pollutants and operate the forward model (1). The simulation result obtained from the forward model is regarded as the “observation data.”

Step 2. Give a guess value of the initial field and operate the forward model again. We will get the simulation result.

Step 3. Compute the cost function (9) with the “observation data” of Step 1 and the simulation results of Step 2.

Step 4. Operate the adjoint model. Here we compute the gradient of the cost function on initial conditions and adjust the initial field of pollutants with the gradient. A new predicted value is got and then go to Step 2. The iterative stops when the cost function is decreased to a given small value or the iteration steps reaches to a given number.

3.2.1. Model Settings. The domain of pollutant transport model (1) is set to $37^\circ N \sim 41^\circ N$ and $117.5^\circ E \sim 122.5^\circ E$ and the horizontal resolution is $4' \times 4'$. The vertical direction is divided into 6 layers and the thickness of each layer is $10m, 10m, 10m, 20m, 25m,$ and $25m$ from top to bottom. The horizontal diffusion coefficient and vertical diffusion coefficient are $100m^2/s$ and $0.00001m^2/s$, respectively. Numerical experiments are implemented with the hydrodynamic background field calculated by FVCOM (Finite Volume Coastal Ocean Model) [24], which has been widely used in the study of tide and storm surge in the Bohai Sea [25, 26]. The simulation time is 30 days and the average flow field of Bohai Sea in May 2009 is used here, the first and third layers of which are shown in Figure 3.

3.2.2. The Inversion of the Initial Field. In order to further explain the advantages of the characteristic finite difference (CFD) scheme, we set the time step size of the CFD to be 48 hours, while we set that of the central difference scheme (CDS) to be 24 hours in the inversion of the initial field.

We first consider an initial field which presents a downwardly directed opening and satisfies the following:

$$C(i, j, k) = \begin{cases} 0, & 1.75 * \text{lon}(i) - 3.5 * \frac{120.5}{2} + 37 - \text{lat}(j) > 0 \text{ or } \text{gs}(i, j, k) = 0, \\ -\frac{(\text{lon}(i) - 120)^2 + (\text{lat}(j) - 39)^2}{5} + 2.1, & \text{otherwise,} \end{cases} \quad (33)$$

where $\text{lon}(i)$ and $\text{lat}(j)$ denote the longitude and latitude at the grid point (i, j) in the simulation domain, and $\text{gs}(i, j, k)$ is the wet and dry condition at the point (i, j, k) and takes 0 for land and 1 for water.

Figure 4 presents the fact that the relative magnitude of the cost function J/J_1 and the mean absolute error (MAE) of observation points of the adjoint model using the characteristic finite difference (CFD) scheme decline more

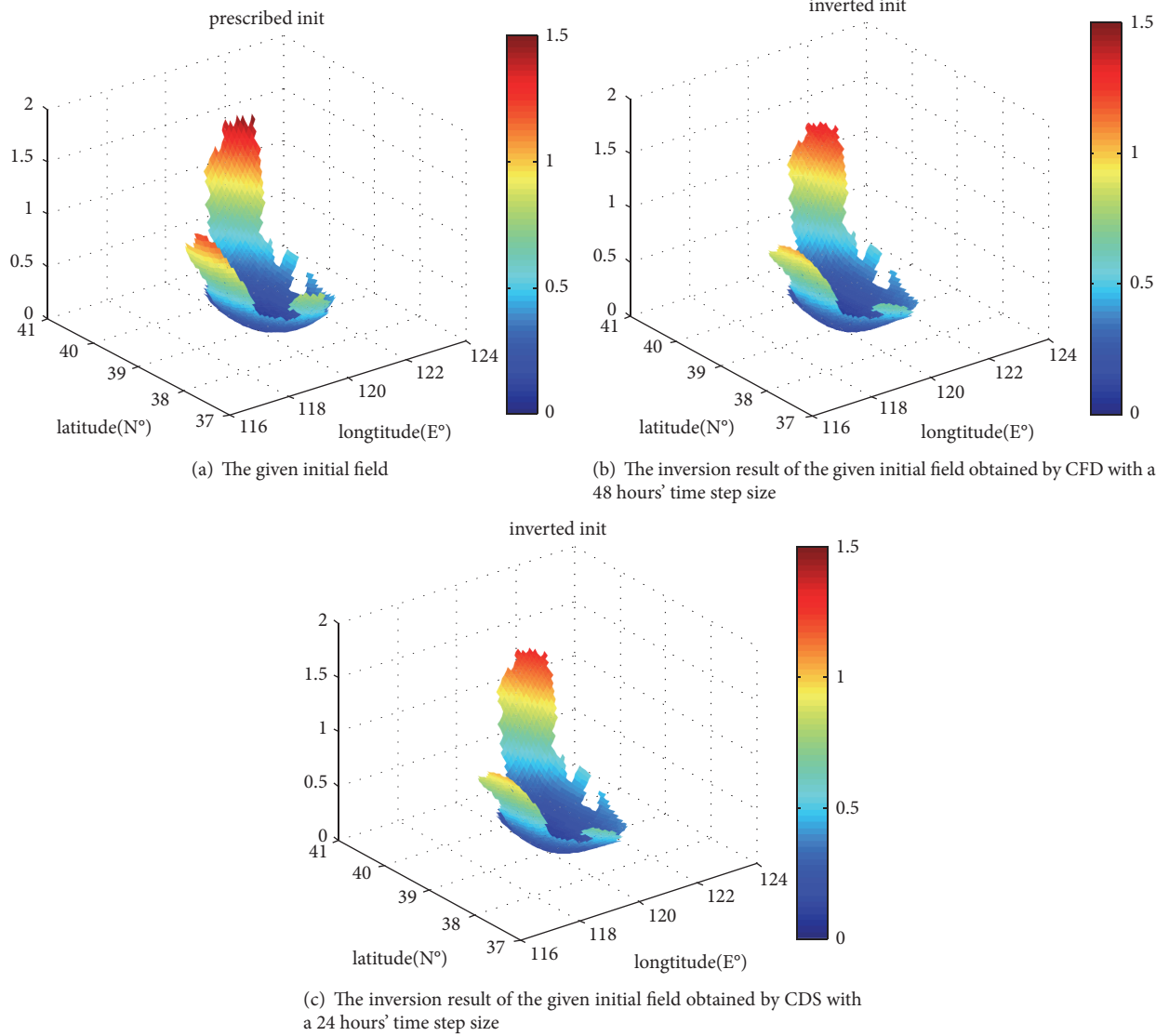


FIGURE 7: Figures of the initial distribution inverted by the adjoint method of data assimilation with CFD and CDS.

quickly. Table 4 shows that when using CFD with a 48 hours' time step size, J/J_1 decreases by 3 orders of magnitude to 6.0650×10^{-3} and the MAE of observation points decreases by 92.87%, from 0.24121 mg/L to 0.01720 mg/L. However, when using the central difference scheme (CDS) with a 24 hours' time step size that is a half of the CFD's, J/J_1 is reduced to 1.3303×10^{-2} and the MAE of observation points decreases by 89.58% only.

Figure 5(a) is the given initial field and Figures 5(b) and 5(c) are the inversion results obtained by CFD with a 48

hours' time step size and CDS with a 24 hours' time step size, respectively. From Figure 5, we can see that the inversion result obtained by CFD with 48 hours is almost the same as the original distribution and better than the CDS with a 24 hours' time step size. That is to say, CFD gets better inversion of the initial distribution of pollutants with a larger time step size.

Then we consider an initial field which presents an upwardly directed opening and satisfies the following:

$$C(i, j, k) = \begin{cases} 0, & 1.75 * lon(i) - 3.5 * \frac{120.5}{2} + 37 - lat(j) > 0 \text{ or } gs(i, j, k) = 0, \\ \frac{(lon(i) - 120)^2 + (lat(j) - 39)^2}{5} + 0.05, & \text{otherwise.} \end{cases} \quad (34)$$

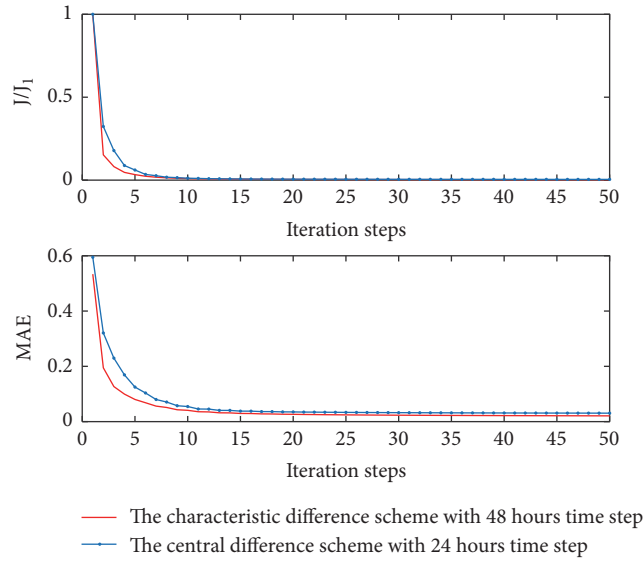


FIGURE 8: The descending curves of the relative magnitude of the cost function J/J_1 and the mean absolute error (MAE) of observation points using CFD and CDS with different time steps.

TABLE 4: The results of the adjoint model using CFD and CDS.

Method	Time step size (h)	Relative magnitude of the cost function	Mean absolute error of observation points		
			Before assimilation (mg/L)	After assimilation (mg/L)	Rate of decline
CFD	48	6.0650×10^{-3}	0.24121	0.01720	92.87%
CDS	24	1.3303×10^{-2}	0.28406	0.02959	89.58%

TABLE 5: The results of the adjoint model using CFD and CDS.

Method	Time step size (h)	Relative magnitude of the cost function	Mean absolute error of observation points		
			Before assimilation (mg/L)	After assimilation (mg/L)	Rate of decline
CFD	48	5.0118×10^{-4}	1.08499	0.01873	98.27%
CDS	24	6.1274×10^{-4}	1.16529	0.02102	98.20%

TABLE 6: The results of the adjoint model using CFD and CDS.

Method	Time step size (h)	Relative magnitude of the cost function	Mean absolute error of observation points		
			Before assimilation (mg/L)	After assimilation (mg/L)	Rate of decline
CFD	48	2.7084×10^{-3}	0.53359	0.02083	96.10%
CDS	24	4.4638×10^{-3}	0.59472	0.03060	94.86%

The relative magnitude of the cost function J/J_1 and the mean absolute error (MAE) of observation points of the adjoint model using CFD decline more quickly, which are shown in Figure 6. The given initial field and the inversion

results obtained by CFD with a 48 hours' time step size and CDS with a 24 hours' time step size are given in Figure 7. Table 5 shows that when using CFD with a 48 hours' time step size, the relative magnitude of the cost function

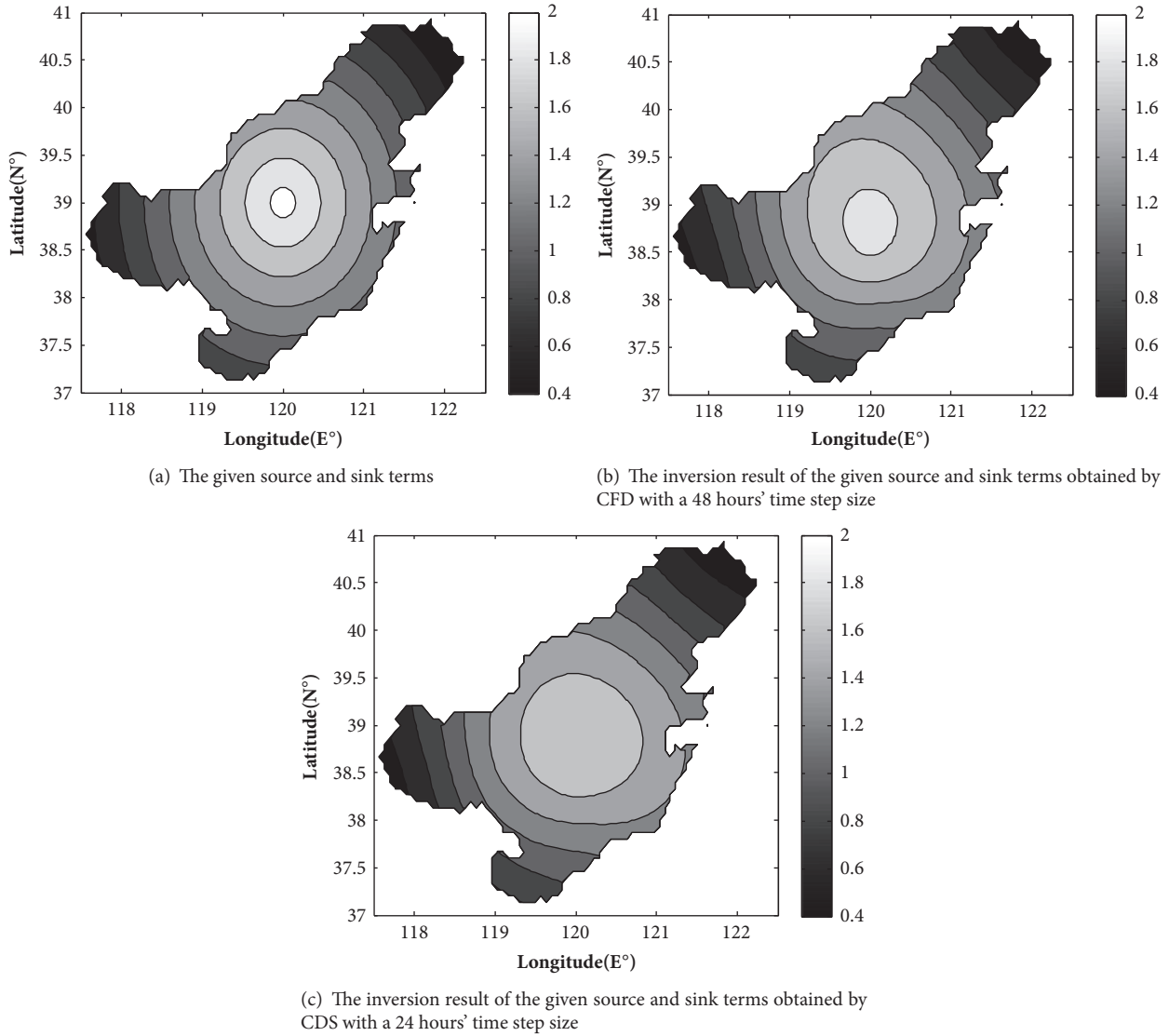


FIGURE 9: Figures of the source and sink terms inverted by the adjoint method of data assimilation with CFD and CDS.

J/J_1 decreases to 5.0118×10^{-4} and the mean absolute error (MAE) of observation points decreases by 98.27%, from 1.08499 mg/L to 0.01873 mg/L. When using CDS with a 24 hours' time step size, J/J_1 is reduced to 6.1274×10^{-4} and the MAE of observation points decreases by 98.20%. The inversion result of the adjoint model obtained by the CDS is inferior to that obtained by CFD with a large time step size.

Based on the inversion of the initial field, it is clearly shown that applying the characteristic finite difference

scheme in the adjoint model can reduce the simulation error and enable using large time steps to improve the calculation efficiency.

3.2.3. The Inversion of the Source and Sink Terms. For the inversion of the source and sink terms, we also set the time step size of the CFD to be 48 hours, while the time step size of the CDS is set to be 24 hours.

We first consider the source and sink terms which present a downwardly directed opening and satisfy the following:

$$\theta(i, j) = \begin{cases} 0, & \text{sur_gs}(i, j, 1) = 0, \\ -\sqrt{[(lon(i) - 120)^2 + (lat(j) - 39)^2]} * 0.41 + 2.1, & \text{otherwise,} \end{cases} \quad (35)$$

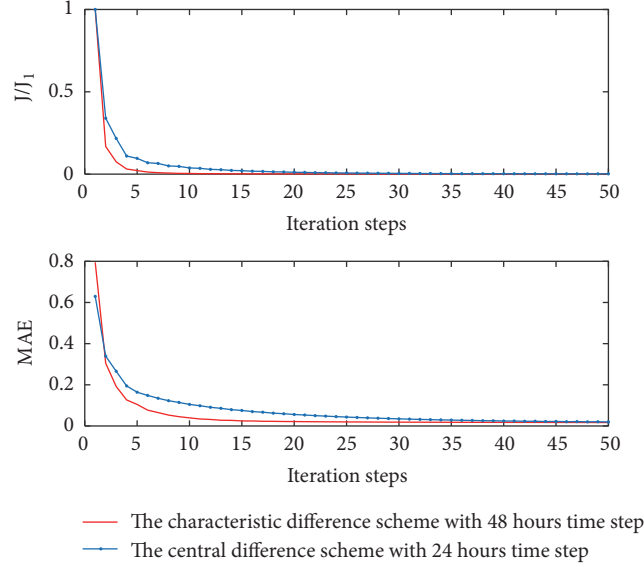


FIGURE 10: The descending curves of the relative magnitude of the cost function J/J_1 and the mean absolute error (MAE) of observation points using CFD and CDS with different time steps.

where $sur_gs(i, j, 1)$ is the wet and dry condition at the surface point (i, j) and takes 0 for land and 1 for water.

Figure 8 also shows that the relative magnitude of the cost function J/J_1 and the mean absolute error (MAE) of observation points of the adjoint model using the characteristic finite difference (CFD) scheme decline more quickly than the central difference scheme (CDS). Figure 9 is the given source and sink terms and the inversion results obtained by CFD with a 48 hours' time step size and the CDS with a 24 hours' time step size. It is clear that in Table 6 the relative magnitude

of the cost function J/J_1 decreases to 2.7084×10^{-3} and the mean absolute error (MAE) of observation points decreases by 96.10%, from 0.53359 mg/L to 0.02083 mg/L, when the time step size of the CFD is 48 hours. And when using CDS with a 24 hours' time step size, J/J_1 is reduced to 4.4638×10^{-3} and the MAE of observation points decreases by 94.86%.

We then consider the source and sink terms which present an upwardly directed opening and satisfy the following:

$$\theta(i, j) = \begin{cases} 0, & sur_gs(i, j, 1) = 0, \\ \sqrt{[(lon(i) - 120)^2 + (lat(j) - 39)^2]} * 0.41 + 0.05, & otherwise. \end{cases} \quad (36)$$

In Figure 10, the relative magnitude of the cost function J/J_1 and the mean absolute error (MAE) of observation points of the adjoint model using the characteristic finite difference (CFD) scheme are presented, which decline more quickly. The given source and sink terms and the inversion results obtained by CFD with a 48 hours' time step size and CDS with a 24 hours' time step size are shown in Figure 11. From Table 7, we can see when using the characteristic finite difference (CFD) scheme with a 48 hours' time step size that the relative magnitude of the cost function J/J_1 decreases to 7.5274×10^{-4} and the mean absolute error (MAE) of observation points decreases by 97.90%, from 0.79497 mg/L to 0.01667 mg/L. And J/J_1 is reduced to 1.7942×10^{-3} and the MAE of observation points decreases by 96.89% using the central difference scheme (CDS) with a 24 hours' time step size.

From simulation results of this part, we can see that, by applying CFD in the adjoint data assimilation model, simulation errors can be reduced when time step sizes are increased, which improves the calculation efficiency a lot.

4. Conclusion

In this paper, we adopt the adjoint method of data assimilation with the characteristic finite difference (CFD) scheme to solve the pollutant transport problem of Bohai Sea. Comparing the results obtained using the CFD and the central difference scheme (CDS) with different time step sizes, it can be seen that the simulation error of the CFD using large time step is smaller than that of the CDS using small time step. From the inversion of the initial field and the source and sink terms of pollutants, we come to the conclusion that the

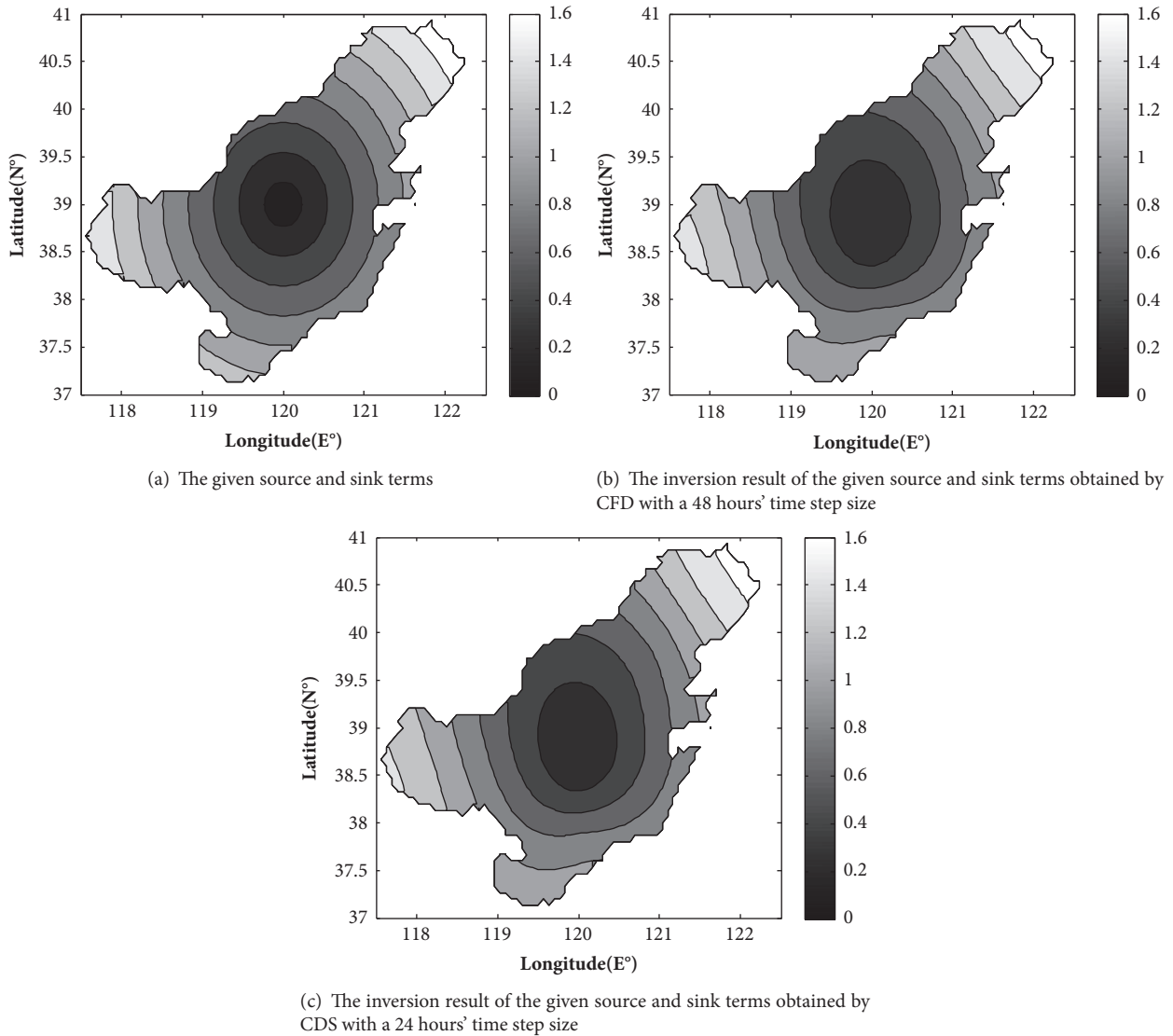


FIGURE 11: Figures of the source and sink terms inverted by the adjoint method of data assimilation with CFD and CDS.

TABLE 7: The results of the adjoint model using CFD and CDS.

Method	Time step size (h)	Relative magnitude of the cost function	Mean absolute error of observation points		
			Before assimilation (mg/L)	After assimilation (mg/L)	Rate of decline
CFD	48	7.5274×10^{-4}	0.79497	0.01667	97.90%
CDS	24	1.7942×10^{-3}	0.62949	0.01960	96.89%

adjoint model with CFD can reduce the simulation error and solve the problems effectively.

Data Availability

All results presented in the article were produced from model simulations. Therefore, there is no data to be made available. Researchers who wish to replicate the study will use the equations and parameters described in the article. With such

equations and parameters, researchers can use modeling simulations to replicate the tables and figures presented in the article.

Conflicts of Interest

The authors declare that there are no conflicts of interest regarding the publication of this paper.

Acknowledgments

Partial support for this research was provided by the National Natural Science Foundation of China (Grant no. 11601497), the Natural Science Foundation of Shandong Province (Grant no. ZR2016AB16), the National Key Research and Development Plan (Grant no. 2016YFC1402304), the Key Research and Development Plan of Shandong Province (Grant no. 2016ZDJS09A02), and the National Natural Science Foundation of China (Grant no. 41606006).

References

- [1] I. Gupta, S. Dhage, A. A. Chandorkar, and A. Srivastav, "Numerical modeling for Thane creek," *Environmental Modeling and Software*, vol. 19, no. 6, pp. 571–579, 2004.
- [2] I. H. Harms, M. J. Karcher, and D. Dethleff, "Modelling Siberian river runoff - Implications for contaminant transport in the Arctic Ocean," *Journal of Marine Systems*, vol. 27, no. 1, pp. 95–115, 2000.
- [3] G. A. Grell, S. E. Peckham, R. Schmitz et al., "Fully coupled 'online' chemistry within the WRF model," *Atmospheric Environment*, vol. 39, no. 37, pp. 6957–6975, 2005.
- [4] Z. Guo, H. Pan, W. Fan, and X. Lv, "Application of surface spline interpolation in inversion of bottom friction coefficients," *Journal of Atmospheric and Oceanic Technology*, vol. 34, no. 9, pp. 2021–2028, 2017.
- [5] Y. Liu, J. Yu, Y. Shen, and X. Lv, "A modified interpolation method for surface total nitrogen in the Bohai Sea," *Journal of Atmospheric and Oceanic Technology*, vol. 33, no. 7, pp. 1509–1517, 2016.
- [6] H. Elbern, H. Schmidt, and A. Ebel, "Variational data assimilation for tropospheric chemistry modeling," *Journal of Geophysical Research: Atmospheres*, vol. 102, no. D13, pp. 15967–15985, 1997.
- [7] S.-Q. Peng and L. Xie, "Effect of determining initial conditions by four-dimensional variational data assimilation on storm surge forecasting," *Ocean Modelling*, vol. 14, no. 1-2, pp. 1–18, 2006.
- [8] J.-C. Zhang and X.-Q. Lu, "Inversion of the bottom friction coefficient in 2D tidal model of the bohai, the yellow and east China seas," *Chinese Journal of Computational Mechanics*, vol. 24, no. 4, pp. 430–435, 2007.
- [9] X.-Q. Lv and W. Fan, "Numerical study on spatially varying parameters of a marine ecosystem model with the adjoint method," *Periodical of Ocean University of China*, vol. 30, no. 1, pp. 7–14, 2009.
- [10] C. Wang, X. Li, and X. Lv, "Numerical study on initial field of pollution in the Bohai sea with an adjoint method," *Mathematical Problems in Engineering*, pp. 389–405, 2013.
- [11] W. Fan and X. Lv, "Data assimilation in a simple marine ecosystem model based on spatial biological parameterizations," *Ecological Modelling*, vol. 220, no. 17, pp. 1997–2008, 2009.
- [12] H. Pan, Z. Guo, and X. Lv, "Inversion of tidal open boundary conditions of the M2 constituent in the bohai and yellow seas," *Journal of Atmospheric and Oceanic Technology*, vol. 34, no. 8, pp. 1661–1672, 2017.
- [13] J. Zhang, X. Lu, P. Wang, and Y. P. Wang, "Study on linear and nonlinear bottom friction parameterizations for regional tidal models using data assimilation," *Continental Shelf Research*, vol. 31, no. 6, pp. 555–573, 2011.
- [14] L. Yu and J. J. O'Brien, "On the Initial Condition in Parameter Estimation," *Journal of Physical Oceanography*, vol. 22, no. 11, pp. 1361–1364, 1992.
- [15] L. M. Lawson, Y. H. Spitz, E. E. Hofmann, and R. B. Long, "A data assimilation technique applied to a predator-prey model," *Bulletin of Mathematical Biology*, vol. 57, no. 4, pp. 593–617, 1995.
- [16] Q. Zhao, X. Hu, X. Lü, X. Xiong, and B. Yang, "Study on the transport of COD in the sea area around Maidaof off Qingdao coast using data assimilation," *Journal of Ocean University of China*, vol. 6, no. 4, pp. 339–344, 2007.
- [17] Q. Zhao and X. Lu, "Parameter estimation in a three-dimensional marine ecosystem model using the adjoint technique," *Journal of Marine Systems*, vol. 74, no. 1, pp. 443–452, 2008.
- [18] P. Qi, C. Wang, X. Li, and X. Lv, "Numerical study on spatially varying control parameters of a marine ecosystem dynamical model with adjoint method," *Acta Oceanologica Sinica*, vol. 30, no. 1, pp. 7–14, 2011.
- [19] J. Douglas Jr. and T. F. Russell, "Numerical methods for convection-dominated diffusion problems based on combining the method of characteristics with finite element or finite difference procedures," *SIAM Journal on Numerical Analysis*, vol. 19, no. 5, pp. 871–885, 1982.
- [20] S. Shen, F. Liu, V. Anh, I. Turner, and J. Chen, "A characteristic difference method for the variable-order fractional advection-diffusion equation," *Applied Mathematics and Computation*, vol. 42, no. 1-2, pp. 371–386, 2013.
- [21] K. Fu and D. Liang, "The conservative characteristic FD methods for atmospheric aerosol transport problems," *Journal of Computational Physics*, vol. 305, pp. 494–520, 2016.
- [22] M. Xu, K. Fu, and X. Lv, "Application of adjoint data assimilation method to atmospheric aerosol transport problems," *Advances in Mathematical Physics*, vol. 2017, no. 4, pp. 1–14, 2017.
- [23] X. Lv, Z. Wu, Y. Gu, and J. Tian, "Study on the adjoint method in data assimilation and the related problems," *Applied Mathematics and Mechanics -English Edition*, vol. 25, no. 6, pp. 636–646, 2004.
- [24] C. Chen, H. Liu, and R. C. Beardsley, "An unstructured grid, finite-volume, three-dimensional, primitive equations ocean model: Application to coastal ocean and estuaries," *Journal of Atmospheric and Oceanic Technology*, vol. 20, no. 1, pp. 159–186, 2003.
- [25] Y. Ding and H. Wei, "Research of the influential factors on the simulation of storm surge in the bohai sea," *Open Mechanical Engineering Journal*, vol. 8, no. 1, pp. 151–156, 2014.
- [26] P. Zhao and W. Jiang, "A numerical study of storm surges caused by cold-air outbreaks in the Bohai Sea," *Natural Hazards*, vol. 59, no. 1, pp. 1–15, 2011.

Research Article

On the Convergence Ball and Error Analysis of the Modified Secant Method

Rongfei Lin ¹, Qingbiao Wu ², Minhong Chen,³ and Xuemin Lei²

¹Department of Mathematics, Taizhou University, Linhai 317000, Zhejiang, China

²Department of Mathematics, Zhejiang University, Hangzhou 310027, Zhejiang, China

³Department of Mathematics, Zhejiang Sci-Tech University, Hangzhou 310012, Zhejiang, China

Correspondence should be addressed to Qingbiao Wu; qbwu@zju.edu.cn

Received 21 January 2018; Revised 14 March 2018; Accepted 11 April 2018; Published 2 July 2018

Academic Editor: Kaliyaperumal Nakkeeran

Copyright © 2018 Rongfei Lin et al. This is an open access article distributed under the Creative Commons Attribution License, which permits unrestricted use, distribution, and reproduction in any medium, provided the original work is properly cited.

We aim to study the convergence properties of a modification of secant iteration methods. We present a new local convergence theorem for the modified secant method, where the derivative of the nonlinear operator satisfies Lipschitz condition. We introduce the convergence ball and error estimate of the modified secant method, respectively. For that, we use a technique based on Fibonacci series. At last, some numerical examples are given.

1. Introduction

A large number of nonlinear dynamic systems and scientific engineering problems can be concluded to the form of nonlinear equation

$$f(x) = 0, \quad (1)$$

where f is a nonlinear operator defined on a convex subset D of a complex dimension space C . Hence, finding the roots of the nonlinear (1) is widely required in both mathematical physics and nonlinear dynamic system. Iterative methods are considerable methods. There are many iterative methods for solving the nonlinear equation.

Secant method [1, 2], which uses divided differences instead of the first derivative of the nonlinear operator, is one of the most famous iterative methods for solving the nonlinear equation. Secant method reads as follows:

$$x_{n+1} = x_n - [x_{n-1}, x_n; f]^{-1} f(x_n), \quad (2)$$

$(n \geq 0) \quad (x_0, x_{-1} \in D)$

where the operator $[x, y; f]$ is called a divided difference of first-order for the operator f on the points x and y ($x \neq y$) if the following equality holds:

$$[x, y; f](x - y) = f(x) - f(y). \quad (3)$$

Due to the well performance of the secant method, secant method and secant-like methods have been widely studied by many authors [3–11]. The authors [12] proposed a new method for solving the nonlinear equation.

Convergence ball is a very important issue in the study of the iterative procedures. When nonlinear operator f is first-order differentiable convex subset D can be open or closed, suppose x_* is the root of the equation $f(x) = 0$, an open area $B(x_*, R)$ is called the convergence ball of the iterative algorithm. Authors [13–17] have discussed the convergence of the iterative methods using a convergence ball $B(x_*, R)$ with center x_* and radius R . For example, Ren and Wu [15] discussed the convergence of the secant method under Hölder continuous divided differences using a convergence ball.

In this study, we consider the modified secant method with the below form based on [12]

$$x_{n+1} = x_n - \frac{f(x_n)(x_n - x_{n-1})}{3f(x_n) + f(x_{n-1}) - 4f((x_n + x_{n-1})/2)} \quad (4)$$

$(n \geq 0),$

and we will establish the convergence ball and give the error analysis of the modified secant method for the nonlinear equation.

2. Convergence Ball Study

Theorem 1. Suppose x_* is the root of the equation $f(x) = 0$ and $f'(x_*) \neq 0$. f is first-order differentiable, where the derivative of f satisfies the Lipschitz condition: $|f'(x_*)^{-1}(f'(x) - f'(y))| \leq K|x - y|$ for all $x, y \in D$ and $K > 0$. Then, the sequence $\{x_n\}$ generated by the modified secant method (4), starting from any two initial points $x_0, x_{-1} \in B(x_*, R)$, converges to the solution x_* . x_* is the unique solution in $B(x_*, 2/K)$, where $B(x_*, R) \subset B(x_*, 2/K)$. Moreover, the following error estimate holds:

$$|x_* - x_n| \leq R \left(\frac{|x_* - x_0|}{R} \right)^{F_n} \left(\frac{|x_* - x_{-1}|}{R} \right)^{F_{n-1}}$$

$$= \frac{2}{5K} \left(\frac{5K}{2} |x_* - x_0| \right)^{F_n} \left(\frac{5K}{2} |x_* - x_{-1}| \right)^{F_{n-1}} \quad (n \geq 1). \quad (5)$$

Here, $R = 2/5K$; $\{F_n\}$ is a Fibonacci series, $F_0 = F_1 = 1, F_{n+1} = F_n + F_{n-1}, (n \geq 1)$.

Proof. From the condition of Theorem 1, we know $x_0, x_{-1} \in B(x_*, R)$. Assume x_1, x_2, \dots, x_n are generated by the modified secant (4) and $x_k \in B(x_*, R) (0 \leq k \leq n)$. Following, we will prove that $x_{n+1} \in B(x_*, R)$; we have

$$\begin{aligned} x_* - x_{n+1} &= x_* - x_n + \frac{f(x_n)(x_n - x_{n-1})}{3f(x_n) + f(x_{n-1}) - 4f((x_n + x_{n-1})/2)} \\ &= x_* - x_n + \frac{(f(x_n) - f(x_*))(x_n - x_{n-1})}{3f[x_n, (x_n + x_{n-1})/2](x_n - (x_n + x_{n-1})/2) + f[x_{n-1}, (x_n + x_{n-1})/2](x_{n-1} - (x_n + x_{n-1})/2)} \\ &= x_* - x_n + \frac{f[x_n, x_*](x_n - x_*)(x_n - x_{n-1})}{(3f[x_n, (x_n + x_{n-1})/2] - f[x_{n-1}, (x_n + x_{n-1})/2])(x_n - x_{n-1})/2} \\ &= x_* - x_n + \frac{2f[x_n, x_*](x_n - x_*)}{3f[x_n, (x_n + x_{n-1})/2] - f[x_{n-1}, (x_n + x_{n-1})/2]} \\ &= (x_* - x_n) \left(1 - \frac{2f[x_n, x_*]}{3f[x_n, (x_n + x_{n-1})/2] - f[x_{n-1}, (x_n + x_{n-1})/2]} \right) \\ &= (x_* - x_n) \left(\frac{3f[x_n, (x_n + x_{n-1})/2] - f[x_{n-1}, (x_n + x_{n-1})/2] - 2f[x_n, x_*]}{3f[x_n, (x_n + x_{n-1})/2] - f[x_{n-1}, (x_n + x_{n-1})/2]} \right), \end{aligned} \quad (6)$$

f is first-order differentiable, so in convex domain D , first-order difference of f can be written in the following integral form:

$$f[x, y] = \frac{f(x) - f(y)}{x - y} = \int_0^1 f'(tx + (1-t)y) dt \quad (7)$$

$(x, y \in D)$.

Now, we give the estimate of

$$\left| \frac{3f[x_n, (x_n + x_{n-1})/2] - f[x_{n-1}, (x_n + x_{n-1})/2] - 2f[x_n, x_*]}{3f[x_n, (x_n + x_{n-1})/2] - f[x_{n-1}, (x_n + x_{n-1})/2]} \right|. \quad (8)$$

Obviously

$$\begin{aligned} &\left| f'(x_*)^{-1} \left(3f \left[x_n, \frac{x_n + x_{n-1}}{2} \right] - f \left[x_{n-1}, \frac{x_n + x_{n-1}}{2} \right] \right. \right. \\ &\quad \left. \left. - 2f[x_n, x_*] \right) \right| = \left| \int_0^1 f'(x_*)^{-1} \right. \\ &\quad \left. \cdot \left(3f' \left(tx_n + (1-t) \frac{x_n + x_{n-1}}{2} \right) \right. \right. \end{aligned}$$

$$\begin{aligned} &\left. - f' \left(tx_{n-1} + (1-t) \frac{x_n + x_{n-1}}{2} \right) \right. \\ &\quad \left. - 2f' \left(tx_n + (1-t)x_* \right) \right) dt \Big|, \end{aligned} \quad (9)$$

and

$$\begin{aligned} &\left| 2 - f'(x_*)^{-1} \left(3f \left[x_n, \frac{x_n + x_{n-1}}{2} \right] \right. \right. \\ &\quad \left. \left. - f \left[x_{n-1}, \frac{x_n + x_{n-1}}{2} \right] \right) \right| = \left| f'(x_*)^{-1} \left(2f'(x_*) \right. \right. \\ &\quad \left. \left. - 3f \left[x_n, \frac{x_n + x_{n-1}}{2} \right] + f \left[x_{n-1}, \frac{x_n + x_{n-1}}{2} \right] \right) \right| \\ &= \left| \int_0^1 f'(x_*)^{-1} \left(2f'(x_*) \right. \right. \\ &\quad \left. \left. - 3f' \left(tx_n + (1-t) \frac{x_n + x_{n-1}}{2} \right) \right. \right. \\ &\quad \left. \left. + f' \left(tx_{n-1} + (1-t) \frac{x_n + x_{n-1}}{2} \right) \right) dt \right|. \end{aligned} \quad (10)$$

Using Lipschitz condition with the above (9) and (10), we have

$$\begin{aligned} & \left| f'(x_*)^{-1} \left(3f \left[x_n, \frac{x_n + x_{n-1}}{2} \right] - f \left[x_{n-1}, \frac{x_n + x_{n-1}}{2} \right] \right. \right. \\ & \left. \left. - 2f[x_n, x_*] \right) \right| \leq \left| K \int_0^1 \left| \left(tx_n + (1-t) \frac{x_n + x_{n-1}}{2} \right) \right. \right. \\ & \left. \left. - \left(tx_{n-1} + (1-t) \frac{x_n + x_{n-1}}{2} \right) \right| dt \right| \\ & + \left| 2K \int_0^1 \left| \left(tx_n + (1-t) \frac{x_n + x_{n-1}}{2} \right) \right. \right. \end{aligned}$$

$$\begin{aligned} & \left. - (tx_n + (1-t)x_*) \right| dt \Big| \\ & \leq K \left| \frac{x_n - x_* + x_* - x_{n-1}}{2} \right| \\ & + 2K \left| \frac{(x_n - x_*) + (x_{n-1} - x_*)}{4} \right| \leq K|x_* - x_n| \\ & + K|x_* - x_{n-1}|, \end{aligned}$$

(11)

and

$$\begin{aligned} & \left| 2 - f'(x_*)^{-1} \left(3f \left[x_n, \frac{x_n + x_{n-1}}{2} \right] - f \left[x_{n-1}, \frac{x_n + x_{n-1}}{2} \right] \right) \right| \\ & \leq \left| \int_0^1 \left(2K|x_* - (tx_n + (1-t) \frac{x_n + x_{n-1}}{2}) \right) + K \left| \left(tx_{n-1} + (1-t) \frac{x_n + x_{n-1}}{2} \right) - \left(tx_n + (1-t) \frac{x_n + x_{n-1}}{2} \right) \right| \right| dt \Big| \\ & \leq 2K \int_0^1 \left| \frac{1+t}{2} (x_* - x_n) + \frac{1-t}{2} (x_* - x_{n-1}) \right| dt + K \int_0^1 |t(x_{n-1} - x_n)| dt \leq 2K \left(\frac{3}{4} |x_* - x_n| + \frac{1}{4} |x_* - x_{n-1}| \right) \\ & + \frac{K}{2} |(x_* - x_n) + (x_{n-1} - x_*)| \leq 2K|x_* - x_n| + K|x_* - x_{n-1}|. \end{aligned}$$

(12)

We divide above inequality (12) number 2, so

$$\begin{aligned} & \left| 1 - \frac{f'(x_*)^{-1}}{2} \left(3f \left[x_n, \frac{x_n + x_{n-1}}{2} \right] \right. \right. \\ & \left. \left. - f \left[x_{n-1}, \frac{x_n + x_{n-1}}{2} \right] \right) \right| \leq K|x_* - x_n| + \frac{K}{2}|x_* \\ & - x_{n-1}|. \end{aligned} \tag{13}$$

According to the definition of R and $x_n, x_{n-1} \in B(x_*, R)$, we get $K|x_* - x_n| + (K/2)|x_* - x_{n-1}| < 3/5 < 1$, by Banach Lemma, so $3f[x_n, (x_n + x_{n-1})/2] - f[x_{n-1}, (x_n + x_{n-1})/2]$ is reversible and also

$$\begin{aligned} & \left| 2f'(x_*) \right. \\ & \left. \cdot \left(3f \left[x_n, \frac{x_n + x_{n-1}}{2} \right] - f \left[x_{n-1}, \frac{x_n + x_{n-1}}{2} \right] \right)^{-1} \right| \end{aligned}$$

$$\leq \frac{1}{1 - K|x_* - x_n| - (K/2)|x_* - x_{n-1}|}.$$

(14)

Dividing (14) inequality number 2, we can get

$$\begin{aligned} & \left| f'(x_*) \right. \\ & \left. \cdot \left(3f \left[x_n, \frac{x_n + x_{n-1}}{2} \right] - f \left[x_{n-1}, \frac{x_n + x_{n-1}}{2} \right] \right)^{-1} \right| \\ & \leq \frac{1}{2 - 2K|x_* - x_n| - K|x_* - x_{n-1}|}, \end{aligned} \tag{15}$$

and with (11) and (15), we get following estimate formula:

$$\begin{aligned} & \left| \frac{3f[x_n, (x_n + x_{n-1})/2] - f[x_{n-1}, (x_n + x_{n-1})/2] - 2f[x_n, x_*]}{3f[x_n, (x_n + x_{n-1})/2] - f[x_{n-1}, (x_n + x_{n-1})/2]} \right| \\ & = \left| f'(x_*)^{-1} (3f[x_n, (x_n + x_{n-1})/2] - f[x_{n-1}, (x_n + x_{n-1})/2] - 2f[x_n, x_*]) \right| \\ & \times \left| f'(x_*) \left(3f \left[x_n, \frac{x_n + x_{n-1}}{2} \right] - f \left[x_{n-1}, \frac{x_n + x_{n-1}}{2} \right] \right)^{-1} \right| \leq \frac{K|x_* - x_n| + K|x_* - x_{n-1}|}{2 - 2K|x_* - x_n| - K|x_* - x_{n-1}|}, \end{aligned} \tag{16}$$

and with (6) and (16) and $x_n, x_{n-1} \in B(x_*, R)$, we get following estimate formula:

$$\begin{aligned}
 |x_* - x_{n+1}| &\leq |x_* - x_n| \left| \frac{3f[x_n, (x_n + x_{n-1})/2] - f[x_{n-1}, (x_n + x_{n-1})/2] - 2f[x_n, x_*]}{3f[x_n, (x_n + x_{n-1})/2] - f[x_{n-1}, (x_n + x_{n-1})/2]} \right| \\
 &\leq |x_* - x_n| \frac{K|x_* - x_n| + K|x_* - x_{n-1}|}{2 - 2K|x_* - x_n| - K|x_* - x_{n-1}|} \leq |x_* - x_n| \frac{KR + KR}{2 - 2KR - KR} = |x_* - x_n| < R.
 \end{aligned}
 \tag{17}$$

This means that $x_{n+1} \in B(x_*, R)$. So, from any $x_0, x_{-1} \in B(x_*, R)$, the sequence $\{x_n\}$ of the modified secant method is convergent, the root $x_* \in B(x_*, R)$, and by mathematical induction $x_n \in B(x_*, R) (n \geq 1)$.

In the following, we will derive the estimate of the modified secant method. Denote $e_n = x_* - x_n, \rho_n = |e_n|/R, (n \geq -1)$; from the above proof we can get $0 \leq \rho_n < 1 (n \geq -1)$; from inequality (17), it is known that $|e_{n+1}| \leq |e_n|$ and

$$\begin{aligned}
 |e_{n+1}| &\leq |e_n| \frac{K|e_n| + K|e_{n-1}|}{2 - 2K|e_n| - K|e_{n-1}|} \\
 &= \frac{K|e_n|^2 + K|e_{n-1}||e_n|}{2 - 2K|e_n| - K|e_{n-1}|} \\
 &< \frac{K|e_n|^2 + K|e_{n-1}||e_n|}{2 - 2KR - KR}.
 \end{aligned}
 \tag{18}$$

Hence, $|\rho_{n+1}| \leq |\rho_n|, (n \geq -1)$; moreover, we have

$$\begin{aligned}
 \rho_{n+1} &\leq \frac{K\rho_n^2 R + K\rho_n \rho_{n-1} R}{2 - 3KR} \leq \frac{K\rho_n \rho_{n-1} R + K\rho_n \rho_{n-1} R}{2 - 3KR} \\
 &= \frac{2KR}{2 - 3KR} \rho_n \rho_{n-1} = \rho_n \rho_{n-1},
 \end{aligned}
 \tag{19}$$

so, we obtain the inequality

$$\rho_n \leq \rho_{n-1} \rho_{n-2}, \quad (n \geq 1).
 \tag{20}$$

Now, we use mathematical induction to proof that the inequality $\rho_k \leq \rho_0^{F_k} \rho_{-1}^{F_{k-1}}, (k \geq 1)$ is correct.

$$\begin{aligned}
 \rho_1 &\leq \rho_0 \rho_{-1} = \rho_0^{F_1} \rho_{-1}^{F_0}, \\
 \rho_2 &\leq \rho_1 \rho_0 \leq \rho_0 \rho_{-1} \rho_0 = \rho_0^{F_2} \rho_{-1}^{F_1}, \\
 \rho_3 &\leq \rho_2 \rho_1 \leq \rho_0 \rho_{-1} \rho_0 \rho_0 = \rho_0^{F_3} \rho_{-1}^{F_2}.
 \end{aligned}
 \tag{21}$$

Suppose the inequality $\rho_k \leq \rho_0^{F_k} \rho_{-1}^{F_{k-1}}, (k \geq 1)$ is correct when $3 \leq k \leq n - 1$; here $\{F_k\}$ is Fibonacci sequence, $F_0 = F_1 = 1, F_{k+1} = F_k + F_{k-1}, (k \geq 1)$. So, when $k = n$, we have

$$\rho_n \leq \rho_{n-1} \rho_{n-2} \leq \rho_0^{F_{n-1}} \rho_{-1}^{F_{n-2}} \rho_0^{F_{n-2}} \rho_{-1}^{F_{n-3}} = \rho_0^{F_n} \rho_{-1}^{F_{n-1}}.
 \tag{22}$$

That means the inequality $\rho_k \leq \rho_0^{F_k} \rho_{-1}^{F_{k-1}}, (k \geq 1)$ has been proved. So

$$\rho_n \leq \rho_0^{F_n} \rho_{-1}^{F_{n-1}} \quad (n \geq 1).
 \tag{23}$$

From the definition of ρ_n and above formulation, we can get

$$\begin{aligned}
 |x_* - x_n| &\leq R \left(\frac{|x_* - x_0|}{R} \right)^{F_n} \left(\frac{|x_* - x_{-1}|}{R} \right)^{F_{n-1}} \\
 &= \frac{2}{5K} \left(\frac{5K}{2} |x_* - x_0| \right)^{F_n} \left(\frac{5K}{2} |x_* - x_{-1}| \right)^{F_{n-1}} \\
 &\quad (n \geq 1).
 \end{aligned}
 \tag{24}$$

At last, we show the uniqueness of the solution in the area $B(x_*, 2/K)$. Assume that there exists another solution $y_* \in B(x_*, 2/K), y_* \neq x_*$. We consider the operator $A = \int_0^1 f'(tx_* + (1-t)y_*) dt$. Since $A[y_* - x_*] = f(y_*) - f(x_*) = 0$, if operator A is invertible, then $y_* = x_*$. Indeed from (24), we have

$$\begin{aligned}
 &|1 - f'(x_*)^{-1} A| \\
 &= \left| f'(x_*)^{-1} \int_0^1 (f'(x_*) - f'(tx_* + (1-t)y_*)) dt \right| \\
 &\leq K \int_0^1 |(1-t)(x_* - y_*)| dt = \frac{K}{2} |x_* - y_*| < 1.
 \end{aligned}
 \tag{25}$$

Then, by Banach lemma, we can tell that operator A is invertible. From the definition of radius R , it is easy to verify that the ball $B(x_*, 2/K)$ is bigger than $B(x_*, R)$.

That completes the proof of Theorem 1. □

3. Numerical Examples

In this section, the convergence ball results were applied to numerical examples.

Example 1. Let us consider

$$f(x) = x^2 - 1, \quad x \in [0, 2].
 \tag{26}$$

It is obviously that $f'(x) = 2x, f(x) = 0$ has a root $x_* = 1$ and $f'(x_*) = 2$. It is easy to know

$$|f'(x_*)^{-1} (f'(x) - f'(y))| \leq |x - y|.
 \tag{27}$$

According to Theorem 1, we can obtain the fact that the radius of the convergence ball of the modified secant method is $R = 2/5K = 2/5 = 0.4$ at least.

Example 2. Let us consider the following numerical problem which has been studied in [4, 11, 13]:

$$\begin{aligned} f(x) &= e^x - 1, \\ D &= [-1, 1]. \end{aligned} \quad (28)$$

$f'(x) = e^x$, $x_* = 0$, and $f'(x_*) = 1$.

We know $|e^x - e^y| \leq e|x - y|$; hence,

$$\left| f'(x_*)^{-1} (f'(x) - f'(y)) \right| \leq e(|x - y|). \quad (29)$$

So $K = e$ in this problem.

By Theorem 1, we can obtain the fact that the radius of the convergence ball of the modified secant method is $R = 2/5K = 2/5e \approx 0.1472$ at least.

Example 3. Let us consider the nonlinear equation

$$f'(x) = \frac{2}{5} \sin x + x, \quad x \in [0, 2]. \quad (30)$$

Here, $f'(x) = (2/5) \cos x + 1$, $x_* = 0$, and $f'(x_*) = 7/5$.

We know that $|\cos x - \cos y| \leq |x - y|$; then it is obvious that

$$\left| f'(x_*)^{-1} (f'(x) - f'(y)) \right| \leq \frac{2}{7} |x - y|. \quad (31)$$

In this case, the radius of the convergence ball of the modified secant method is $R = 2/5K = 7/5 = 1.4$ at least, according to Theorem 1.

Data Availability

No data were used to support this study.

Conflicts of Interest

The authors declare that they have no conflicts of interest.

Acknowledgments

This work is supported by National Natural Science Foundation of China (Grant nos. 11771393, 11371320, and 11632015), Zhejiang Natural Science Foundation (Grant nos. LZ14A010002, LQ18A010008), Scientific Research Fund of Zhejiang Provincial Education Department (Grant no. FX2016073), and the Science Foundation of Taizhou University (Grant no. 2017PY028).

References

- [1] J. W. Schmidt, "Regula-falsi-Verfahren mit konsistenter Steigung und Majorantenprinzip," *Periodica Mathematica Hungarica*, vol. 5, pp. 187–193, 1974.
- [2] A. S. Sergeev, "The method of chords," *Sibirskii Matematicheskii Zhurnal*, vol. 2, pp. 282–289, 1961.
- [3] M. A. Hernandez, M. J. Rubio, and J. A. Ezquerro, "Secant-like methods for solving nonlinear integral equations of the Hammerstein type," *Journal of Computational and Applied Mathematics*, vol. 115, pp. 245–254, 2000.
- [4] M. A. Hernandez and M. J. Rubio, "The secant method and divided differences Hölder continuous," *Applied Mathematics and Computation*, vol. 124, no. 2, pp. 139–149, 2001.
- [5] H. M. Ren, S. J. Yang, and Q. B. Wu, "A new semilocal convergence theorem for the Secant method under Hölder continuous divided differences," *Applied Mathematics and Computation*, vol. 182, no. 1, pp. 41–48, 2006.
- [6] J. A. Ezquerro, M. Grau-Sánchez, M. A. Hernández, and M. Noguera, "Semilocal convergence of secant-like methods for differentiable and nondifferentiable operator equations," *Journal of Mathematical Analysis and Applications*, vol. 398, no. 1, pp. 100–112, 2013.
- [7] M. J. Nijmeijer, "A method to accelerate the convergence of the secant algorithm," *Advances in Numerical Analysis*, vol. 2014, Article ID 321592, 14 pages, 2014.
- [8] J. A. Ezquerro, M. A. Hernandezveron, and A. I. Velasco, "An analysis of the semilocal convergence for secant-like methods," *Applied Mathematics and Computation*, vol. 266, pp. 883–892, 2015.
- [9] A. A. Magrenan and I. K. Argyros, "New improved convergence analysis for the secant method," *Mathematics and Computers in Simulation*, vol. 119, pp. 161–170, 2016.
- [10] A. Caliciotti, G. Fasano, and M. Roma, "Preconditioned nonlinear conjugate gradient methods based on a modified secant equation," *Applied Mathematics and Computation*, vol. 318, pp. 196–214, 2018.
- [11] A. Kumar, D. K. Gupta, E. Martínez, and S. Singh, "Semilocal convergence of a secant-type method under weak Lipschitz conditions in Banach spaces," *Journal of Computational and Applied Mathematics*, vol. 330, pp. 732–741, 2018.
- [12] X.-H. Lei and L.-P. Chen, "A new method for solving the nonlinear equation (in Chinese)," *Journal of Capital Normal University (Natural Science Edition)*, vol. 22, pp. 20–24, 2001.
- [13] X.-H. Wang, "On the Mysovskich theorem of Newton method (in Chinese)," *Chinese Annals of Mathematics*, vol. 2, pp. 283–288, 1980.
- [14] Z. Huang, "The oververgence ball of Newton's method and uniqueness ball of equations under Hölder-type continuous derivatives," *Computers & Mathematics with Applications. An International Journal*, vol. 47, no. 2-3, pp. 247–251, 2004.
- [15] H. M. Ren and Q. B. Wu, "The convergence ball of the Secant method under Hölder continuous divided differences," *Journal of Computational and Applied Mathematics*, vol. 194, no. 2, pp. 284–293, 2006.
- [16] Q. Wu and H. Ren, "Convergence ball of a modified secant method for finding zero of derivatives," *Applied Mathematics and Computation*, vol. 174, no. 1, pp. 24–33, 2006.
- [17] H. Ren and Q. Wu, "Convergence ball of a modified secant method with convergence order 1.839. . .," *Applied Mathematics and Computation*, vol. 188, no. 1, pp. 281–285, 2007.

Research Article

CIP Method of Characteristics for the Solution of Tide Wave Equations

Yafei Nie,¹ Kai Fu ,² and Xianqing Lv ¹

¹Physical Oceanography Laboratory, Ocean University of China, Qingdao 266100, China

²School of Mathematical Sciences, Ocean University of China, Qingdao 266100, China

Correspondence should be addressed to Kai Fu; kfu@ouc.edu.cn

Received 2 February 2018; Accepted 26 May 2018; Published 2 July 2018

Academic Editor: Zhi-Yuan Sun

Copyright © 2018 Yafei Nie et al. This is an open access article distributed under the Creative Commons Attribution License, which permits unrestricted use, distribution, and reproduction in any medium, provided the original work is properly cited.

The CIP-MOC (Constrained Interpolation Profile/Method of Characteristics) is proposed to solve the tide wave equations with large time step size. The bottom topography and bottom friction, which are very important factor for the tidal wave model, are included to the equation of Riemann invariants as the source term. Numerical experiments demonstrate the good performance of the scheme. Compared to traditional semi-implicit (SI) finite difference scheme which is widely used in tidal wave simulation, CIP-MOC has better stability in simulating large gradient water surface change and has the ability to use much longer time step size under the premise of maintaining accuracy. Besides, numerical tests with reflective boundary conditions are carried out by CIP-MOC with large time step size and good results are obtained.

1. Introduction

Tide wave is the water movement caused by the gravitational force of the celestial body. The control equations of tidal wave model are the original shallow water equations including source terms (e.g., bottom friction, bottom topography and horizontal eddy viscosity term) [1]. Therefore, getting the solution of shallow water equations with source terms is of great significance.

In the simulation of ocean tidal waves, Eulerian schemes are widely used, for example, Backhaus [2] and Casulli [3] used semi-implicit scheme (hereafter SI) for the solution of shallow water equations; Lv and Zhang [4] used the semi-implicit scheme to solve tide wave equations and their computational format was used to study bottom friction coefficients [5] and tidal open boundary conditions [6]; the finite volume method is also frequently used [7, 8]. However, since the phase speed of the gravity waves is so fast, time step is strictly limited by CFL condition when using Eulerian schemes [9].

There are growing interests in finding methods that enable using large time steps to solve shallow water equations. Erbes [9] proposed a semi-Lagrangian method of

characteristics (MOC) with quadratic interpolation to solve the shallow water equations with a large CFL number, but there was dispersion error produced. Ogata and Yabe [10] applied the CIP method to shallow waters combined with the MOC and showed low dispersion error and low numerical damping even with large CFL number. Toda et al. [11] proposed a new scheme by adopting the Conservative Semi-Lagrangian (CSL) based on the CIP method which shows good conservation. However, applying this method in realistic simulation of ocean tidal wave will meet a difficulty treating source terms including bottom topography, bottom friction, and boundary conditions.

This paper is designated to apply the CIP-MOC [9] to the solution of tide wave equations which are based on shallow water equations and include source terms of bottom topography and friction. The ideal numerical experiment shows that the CIP-MOC method outperforms SI scheme in stability and dispersion errors when using large time step. Problem with reflection boundary condition is also discussed.

This paper is organized as follows. Section 2 presents the CIP-MOC method. In Section 3, numerical experiments are carried out and comparison is made between the CIP and SI. Conclusion is given in Section 4.

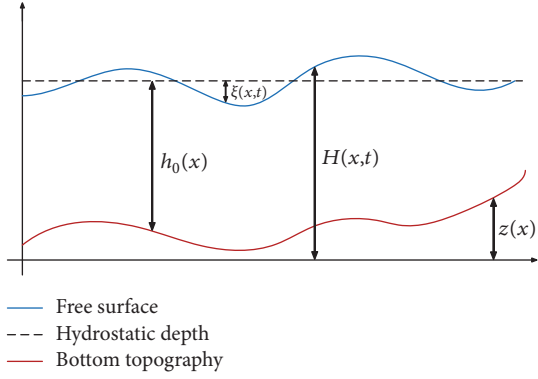
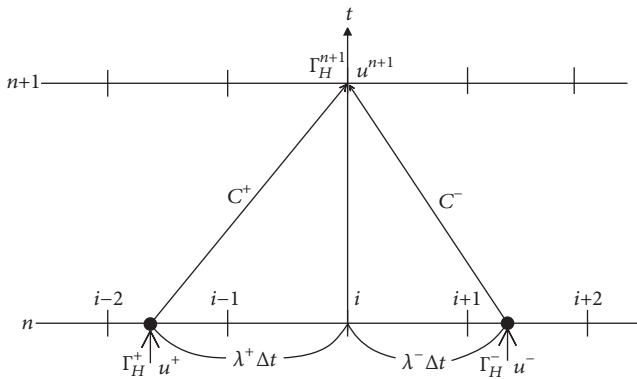


FIGURE 1: Shallow water variables.

FIGURE 2: Space-time diagram that shows the characteristics C^\pm . The Riemann invariants consist of Γ_H^\pm and u^\pm , λ^\pm are characteristic speeds.

2. Model and Method

2.1. CIP Method. CIP method is a compact, robust, less diffusive, and high-order scheme in computational fluid dynamics [12]. Compared with other traditional interpolation methods, the internal information of grid is better described by CIP which uses spatial derivative in the description of function distribution in grid cells. We consider the following advection problem:

$$\frac{\partial f}{\partial t} + u \frac{\partial f}{\partial x} = 0, \quad (1)$$

the solution is [13]

$$\begin{aligned} f^{n+1} &= F(x - u\Delta t), \\ \partial_x f^{n+1} &= \frac{dF(x - u\Delta t)}{dx}. \end{aligned} \quad (2)$$

If f and $\partial_x f$ are known at each grid point, the profile between two adjacent points can be approximated by cubic polynomial

$$F_i(X) = a_i X^3 + b_i X^2 + \partial_x f_i X + f_i, \quad (3)$$

where $X = x - x_i$. Consider four constraints

$$\begin{aligned} F(x_i) &= f_i^n, \\ F(x_{iup}) &= f_{iup}^n, \\ \partial_x F(x_i) &= \partial_x f_i^n, \\ \partial_x F(x_{iup}) &= \partial_x f_{iup}^n. \end{aligned} \quad (4)$$

then coefficients can be given as

$$a_i = \frac{(\partial_x f_i + \partial_x f_{iup})}{D^2} + \frac{2(f_i - f_{iup})}{D^3}, \quad (5)$$

$$b_i = \frac{3(f_{iup} - f_i)}{D^2} - \frac{(2\partial_x f_i + \partial_x f_{iup})}{D}, \quad (6)$$

where $\text{sgn}(u_i) = 1$ ($u_i \geq 0$), -1 ($u_i < 0$), $iup = i - \text{sgn}(u_i)$, and $D = -\Delta x \cdot \text{sgn}(u_i)$.

Thus, the profile of f and $\partial_x f$ at next time step can be obtained as

$$f_i^{n+1} = F_i(x_i - u_i \Delta t) = a_i \xi^3 + b_i \xi^2 + \partial_x f_i^n \cdot \xi + f_i^n, \quad (7)$$

$$\partial_x f_i^{n+1} = \frac{dF_i(x_i - u_i \Delta t)}{dx} = 3a_i \xi^2 + 2b_i \xi + \partial_x f_i^n, \quad (8)$$

where $\xi = -u_i \Delta t$.

2.2. One-Dimensional Tide Wave Equations. Let bottom friction term be the linear form, then the one-dimensional tide wave equations in a primitive form are written as [14]

$$\begin{aligned} \frac{\partial \zeta}{\partial t} + \frac{\partial [(h_0 + \zeta)u]}{\partial x} &= 0, \\ \frac{\partial u}{\partial t} + u \frac{\partial u}{\partial x} + g \frac{\partial \zeta}{\partial x} + ku &= 0, \end{aligned} \quad (9)$$

where t is time, x is Cartesian coordinate, $h_0(x)$ is undisturbed water depth, $\zeta(x, t)$ is sea surface elevation above the undisturbed sea level, $u(x, t)$ is the flow velocity, k is the bottom friction coefficient, and g is the gravitational acceleration.

To solve (9) with the method of characteristics and preserve the balance between the depth gradient and the bottom effect, the surface gradient method [15] is used here. Replace the variable ζ with the water level $H = \zeta + h_0 + z$, where $z(x)$ represents the bottom topographic height (see Figure 1), we get the equivalent of (9) which can be written as

$$\begin{aligned} \frac{\partial H}{\partial t} + \frac{\partial (Hu)}{\partial x} &= \frac{\partial (uz)}{\partial x}, \\ \frac{\partial u}{\partial t} + u \frac{\partial u}{\partial x} + g \frac{\partial H}{\partial x} + ku &= 0. \end{aligned} \quad (10)$$

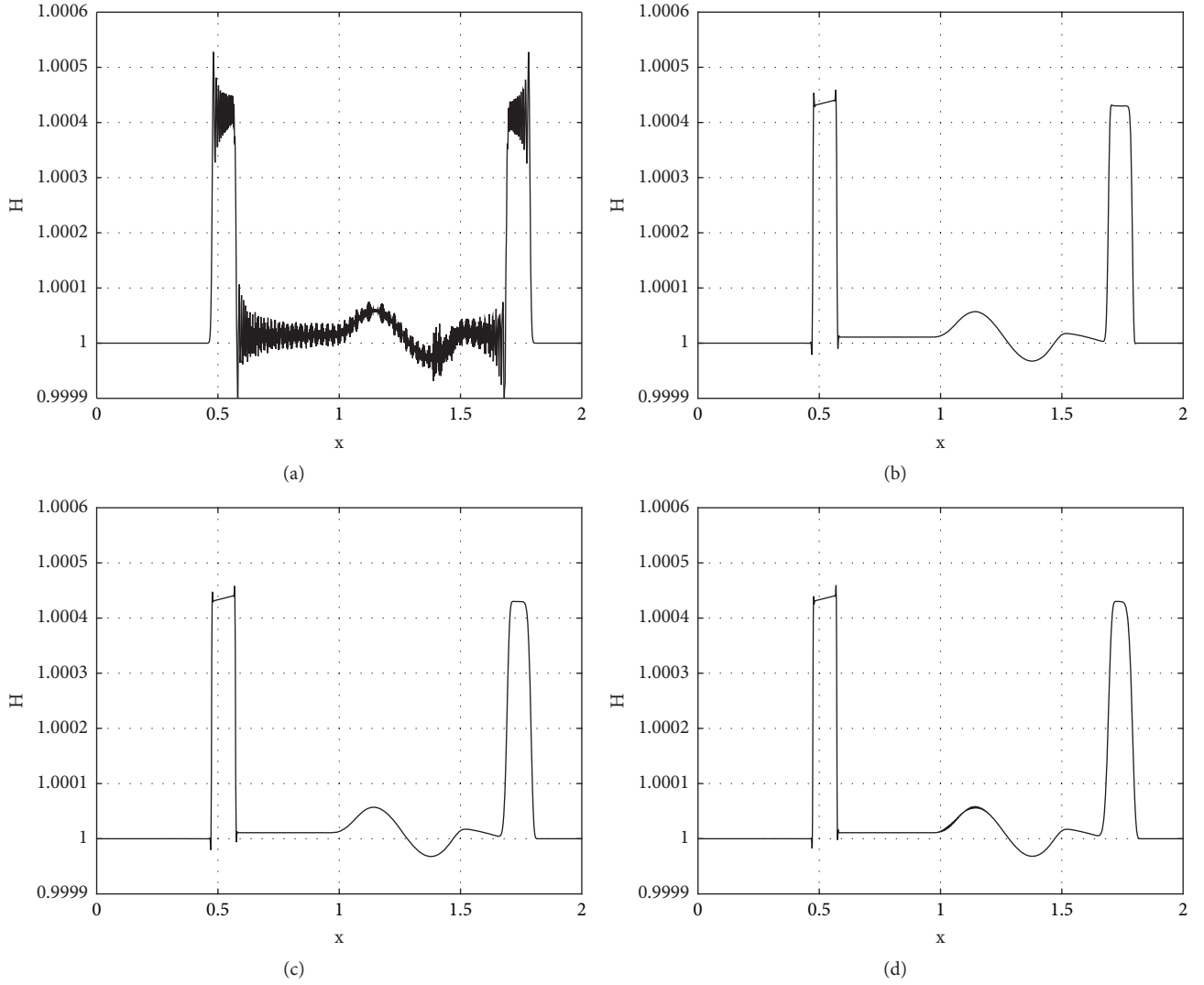


FIGURE 3: A small perturbation of one-dimensional steady state water with a pulse $\zeta = 0.001$. (a) shows SI scheme with CFL=0.63; (b), (c), and (d) are the results of the CIP method with CFL=0.63, 1.57, and 2.61.

In a vector-matrix form, (10) can be rewritten as

$$\begin{aligned} \frac{\partial}{\partial t} \begin{pmatrix} H \\ u \end{pmatrix} + \begin{pmatrix} u & H \\ g & u \end{pmatrix} \frac{\partial}{\partial x} \begin{pmatrix} H \\ u \end{pmatrix} &\equiv \frac{\partial W}{\partial t} + A(W) \frac{\partial W}{\partial x} \\ &= \begin{pmatrix} \frac{\partial (uz)}{\partial x} \\ -ku \end{pmatrix}. \end{aligned} \quad (11)$$

The eigenvalue matrix Λ and eigenvector matrix L of coefficient matrix A are

$$\begin{aligned} \Lambda &= \begin{pmatrix} \lambda^+ & 0 \\ 0 & \lambda^- \end{pmatrix}, \\ L &= \begin{pmatrix} \Gamma_H & -\Gamma_H \\ g & g \end{pmatrix}, \end{aligned} \quad (12)$$

where $\Gamma_H = \sqrt{gH}$ and $\lambda^\pm = u \pm \Gamma_H$. Thus, matrix A can be diagonalized as $L^{-1}AL$, where

$$L^{-1} = \frac{1}{2} \begin{pmatrix} g & 1 \\ \Gamma_H & 1 \\ -g & 1 \\ \Gamma_H & 1 \end{pmatrix} \quad (13)$$

is the inverse of L . Then (11) can be written as

$$L^{-1} \frac{\partial W}{\partial t} + (L^{-1}AL) L^{-1} \frac{\partial W}{\partial x} = L^{-1}S, \quad (14)$$

where S represents the right hand side of (11).

Two characteristics about Riemann invariants $R^\pm = \Gamma_H \pm u/2$ can be obtained from (14) as

$$\frac{\partial R^\pm}{\partial t} + \lambda^\pm \frac{\partial R^\pm}{\partial x} = \frac{g}{2\Gamma_H} \frac{\partial (uz)}{\partial x} \mp \frac{1}{2}ku. \quad (15)$$

By using CIP method, we have

$$\Gamma_H^{n+1} \pm \frac{u^{n+1}}{2} = \Gamma_H^\pm \pm \frac{u^\pm}{2} + \frac{g}{2} \int_{t^n}^{t^{n+1}} \frac{1}{\Gamma_H} \frac{\partial(uz)}{\partial x} d\tau^\pm \mp \frac{1}{2} k \cdot \Delta t \frac{(u^\pm + u^{n+1})}{2}, \quad (16)$$

$$\Gamma_H^{n+1} = \frac{1}{2} \left[\Gamma_H^+ + \Gamma_H^- + \frac{1}{2} (u^+ - u^-) + \frac{g}{2} \left(\int_{t^n}^{t^{n+1}} \frac{1}{\Gamma_H} \frac{\partial(uz)}{\partial x} d\tau^+ + \int_{t^n}^{t^{n+1}} \frac{1}{\Gamma_H} \frac{\partial(uz)}{\partial x} d\tau^- \right) - \frac{1}{2} k \Delta t \frac{(u^+ - u^-)}{2} \right], \quad (18)$$

$$u^{n+1} = \frac{(1/2) \left[u^+ + u^- + 2(\Gamma_H^+ - \Gamma_H^-) + g \left(\int_{t^n}^{t^{n+1}} (1/\Gamma_H) (\partial(uz)/\partial x) d\tau^+ - \int_{t^n}^{t^{n+1}} (1/\Gamma_H) (\partial(uz)/\partial x) d\tau^- \right) - (1/2) k \Delta t ((u^+ + u^-)/2) \right]}{1 + (1/2) k \Delta t} \quad (19)$$

Time integration of the bottom topographic term in (18) and (19) can be approximated using $dx^\pm/d\tau^\pm = u \pm \Gamma_H$ as follows [16]:

$$\int_{t^n}^{t^{n+1}} \frac{1}{\Gamma_H} \frac{\partial(uz)}{\partial x} d\tau^\pm \approx - \frac{(uz)^\pm - (uz)^n}{\Gamma_H^\pm (u \pm \Gamma_H)^\pm}. \quad (20)$$

When applying the CIP method, spatial gradient at the next time step is also needed. Take spatial derivative of (15)

$$\frac{\partial(\partial_x R^\pm)}{\partial t} + \lambda^\pm \frac{\partial(\partial_x R^\pm)}{\partial x} = G^\pm, \quad (21)$$

G^\pm includes the terms related to spatial derivatives of λ^\pm , Γ_H , and u . Considering that the influence of G^\pm is not significant in this problem, we neglect G^\pm here. Then (21) can be solved as

$$\partial_x \Gamma_H^{n+1} = \frac{1}{2} \left[\partial_x \Gamma_H^+ + \partial_x \Gamma_H^- + \frac{1}{2} (\partial_x u^+ - \partial_x u^-) \right], \quad (22)$$

$$\partial_x u^{n+1} = \frac{1}{2} [\partial_x u^+ + \partial_x u^- + 2(\partial_x \Gamma_H^+ - \partial_x \Gamma_H^-)], \quad (23)$$

then values and derivatives of each value at time step $(n+1)$ are obtained.

2.3. Two-Dimensional Tide Wave Equations. Assuming that pressure is hydrostatic and density is constant, the depth

where Γ_H^\pm and u^\pm are calculated by

$$\begin{aligned} \Gamma_H^\pm &= \Gamma_{HCIP}(x_i - \lambda^\pm \Delta t), \\ u^\pm &= u_{CIP}(x_i - \lambda^\pm \Delta t), \end{aligned} \quad (17)$$

the subscript CIP in variables means that they are interpolated with the CIP scheme, and the bottom friction term is discretized with the Crank-Nicholson method which is implicit in time. Γ_H and u at time step t^{n+1} can be obtained by solving linear equations (16) (see Figure 2):

averaged two-dimensional tidal model without horizontal eddy viscosity is given as follows [17]:

$$\begin{aligned} \frac{\partial \zeta}{\partial t} + \frac{\partial [(h_0 + \zeta) u]}{\partial x} + \frac{\partial [(h_0 + \zeta) v]}{\partial y} &= 0, \\ \frac{\partial u}{\partial t} + u \frac{\partial u}{\partial x} + v \frac{\partial u}{\partial y} - f v + \frac{k u \sqrt{u^2 + v^2}}{h_0 + \zeta} + g \frac{\partial \zeta}{\partial x} &= 0, \\ \frac{\partial v}{\partial t} + u \frac{\partial v}{\partial x} + v \frac{\partial v}{\partial y} + f u + \frac{k v \sqrt{u^2 + v^2}}{h_0 + \zeta} + g \frac{\partial \zeta}{\partial y} &= 0, \end{aligned} \quad (24)$$

where $u(x, y, t)$ and $v(x, y, t)$ are x and y components of flow velocity and f represents the Coriolis parameter.

In the same way as one dimension, replace variable ζ with water level $H = \zeta + h_0 + z$; we get the equivalent of (24) which can be written in vector-matrix form as

$$\frac{\partial W}{\partial t} + A(W) \frac{\partial W}{\partial x} + B(W) \frac{\partial W}{\partial y} + S = 0, \quad (25)$$

where

$$W = \begin{pmatrix} H \\ u \\ v \end{pmatrix},$$

$$A(W) = \begin{pmatrix} u & H & 0 \\ g & u & 0 \\ 0 & 0 & u \end{pmatrix},$$

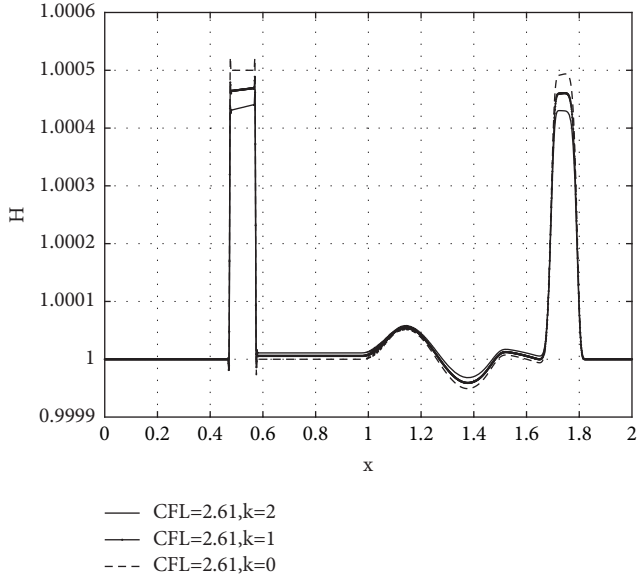


FIGURE 4: Effect of bottom friction. Results computed by CIP with CFL=2.61 for $k=0, 1,$ and 2 .

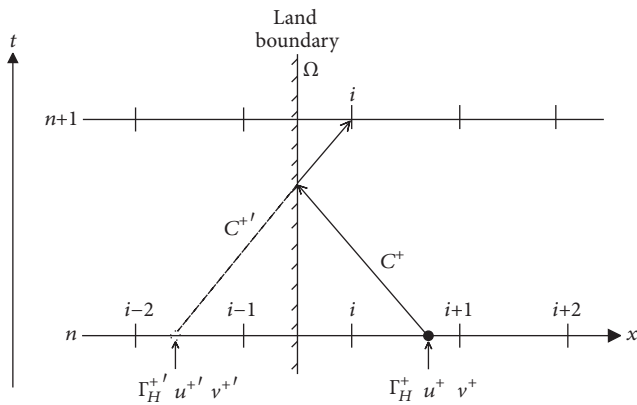


FIGURE 5: Space-time diagram that shows the reflecting boundary conditions. The filled circle represents the approximated upstream departure point, while the hollow circle represents the virtual upstream point on the shore.

$$B(W) = \begin{pmatrix} \nu & 0 & H \\ 0 & \nu & 0 \\ g & 0 & \nu \end{pmatrix},$$

$$S = \begin{pmatrix} -\left(\frac{\partial(uz)}{\partial x} + \frac{\partial(vz)}{\partial y}\right) \\ -fv + k \frac{u\sqrt{u^2 + v^2}}{H-z} \\ fu + k \frac{v\sqrt{u^2 + v^2}}{H-z} \end{pmatrix}. \quad (26)$$

Since matrices A and B are not commutative; thus, there is no matrix to diagonalize them at the same time. Split (25)

into two sequential phases; the source term is divided into two terms added to each directional phase:

$$\frac{\partial W}{\partial t} + A \frac{\partial W}{\partial x} + S_x = 0 \quad W^n \longrightarrow W^*, \quad (27)$$

$$\frac{\partial W^*}{\partial t} + B \frac{\partial W^*}{\partial y} + S_y = 0 \quad W^* \longrightarrow W^{n+1}, \quad (28)$$

where

$$S_x = \begin{pmatrix} -\frac{\partial(uz)}{\partial x} \\ -\frac{1}{2}fv + \frac{1}{2}k \frac{u\sqrt{u^2 + v^2}}{H-z} \\ \frac{1}{2}fu + \frac{1}{2}k \frac{v\sqrt{u^2 + v^2}}{H-z} \end{pmatrix}, \quad (29)$$

$$S_y = \begin{pmatrix} -\frac{\partial(vz)}{\partial y} \\ -\frac{1}{2}fv + \frac{1}{2}k \frac{u\sqrt{u^2 + v^2}}{H-z} \\ \frac{1}{2}fu + \frac{1}{2}k \frac{v\sqrt{u^2 + v^2}}{H-z} \end{pmatrix}.$$

In order to get high accuracy in time, we calculate alternately in the x - and y -directions as follows:

$$W^{n+2} = L_x L_y L_y L_x W^n, \quad (30)$$

where L_x and L_y represent operation of (27) and (28), respectively.

Here we give the solution process in x -direction. Similar to the one-dimensional case, left multiply (27) by the eigenvector matrix L :

$$L^{-1} \frac{\partial W}{\partial t} + (L^{-1}AL) L^{-1} \frac{\partial W}{\partial x} + L^{-1}S_x$$

$$\equiv L^{-1} \frac{\partial W}{\partial t} + \begin{pmatrix} \lambda_x^- & 0 & 0 \\ 0 & \lambda_x^+ & 0 \\ 0 & 0 & u \end{pmatrix} L^{-1} \frac{\partial W}{\partial x} + L^{-1}S_x = 0, \quad (31)$$

where

$$\lambda_x^\pm = u \pm \Gamma_H,$$

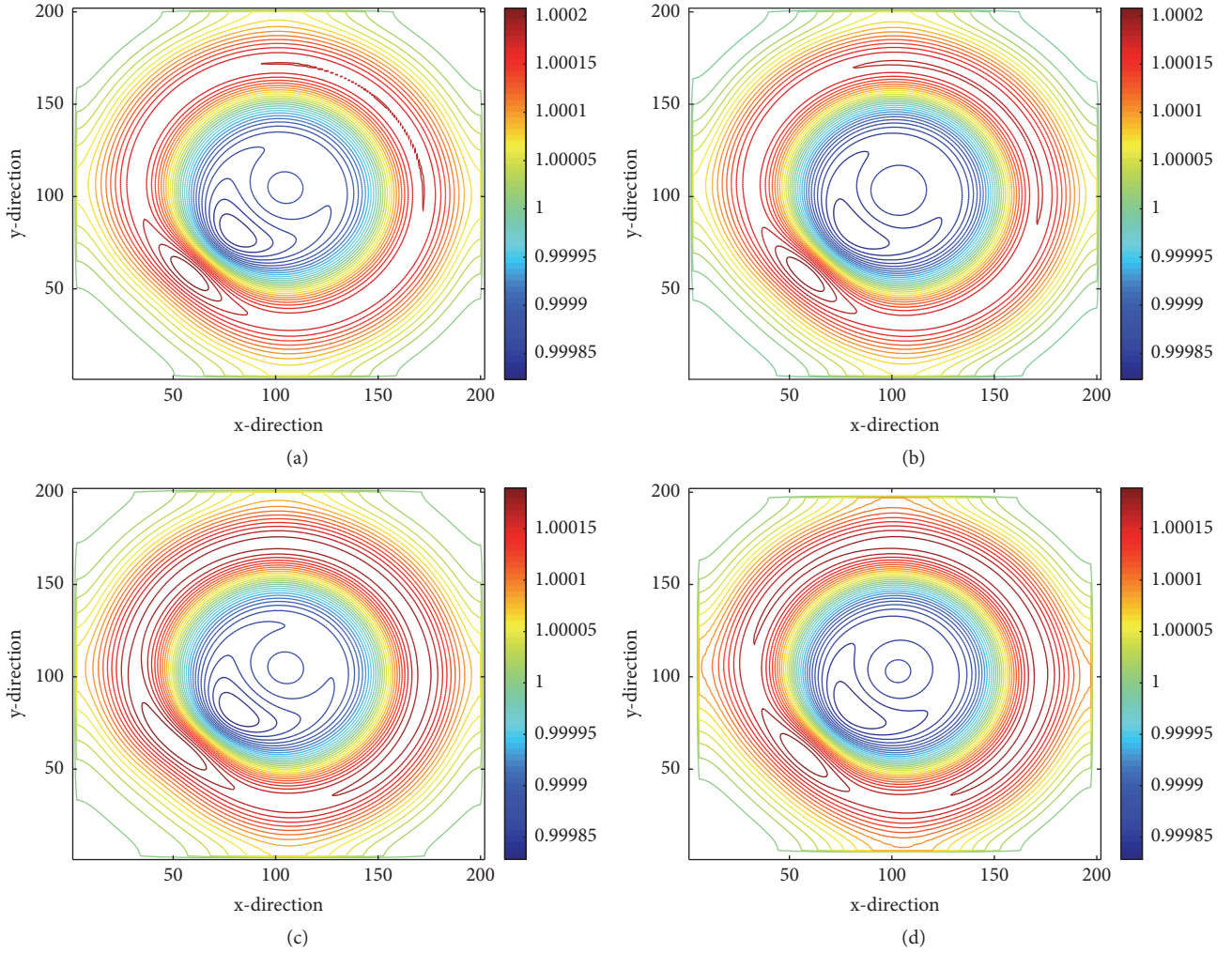


FIGURE 6: Smooth surface wave propagation problem. The contour of the water level H at $t=20$. (a) is the result of SI with $CFL=0.63$; (b), (c), and (d) are the results of CIP-MOC with $CFL=0.63, 1.42$, and 1.90 .

$$L = \begin{pmatrix} -\frac{\Gamma_H}{g} & \frac{\Gamma_H}{g} & 0 \\ 1 & 1 & 0 \\ 0 & 0 & 1 \end{pmatrix},$$

$$L^{-1} = \frac{1}{2} \begin{pmatrix} -\frac{g}{\Gamma_H} & 1 & 0 \\ \frac{g}{\Gamma_H} & 1 & 0 \\ 0 & 0 & 2 \end{pmatrix}.$$
(32)

Equation (31) leads to the following three equations:

$$\frac{\partial R_x^\pm}{\partial t} + \lambda_x^\pm \frac{\partial R_x^\pm}{\partial x} \mp \frac{1}{4} f v \pm \frac{1}{4} k u \frac{\sqrt{u^2 + v^2}}{H - z} - \frac{g}{2\Gamma_H} \frac{\partial(uz)}{\partial x} = 0,$$
(33)

$$\frac{\partial v}{\partial t} + u \frac{\partial v}{\partial x} + \frac{1}{2} f u + \frac{1}{2} k v \frac{\sqrt{u^2 + v^2}}{H - z} = 0,$$
(34)

where $R_x^\pm = \Gamma_H \pm u/2$ are the Riemann invariants. These three equations all have the form of convective equations that can be calculated by CIP method. The Coriolis force, bottom topography, and bottom friction term are added to each Riemann invariant along characteristic line. Thus, the Riemann invariants and v can be discretized as follows:

$$\Gamma_H^* \pm \frac{1}{2} u^* = \Gamma_H^\pm \pm \frac{1}{2} u^\pm \pm \frac{1}{4} f \Delta t \frac{(v^\pm + v^*)}{2}$$

$$\mp \frac{1}{4} k \Delta t \frac{(u^\pm + u^*)}{2} \frac{\sqrt{(u^n)^2 + (v^n)^2}}{H^n - z}$$

$$+ \frac{g}{2} \int_{t^n}^{t^{n+1}} \frac{1}{\Gamma_H} \frac{\partial(uz)}{\partial x} d\tau^\pm,$$

$$v^* = v^0 - \frac{1}{2} f \Delta t \frac{(u^0 + u^*)}{2}$$

$$- \frac{1}{2} k \Delta t \frac{(v^0 + v^*)}{2} \frac{\sqrt{(u^n)^2 + (v^n)^2}}{H^n - z}.$$
(35)
(36)

So we have

$$\Gamma_H^* = \frac{1}{2} \left[\Gamma_H^+ + \Gamma_H^- + \frac{k_2'}{2} (u^+ - u^-) + \frac{f'}{2} (v^+ - v^-) + \frac{g}{2} (s_x^+ + s_x^-) \right], \quad (37)$$

$$u^* = \frac{(1/2) \left[k_1' (u^+ + u^-) + 2 (\Gamma_H^+ - \Gamma_H^-) + f' (v^+ + v^-) + 2 (f'/k_1') [k_2' v^0 - f' u^0] + g (s_x^+ - s_x^-) \right]}{k_1' + f'^2/k_1}, \quad (38)$$

$$v^* = \frac{k_2' v^0 - f' (u^0 + u^*)}{k_1'}, \quad (39)$$

where $k_1' = 1 + (1/4)k\Delta t(\sqrt{(u^n)^2 + (v^n)^2}/(H^n - z))$, $k_2' = 1 - (1/4)k\Delta t(\sqrt{(u^n)^2 + (v^n)^2}/(H^n - z))$, $f' = (1/4)f\Delta t$,

$$\begin{aligned} s_x^+ &= \frac{g}{2} \int_{t^n}^{t^{n+1}} \frac{1}{\Gamma_H} \frac{\partial(uz)}{\partial x} d\tau^+, \\ s_x^- &= \frac{g}{2} \int_{t^n}^{t^{n+1}} \frac{1}{\Gamma_H} \frac{\partial(uz)}{\partial x} d\tau^-. \end{aligned} \quad (40)$$

Similar to the derivation in one dimension, neglecting the influence of G^\pm , the derivatives of each value at time step $(n+1)$ are obtained

$$\partial_x \Gamma_H^* = \frac{1}{2} \left[\partial_x \Gamma_H^+ + \partial_x \Gamma_H^- + \frac{1}{2} (\partial_x u^+ - \partial_x u^-) \right], \quad (41)$$

$$\partial_x u^* = \frac{1}{2} [\partial_x u^+ + \partial_x u^- + 2 (\partial_x \Gamma_H^+ - \partial_x \Gamma_H^-)], \quad (42)$$

$$\partial_x v^* = \frac{\partial v^0}{\partial x}. \quad (43)$$

The operation in the x-direction is completed.

The operation in y-direction is essentially the same as the x-direction and the y derivative is computed by linear interpolation

$$\begin{aligned} \partial_y f_{i,j}^* &= \partial_y f_{i,j} - \text{sgn}(\lambda_x) \\ &\cdot \frac{\partial_y f_{i,j} - \partial_y f_{i-\text{sgn}(\lambda_x),j}}{\Delta x} \lambda_x \Delta t, \end{aligned} \quad (44)$$

where $\text{sgn}(\lambda_x) = 1$ ($\lambda_x \geq 0$), -1 ($\lambda_x < 0$).

3. Numerical Results

3.1. A Small Perturbation of One-Dimensional Steady State Water. To demonstrate that the CIP method can be applied to the computation of ocean tidal waves with bottom topography and bottom friction, we first consider the quasi-stationary test case given in [18]. The difference is that we add the effect of the bottom friction here.

The bottom topography is given by

$$\begin{aligned} b(x) &= \begin{cases} 0.25 (\cos(10\pi(x-1.5)) + 1), & \text{if } 1.4 \leq x \leq 1.6, \\ 0, & \text{otherwise.} \end{cases} \end{aligned} \quad (45)$$

The initial conditions are

$$H(x, 0) = \begin{cases} 1 + \zeta, & \text{if } 1.1 \leq x \leq 1.2, \\ 1, & \text{otherwise.} \end{cases} \quad (46)$$

$$u(x, 0) = 0, \quad k = 2.0,$$

where $\zeta = 0.001$ is constant amplitude of the perturbation. According to the propagation mechanism of wave, the small disturbance will be split into two smaller waves propagating to both sides. However, because of the Gibbs phenomenon, the small pulse of perturbation is a challenge for many numerical schemes [19]. Numerical experiments are carried out with both the CIP and SI schemes; the surface level with $Nx = 2000$ cells at the final time $T = 0.2$ is shown in Figure 3. We keep $\Delta t = T/1000$ as the SI scheme is strictly restricted by the CFL condition, and $\Delta t = T/1000, T/400, T/240$ when using the CIP.

Since flow velocity u and v are far smaller than wave velocity Γ_H , the CFL number is defined as

$$CFL \approx \Gamma_{H\max} \cdot \frac{\Delta t}{\Delta x}. \quad (47)$$

The experimental results are similar to those in [19, 20]. It can be seen that nonphysical oscillations occur when simulating marching wave using the SI scheme, waves are broken in the process of travel, and the amplitude of nonphysical oscillations increases gradually in time, which also means that the scheme does not have the ability to simulate large gradient surface change. However, the shape of the simulated wave is smooth and has no oscillations when using CIP until $CFL = 2.61$. Figure 4 gives the results computed by CIP with $CFL=2.61$ for $k=0, 1$, and 2 . It can be seen that the separated wave height is less than half of the initial perturbation because of the bottom friction. Numerical experiments show that the

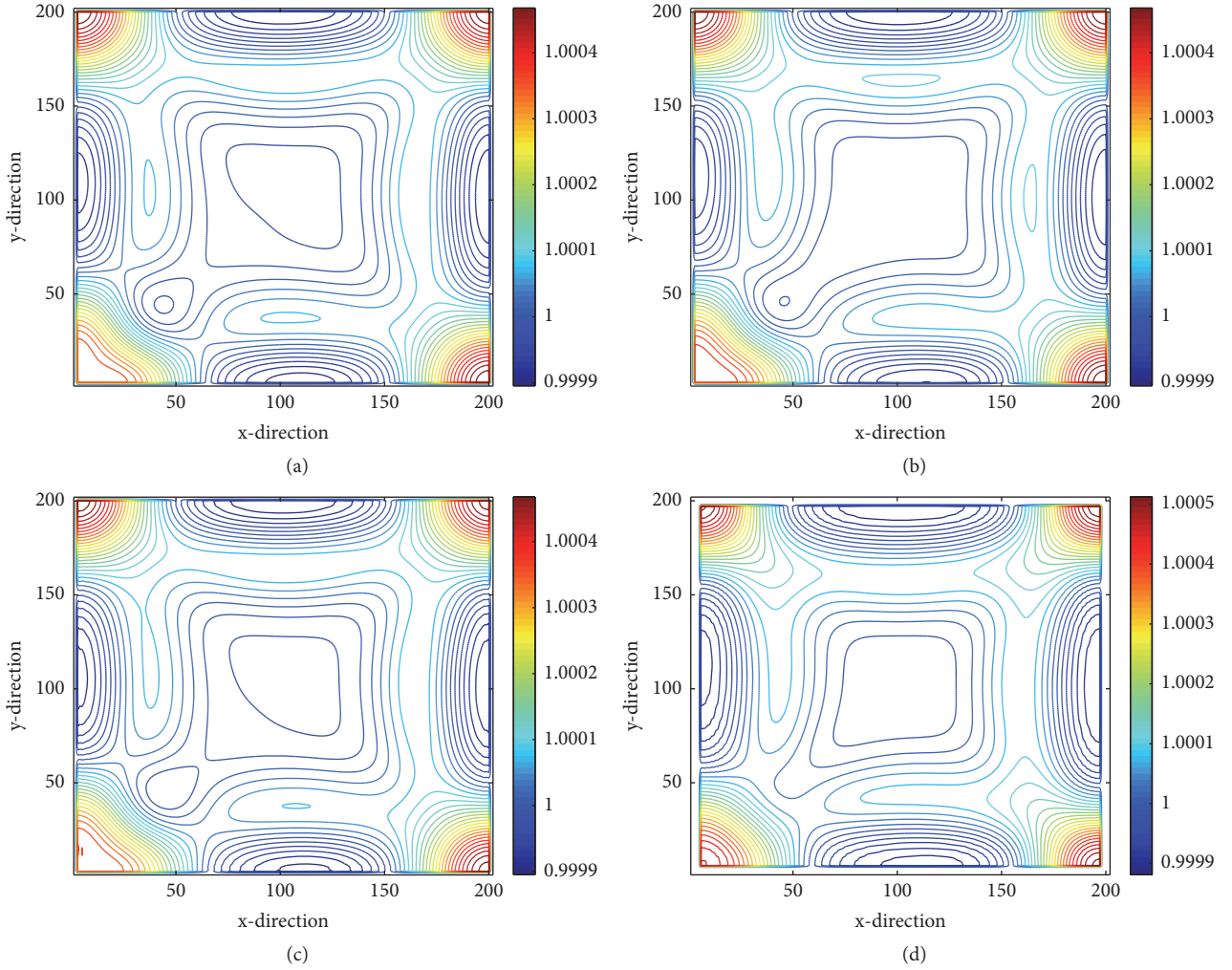


FIGURE 7: Smooth surface wave propagation problem. The contour of the water level H at $t=40$. (a) is the result of SI with $CFL=0.63$; (b), (c), and (d) are the results of CIP-MOC with $CFL=0.63, 1.42$, and 1.90 .

CIP method can successfully simulate large gradient water surface with both bottom topography and bottom friction using large time step sizes.

3.2. Smooth Surface Wave Propagation Problem. Since boundary condition plays a significant role in the shallow water flow of an actual marine area, we consider a smooth surface wave propagation problem here with reflective boundary conditions. The conditions for the x-direction are

$$\begin{aligned} \frac{\partial H}{\partial \Omega} &= 0, \\ \frac{\partial v}{\partial \Omega} &= 0, \\ u(\Omega) &= 0. \end{aligned} \quad (48)$$

Since the spatial gradient is also required when using the CIP method, the spatial gradient condition at the boundary is obtained according to (48):

$$\begin{aligned} \partial_x H(\Omega) &= 0, \\ \partial_x v(\Omega) &= 0, \\ \frac{\partial_x u}{\partial \Omega} &= 0. \end{aligned} \quad (49)$$

When the traced upstream departure point on the shore, the corresponding actual upstream departure point in the waters is approximated using reflective boundary conditions (see Figure 5).

The initial conditions are given as follows:

$$\begin{aligned} \zeta(x, y, 0) \\ = 0.001 \end{aligned}$$

$$\cdot \exp \left[- \left(\frac{x - X_{\max}/2}{\sigma_x} \right)^2 - \left(\frac{y - Y_{\max}/2}{\sigma_y} \right)^2 \right],$$

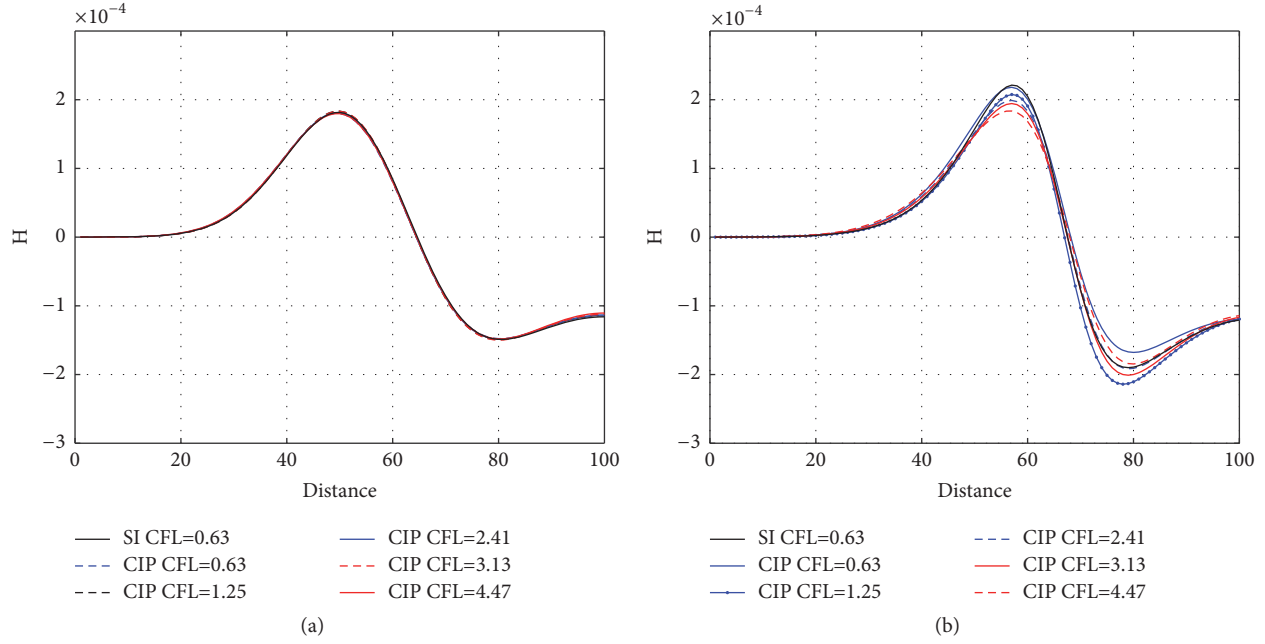


FIGURE 8: The comparison of cross-sections between topographic (a) and nontopographic conditions (b) with different CFL numbers.

$$\begin{aligned}
 z(x, y) &= 0.5 \\
 &\cdot \exp \left[- \left(\frac{x - X_{\max}/3}{\sigma_x} \right)^2 - \left(\frac{y - Y_{\max}/3}{\sigma_y} \right)^2 \right], \\
 H(x, y, 0) &= 1 + \zeta(x, y, 0) - z(x, y), \\
 u(x, y, 0) &= 0, \\
 v(x, y, 0) &= 0,
 \end{aligned} \tag{50}$$

where $\sigma_x = \sigma_y = 25$. Let the bottom friction coefficient $k = 2 \times 10^{-3}$ and the constant Coriolis parameter f be 1×10^{-3} .

The computation domain is $\Omega = [0, 200] \times [0, 200]$, and Δx and Δy are set to 1.0. The contour map of the water surface at $t=20$ and $t=40$ is shown in Figures 6 and 7, respectively. It can be seen that at $t=20$ the contour line is not a complete circle because of the impact of the bottom topography (similar to the one-dimensional case). At $t = 40$, the reflected waves are superimposed on each other and eventually form what is shown in Figure 7. The results show that when time step increases to three times to the SI method, CIP-MOC scheme still simulate the change process of water surface very well, even considering the bottom topography (see Figure 8), boundary, and Coriolis effect.

4. Conclusion

In this paper, we apply the CIP-MOC to the solution of tide wave equations using large time step size. Bottom topography, bottom friction, and Coriolis term are included to the

equation of Riemann invariants as the source term. One-dimensional experiment shows that the CIP-MOC scheme can keep the shape very well and has no oscillations even when the time step is increased to four times of the SI scheme in the simulation of large gradient water surface. Bottom friction effect is also tested in the experiment. In two-dimensional case, the problem with reflected boundary conditions is considered. Numerical experiments show that the CIP-MOC scheme is succeeded in simulating the change process of water surface using time step that is three times of the SI method. All the results validated the good stability and low dispersion error of the CIP-MOC method.

Data Availability

All results presented in the article were produced from model simulations. Therefore, there is no data to be made available. Researchers who wish to replicate the study will use the equations and parameters described in the article. With such equations and parameters, researchers can use modeling simulations to replicate the figures presented in the article.

Conflicts of Interest

The authors declare that there are no conflicts of interest regarding the publication of this paper.

Acknowledgments

Partial support for this research was provided by the National Key Research and Development Plan through Grant 2016YFC1402304, the Key Research and Development Plan of Shandong Province through Grants 2016ZDJS09A02 and

ZR2016AB16, and the National Natural Science Foundation of China through Grant 41606006.

References

- [1] J. Pedlosky, *Geophysical fluid dynamics*, Springer Science & Business Media, 2013.
- [2] J. O. Backhaus, "A semi-implicit scheme for the shallow water equations for application to shelf sea modelling," *Continental Shelf Research*, vol. 2, no. 4, pp. 243–254, 1982.
- [3] V. Casulli, "Semi-implicit finite difference methods for the two-dimensional shallow water equations," *Journal of Computational Physics*, vol. 86, no. 1, pp. 56–74, 1990.
- [4] X. Lu and J. Zhang, "Numerical study on spatially varying bottom friction coefficient of a 2D tidal model with adjoint method," *Continental Shelf Research*, vol. 26, no. 16, pp. 1905–1923, 2006.
- [5] H. Pan, Z. Guo, and X. Lv, "Inversion of tidal open boundary conditions of the M2 constituent in the bohai and yellow seas," *Journal of Atmospheric and Oceanic Technology*, vol. 34, no. 8, pp. 1661–1672, 2017.
- [6] Z. Guo, H. Pan, W. Fan, and X. Lv, "Application of surface spline interpolation in inversion of bottom friction coefficients," *Journal of Atmospheric and Oceanic Technology*, vol. 34, no. 9, pp. 2021–2028, 2017.
- [7] R. H. Weisberg and L. Zheng, "A finite volume coastal ocean model simulation of the tide, buoyancy, and wind-driven circulation of Tampa Bay," *Journal of Geophysical Research*, vol. 111, article C01005, 2006.
- [8] C. Chen, H. Huang, R. C. Beardsley, H. Liu, Q. Xu, and G. Cowles, "A finite volume numerical approach for coastal ocean circulation studies: comparisons with finite difference models," *Journal of Geophysical Research: Oceans*, vol. 112, no. 3, Article ID C03018, 2007.
- [9] G. Erbes, "A Semi-Lagrangian Method of Characteristics for the Shallow-Water Equations," *Monthly Weather Review*, vol. 121, no. 12, pp. 3443–3452, 1993.
- [10] Y. Ogata and T. Yabe, "Multi-dimensional semi-lagrangian characteristic approach to the shallow water equations by the CIP method," *International Journal of Computational Engineering Science*, vol. 5, no. 3, pp. 699–730, 2004.
- [11] K. Toda, Y. Ogata, and T. Yabe, "Multi-dimensional conservative semi-Lagrangian method of characteristics CIP for the shallow water equations," *Journal of Computational Physics*, vol. 228, no. 13, pp. 4917–4944, 2009.
- [12] T. Yabe and T. Aoki, "A universal solver for hyperbolic equations by cubic-polynomial interpolation. I. One-dimensional solver," *Computer Physics Communications*, vol. 66, no. 2-3, pp. 219–232, 1991.
- [13] T. Yabe and E. Takei, "A new higher-order Godunov method for general hyperbolic equations," *Journal of the Physical Society of Japan*, vol. 57, no. 8, pp. 2598–2601, 1988.
- [14] Y. Anle and L. Fengqi, *Physical Oceanography*, China Ocean University Press, 1992.
- [15] J. G. Zhou, D. M. Causon, C. G. Mingham, and D. M. Ingram, "The surface gradient method for the treatment of source terms in the shallow-water equations," *Journal of Computational Physics*, vol. 168, no. 1, pp. 1–25, 2001.
- [16] R. Akoh, S. Ii, and F. Xiao, "A CIP/multi-moment finite volume method for shallow water equations with source terms," *International Journal for Numerical Methods in Fluids*, vol. 56, no. 12, pp. 2245–2270, 2008.
- [17] R. W. Lardner, "Optimal assimilation of current and surface elevation data in a two-dimensional numerical tidal model," *Applied Mathematical Modelling*, vol. 19, no. 1, pp. 30–38, 1995.
- [18] R. J. LeVeque, "Balancing source terms and flux gradients in high-resolution Godunov methods: the quasi-steady wave-propagation algorithm," *Journal of Computational Physics*, vol. 146, no. 1, pp. 346–365, 1998.
- [19] Q. Zhu, Z. Gao, W. S. Don, and X. Lv, "Well-balanced hybrid compact-WENO scheme for shallow water equations," *Applied Numerical Mathematics*, vol. 112, pp. 65–78, 2017.
- [20] Y. Xing and C.-W. Shu, "High order finite difference WENO schemes with the exact conservation property for the shallow water equations," *Journal of Computational Physics*, vol. 208, no. 1, pp. 206–227, 2005.

Research Article

The Global Existence and Uniqueness of the Classical Solution with the Periodic Initial Value Problem for One-Dimension Klein-Gordon-Zakharov Equations

Cong Sun ¹ and Lixia Li²

¹School of Applied Mathematics, Jilin University of Finance and Economics, Changchun, Jilin 130117, China

²College of Mathematics and Physics, Bohai University, Liaoning 121013, China

Correspondence should be addressed to Cong Sun; 3211519@163.com

Received 2 January 2018; Accepted 15 March 2018; Published 28 June 2018

Academic Editor: Zhi-Yuan Sun

Copyright © 2018 Cong Sun and Lixia Li. This is an open access article distributed under the Creative Commons Attribution License, which permits unrestricted use, distribution, and reproduction in any medium, provided the original work is properly cited.

Through applying Galerkin method, we establish the approximating solution for one-dimension Klein-Gordon-Zakharov equations and obtain the local classical solution. By applying integral estimates, we also obtain the existence and uniqueness of the global classical solution of Klein-Gordon-Zakharov equations.

1. Introduction

The Klein-Gordon-Zakharov equations are used to show the interaction between Langmuir wave and ion wave in the plasma, where

$$\begin{aligned}u_{tt} - u_{xx} + u + nu &= 0, \\ n_{tt} - n_{xx} &= (|u|^2)_{xx},\end{aligned}\tag{1}$$

with periodic initial condition

$$\begin{aligned}u(x, 0) &= u_0, \\ n(x, 0) &= n_0.\end{aligned}\tag{2}$$

Here, $u(x, t)$ (complex function) denotes the biggest moment scale component produced by electron in electric field. $n(x, t)$ (real function) denotes the speed of deviations between the ion at any position and that at equilibrium position. $x \in R$; $0 \leq t \leq T$.

Inspired by B. L. Guo's idea and method [1], our paper focuses on the existence and uniqueness of the local and global classical solution of the periodic initial value problem

for the above one-dimension Klein-Gordon-Zakharov equations. In past decades, many scholars devoted their researches to Zakharov system and have obtained some important results [2–4].

In [5], H. Pecher has researched the following Klein-Gordon equation:

$$\phi_{tt} - \Delta\phi + \phi = \phi|\phi|^{p-1},\tag{3}$$

where $\phi = \phi(x, t)$, $x \in R^n$, $t \geq 0$. Given the existence of the Cauchy problem of (3), H. A. Levine in [6] adopted potential well method and concave function method to study the blowing up of the solution of the Cauchy problem of this equation. Moreover, in [7], W. A. Strauss introduced a compactness lemma, which proved existence of the solitary wave of these equations. In [4], Ozawa, Tsutaya, and Tsutsumi studied the following Klein-Gordon-Zakharov system:

$$\begin{aligned}\phi_{tt} - \Delta\phi + \phi &= -\psi\phi, \\ \psi_{tt} - c^2\Delta\psi &= \Delta|\phi|^2,\end{aligned}\tag{4}$$

with initial condition

$$\begin{aligned}\phi(x, 0) &= \phi_0, \\ \phi_t(x, 0) &= \phi_1, \\ \psi(x, 0) &= \psi_0, \\ \psi_t(x, 0) &= \psi_1.\end{aligned}\quad (5)$$

Through applying harmonic analysis method and contracting mapping principle, they obtained that the Cauchy problem (4)-(5) had local well-posedness about t in energy space $H^1(\mathbb{R}^3) \times L^2(\mathbb{R}^3)$. Furthermore, based on conservation of energy, they also obtained global existence and uniqueness with small initial value of above Cauchy problem.

Furthermore, in [8], T. C. Wang et al considered the following Klein-Gordon-Zakharov equations:

$$\begin{aligned}u_{tt} - u_{xx} + u + nu + |u|^2 u &= 0, \\ n_{tt} - n_{xx} &= (|u|^2)_{xx}.\end{aligned}\quad (6)$$

By applying Leray-Schauder fixed-point theorem, they proved the existence of different solutions of system (6).

Recently, Z. Y. Zhang et al. studied [9] the following Klein-Gordon-Zakharov equations:

$$\begin{aligned}u_{tt} - u_{xx} + u + \alpha nu &= 0, \\ n_{tt} - n_{xx} &= \beta (|u|^2)_{xx}.\end{aligned}\quad (7)$$

With different parameter conditions, they adopted the bifurcation method and dynamical systems approach to research bifurcation analysis and dynamic behaviour of travelling wave solutions of (7).

Besides, in [10], by combining the trigonometric function series method and the exp-function method, Y. Zhang et al. considered the travelling wave solutions of (7).

Now, let us describe our results. Inspired by [1], we first introduced the following equations:

$$n_t = \phi_{xx}, \quad (8)$$

$$\phi_t = n + |u|^2, \quad (9)$$

$$u_t = \psi_{xx}, \quad (10)$$

$$\psi_{xxt} = u_{xx} - u - nu, \quad (11)$$

with periodic initial data

$$\begin{aligned}n(x, 0) &= n_0, \\ \phi(x, 0) &= \phi_0, \\ u(x, 0) &= u_0, \\ \psi(x, 0) &= \psi_0.\end{aligned}\quad (12)$$

Moreover, $n(x, t)$, $\phi(x, t)$, $u(x, t)$, $\psi(x, t)$, $n(x, 0)$, $\phi(x, 0)$, $u(x, 0)$, and $\psi(x, 0)$ are periodic functions with L about $x(-\infty < x < +\infty, L > 0, 0 \leq t \leq T)$. Firstly, applying

Galerkin method, we structure the approximate solution of (8)–(11); the aim is to obtain the local classical solution. Next, we employ this method of integral estimates to prove the existence and uniqueness of the global solution of (1)-(2).

We divide this paper into four parts. In Section 2, we establish a priori estimate of (8)–(11). In Section 3, we give the existence of local and global smooth solutions of the above equations. Lastly, in Section 4, we prove existence and uniqueness of the global classical solution of (1)-(2).

Notation. In complex Hilbert function space, inner product and standard norm are defined as follows:

$$(f, g) = \int_0^L f(x) \overline{g(x)} dx, \quad (13)$$

$$\|f\|_{L_2} = \|f\| = \int_0^L |f|^2 dx,$$

where $\overline{g(x)}$ is conjugate function of $g(x)$.

H^s is complex function space with generalized differentiable function $D^k u (k \leq s) \in L^2$, and the norm is defined as follows:

$$\|f\|_s^2 = \sum_{k \leq s} \|D^k f\|_{L^2}^2. \quad (14)$$

$L^s(0, T; H^s)$ denotes function space about complex function of $f(x, t)$. Moreover, for any $0 \leq t \leq T$, $f(x, t) \in H^s$, and $\sup_{0 \leq t \leq T} \|f\|_{H^s}$ is bound. Particularly,

$$\|f(x, t)\|_{L^\infty} = \sup |f(x, t)|. \quad (15)$$

Furthermore, $C_0, C_1, C_2, \dots, D_0, D_1, D_2, \dots, E_0, E_1, E_2, \dots$ are estimate constants, which relate to initial conditions.

2. A Priori Estimate of Integrating

Lemma 1. *If $u_0 \in L^2$, $|\psi_{xx}| \leq C_0|u|$, and $E_0 = \|u_0\|^2$, then $\|u\|^2 \leq C_1 E_0$.*

Proof. Equation (10) makes inner product with u and takes real part; we have

$$\int_0^L \frac{1}{2} (uu_t) dx = \int_0^L \psi_{xx} \bar{u} dx \leq \int_0^L |\psi_{xx}| |\bar{u}| dx, \quad (16)$$

$$\frac{1}{2} \frac{d}{dt} \|u\|^2 \leq C_0 \|u\|^2.$$

By Gronwall inequality, we can obtain that

$$\|u\|^2 \leq C_1 E_0. \quad (17)$$

□

Lemma 2. *If $u_{0t}, u_{0x}, u_0, n_{0x}, \phi_{0x}, \psi_{0x} \in L^2$, then*

$$\begin{aligned}\|u_t\|^2 + \|u_x\|^2 + \|u\|^2 + \int_0^L n |u|^2 dx + \frac{1}{2} \int_0^L \phi_x^2 dx \\ + \frac{1}{2} \int_0^L n^2 dx = M_1,\end{aligned}\quad (18)$$

where

$$\begin{aligned} & \|u_{0t}\|^2 + \|u_{0x}\|^2 + \|u_0\|^2 + \int_0^L n_0 |u_0|^2 dx \\ & + \frac{1}{2} \int_0^L \phi_{0x}^2 dx + \frac{1}{2} \int_0^L n_0^2 dx = M_1. \end{aligned} \quad (19)$$

Proof. Taking inner product (11) with u_t and making real part, we have that

$$\begin{aligned} \int_0^L \psi_{xxt} \bar{u}_t dx &= \int_0^L u_{tt} \bar{u}_t dx = \frac{1}{2} \frac{d}{dt} \int_0^L |u_t|^2 dx \\ &= \frac{1}{2} \frac{d}{dt} \|u_t\|^2, \end{aligned} \quad (20)$$

$$\int_0^L u_{xx} \bar{u}_t dx = -\frac{1}{2} \frac{d}{dt} \int_0^L |u_x|^2 dx = -\frac{1}{2} \frac{d}{dt} \|u_x\|^2, \quad (21)$$

$$\int_0^L u \bar{u}_t dx = \frac{1}{2} \frac{d}{dt} \int_0^L |u|^2 dx = \frac{1}{2} \frac{d}{dt} \|u\|^2, \quad (22)$$

$$\begin{aligned} \int_0^L n u \bar{u}_t dx &= \frac{1}{2} \frac{d}{dt} n \|u\|^2 dx + \frac{1}{4} \frac{d}{dt} \int_0^L \phi_x^2 dx \\ &+ \frac{1}{4} \frac{d}{dt} \int_0^L n^2 dx. \end{aligned} \quad (23)$$

Combining (20)–(23) yields

$$\begin{aligned} & \frac{d}{dt} \left(\|u_t\|^2 + \|u_x\|^2 + \|u\|^2 + \int_0^L n |u|^2 dx \right. \\ & \left. + \frac{1}{2} \int_0^L \phi_x^2 dx + \frac{1}{2} \int_0^L n^2 dx \right) = 0. \end{aligned} \quad (24)$$

Therefore,

$$\begin{aligned} & \|u_{0t}\|^2 + \|u_{0x}\|^2 + \|u_0\|^2 + \int_0^L n_0 |u_0|^2 dx \\ & + \frac{1}{2} \int_0^L \phi_{0x}^2 dx + \frac{1}{2} \int_0^L n_0^2 dx = M_1. \end{aligned} \quad (25)$$

Lemma 3. If $u_0 \in H^1$, $\phi_0 \in H^1$, and $n_0 \in L^2$, then

$$\begin{aligned} & \|u\|_{H^1}^2 \leq E_1, \\ & \|n\|^2 \leq E_2, \\ & \|\phi\|_{H^1} \leq E_3, \\ & \|\phi_t\|^2 \leq E_4, \end{aligned} \quad (26)$$

where E_1 , E_2 , E_3 , and E_4 are constants, which only relate to $\|n_0\|$, $\|u_0\|_{H^1}$, $\|\phi_0\|_{H^1}$, and T .

Proof. From (18), we can easily obtain that

$$\|u_x\|^2 + \|u\|^2 \leq M_1. \quad (27)$$

So that,

$$\|u\|_{H^1} \leq E_1. \quad (28)$$

By (9) and (18), we have

$$\begin{aligned} \int_0^L n^2 dx &= \int_0^L (\phi_t - |u|)^2 dx \leq 2 \int_0^L (\phi_t^2 + |u|^4) dx \\ &\leq 2 |M_1|. \end{aligned} \quad (29)$$

Hence,

$$\begin{aligned} & \|n\|^2 \leq 2M_1 = E_2, \\ & \|\phi_t\|^2 \leq E_4. \end{aligned} \quad (30)$$

Furthermore, (9) takes inner product with ϕ ; we get

$$\begin{aligned} \frac{d}{dt} \|\phi\|^2 &\leq \left[\|\phi\|^2 + 2 \left(\|n\|^2 + \|u^2\|^2 \right) \right] \\ &\leq \|\phi\|^2 + E_2 + M_1 \leq E_5 \|\phi\|^2. \end{aligned} \quad (31)$$

By Gronwall inequality, we have

$$\|\phi\|^2 \leq \|\phi_0\|^2 e^T. \quad (32)$$

Hence, in combination with (18), we can deduce that

$$\|\phi\|_{H^1} \leq E_3. \quad (33)$$

□

Lemma 4. If $u_0 \in H^1$, $u_{0t} \in H^2$, $u_{0x} \in H^2$, and $n_0 \in H^1$, then

$$\|u_t\|^2 + \|u_x\|^2 + \|u\|^2 \leq E_5. \quad (34)$$

Proof. The first equation of (1) makes inner product with u_t and takes real part; we have that

$$\begin{aligned} & \frac{d}{dt} \left(\|u_t\|^2 + \|u_x\|^2 + \|u\|^2 \right) \leq \frac{1}{2} \left(\int_0^T |n|^4 dx \right. \\ & \left. + \int_0^T |u|^4 dx + 2 \|u_t\|^2 \right) \leq \frac{1}{2} \|n\|^2 \|n\|_{L^\infty}^2 + \frac{1}{2} \|u\|^2 \\ & \cdot \|u\|_{L^\infty}^2 + \|u_t\|^2 \leq \left[(\alpha_1^2 \|n_x\|^2 + c_1^2 \|n\|^2) \|n\|^2 \right. \\ & \left. + (\alpha_2^2 \|u\|^2 + c_2^2 \|u_x\|^2) \|u\|^2 + \|u_t\|^2 \right] \leq B_1 \left(\|u_t\|^2 \right. \\ & \left. + \|u_x\|^2 + \|u\|^2 \right) + B_2, \end{aligned} \quad (35)$$

where $B_1 = \max\{1, \alpha_2^2 C_1 E_0, c_2^2 C_1 E_0\}$ and $B_2 = \alpha_1^2 E_1 \|n_x\|^2$.

So that, by Gronwall inequality, we obtain that

$$\|u_t\|^2 + \|u_x\|^2 + \|u\|^2 \leq E_5. \quad (36)$$

□

Corollary 5. $\|u\|_{L^\infty}^2 \leq E_{51}$, $\|u_t\|_{L^\infty}^2 \leq E_{52}$, $\|u_x\|_{L^\infty}^2 \leq E_{53}$, and $\|n\|_{L^\infty} \leq E_{54}$.

Lemma 6. If $n_{0tt}, n_{0xt}, u_{0tt}, u_{0xx} \in L^2$, then one has

$$\|n_{tt}\|^2 + \|n_{xt}\|^2 + \|u_{tt}\|^2 + \|u_{xx}\|^2 \leq E_6. \quad (37)$$

Proof. We differentiate t with respect to the second equation of (1); we obtain that

$$n_{ttt} - n_{xxt} = (|u|^2)_{xxt}. \quad (38)$$

Equation (38) takes inner product with n_{tt} ; we have that

$$\frac{d}{dt} \|n_{tt}\|^2 + \frac{d}{dt} \|n_{xt}\|^2 \leq \|n_{tt}\|^2 + \|(|u|^2)_{xxt} \|^2. \quad (39)$$

Furthermore,

$$\begin{aligned} \| |u|^2_{xxt} \|^2 &= \| 4u_{tx}\bar{u}_x + 2u_{txx}\bar{u} + 2u_{xx}\bar{u}_t \|^2 \\ &\leq 4 \|\bar{u}_x\| \|u_{tx}\|_{L^\infty} + 2 \|u_{txx}\| \|\bar{u}\|_{L^\infty} \\ &\quad + 2 \|u_{xx}\| \|u_t\|_{L^\infty} \\ &\leq 4 \frac{c_{11} \|u\|}{1 - \alpha_{12}} \|u_{tx}\|_{L^\infty} + 2\sqrt{E_{51}} \|u_{txx}\| \\ &\quad + 2\sqrt{E_{52}} \|u_{xx}\| \\ &\leq 4 \frac{c_{11}\sqrt{C_1E_0}}{1 - \alpha_{12}} \left(c_{12}\sqrt{E_5} + \alpha_{13} \|u_{txx}\| \right) \\ &\quad + 2\sqrt{E_{51}} \|u_{txx}\| + 2\sqrt{E_{52}} \|u_{xx}\| \\ &\leq 4 \frac{c_{11}\sqrt{C_1E_0}}{1 - \alpha_{12}} c_{12}\sqrt{E_5} \\ &\quad + \frac{4c_{11}\sqrt{C_1E_0}\alpha_{13}}{1 - \alpha_{12}} \frac{c_{13}}{1 - \alpha_{14}} \|u_{xx}\| \\ &\quad + 2\sqrt{E_{51}} \frac{c_{13} \|u_{xx}\|}{1 - \alpha_{14}} + 2 \|u_{xx}\| \sqrt{E_{52}} \\ &\leq B_3 (1 + \|u_{xx}\|), \end{aligned} \quad (40)$$

where $B_3 = \max\{4c_{11}\sqrt{C_1E_0}c_{12}\sqrt{E_5}/(1 - \alpha_{12}), 4c_{11}c_{13}\sqrt{C_1E_0}\alpha_{13}/(1 - \alpha_{12})(1 - \alpha_{14}) + 2\sqrt{E_{51}}c_{13}/(1 - \alpha_{14}) + 2\sqrt{E_{52}}\}$.
So,

$$\| |u|^2_{xxt} \|^2 \leq B_3^2 (1 + \|u_{xx}\|^2). \quad (41)$$

Differentiating (1) with respect to t , we have that

$$u_{ttt} - u_{xxt} + u_t + nu_t + n_tu = 0. \quad (42)$$

Next, (42), respectively, makes inner product with u_{xx} and u_{tt} and takes real part; we can obtain that

$$\begin{aligned} \frac{d}{dt} \|u_{xx}\|^2 &\leq \|u_{xx}\|^2 + \|u_{ttt}\|^2 + 2 \|u_t\|_{L^\infty}^2 \|u_{xx}\|^2 \\ &\quad + \|u_t\|_{L^\infty} (\|n\|^2 + \|u_x\|^2) \\ &\quad + (\|n_{tx}\|^2 + \|u\|^2) \|u_x\|^2 \\ &\leq \|u_{xx}\|^2 + \frac{c_{14}^2}{1 - \alpha_{14}} \|u_{ttt}\|^2 + 2E_5 \|u_{xx}\|^2 \\ &\quad + E_5 \|n_{tx}\|^2 + E_5^{3/2} + \sqrt{E_5}M_1 + E_5C_1E_0 \\ &\leq B_4 (\|u_{xx}\|^2 + \|u_{tt}\|^2 + \|n_{tx}\|^2 + 1), \end{aligned} \quad (43)$$

$$\begin{aligned} \frac{d}{dt} \|u_{tt}\|^2 &\leq \|\bar{u}_{xxt}\|^2 + 2 \|u_{tt}\|^2 \\ &\quad + \|n\|_{L^\infty} (\|u_t\|^2 + \|u_{tt}\|^2) \\ &\quad + \|n_t\|_{L^\infty} (\|u\|^2 + \|u_{tt}\|^2) \\ &\leq \frac{c_{15}^2}{(1 - \alpha_{15})^2} \|u_{xx}\|^2 + (3 + \sqrt{E_2}) \|u_{tt}\|^2 \\ &\quad + \alpha_{16} \|n_{tt}\|^2 + C_1E_0 + \sqrt{E_2}E_5 + c_{16}^2E_2 \\ &\leq B_5 (\|u_{xx}\|^2 + \|u_{tt}\|^2 + \|n_{tt}\|^2 + 1). \end{aligned} \quad (44)$$

Here,

$$\begin{aligned} B_4 &= \max \left\{ 1 + 2E_5, \frac{c_{14}^2}{(1 - \alpha_{14})^2}, E_5, E_5^{3/2} + \sqrt{E_5}M_1 \right. \\ &\quad \left. + E_5C_1E_0 \right\}, \\ B_5 &= \max \left\{ \frac{c_{15}^2}{(1 - \alpha_{15})^2}, 3 + \sqrt{E_2}, C_1E_0 + \sqrt{E_2}E_5 \right. \\ &\quad \left. + c_{16}^2E_2 \right\}. \end{aligned} \quad (45)$$

Combining (39), (41), (43), and (44) yields

$$\begin{aligned} \frac{d}{dt} (\|n_{tt}\|^2 + \|n_{xt}\|^2 + \|u_{tt}\|^2 + \|u_{xx}\|^2) \\ \leq B_6 (\|n_{tt}\|^2 + \|n_{xt}\|^2 + \|u_{tt}\|^2 + \|u_{xx}\|^2 + 1). \end{aligned} \quad (46)$$

Therefore, applying Gronwall inequality, we can obtain

$$\|n_{tt}\|^2 + \|n_{xt}\|^2 + \|u_{tt}\|^2 + \|u_{xx}\|^2 \leq E_6. \quad (47)$$

□

Lemma 7. If $\|n_{0ttt}\|^2 + \|n_{0xxt}\|^2 + \|u_{0ttt}\|^2 \leq E_7$, then

$$\|n_{ttt}\|^2 + \|n_{xxt}\|^2 + \|u_{ttt}\|^2 \leq E_8. \quad (48)$$

Proof. Differentiating (8) with respect to t thrice and differentiating (9) with respect to x and t twice and eliminating ϕ_{xxtt} , we have

$$n_{tttt} - n_{xxtt} = |u|_{xxtt}^2. \quad (49)$$

Furthermore, also differentiating (10) with respect to t thrice and differentiating (11) with respect to t twice and eliminating ψ_{xxtt} , we can obtain

$$u_{tttt} - u_{xxtt} + u_{tt} + 2n_t u_t + n u_{tt} + n_{tt} u = 0. \quad (50)$$

Equation (49) makes inner product with n_{ttt} ; then

$$\frac{d}{dt} (\|n_{ttt}\|^2 + \|n_{xxt}\|^2) \leq 4 \|n_{ttt}\|^2 + \| |u|_{xxtt}^2 \|^2. \quad (51)$$

Furthermore,

$$\begin{aligned} \| |u|_{xxtt}^2 \| \leq & 2 \|\bar{u}\|_{L^\infty} \|u_{ttxx}\| + 4 \|\bar{u}_x\|_{L^\infty} \|u_{ttx}\| + \|u_{tt}\|^2 \\ & + \|u_{xx}\|^2 + 4 \|u_{txx}\| \|\bar{u}_t\|_{L^\infty} + 4 \|u_{tx}\|^2, \end{aligned} \quad (52)$$

$$\|u_{ttx}\| \leq c_{17} \|u_{tt}\| + \alpha_{17} \|u_{ttxx}\|, \quad (53)$$

$$\|u_{xxt}\| \leq c_{18} \|u_{xx}\| + \alpha_{18} \|u_{ttxx}\|,$$

$$\|u_{tttt}\| \leq \frac{c_{19}}{1 - \alpha_{19}} \|u_{ttt}\|, \quad (54)$$

$$\begin{aligned} \|u_{xxtt}\| \leq & \|u_{tttt}\| + \|u_{tt}\| + \|n_t\|^2 + \|u_t\|^2 + \frac{1}{2} \|n\|^2 \\ & + \frac{1}{2} \|u_{tt}\|^2 + \frac{1}{2} \|u\|^2 + \frac{1}{2} \|n_{tt}\|^2 \\ \leq & \frac{c_{19}}{1 - \alpha_{19}} \|u_{ttt}\| + \sqrt{E_6} + c_{20}^2 E_2 + \alpha_{20}^2 \|n_{ttt}\|^2 \\ & + \frac{1}{2} E_2 + \sqrt{E_5} + \frac{1}{2} C_1 E_0 + E_6. \end{aligned} \quad (55)$$

Due to Lemmas 4 and 6, Corollary 5, and (53) and (54), we have that

$$\begin{aligned} \| |u|_{xxtt}^2 \| \leq & \left(2\sqrt{E_{51}} + 4\sqrt{E_{53}\alpha_{18}} + 4\sqrt{E_{52}\alpha_{17}} \right) \|u_{ttxx}\| \\ & + 4\sqrt{E_{52}c_{17}}\sqrt{E_6} + 2\sqrt{E_6} + 4\sqrt{E_{53}c_{18}}\sqrt{E_6} \\ \leq & B_7 \|u_{ttt}\| + B_8 \|n_{ttt}\|^2 + B_9, \end{aligned} \quad (56)$$

where

$$\begin{aligned} B_7 &= \left(2\sqrt{E_{51}} + 4\sqrt{E_{53}\alpha_{18}} + 4\sqrt{E_{52}\alpha_{17}} \right) \frac{c_{19}}{1 - \alpha_{19}}, \\ B_8 &= \left(2\sqrt{E_{51}} + 4\sqrt{E_{53}\alpha_{18}} + 4\sqrt{E_{52}\alpha_{17}} \right) \alpha_{20}^2, \\ B_9 &= \left(2\sqrt{E_{51}} + 4\sqrt{E_{53}\alpha_{18}} + 4\sqrt{E_{52}\alpha_{17}} \right) \\ &\cdot \left(\sqrt{E_6} + c_{20}^2 E_2 + \frac{1}{2} E_2 + \sqrt{E_5} + \frac{1}{2} C_1 E_0 + E_6 \right) \\ &+ 4\sqrt{E_{52}c_{17}}\sqrt{E_6} + 2\sqrt{E_6} + 4\sqrt{E_{53}c_{18}}\sqrt{E_6}. \end{aligned} \quad (57)$$

Equation (50) makes inner product with u_{ttt} and takes real part; we have that

$$\begin{aligned} \frac{1}{2} \frac{d}{dt} \|u_{ttt}\|^2 \leq & \frac{1}{2} (\|u_{xxtt}\|^2 + \|u_{ttt}\|^2) \\ & + \frac{1}{2} (\|u_{tt}\|^2 + \|u_{ttt}\|^2) \\ & + \|u_t\|_{L^\infty} (\|n_t\|^2 + \|u_{ttt}\|^2) \\ & + \frac{1}{2} \|n\|_{L^\infty} (\|u_{tt}\|^2 + \|u_{ttt}\|^2) \\ & + \frac{1}{2} \|u\|_{L^\infty} (\|n_{tt}\| + \|u_{ttt}\|^2). \end{aligned} \quad (58)$$

Combining (51), (56), and (58) and Corollary 5 and applying Gronwall inequality, Lemma 7 can easily be proven. \square

3. Existence of Local Classical Solution

Firstly, we apply Galerkin method to establish approximating solution for (8)–(11) as follows:

$$\begin{aligned} n^m &= n^m(x, t) = \sum_{j=1}^m n_{jm}(t) W_j(x), \\ \phi^m &= \phi^m(x, t) = \sum_{j=1}^m \phi_{jm}(t) W_j(x), \\ u^m &= u^m(x, t) = \sum_{j=1}^m u_{jm}(t) W_j(x), \\ \psi^m &= \psi^m(x, t) = \sum_{j=1}^m \psi_{jm}(t) W_j(x). \end{aligned} \quad (59)$$

Moreover, n^m , ϕ^m , u^m , and ψ^m satisfy the following equations and initial condition:

$$(n_t^m, W_j) - (\phi_{xx}^m, W_j) = 0, \quad (60)$$

$$(\phi_t^m, W_j) - (n^m + |u^m|^2, W_j) = 0, \quad (61)$$

$$(u_t^m, W_j) - (\psi_{xx}^m, W_j) = 0, \quad (62)$$

$$(\psi_{xxt}^m, W_j) - (u_{xx}^m, W_j) + (u^m, W_j) + (n^m u^m, W_j) = 0. \quad (63)$$

$$(n^m(x, 0), W_j) = (n_0, W_j), \quad (64)$$

$$(\phi^m(x, 0), W_j) = (\phi_0, W_j), \quad (65)$$

$$(u^m(x, 0), W_j) = (u_0, W_j), \quad (66)$$

$$(\psi^m(x, 0), W_j) = (\psi_0, W_j). \quad (67)$$

Next, by implementing integration estimates for the approximation solution of (60)–(63), we establish local classical solution of (60)–(63).

Lemma 8. *If $u^m(x, 0) \in L^2$, $|\psi_{xx}^m| \leq C$, and $\|u^m(x, 0)\| = E_9$, then we have*

$$\|u^m\| \leq CE_9. \quad (68)$$

Proof. Equation (62) multiplies $\overline{u_j^m}$ and makes summation for $j = 1, 2, \dots, n$; we obtain

$$(u_t^m, u^m) - (\psi_{xx}^m, u^m) = 0. \quad (69)$$

Taking real part, we have that

$$\frac{d}{dt} \|u^m\|^2 \leq C \|u^m\|^2. \quad (70)$$

Therefore, by Gronwall inequality, we have $\|u^m(t)\| \leq CE_9$. \square

Lemma 9. *If $n^m(x, 0) \in L^2$, $n_x^m(x, 0) \in L^2$, $n_t^m(x, 0) \in L^2$, $\phi_x^m(x, 0) \in L^2$, and $\|u^m\|_{L^\infty} \leq E_{91}$, then*

$$\|n_x^m\|^2 + \|\phi^m\|^2 + \|n_t^m\|^2 \leq E_{10}. \quad (71)$$

Proof. Equation (60) multiplies $\overline{n_j^m}$ and makes summation for $j = 1, 2, \dots, n$; we can obtain

$$(n_t^m, n^m) = \frac{1}{2} \frac{d}{dt} \|n^m\|^2, \quad (72)$$

$$(\phi_{xx}^m, n^m) \leq \|\phi_x^m\|^2 + \|n_x^m\|^2. \quad (73)$$

Furthermore, (60) differentiates with respect to t and (61) differentiates with respect to x twice; we have that

$$(n_{tt}^m, w_j) - (n_{xx}^m + |u^m|_{xx}^2, w_j) = 0. \quad (74)$$

Next, (74) multiplies $\overline{n_{jt}^m}$ and makes summation for $j = 1, 2, \dots, n$; it is easy to obtain the following equation:

$$(n_{tt}^m, n_t^m) - (n_{xx}^m + |u^m|_{xx}^2, n_t^m) = 0. \quad (75)$$

So, we obtain that

$$(n_{tt}^m, n_t^m) = \frac{1}{2} \frac{d}{dt} \|n_t^m\|^2, \quad (76)$$

$$-(n_{xx}^m, n_t^m) = \frac{1}{2} \frac{d}{dt} \|n_x^m\|^2. \quad (77)$$

$$|(|u^m|_{xx}^2, n_t^m)| \leq \frac{1}{2} \left(\|n_t^m\|^2 + 4 \| |u_x^m|^2 + u_{xx}^m \overline{u^m} \|^2 \right). \quad (78)$$

Furthermore,

$$\begin{aligned} \| |u_x^m|^2 + u_{xx}^m \overline{u^m} \| &\leq \| |u_x^m|^2 \| + \| \overline{u^m} \|_{L^\infty} \|u_{xx}^m\| \\ &\leq (c_{18} \|u^m\| + \alpha_{19} \|u_{xx}^m\|) \|u_x^m\| \\ &\quad + (c_{19} \| \overline{u^m} \| + \alpha_{20} \|u_{xx}^m\|) \|u_{xx}^m\|, \end{aligned} \quad (79)$$

$$\|u_{xx}^m\| \leq \frac{c_{20}}{1 - \alpha_{21}} \|u_x^m\|. \quad (80)$$

Therefore,

$$\| |u_x^m|^2 + u_{xx}^m \overline{u^m} \|^2 \leq D_1 + (1 + D_2) \|u_x^m\|^2, \quad (81)$$

where $D_1 = (c_{18}CE_9 + (c_{20}/(1 - \alpha_{21}))c_{19}CE_9)^2$ and $D_2 = (\alpha_{19}(c_{20}/(1 - \alpha_{21})) + \alpha_{20}(c_{20}^2/(1 - \alpha_{21})^2))^2$.

Equation (61) multiplies $(-\lambda_j)$; we have that

$$(\phi_t^m, w_{jxx}) - (n^m + |u^m|^2, w_{jxx}) = 0. \quad (82)$$

Equation (82) multiplies $\phi_{jm}(t)$; then

$$(\phi_t^m, \phi_{xx}^m) - (n^m + |u^m|^2, \phi_{xx}^m) = 0. \quad (83)$$

Furthermore,

$$|(\phi_t^m, \phi_{xx}^m)| = \frac{1}{2} \frac{d}{dt} \|\phi_x\|^2, \quad (84)$$

$$\begin{aligned} |(n^m + |u^m|^2, \phi_{xx}^m)| &= \int_0^{2\pi} (n^m + |u^m|^2)_x \phi_x dx \\ &\leq \frac{1}{2} \left[\|n_x^m\|^2 + \|\phi_x^m\|^2 + 4 \|u^m\|_{L^\infty} \left(\|n_x^m\|^2 + \| \overline{u_x^m} \|^2 \right) \right] \\ &\leq \frac{1}{2} \left[\|n_x^m\|^2 + \|\phi_x^m\|^2 + 4E_{91} \|n_x^m\|^2 + 4 \|u_x^m\|^2 \right]. \end{aligned} \quad (85)$$

So,

$$\frac{d}{dt} \|\phi_x^m\|^2 \leq D_3 \left(\|n_x^m\|^2 + \|\phi_x^m\|^2 + \|u_x^m\|^2 \right), \quad (86)$$

where $D_3 = \max\{4, 4E_{91}\}$.

Combining (76), (77), (78), (81), (84), and (86), we can obtain that

$$\begin{aligned} & \frac{d}{dt} (\|n_x^m\|^2 + \|n_t^m\|^2 + \|\phi_x^m\|^2) \\ & \leq D_4 (1 + \|n_t^m\|^2 + \|n_x^m\|^2 + \|\phi_x^m\|^2 + \|u_x^m\|^2), \end{aligned} \quad (87)$$

where $D_4 = \max\{1, 2D_3 + 2, 8D_1, 8(1 + D_2) + 2D_3\}$. So, by Gronwall inequality, we have that

$$\|n_x^m\|^2 + \|\phi_x^m\|^2 + \|n_t^m\|^2 \leq E_{10}. \quad (88)$$

□

Lemma 10. $\|\phi_t^m\|^2 \leq E_{11}$, $\|\phi_{xx}^m\| \leq E_{12}$, $\|u_{tt}^m\| \leq E_{13}$, and $\|u_{xx}^m\| \leq E_{14}$.

Proof. The proof is similar to that of Lemma 9. For details, see Lemma 9. □

Definition 11. If $n(x, t) \in L^\infty(0, T_0, H^0)$, $\phi(x, t) \in L^\infty(0, T_0, H^2)$, $u(x, t) \in L^\infty(0, T_0, H^2)$, $\psi(x, t) \in L^\infty(0, T_0, H^3)$, and $n_t, \phi_t, u_t, \psi_t \in L^\infty(0, T_0, H^0)$. Moreover, they satisfy the following integral identity:

$$\begin{aligned} (n_t, v) &= (\phi_{xx}, v) \\ (\phi_t, v) &= (n + |u|^2, v) \\ (u_t, v) &= (\psi_{xx}, v) \\ (\psi_{xxt}, v) &= (u_{xx} - u - nu, v), \end{aligned} \quad (89)$$

and

$$\begin{aligned} (n(x, 0), v) &= (n_0(x), v) \\ (\phi(x, 0), v) &= (\phi_0(x), v) \\ (u(x, 0), v) &= (u_0(x), v) \\ (\psi(x, 0), v) &= (\psi_0(x), v). \end{aligned} \quad (90)$$

Then, n , ϕ , u , and ψ are local generalized solutions of (60)–(63). Besides, n , ϕ , u , and ψ are periodic functions with L about x .

Theorem 12. If $n^m(x, 0) \in L^2$, $n_x^m(x, 0) \in L^2$, $n_t^m(x, 0) \in L^2$, $\phi_x^m(x, 0) \in L^2$, $\|u^m\|_{L^\infty} \leq E_{91}$, n_0, ϕ_0, u_0 , and ψ_0 are period functions with L about x . Then, (60)–(63) have local generalized solution.

Proof. By Lemmas 8, 9, and 10, $\|n_x^m\|, \|n_t^m\|, \|\phi_x^m\|, \|u_{xx}^m\|$, and $\|u_{tt}^m\|$ have uniform boundedness. So, we can select a subsequence and satisfy $n_t^m \xrightarrow{weak} n_t, \phi_x^m \xrightarrow{weak} \phi_x, u_{tt}^m \xrightarrow{weak} u_{tt}$, and $u_{xx}^m \xrightarrow{weak} u_{xx}$. Moreover, there exists subsequences, $n^m \xrightarrow{strong} n, \phi^m \xrightarrow{strong} \phi$, and $u^m \xrightarrow{strong} u$.

In (60)–(63), let $m \rightarrow \infty$; we have

$$(n_t, W_j) - (\phi_{xx}, W_j) = 0, \quad (91)$$

$$(\phi_t, W_j) - (n + |u|^2, W_j) = 0, \quad (92)$$

$$(u_t, W_j) - (\psi_{xx}, W_j) = 0, \quad (93)$$

$$(\psi_{xxt}, W_j) - (u_{xx}, W_j) + (u, W_j) + (nu, W_j) = 0. \quad (94)$$

Moreover $W_j \in H^2$ and it is dense in H^0 , W_j approximates to v . We complete the proof of this theorem. Similarly, we also can prove (64)–(67). □

Lemma 13. If $\|n_{tt}^m(x, 0)\|, \|n_{xt}^m(x, 0)\|, \|u_{xx}^m(x, 0)\|$, and $\|u_{tt}^m(x, 0)\|$ are bound, then

$$\|n_{tt}^m\|^2 + \|n_{xt}^m\|^2 + \|u_{xx}^m\|^2 + \|u_{tt}^m\|^2 \leq E_{10}. \quad (95)$$

Proof. Equation (74) differentiates with respect to t . Next, it multiplies $\overline{n_{jt}^m}$ and makes summation for $j = 1, 2, \dots, n$. We can easily obtain the following equation:

$$(n_{ttt}^m, n_{tt}^m) - (n_{xxt}^m + |u_{xxt}^m|^2, n_{tt}^m) = 0. \quad (96)$$

Furthermore,

$$(n_{ttt}^m, n_{tt}^m) = \frac{1}{2} \frac{d}{dt} \|n_{tt}^m\|^2, \quad (97)$$

$$(n_{xxt}^m, n_{tt}^m) = -\frac{1}{2} \frac{d}{dt} \|n_{xt}^m\|^2, \quad (98)$$

$$(|u_{xxt}^m|, n_{tt}^m) \leq \frac{1}{2} (\|u_{xxt}^m\|^2 + \|n_{tt}^m\|^2). \quad (99)$$

Meanwhile, by CoóojieB inequality,

$$\begin{aligned} \| |u^m|_{xxt} \| &= \| 4u_{tx}^m \overline{u_x^m} + 2u_{txx}^m \overline{u^m} + 2u_{xxt}^m \overline{u_t} \| \\ &\leq 4 \| \overline{u_x^m} \| \| u_{tx}^m \|_{L^\infty} + 2 \| u_{txx}^m \| \| u^m \|_{L^\infty} \\ &\quad + 2 \| u_{xxt}^m \| \| u_t^m \|_{L^\infty} \\ &\leq 4 (c_{22} \| \overline{u^m} \| + \alpha_{22} \| \overline{u_{xx}^m} \|) (c_{23} \| u_t^m \| + \alpha_{23} \| u_{xxt}^m \|) \\ &\quad + 2 \| u_{ttx}^m \| (c_{24} \| \overline{u^m} \| + \alpha_{24} \| \overline{u_{xx}^m} \|) \\ &\quad + 2 \| u_{xx}^m \| (c_{25} \| \overline{u^m} \| + \alpha_{25} \| u_{tt}^m \|) \\ &\leq D_5 + D_6 \| u_{tt}^m \|^2 + D_7 \| u_{xxt}^m \|^2. \end{aligned} \quad (100)$$

Here,

$$\begin{aligned} D_5 &= 4c_{22}^2 C^2 E_9 + \frac{c_{27}}{1 - \alpha_{27}} (c_{24} C E_9)^2 + (c_{25} C E_9)^2, \\ D_6 &= 4c_{23}^2 \left(\frac{c_{28}}{1 - \alpha_{28}} \right)^2 + \frac{c_{27}}{1 - \alpha_{27}} + \alpha_{25}^2, \\ D_7 &= 4\alpha_{22}^2 + 4\alpha_{23} \left(\frac{c_{26}}{1 - \alpha_{26}} \right)^2. \end{aligned} \quad (101)$$

Moreover, (62) differentiates with respect to t twice, multiplies $\overline{u_{jtt}^m}$, and makes summation for $j = 1, 2, \dots, n$; we can obtain that

$$(u_{ttt}^m, u_{tt}^m) - (\psi_{xxtt}^m, u_{tt}^m) = 0, \quad (102)$$

$$(u_{ttt}^m, u_{tt}^m) = \frac{1}{2} \frac{d}{dt} \|u_{tt}^m\|^2, \quad (103)$$

$$|(\psi_{xxtt}, u_{tt}^m)| \leq \frac{1}{2} (\|\psi_{xxtt}^m\|^2 + \|u_{tt}^m\|^2). \quad (104)$$

Next, (62) differentiates with respect to x twice, multiplies $(-\lambda)$, and makes summation for $j = 1, 2, \dots, n$; we have that

$$(u_{txx}^m, u_{xx}^m) - (\psi_{xxxx}, u_{xx}^m) = 0, \quad (105)$$

$$(u_{txx}^m, u_{xx}^m) = \frac{1}{2} \frac{d}{dt} \|u_{xx}^m\|^2, \quad (106)$$

$$|(\psi_{xxxx}, u_{xx}^m)| \leq \frac{1}{2} (\|u_{xx}^m\|^2 + \|\psi_{xxxx}^m\|^2), \quad (107)$$

and (60) differentiates with respect to t and x ; we can obtain that

$$(n_{ttx}^m, W_j) - (\phi_{xxtt}^m, W_j) = 0, \quad (108)$$

where $(n_{ttx}^m, W_{jx}) - (\phi_{xxtt}^m, W_{jx}) = 0$ multiplies $\overline{n_{jt}^m}$ and makes summation for $j = 1, 2, \dots, n$; we can obtain that

$$(n_{ttx}^m, n_{xt}) - (\phi_{xxtt}^m, n_{xt}) = 0. \quad (109)$$

Taking real part, we have that

$$(n_{ttx}^m, n_{xt}^m) = \frac{1}{2} \frac{d}{dt} \|n_{tx}^m\|^2, \quad (110)$$

$$|(\psi_{xxtt}, n_{xt}^m)| \leq \frac{1}{2} (\|n_{tx}^m\|^2 + \|\psi_{xxtt}^m\|^2). \quad (111)$$

By (97), (98), (99), (100), (103), (104), (107), (110), and (111) and applying Gronwall inequality, we can obtain the result of Lemma 13. \square

Corollary 14. *If $\|u_{tx}^m(x, 0)\|$, $\|\psi_{tx}^m(x, 0)\|$, and $\|n_{xx}^m(x, 0)\|$ are bound, then there exist T_0 , $0 \leq t \leq T_0$, $\|u_{tx}^m(t)\| \leq E_{11}$, $\|\psi_{tx}^m(t)\| \leq E_{12}$, and $\|n_{xx}^m(t)\| \leq E_{13}$.*

Theorem 15. *Assume that the conditions of Lemmas 8, 9, 10, and 13 are satisfied, then initial value problem (1) has local classical solution.*

Proof. The idea and method are similar to Theorem 3.2 of [1]. For details, please see this paper. \square

4. Initial Value Function and Its Derivative Estimate in L^2

In this section, we apply the idea and method of [1] to discuss boundedness of $\|n_t^m(0)\|$, $\|\phi_t^m(0)\|$, $\|u_t^m(0)\|$, and $\|\psi_{xxt}^m\|$.

Assume that $n_0 \in H^6$, $\phi_0 \in H^4$, $u_0 \in H^4$, and $\psi_0 \in H^4$, and take n_0^m, ϕ_0^m, u_0^m , and ψ_0^m ; they satisfy $n_0^m \xrightarrow{H^6} n_0, \phi_0^m \xrightarrow{H^4} \phi_0, u_0^m \xrightarrow{H^4} u_0$, and $\psi_0^m \xrightarrow{H^4} \psi_0$.

Due to (64), (65), (66), and (67) and above assumption, it is easy to deduce that $\|n_0^m\|_{H^6}, \|\phi_0^m\|_{H^4}, \|u_0^m\|_{H^4}$, and $\|\psi_0^m\|_{H^4}$ have uniform boundedness about m .

Next, we denote an orthogonal projection operator $P \in H^0$, which is spanned by $\{W_1, W_2, \dots, W_m\}$. By (60), (61), (62), and (63), we have that

$$P(n_t^m(0) - \phi_{xx}^m(0)) = 0$$

$$P(\phi_t^m(0)) - (n^m(0) + |u^m(0)|^2) = 0 \quad (112)$$

$$P(u_t^m(0) - \psi_{xx}^m(0)) = 0$$

$$P(\psi_{xxt}^m(0) - u_{xx}^m(0) + u^m(0) + u^m(0)n^m(0)) = 0,$$

and by $\|PY\| \leq \|Y\|$, we have

$$\|n_t^m(0)\| \leq \|\phi_{xx}^m(0)\|,$$

$$\|\phi_t^m(0)\| \leq \|\phi_t^m(0)\| + \|n^m(0)\| + \| |u^m(0)|^2 \|,$$

$$\|u_t^m(0)\| \leq \|\psi_{xx}^m(0)\|, \quad (113)$$

$$\begin{aligned} \|\psi_{xxt}^m(0)\| &\leq \|u_{xx}^m(0)\| + \|u_{xx}^m(0)\| + \|u^m(0)\| \\ &\quad + \|u^m(0)\| \|n^m(0)\|. \end{aligned}$$

So, we obtain that $\|n_{0t}^m\|, \|\phi_{0t}^m\|, \|u_{0t}^m\|$, and $\|\psi_{0xxt}^m\|$ have uniform boundedness about m .

Similarly, it is not difficult to obtain some higher-order derivative estimation, including $n_{0t}^m, \phi_{0t}^m, u_{0t}^m$, and ψ_{0xxt}^m . For details, we do not discuss. We have the following Lemma.

Lemma 16. *Assume that $n_0 \in H^6, \phi_0 \in H^4, u_0 \in H^4, \psi_0 \in H^4$, then $\|n_t^m(0)\|, \|\phi_t^m(0)\|, \|u_t^m(0)\|, \|\psi_{xxt}^m(0)\|, \|n_{tt}^m(0)\|, \|\phi_{tt}^m(0)\|, \|u_{tt}^m(0)\|, \|\psi_{xxtt}^m(0)\|, \|n_{ttt}^m(0)\|, \|n_{ttx}^m(0)\|, \|n_{txx}^m(0)\|, \|\phi_{ttt}^m(0)\|, \|\phi_{ttx}^m(0)\|, \|\phi_{txx}^m(0)\|, \|u_{ttt}^m(0)\|, \|u_{ttx}^m(0)\|, \|u_{txx}^m(0)\|, \|\psi_{xxtt}^m(0)\|$, and $\|\psi_{xxtt}^m(0)\|$ have uniform boundedness about m .*

5. Existence and Uniqueness of the Global Classical Solution

Theorem 17. *Assume that $n_0 \in H^6, \phi_0 \in H^4, u_0 \in H^4, \psi_0 \in H^4$, and they are periodic functions with L about x ; then initial value problem (1) has global classical solution.*

Proof. The idea and method are similar to Theorem 4.1 of [1]. For details, please see this paper. \square

Theorem 18. *Global classical solution of (1)-(2) is unique.*

Proof. Assume that u_1, n_1 and u_2, n_2 are both classical solutions with the same periodic initial value of (1)-(2). Let

$V = u_1 - u_2$ and $W = n_1 - n_2$; by (1)-(2), we obtain the following equations about V and W :

$$V_{tt} - V_{xx} + V + n_1 V + W u_2 = 0, \quad (114)$$

$$\begin{aligned} W_{tt} - W_{xx} \\ = V_{xx} \overline{u_1} + u_{2xx} V + 2(V_x \overline{u_{1x}} + u_{2x} \overline{V_x}) + \overline{u_{1xx}} V \\ + u_2 \overline{V_{xx}}, \end{aligned} \quad (115)$$

where V is a complex function and W is a real function.

Equation (114) makes inner product with V_t and takes real part; we have that

$$(V_{tt}, V_t) = \frac{1}{2} \frac{d}{dt} \|V_t\|^2, \quad (116)$$

$$(V_{tx}, V_t) = -\frac{1}{2} \frac{d}{dt} \|V_x\|^2, \quad (117)$$

$$\begin{aligned} |(n_1 V, V_t)| &\leq \frac{1}{2} \|n_1\|_{L^\infty} (\|V\|^2 + \|V_t\|^2) \\ &\leq \frac{1}{2} E_{54} (\|V\|^2 + \|V_t\|^2), \end{aligned} \quad (118)$$

$$(V, V_t) = \frac{1}{2} \frac{d}{dt} \|V\|^2, \quad (119)$$

$$\begin{aligned} (W u_2, V_t) &\leq \frac{1}{2} \|u_2\|_{L^\infty} (\|W\|^2 + \|V_t\|^2), \\ &\leq \frac{1}{2} E_{51} (\|W\|^2 + \|V_t\|^2). \end{aligned} \quad (120)$$

Meanwhile, (115) makes inner product with W_t and takes real part; we have that

$$(W_{tt}, W_t) = \frac{1}{2} \frac{d}{dt} \|W_t\|^2, \quad (121)$$

$$(W_{xx}, W_t) = -\frac{1}{2} \frac{d}{dt} \|W_x\|^2, \quad (122)$$

$$\begin{aligned} |(V_{xx} \overline{u_1}, W_t)| &\leq \frac{1}{2} \|\overline{u_1}\|_{L^\infty} (\|V_{xx}\|^2 + \|W_{tt}\|^2) \\ &\leq \frac{1}{2} E_{51} \left[\left(\frac{c_{28}}{1 - \alpha_{23}} \right)^2 \|V_x\|^2 + \|W_t\|^2 \right], \end{aligned} \quad (123)$$

$$\begin{aligned} |(u_{2xx} V, W_t)| &\leq \frac{1}{2} \|u_{2xx}\|_{L^\infty} (\|V\|^2 + \|W_t\|^2) \\ &\leq \frac{1}{2} (c_{28} \|u_2\| + \alpha_{23} \|u_{2xxx}\|) (\|V\|^2 + \|W_t\|^2) \\ &\leq \frac{1}{2} (c_{28} \sqrt{C_1 E_0} + \alpha_{23} \sqrt{E_8}) (\|V\|^2 + \|W_t\|^2), \end{aligned} \quad (124)$$

$$\begin{aligned} |(V_x \overline{u_{1x}}, W_t)| &\leq \frac{1}{2} \|u_{1x}\|_{L^\infty} (\|V_x\|^2 + \|W_t\|^2) \\ &\leq \frac{1}{2} (c_{29} \|u_1\| + \alpha_{24} \|u_{1xx}\|) (\|V_x\|^2 + \|W_t\|^2) \end{aligned} \quad (125)$$

$$\leq \frac{1}{2} (c_{29} \sqrt{C_1 E_0} + \alpha_{24} \sqrt{E_6}) (\|V_x\|^2 + \|W_t\|^2)$$

$$\begin{aligned} |(u_{2x} \overline{V_x}, W_t)| &\leq \frac{1}{2} \|u_{2x}\|_{L^\infty} (\|V_x\|^2 + \|W_t\|^2) \\ &\leq \frac{1}{2} (c_{30} \|u_2\| + \alpha_{25} \|u_{2xx}\|) (\|V_x\|^2 + \|W_t\|^2) \end{aligned} \quad (126)$$

$$\leq \frac{1}{2} (c_{30} \sqrt{C_1 E_0} + \alpha_{25} \sqrt{E_6}) (\|V_x\|^2 + \|W_t\|^2),$$

$$\begin{aligned} |(\overline{u_{1xx}} V, W_t)| &\leq \frac{1}{2} \|\overline{u_{1xx}}\|_{L^\infty} (\|V\|^2 + \|W_t\|^2) \\ &\leq \frac{1}{2} (c_{31} \|u_1\| + \alpha_{26} \|u_{1xxx}\|) (\|V\|^2 + \|W_t\|^2) \end{aligned} \quad (127)$$

$$\leq \frac{1}{2} (c_{31} \sqrt{C_1 E_0} + \alpha_{26} \sqrt{E_8}) (\|V\|^2 + \|W_t\|^2),$$

$$\begin{aligned} |(u_2 \overline{V_{xx}}, W_t)| &\leq \frac{1}{2} \|u_2\|_{L^\infty} (\|V_{xx}\|^2 + \|W_t\|^2) \\ &\leq \frac{1}{2} E_{51} \left[\left(\frac{c_{28}}{1 - \alpha_{23}} \right)^2 \|V_x\|^2 + \|W_t\|^2 \right]. \end{aligned} \quad (128)$$

Combining (117)-(128), we have that

$$\begin{aligned} \frac{d}{dt} (\|V_t\|^2 + \|V_x\|^2 + \|V\|^2 + \|W_t\|^2 + \|W_x\|^2) \\ \leq D_8 (\|V_t\|^2 + \|V_x\|^2 + \|V\|^2 + \|W_t\|^2), \end{aligned} \quad (129)$$

where

$$\begin{aligned} D_8 = \max \left\{ 6E_{54}, 6E_{51}, 12E_{51} \left(\frac{c_{28}}{1 - \alpha_{23}} \right)^2, \right. \\ 6(c_{28} \sqrt{C_1 E_0} + \alpha_{23} \sqrt{E_8}), \\ 6(c_{29} \sqrt{C_1 E_0} + \alpha_{24} \sqrt{E_6}), \\ 12(c_{30} \sqrt{C_1 E_0} + \alpha_{25} \sqrt{E_6}), \\ \left. 6(c_{31} \sqrt{C_1 E_0} + \alpha_{26} \sqrt{E_8}) \right\}. \end{aligned} \quad (130)$$

Integrating (130) from $[0, T]$, we obtain that

$$\begin{aligned} (\|V_t(T)\|^2 + \|V_x(T)\|^2 + \|V(T)\|^2 + \|W_t(T)\|^2 \\ + \|W_x(T)\|^2) e^{-D_8 T} \leq 0. \end{aligned} \quad (131)$$

Hence, $u_1 = u_2$ and $n_1 = n_2$. \square

Data Availability

No data were used to support this study. In our manuscript, any reader can access the data supporting the conclusions of the study and this clearly outlines the reasons why unavailable data cannot be released.

Conflicts of Interest

The authors declare that there are no conflicts of interest regarding the publication of this paper.

Acknowledgments

This paper is funded by the new entry doctoral research project of Jilin University of Finance and Economics (2017B2013).

References

- [1] B. L. Guo and L. J. Shen, "The existence and uniqueness of the classical solution to the periodic initial value problem for the Zakharov equation," *Acta Mathematicae Applicatae Sinica*, vol. 5, no. 3, pp. 310–324, 1982 (Chinese).
- [2] F. Oliveira, "Stability of the solitons for the one-dimensional Zakharov-Rubenchik equation," *Physica D: Nonlinear Phenomena*, vol. 175, no. 3-4, pp. 220–240, 2003.
- [3] T. Ozawa, K. Tsutaya, and Y. Tsutsumi, *Normal Form and Global Solutions for the Klein-Gordon-Zakharov Equation*, University of Tokyo, 1994.
- [4] T. Ozawa, K. Tsutaya, and Y. Tsutsumi, "Well-posedness in energy space for the Cauchy problem of the Klein-Gordon-Zakharov equations with different propagation speeds in three space dimensions," *Mathematische Annalen*, vol. 313, no. 1, pp. 127–140, 1999.
- [5] H. Pecher, " L^p Abschätzungen and klassische Lösungen für nichtlineare wellenrichtungen. I," *Mathematische Zeitschrift*, vol. 150, no. 2, pp. 159–183, 1976.
- [6] H. A. Levine, "Instability and nonexistence of global solution to nonlinear wave equation of the form $u_t = -\Delta u - F(u)$," *Transactions of the American Mathematical Society*, vol. 192, pp. 1–21, 1974.
- [7] W. A. Strauss, "Existence of solitary waves in higher dimensions," *Communications in Mathematical Physics*, vol. 55, no. 2, pp. 149–162, 1977.
- [8] T. Wang, J. Chen, and L. Zhang, "Conservative difference methods for the Klein-Gordon-Zakharov equations," *Journal of Computational and Applied Mathematics*, vol. 205, no. 1, pp. 430–452, 2007.
- [9] Z. Zhang, F.-L. Xia, and X.-P. Li, "Bifurcation analysis and the travelling wave solutions of the Klein-Gordon-Zakharov equations," *Pramana—Journal of Physics*, vol. 80, no. 1, pp. 41–59, 2013.
- [10] Z. Y. Zhang, Y. H. Zhang, X. Y. Gan, and D. M. Yu, "A note on exact travelling wave solutions for the Klein-Gordon-Zakharov equations," *Zeitschrift für Naturforschung*, vol. A67, no. 167, 2012.

Research Article

Nonlinear Green's Functions for Wave Equation with Quadratic and Hyperbolic Potentials

Asatur Zh. Khurshudyan 

Department of Dynamics of Deformable Systems and Coupled Fields, Institute of Mechanics, National Academy of Sciences of Armenia, 24B Baghramyan Ave., 0019 Yerevan, Armenia

Correspondence should be addressed to Asatur Zh. Khurshudyan; khurshudyan@mechins.sci.am

Received 2 February 2018; Revised 7 March 2018; Accepted 29 April 2018; Published 3 June 2018

Academic Editor: Kaliyaperumal Nakkeeran

Copyright © 2018 Asatur Zh. Khurshudyan. This is an open access article distributed under the Creative Commons Attribution License, which permits unrestricted use, distribution, and reproduction in any medium, provided the original work is properly cited.

The advantageous Green's function method that originally has been developed for nonhomogeneous linear equations has been recently extended to nonlinear equations by Frasca. This article is devoted to rigorous and numerical analysis of some second-order differential equations new nonlinearities by means of Frasca's method. More specifically, we consider one-dimensional wave equation with quadratic and hyperbolic nonlinearities. The case of exponential nonlinearity has been reported earlier. Using the method of generalized separation of variables, it is shown that a hierarchy of nonlinear wave equations can be reduced to second-order nonlinear ordinary differential equations, to which Frasca's method is applicable. Numerical error analysis in both cases of nonlinearity is carried out for various source functions supporting the advantage of the method.

1. Introduction

The most simplistic models for real-life objects and phenomena are formulated in terms of linear constraints. For a better understanding of various phenomena having a nonlinear character, strongly nonlinear constraints must be involved. Nevertheless, numerical and especially rigorous analysis of nonlinear constraints can be significantly sophisticated and can require burdensome computational costs. In such cases, the so-called semianalytical methods such as Adomian decomposition method [1], Hirota direct method [2], and (G'/G) expansion method [3] usually become very convenient. The reason is that they allow deriving an approximate analytical solution to the nonlinear constraints and, on its basis, to perform a sensitivity analysis of the solution dependence on, e.g., boundary/initial data and external influence.

For linear constraints, the sensitivity analysis is usually carried out by Green's function method [4]. The solution of nonhomogeneous differential equations is represented in the form of convolution of Green's function and the right-hand side of the equation. At this, Green's representation

formula is derived on the basis of the superposition principle. Therefore it holds true exceptionally for linear constraints. Nevertheless, there exist several studies attempting to generalize Green's function concept and Green's representation formula to nonlinear systems. An exact extension has been reported in [5–7] (see also other works by Cacuci). Assuming that the first Gâteaux derivative of the state equation exists, the concept of the forward and backward propagators is introduced and the general solution is represented as the inner product of the propagators with the right-hand side (nonlinear Green's representation formula). In other words, the propagators play the same role for nonlinear systems as Green's function does for linear systems.

Another extension has been reported a decade ago by Frasca in [8, 9]. It has been shown that the general solution of the nonlinear “oscillating” equations of the form

$$\frac{d^2 w}{dt^2} + N(w, t) = f(t), \quad t > 0, \quad (1)$$

for a generic nonlinear function N , a given right-hand side f , and appropriate Cauchy conditions can be represented in terms of the short time expansion as follows:

$$\begin{aligned} w(t) &= a_0 \int_0^t G(t-\tau) f(\tau) d\tau \\ &+ a_1 \int_0^t (t-\tau) G(t-\tau) f(\tau) d\tau \\ &+ a_2 \int_0^t (t-\tau)^2 G(t-\tau) f(\tau) d\tau \\ &+ a_3 \int_0^t (t-\tau)^3 G(t-\tau) f(\tau) d\tau + \dots \\ &= \sum_{k=0}^{\infty} a_k \int_0^t (t-\tau)^k G(t-\tau) f(\tau) d\tau, \end{aligned} \quad (2)$$

where a_k , $k = 0, 1, 2, \dots$, are the unknown expansion coefficients determined in terms of the quantities $w^{(k)}(0)$. Usually, in numerical computations, a truncated part of expansion (2) is considered once the required precision is achieved. In [10] it has been shown that if the consideration is restricted to the interval $t \in [0, 1]$, the first-order term

$$w(t) \approx a_0 \int_0^t G(t-\tau) f(\tau) d\tau \quad (3)$$

provides an efficient approximation.

Above, G is the formal extension of Green's function, i.e., the general solution of the corresponding nonlinear differential equation

$$\frac{d^2 G}{dt^2} + N(G, t) = s\delta(t), \quad t > 0, \quad (4)$$

under appropriate Cauchy conditions; δ is the Dirac function

$$\delta(t) = \begin{cases} 0, & t \neq 0, \\ \infty, & t = 0, \end{cases} \quad (5)$$

and s is a scale factor for minimizing the approximation error. It is noteworthy that in Frasca's original paper $a_0 = 1$. It was introduced in [10] to reduce the approximation error further. Moreover, for the comparison of the short time expansion with the functional iteration method, see [9].

Here we study new forms of N , for which nonlinear Green's function is determined from (4) exactly. More specifically, we consider the cases of quadratic and hyperbolic nonlinearities (see Section 3). Moreover, we show that there exists a hierarchy of nonlinear wave equations that can be reduced to a second-order nonlinear differential equations, the solution of which can be represented by nonlinear Green's formula (2). For the sake of simplicity, in this paper we restrict ourselves only by the first-order approximation (3). A numerical error analysis (see Section 4) is carried out in

comparison with the well-known method of lines (MoL). It is established that even the first-order approximation gives a solution compatible with a numerical one. The approximation error can be reduced further by considering higher-order terms in the short time expansion above.

Such techniques are quite useful for a deeper practical analysis, since they allow avoidance of any linearization of the state equation, which often leads to a loss of some key information about the nature of the nonlinear processes [11, 12]. Note that this approach is applicable as long as nonlinear Green's equation (4) is resolvable under the corresponding Cauchy conditions. Note also that the idea of [13, 14] can be applied on the results of this paper, in order to consider control problems for new nonlinear dynamic systems described by the "oscillating" equations (1) and related partial differential equations.

2. Exactly Integrable Cases

Two particular nonlinearities are considered in [8] allowing construction of the exact solution of (4). Particularly, the cubic nonlinearity

$$N(w, t) = w^3 \quad (6)$$

provides

$$G(t) = 2^{1/4} \theta(t) \cdot \text{sn} \left[\frac{t}{2^{1/4}}, i \right], \quad (7)$$

where θ is the Heaviside function

$$\theta(t) = \begin{cases} 1, & t > 0, \\ \frac{1}{2}, & t = 0, \\ 0, & t < 0, \end{cases} \quad (8)$$

and sn is the Jacobi snoidal function. Here it is taken into account that in the sense of distributions

$$\theta'(t) = \delta(t). \quad (9)$$

Furthermore, the trigonometric nonlinearity

$$N(w, t) = \sin w \quad (10)$$

admits exact integration of (4) as follows:

$$G(t) = 2\theta(t) \cdot \text{am} \left[\frac{t}{\sqrt{2}}, \sqrt{2} \right]. \quad (11)$$

Here am is the Jacobi amplitude function.

Some new nonlinearities are studied in [10]. In particular, the reciprocal and exponential nonlinearities are shown to be exactly integrable cases. For instance, in the case of the exponential nonlinearity (Liouville equation)

$$N(w, t) = \exp w, \quad (12)$$

nonlinear Green's function is found as follows:

$$G(t) = \theta(t) \cdot \ln \left[1 - \tanh^2 \left(\frac{t}{\sqrt{2}} \right) \right]. \quad (13)$$

3. Generalized Variable Separation and Wave Equations with Nonlinear Potentials

Consider the one-dimensional wave equation

$$\frac{\partial^2 \bar{w}}{\partial t^2} = \frac{\partial}{\partial x} \left[\exp(\lambda x) \frac{\partial \bar{w}}{\partial x} \right] + \tilde{N}(\bar{w}, x, t), \quad (14)$$

$$-\infty < x < \infty, \quad t > 0,$$

describing the nonlinear wave propagation in inhomogeneous media with the quadratic nonlinearity

$$\tilde{N}(\bar{w}, x, t) = \bar{w}^2. \quad (15)$$

The transformation [15, 16]

$$\chi^2 = \exp(-2x) - t^2, \quad (16)$$

reduces the wave equation (14) to

$$\frac{d^2 w}{d\chi^2} + w^2(\chi) = 0, \quad (17)$$

where

$$w(\chi) = \bar{w}(x, t). \quad (18)$$

In this case, Green's function is determined as follows:

$$G(\chi) = -\frac{1}{c} \theta(\chi) \cdot \wp(c\chi + c_1; 0, c_2), \quad c = (-6)^{-1/3}, \quad (19)$$

subject to appropriate Cauchy conditions. Here \wp is the Weierstrass elliptic function

$$\begin{aligned} &\wp(\chi; \omega_1, \omega_2) \\ &= \frac{1}{\chi^2} \\ &+ \sum_{n^2+m^2 \neq 0} \left[\frac{1}{(\chi + \omega_1 m + \omega_2 n)^2} - \frac{1}{(\omega_1 m + \omega_2 n)^2} \right], \end{aligned} \quad (20)$$

and c_1 and c_2 , as in all cases below, are integration constants that must be determined from the corresponding Cauchy conditions.

The same transformation reduces (14) with

$$\tilde{N}(\bar{w}, x, t) = \frac{1}{\bar{w}} \quad (21)$$

to

$$\frac{d^2 w}{d\chi^2} + \frac{1}{w(\chi)} = 0. \quad (22)$$

In this case, Green's function reads as

$$G(\chi) = c_1 \theta(\chi) \cdot \exp[-\varphi^2(\chi; c_1, c_2)], \quad (23)$$

where

$$\varphi(\chi; c_1, c_2) = \operatorname{erf}^{-1} \left[-\sqrt{\frac{2}{\pi}} |c_1| |\chi + c_2| \right], \quad (24)$$

erf^{-1} is the inverse of the Gauss error function

$$\operatorname{erf}(\chi) = \frac{2}{\sqrt{\pi}} \int_0^\chi \exp[-\xi^2] d\xi. \quad (25)$$

Consider also the case when

$$\tilde{N}(\bar{w}, x, t) = \tanh \bar{w}, \quad (26)$$

leading in (14) to

$$\frac{d^2 w}{d\chi^2} + \tanh w(\chi) = 0. \quad (27)$$

This case is interesting from the perspective that corresponding Green's function is found implicitly as the solution of

$$\left[\int_0^{G(\chi)} \frac{1}{\sqrt{c_1 - 2 \ln(\cosh z)}} dz \right]^2 = (\chi + c_2)^2. \quad (28)$$

If the solution of the ordinary differential equations above is approximated by (3), then the general solution of the wave equation (14) can be approximated by

$$w(x, t) \approx s_2 \int_{-\infty}^{\infty} \int_0^t \bar{G}(x - \xi, t - \tau) f(\xi, \tau) d\xi d\tau, \quad (29)$$

where

$$\bar{G}(x, t) = G(\chi(x, t)), \quad (30)$$

and f represents either boundary/initial data or the right-hand side.

Nonlinear wave equations like (14) arise, e.g., in biology [17], in many areas of physics, mechanics, and engineering, describing, as a rule, nonlinear vibrations in solids or fluids [18]. In particular, they describe vibrations of a pendulum, vibrations of nonlinear elastic rods, nonlinear electromagnetic oscillations, nonlinear gravitational waves, etc.

4. Numerical versus Green's solutions

In this section we study the error of approximation by (3) numerically for some of the nonlinearities considered in the previous section. Various source functions are considered. The approximation error is evaluated by the logarithmic function

$$\operatorname{Er}(t) = \log_{10} |w_{\text{Green's}}(t) - w_{\text{MoL}}(t)|, \quad (31)$$

measuring the absolute error between nonlinear Green's solution $w_{\text{Green's}}$ and the numerical solution w_{MoL} , derived by means of the method of lines, in degrees of 10. For $w_{\text{Green's}}$ we use the first-order approximation (3).

4.1. Quadratic Potential. Let the nonlinear potential be given by (15). First, consider the case when $f(t) = \delta(t)$. Figure 1, where the discrete plot of $w_{\text{Green's}}$ and w_{MoL} and the logarithmic error function Er are plotted, shows an impressively small approximation error. Moreover, consideration of several other source functions such as switching, trigonometric,

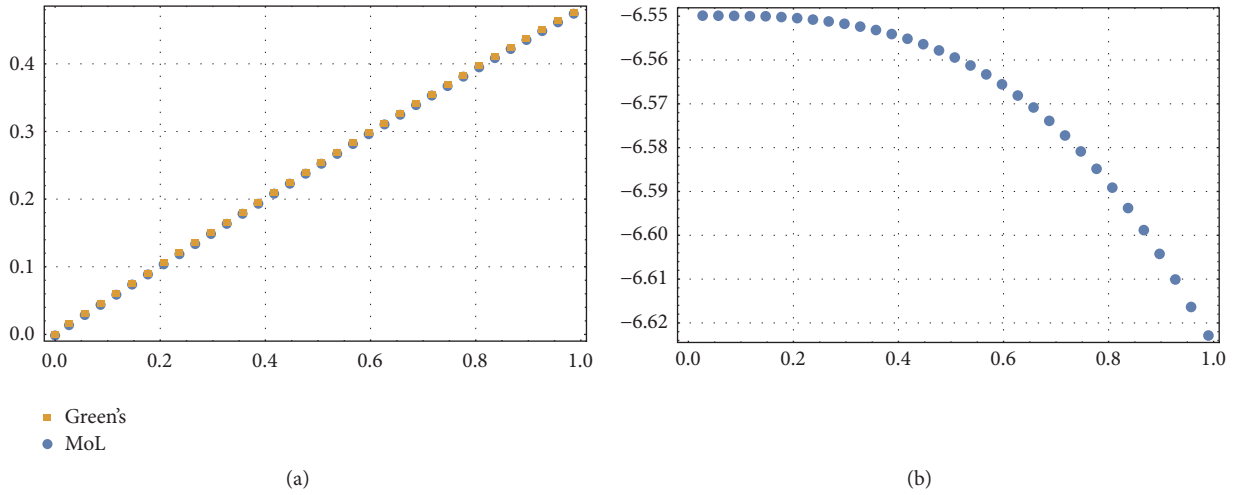


FIGURE 1: Discrete plot of $w_{\text{Green's}}$ and w_{MoL} (a) and Er (b) against $t \in [0, 1]$ for $f(t) = \delta(t)$: quadratic potential.

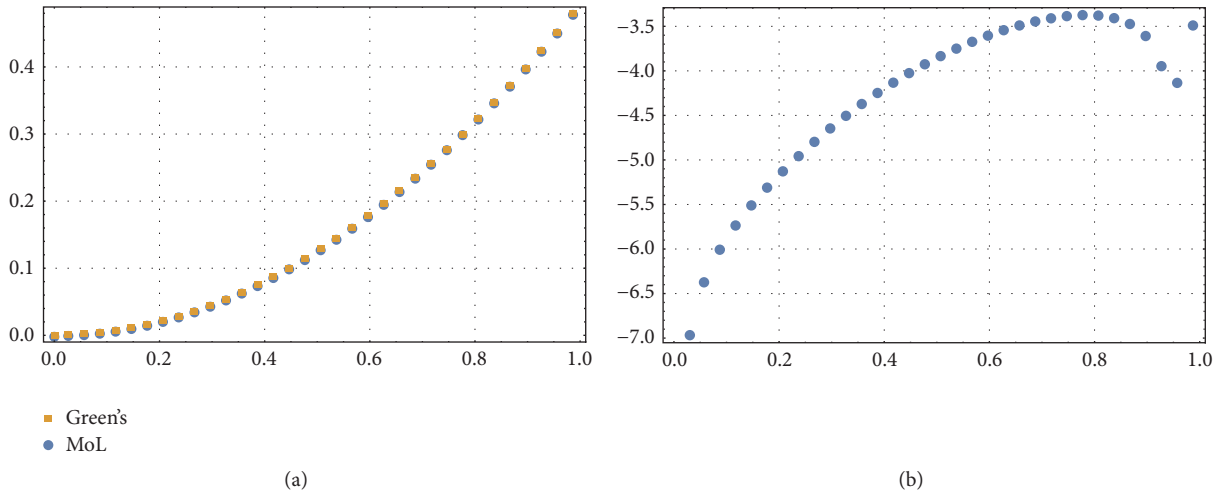


FIGURE 2: Discrete plot of $w_{\text{Green's}}$ and w_{MoL} (a) and Er (b) against $t \in [0, 1]$ for $f(t) = \theta(t)$: quadratic potential.

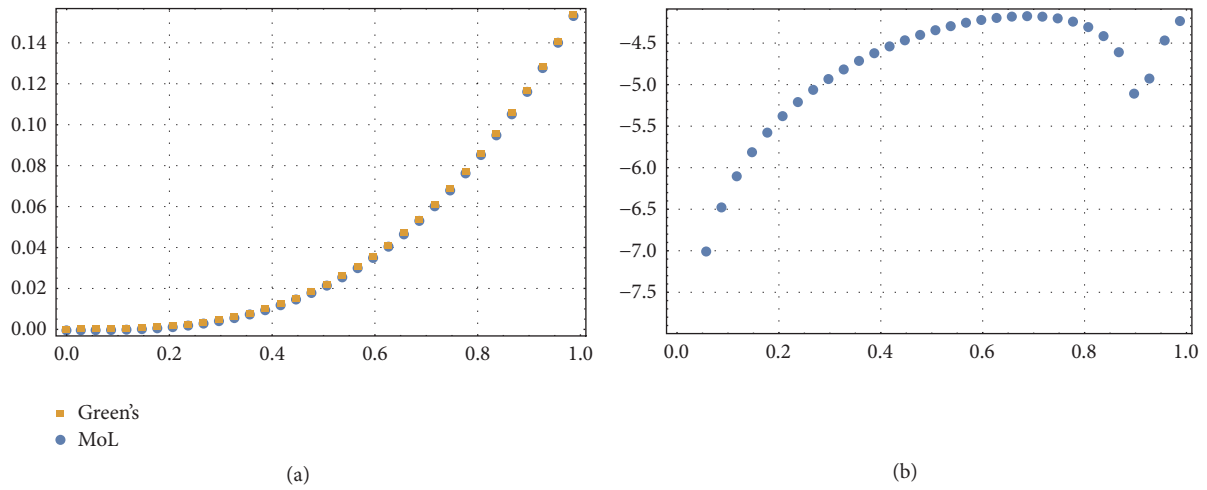


FIGURE 3: Discrete plot of $w_{\text{Green's}}$ and w_{MoL} (a) and Er (b) against $t \in [0, 1]$ for $f(t) = \sin(t)$: quadratic potential.

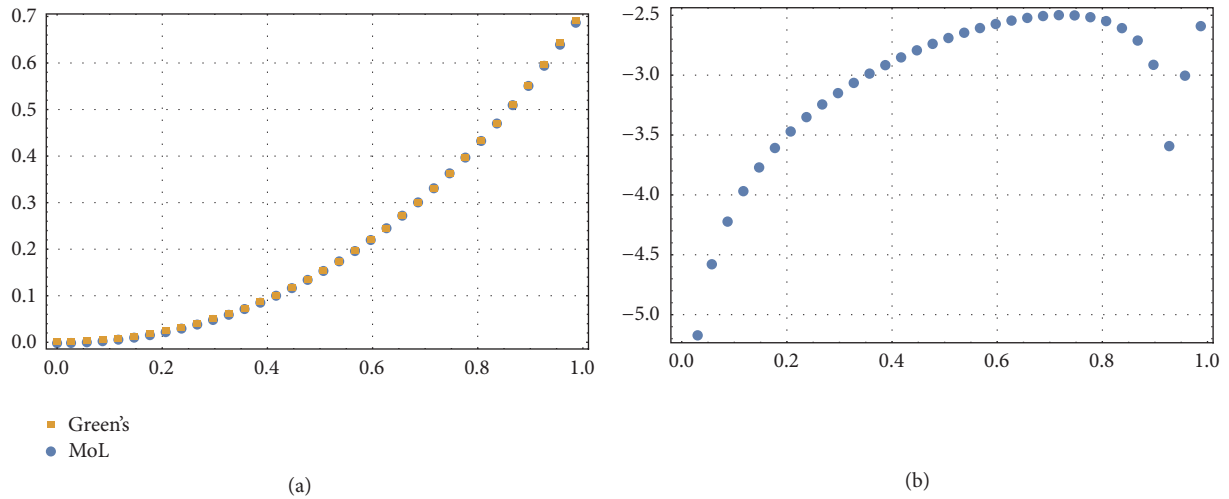


FIGURE 4: Discrete plot of $w_{\text{Green's}}$ and w_{MoL} (a) and Er (b) against $t \in [0, 1]$ for $f(t) = \exp(t)$: quadratic potential.

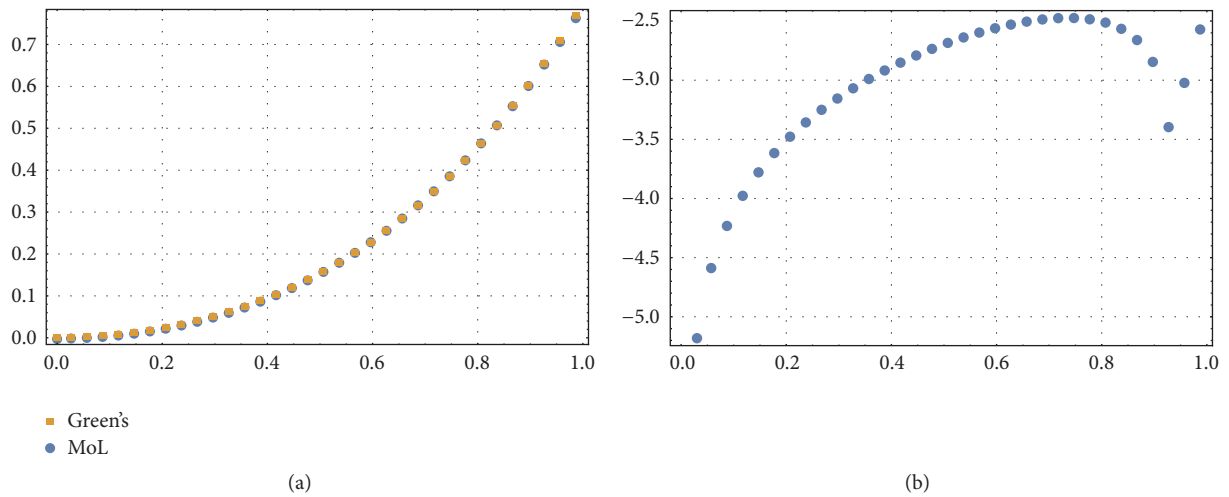


FIGURE 5: Discrete plot of $w_{\text{Green's}}$ and w_{MoL} (a) and Er (b) against $t \in [0, 1]$ for $f(t) = 1 + t + t^2 + t^3$: quadratic potential.

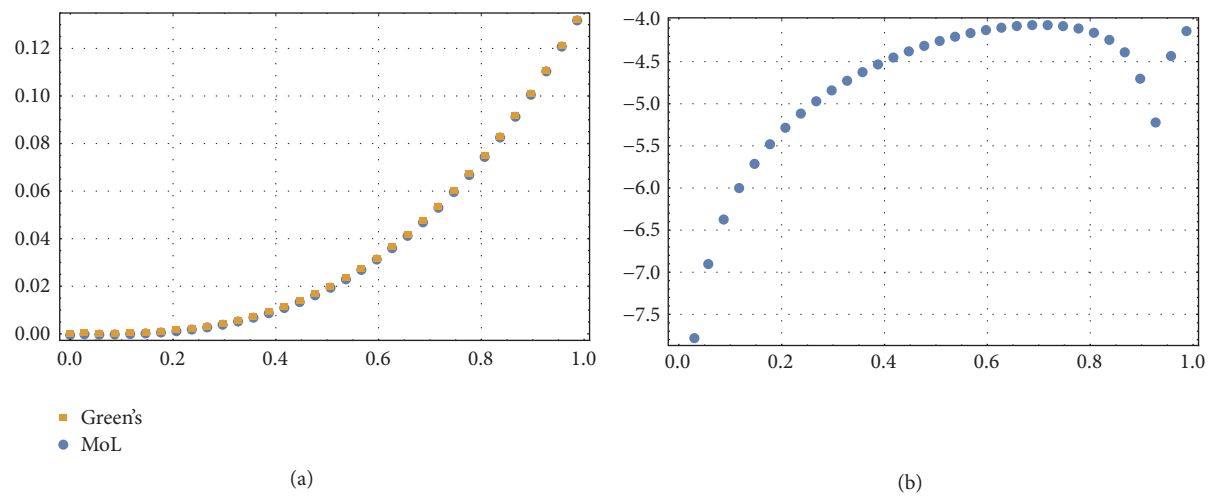


FIGURE 6: Discrete plot of $w_{\text{Green's}}$ and w_{MoL} (a) and Er (b) against $t \in [0, 1]$ for $f(t) = \ln(1 + t)$: quadratic potential.

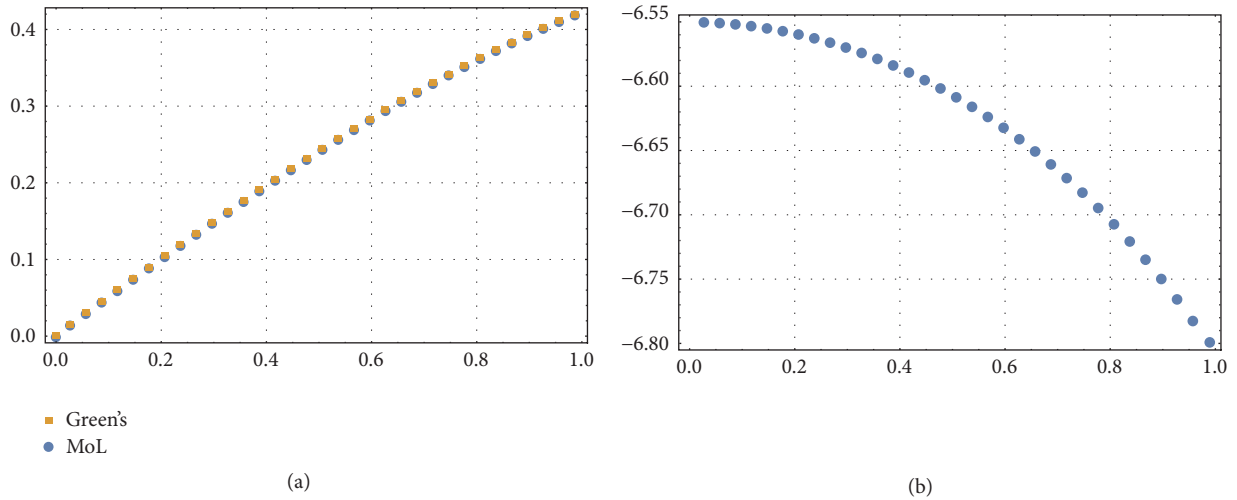


FIGURE 7: Discrete plot of $w_{\text{Green's}}$ and w_{MoL} (a) and Er (b) against $t \in [0, 1]$ for $f(t) = \delta(t)$: hyperbolic potential.

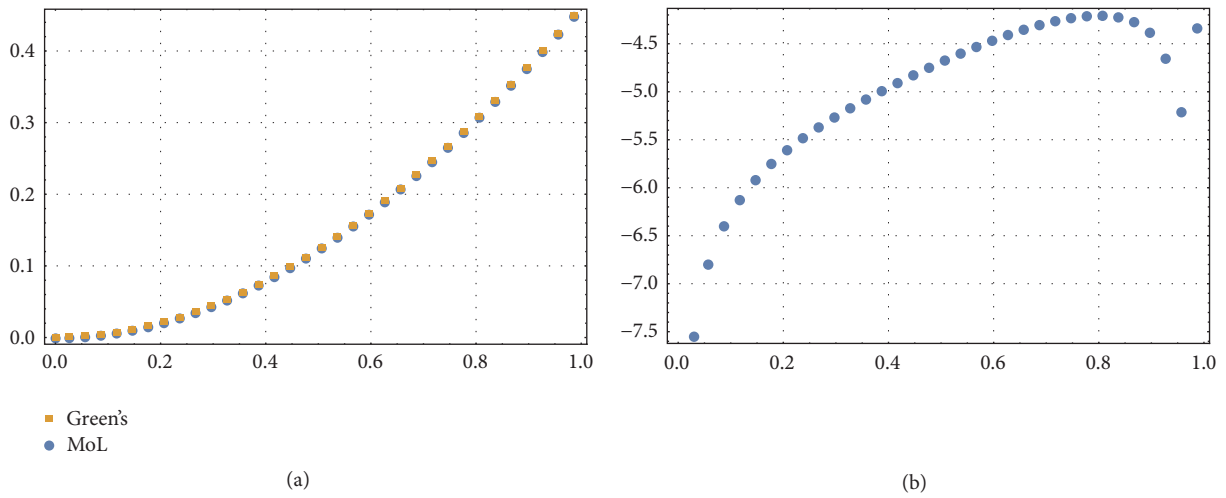


FIGURE 8: Discrete plot of $w_{\text{Green's}}$ and w_{MoL} (a) and Er (b) against $t \in [0, 1]$ for $f(t) = \theta(t)$: hyperbolic potential.

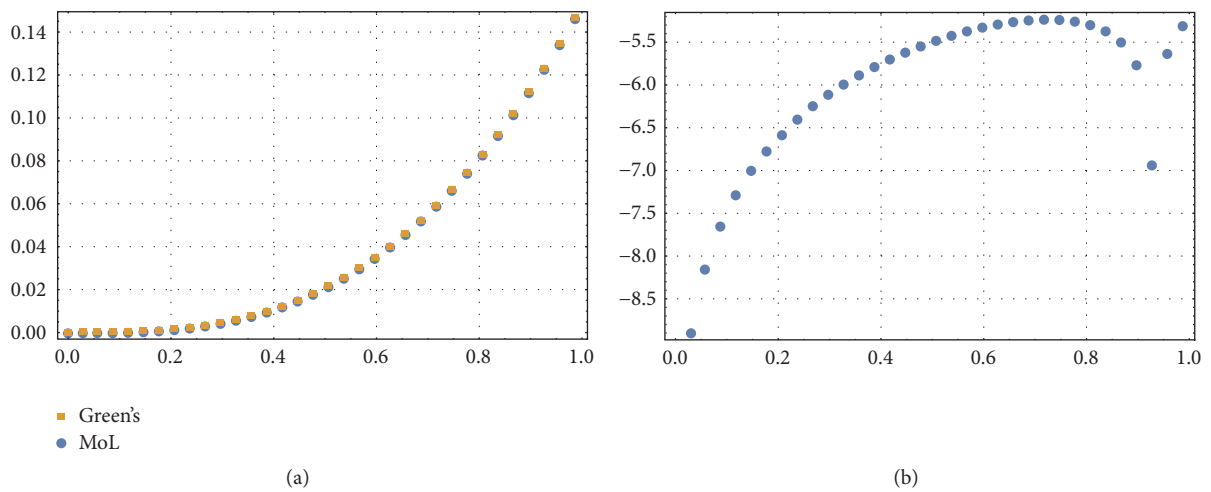


FIGURE 9: Discrete plot of $w_{\text{Green's}}$ and w_{MoL} (a) and Er (b) against $t \in [0, 1]$ for $f(t) = \sin(t)$: hyperbolic potential.

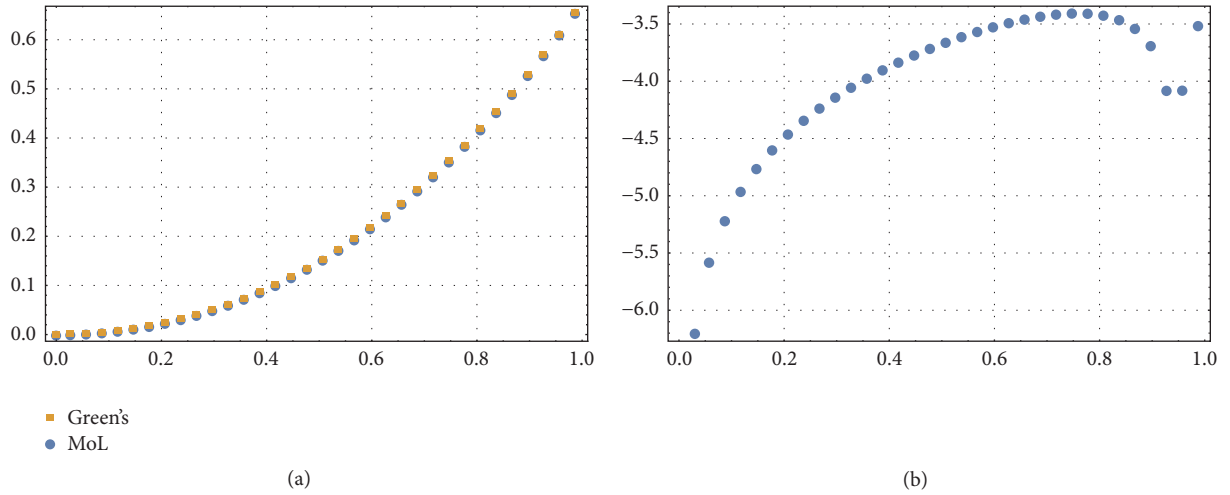


FIGURE 10: Discrete plot of $w_{\text{Green's}}$ and w_{MoL} (a) and Er (b) against $t \in [0, 1]$ for $f(t) = \exp(t)$: hyperbolic potential.

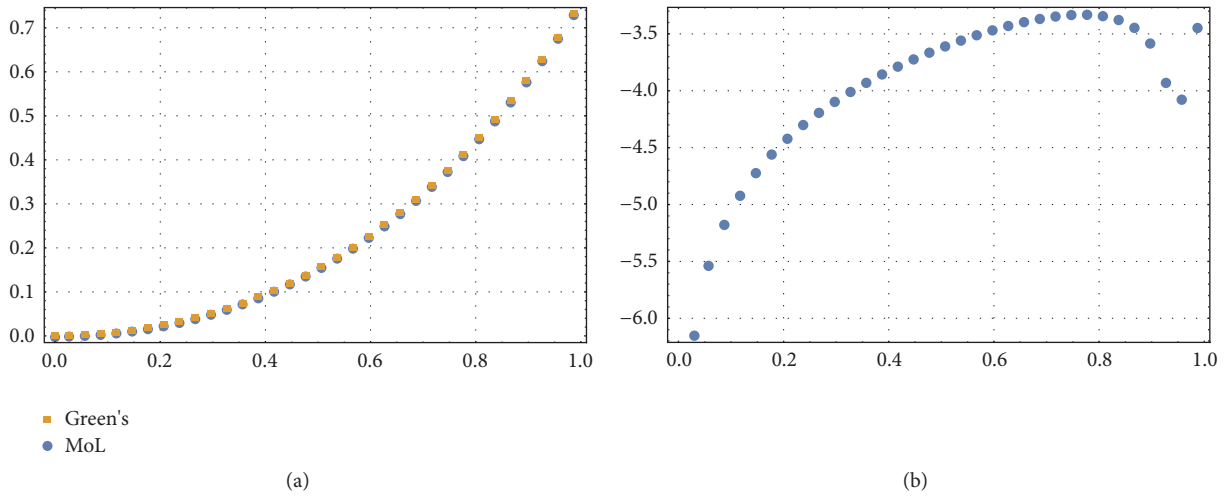


FIGURE 11: Discrete plot of $w_{\text{Green's}}$ and w_{MoL} (a) and Er (b) against $t \in [0, 1]$ for $f(t) = 1 + t + t^2 + t^3$: hyperbolic potential.

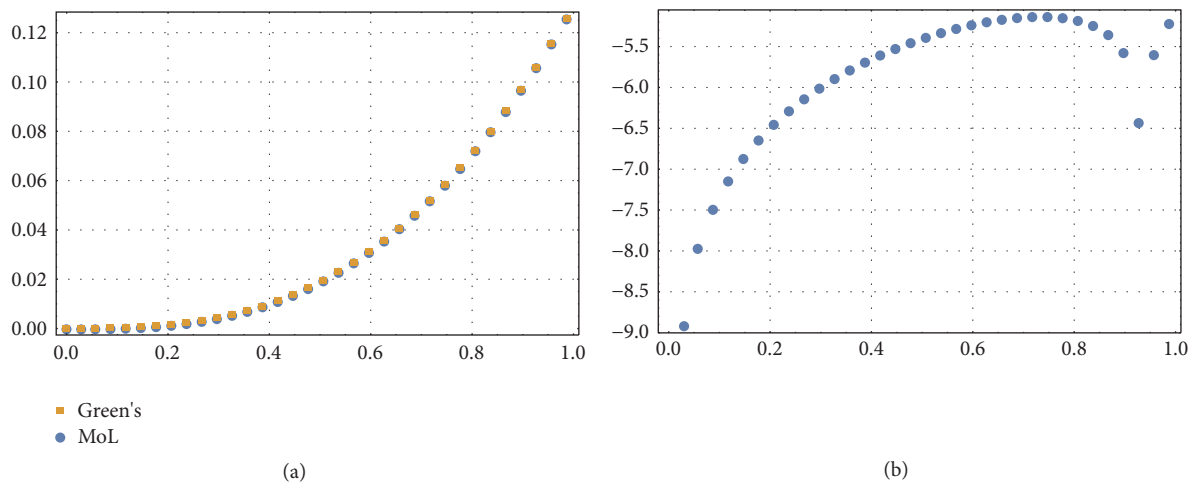


FIGURE 12: Discrete plot of $w_{\text{Green's}}$ and w_{MoL} (a) and Er (b) against $t \in [0, 1]$ for $f(t) = \ln(1 + t)$: hyperbolic potential.

TABLE 1: Minimal and maximal logarithmic errors of approximation for various source functions: quadratic potential.

$f(t)$	min Er	max Er	a_0	s
$\delta(t)$	-6.63	-6.55	2	1
$\theta(t)$	-8	-3.5	2.1475	0.93107
$\sin(t)$	-9.5	-4.25	2.7807	0.72126
$\exp(t)$	-6	-2.5	197.1	0.01
$1 + t + t^2 + t^3$	-6.1	-2.5	27.5783	0.07149
$\ln(1 + t)$	-9.1	-4	2.5925	0.7743

TABLE 2: Minimal and maximal logarithmic errors of approximation for various source functions: hyperbolic potential.

$f(t)$	min Er	max Er	a_0	s
$\delta(t)$	-6.8	-6.55	2	1
$\theta(t)$	-9.1	-4.25	2.1483	0.93107
$\sin(t)$	-9.8	-5.7	2.77245	0.72126
$\exp(t)$	-7.3	-3.5	200.3	0.01
$1 + t + t^2 + t^3$	-7.2	-3.4	28.0215	0.07149
$\ln(1 + t)$	-9.7	-5.25	2.5824	0.7743

exponential, polynomial, and logarithmic influences shows a high efficiency as well (see Figures 2–6).

The minimal and maximal logarithmic errors for the considered source functions are reported in Table 1. The scale factors a_0 and s are chosen to minimize the Er function.

4.2. Hyperbolic Potential. Now consider the case when the potential is given by (26). The error analysis for the same source functions as above is reported in Figures 7–12 and Table 2. It is observed that when we use the same values of the scaling factor s for both nonlinearities, then the corresponding values of a_0 are also close to each other.

5. Conclusion

The validity of Frasca’s short time expansion (nonlinear Green’s representation formula) developed recently for second-order ordinary differential equations of a specific form is established numerically for new classes of nonlinear equations. It is shown that by means of the method of generalized separation of variables, a hierarchy of nonlinear wave equations can be reduced to second-order nonlinear ordinary differential equations, the solution of which can be represented in terms of the nonlinear Green’s function.

The numerical solution derived by means of the method of lines is compared with the approximate solution represented in terms of nonlinear Green’s function in the case of quadratic and hyperbolic nonlinearities. Consideration of different types of source influences ensures the robustness of the technique. It is observed that the logarithmic error of the two solutions strongly depends on the right-hand side of the equation, corresponding to the source influencing the real-life object or phenomena. The approximation error is minimized with respect to two scaling factors occurring in the right-hand side of the nonlinear equation for Green’s

function and in the first-order term in Frasca’s short time expansion. The approach can be used to derive explicit-approximate solutions to various other nonlinear partial differential equations.

Data Availability

No data were used to support this study.

Conflicts of Interest

The author declares that there are no conflicts of interest regarding the publication of this paper.

References

- [1] G. Adomian, *Solving Frontier Problems of Physics: The Decomposition Method*, Kluwer Academic, Dordrecht, The Netherlands, 1994.
- [2] R. Hirota, *The Direct Method in Soliton Theory*, Cambridge University Press, Cambridge, UK, 2004.
- [3] M. Wang, X. Li, and J. Zhang, “The G'/G -expansion method and travelling wave solutions of nonlinear evolution equations in mathematical physics,” *Physics Letters A*, vol. 372, no. 4, pp. 417–423, 2008.
- [4] D. G. Duffy, *Green’s Functions with Applications*, Studies in Advanced Mathematics, Chapman & Hall/CRC, Boca Raton, FL, USA, 2 edition, 2001.
- [5] D. G. Cacuci, R. B. Perez, and V. Protopopescu, “Duals and propagators: a canonical formalism for nonlinear equations,” *Journal of Mathematical Physics*, vol. 29, no. 2, pp. 353–361, 1988.
- [6] D. G. Cacuci and V. Protopopescu, “Propagators for nonlinear systems,” *Journal of Physics A: Mathematical and General*, vol. 22, no. 13, pp. 2399–2414, 1989.
- [7] D. G. Cacuci and O. A. Karakashian, “Benchmarking the propagator method for nonlinear systems: a Burgers-Korteweg-de Vries equation,” *Journal of Computational Physics*, vol. 89, no. 1, pp. 63–79, 1990.
- [8] M. Frasca, “Green function method for nonlinear systems,” *Modern Physics Letters A*, vol. 22, no. 18, pp. 1293–1299, 2007.
- [9] M. Frasca, “Green functions and nonlinear systems: short time expansion,” *International Journal of Modern Physics A*, vol. 23, no. 2, pp. 299–308, 2008.
- [10] As. Zh. Khurshudyan, “New Green’s functions for some nonlinear oscillating systems and related PDEs,” *International Journal of Modern Physics C*, vol. 29, no. 4, Article ID 1850032, 2018.
- [11] C. Guo, J. Guo, Y. Gao, and S. h. Kang, “Existence of Positive Solutions for Two-Point Boundary Value Problems of Nonlinear Finite Discrete Fractional Differential Equations and Its Application,” *Advances in Mathematical Physics*, 2016.
- [12] Z. Gao and J. Wang, “Hyers-Ulam Stability and Existence of Solutions for Nigmatullin’s Fractional Diffusion Equation,” *Advances in Mathematical Physics*, vol. 2017, pp. 1–6, 2017.
- [13] A. S. Avetisyan and A. Z. Khurshudyan, “Green’s function approach in approximate controllability for nonlinear physical processes,” *Modern Physics Letters A*, vol. 32, no. 21, 1730015, 7 pages, 2017.
- [14] A. S. Avetisyan and As. Zh. Khurshudyan, *Controllability of Dynamic Systems: The Greens Function Approach*, Cambridge Scholars Publishing, Cambridge, 2018.

- [15] A. D. Polyanin, A. I. Zhurov, and A. V. Vyaz'min, "Exact solutions of nonlinear heat- and mass-transfer equations," *Theoretical Foundations of Chemical Engineering*, vol. 34, no. 5, pp. 403–415, 2000.
- [16] A. F. Barannyk, T. A. Barannyk, and I. I. Yuryk, "Generalized separation of variables and exact solutions of nonlinear equations," *Ukrainian Mathematical Journal*, vol. 62, no. 12, pp. 1851–1865, 2011.
- [17] J. D. Murray, *Mathematical Biology. Vol. 1: An Introduction & Vol. 2: Spatial Models and Biomedical Applications*, Springer, Berlin, Germany, 3 edition, 2002.
- [18] D. S. Drumheller, *Introduction to Wave Propagation in Nonlinear Fluids and Solids*, Cambridge University Press, Cambridge, 1998.

Research Article

Adaptive Fuzzy Synchronization of Fractional-Order Chaotic Neural Networks with Backlash-Like Hysteresis

Wenqing Fu ¹ and Heng Liu ²

¹School of Science, Xi'an Technological University, Xi'an 710021, China

²Department of Applied Mathematics, Huainan Normal University, Huainan 2320389, China

Correspondence should be addressed to Heng Liu; liuheng122@gmail.com

Received 6 January 2018; Revised 11 April 2018; Accepted 26 April 2018; Published 3 June 2018

Academic Editor: Christos Volos

Copyright © 2018 Wenqing Fu and Heng Liu. This is an open access article distributed under the Creative Commons Attribution License, which permits unrestricted use, distribution, and reproduction in any medium, provided the original work is properly cited.

An adaptive fuzzy synchronization controller is designed for a class of fractional-order neural networks (FONNs) subject to backlash-like hysteresis input. Fuzzy logic systems are used to approximate the system uncertainties as well as the unknown terms of the backlash-like hysteresis. An adaptive fuzzy controller, which can guarantee the synchronization errors tend to an arbitrary small region, is given. The stability of the closed-loop system is rigorously analyzed based on fractional Lyapunov stability criterion. Fractional adaptation laws are established to update the fuzzy parameters. Finally, some simulation examples are provided to indicate the effectiveness and the robust of the proposed control method.

1. Introduction

In the past two decades, study results of fractional calculus have received more and more attention because, compared with the classical integer-order calculus, the fractional-order one has many interesting and special properties. It has also been proven that a lot kinds of actual systems, ranging from life science and engineering to secret communication and system control, can be better modeled by using fractional-order differential equations (FDE) [1–10]. The nonlinear system, which is described by FDE, has memory. This advantage makes it possible to describe the hereditary as well as memory characters of many systems and processes. On this account, a lot of scholars employed the fractional-order derivative to replace the integer-order one in neural networks to get the FONNs [11–18]. It is known that the fractional model equips the neurons with more powerful computation ability, and these abilities could be used in information processing, frequency-independent phase shifts of oscillatory neuronal firing, and stimulus anticipation [13, 19]. By far, lots of methods have been given to synchronize FONNs [5, 12, 13, 20–22]. It should be mentioned that, in above works, the model of the master FONN should be known in advance.

How to design synchronization controller when the master system's model is unknown is a challenging but interesting work.

It is well known that hysteresis can be found in a great amount of physical systems or devices, for instance, biology optics, mechanical actuators, electromagnetism, and electronic circuits [6, 23–26]. Hysteresis can damage the control performance or even lead to the instability of the controlled system. How to construct proper controller for these kinds of systems is an interesting work. With respect to integer-order systems subject to hysteresis, a lot of results have been given. In [27], a feedback controller was introduced to control nonlinear systems with hysteresis. The control of systems subject to Prandtl-Ishlinskii hysteresis was studied in [28]. To see more results on the control of integer-order systems with hysteresis please refer to [29–33]. However, with respect to fractional-order nonlinear systems with hysteresis, the related literatures are very few.

Up to now, fuzzy control methods have been studied extensively [34–42]. Specially, this approach has been particularly used to synchronize or control integer-order neural networks (IONNs) [43–47]. In above literature, fuzzy logic systems were employed to approximate the uncertain

functions. To enhance the approximation ability of the fuzzy system, some robust terms, for example, sliding mode control, H_∞ control should be used together with the main fuzzy adaptive control term. It should be pointed out that the above results are limited to uncertain IONNs. It is advisable to discuss the synchronization problem for uncertain FONNs.

In our paper, an adaptive fuzzy control approach is introduced for synchronizing two uncertain FONNs. Based on some fractional Lyapunov stability theorems, the stability analysis and the controller implement are given. To show the effectiveness of the proposed synchronization method, some illustrative examples are presented. Bearing the results of aforementioned works in mind, the main contributions of our study consist of the following: (1) by designing an adaptive fuzzy controller, a practical synchronization is proposed for a class of uncertain FONNs. To the best of our knowledge, how to construct fuzzy adaptive control for FONNs has not been previously investigated up to now, except some preliminaries works in [8, 46]. It should be pointed out that, in these works, the integer-order stability analysis method is used. However, in this paper, we will use the fractional stability analysis approach, and the stability of the closed-loop system is proved rigorously. (2) The models of the FONNs are assumed to be fully unknown (i.e., the controller designed is free of the models of both master and slave systems). (3) The control of fractional-order nonlinear systems with backlash-like hysteresis input is studied.

2. Preliminaries

2.1. Some Basic Results of Fractional Calculus. The q th fractional integral is defined by

$$\mathbb{I}^{-q} f(t) = \frac{1}{\Gamma(q)} \int_0^t \frac{f(\tau)}{(t-\tau)^{1-q}} d\tau, \quad (1)$$

where $\Gamma(q) = \int_0^{+\infty} \tau^{q-1} e^{-\tau} d\tau$. The q th fractional-order derivative is given as

$$\mathbb{D}^q f(t) = \frac{1}{\Gamma(n-q)} \int_0^t \frac{f^{(n)}(\tau)}{(t-\tau)^{q+1-n}} d\tau, \quad (2)$$

where $n-1 \leq q < n$ ($n \in \mathbb{N}$). The Laplace transform of the Caputo fractional derivative is

$$\int_0^\infty e^{-st} \mathbb{D}^q f(t) dt = s^q F(s) - \sum_{k=0}^{n-1} s^{q-k-1} f^{(k)}(0), \quad (3)$$

where $F(s) = \mathcal{L}\{f(t)\}$. For convenience, we always assume that $0 < q \leq 1$ in the rest of this paper.

The following results on fractional calculus will help us to facilitate the synchronization controller design as well as the stability analysis.

Definition 1 (see [1]). The Mittag-Leffler function is defined by

$$E_{q_1, q_2}(\zeta) = \sum_{k=0}^{\infty} \frac{\zeta^k}{\Gamma(q_1 k + q_2)}, \quad (4)$$

where $q_1, q_2 > 0$, and $\zeta \in \mathbb{C}$.

The Laplace transform of (4) is as follows [1]:

$$\mathcal{L}\{t^{\beta-1} E_{q_1, q_2}(-at^{q_1})\} = \frac{s^{q_1 - q_2}}{s^{q_1} + a}. \quad (5)$$

Lemma 2 (see [1]). Let $x(t) \in C^1[0, T]$ with $T > 0$; then one has

$$\begin{aligned} {}_0\mathbb{I}_t^{-q} \mathbb{D}^q x(t) &= x(t) - x(0), \\ \mathbb{D}^q {}_0\mathbb{I}_t^{-q} x(t) &= x(t). \end{aligned} \quad (6)$$

Lemma 3 (see [1]). Let $\beta \in \mathbb{C}$ and to constants q, μ satisfying $0 < q < 2$ and

$$\frac{\pi q}{2} < \mu < \min\{\pi, \pi q\}, \quad (7)$$

and then the following equality holds:

$$\begin{aligned} E_{q, \beta}(z) &= -\sum_{j=1}^n \frac{1}{\Gamma(\beta - qj)} z^j + o\left(\frac{1}{|z|^{n+1}}\right), \\ |z| &\rightarrow \infty, \quad \mu \leq |\arg(z)| \leq \pi. \end{aligned} \quad (8)$$

Lemma 4 (see [1]). Let $0 < q < 2$ and $\beta \in \mathbb{R}$. If there exists a positive constant μ such that $\pi q/2 < \mu \leq \min\{\pi, \pi q\}$, then one has

$$|E_{q, \beta}(z)| \leq \frac{b_0}{1 + |z|}, \quad (9)$$

where b_0 is a positive real constant, $\mu \leq |\arg(z)| \leq \pi$ and $|z| \geq 0$.

Lemma 5 (see [2]). Let $x(t) = 0$ be an equilibrium point of the following fractional-order nonlinear system:

$$\mathbb{D}^q x(t) = f(t, x(t)). \quad (10)$$

If one can find a Lyapunov function $V(t, x(t))$ as well as three class-K functions g_i , $i = 1, 2, 3$ such that

$$g_1(\|x(t)\|) \leq V(t, x(t)) \leq g_2(\|x(t)\|), \quad (11)$$

$$\mathbb{D}^q V(t, x(t)) \leq -g_3(\|x(t)\|),$$

then system (10) will be asymptotically stable.

Lemma 6 (see [4]). Let $x(t) \in \mathcal{R}^n$ be a continuous and derivable function. Then, for any $t > 0$,

$$\frac{1}{2} \mathbb{D}^q x^T(t) x(t) \leq x^T(t) \mathbb{D}^q x(t). \quad (12)$$

Lemma 7 (see [3]). Let $x(t) \in \mathcal{R}^n$ be a continuous and derivable function. Then, for any $t > 0$,

$$\frac{1}{2} \mathbb{D}^q x^T(t) Bx(t) \leq x^T(t) B \mathbb{D}^q x(t), \quad (13)$$

where $B \in \mathcal{R}^{n \times n}$ is a positive definite constant matrix.

2.2. Description of a Fuzzy System. A fuzzy logic system consists of four parts: the knowledge base, the fuzzifier, the fuzzy inference engine working on the fuzzy rules, and the defuzzifier [34–40, 48]. Usually, a fuzzy logic system is modeled by

$$\hat{f}(x(t)) = \frac{\sum_{j \in J} \vartheta_j(t) \mu_j(x(t))}{\sum_{j \in J} \mu_j(x(t))}, \quad (14)$$

where \hat{f} (a Lipschitz-continuous mapping from a compact subset $\Omega \subseteq \mathcal{R}^n$ to the real line \mathcal{R}) is called the output of the fuzzy logic system, $x = [x_1, \dots, x_n]^T \in C^1[\mathcal{S}, \Omega]$ (the set of all continuous mappings from $\mathcal{S} = [0, +\infty) \subseteq \mathcal{R}$ to Ω which have continuous derivatives) is called the input vector, $J = \prod_{i=1}^n \mathcal{F}_i$, \mathcal{F}_i consists of N_i fuzzy sets ($1 \leq i \leq n$), μ_j (a mapping from \mathcal{R}^n to the closed unit interval $[0, 1] \subseteq \mathcal{R}$) is called the membership function of rule j ($j \in J$), and ϑ_j (a mapping from \mathcal{S} to \mathcal{R}) is called the centroid of the j th consequent set ($j \in J$); we may identify J with $\{1, 2, \dots, N\}$ for the sake of convenience. Write $\vartheta(t) = [\vartheta_1(t), \dots, \vartheta_N(t)]^T$ and $\varphi(x(t)) = [q_1(x(t)), q_2(x(t)), \dots, q_N(x(t))]^T$, where q_j (called the j th fuzzy basis function, $j \in J$) is a continuous mapping (and thus $\varphi : \Omega \rightarrow \mathcal{R}^N$ is continuous) defined by

$$q_j(x(t)) = \frac{\vartheta_j(t)}{\sum_{s \in J} \mu_s(x(t))}. \quad (15)$$

Then system (14) can be rewritten as

$$\hat{f}(x(t)) = \vartheta^T(t) \varphi(x(t)). \quad (16)$$

3. Main Results

3.1. Problem Description. Consider a class of FONNs described as

$$\mathbb{D}^q x_i(t) = -a_i x_i(t) + \sum_{k=1}^n b_{ik} f_k(x_k(t)) + I_i, \quad (17)$$

where $i = 1, \dots, n$, $x_i(t)$ is the state variable, $a_i > 0$ and b_{ik} , $k = 1, 2, \dots, m$ are constants, I_i represents the external input, and $f_k(\cdot)$ is a smooth nonlinear function.

Write $x(t) = [x_1(t), \dots, x_n(t)]^T \in \mathbb{R}^n$, $f(\cdot) = [f_1(\cdot), \dots, f_n(\cdot)]^T \in \mathbb{R}^n$, $I = [I_1, \dots, I_n]^T \in \mathbb{R}^n$, $A = -\text{diag}(a_1, \dots, a_n) \in \mathbb{R}^{n \times n}$, $u(t) = [u_1(t), \dots, u_m(t)] \in \mathbb{R}^m$,

$$B = \begin{bmatrix} b_{11} & \cdots & b_{1n} \\ \vdots & \ddots & \vdots \\ b_{1n} & \cdots & b_{nn} \end{bmatrix} \in \mathbb{R}^{n \times n}, \quad (18)$$

then (17) can be written into the following compact form:

$$\mathbb{D}^q x(t) = Ax(t) + Bf(x(t)) + I. \quad (19)$$

To guarantee the existence and uniqueness of the solutions of the fractional-order neural network (19) (see, [3]), we

assume that the functions f are Lipschitz-continuous, i.e., for all $x(t), y(t) \in \mathcal{R}^n$,

$$\|f(x(t)) - f(y(t))\| \leq \sigma \|x(t) - y(t)\|, \quad (20)$$

where σ is a positive constant.

The slave system is expressed by

$$\mathbb{D}^\alpha y(t) = Ay(t) + Bf(y(t)) + I + Gv(t) + d(t), \quad (21)$$

where $y(t) \in \mathcal{R}^n$ is the state vector of the slave system, $G \in \mathbb{R}^{n \times n}$ is a positive definite control gain matrix, $d(t) = [d_1(t), d_2(t), \dots, d_n(t)]^T \in \mathcal{R}^n$ is an unknown external disturbance, and $v(t) \in \mathbb{R}^n$ represents hysteresis type of nonlinear control input which is described by

$$\frac{dv(t)}{dt} = \gamma_1 \left| \frac{du(t)}{dt} \right| (\gamma_3 u(t) - v(t)) + \gamma_2 \frac{du(t)}{dt}, \quad (22)$$

where $u(t) = [u_1(t), \dots, u_n(t)]^T \in \mathbb{R}^n$ is the control input, γ_1 , γ_2 and γ_3 are three constants satisfying $\gamma_3 > 0$ and $\gamma_3 > \gamma_2$. One can rewrite (22) as

$$\begin{aligned} v(t) &= \gamma_3 u(t) + \hbar(t) \\ \hbar(t) &= [\omega(0) - cu(0)] e^{-a(u(t)-u(0)) \text{sign}(\dot{u}(t))} \\ &\quad + e^{-au(t) \text{sign}(\dot{u}(t))} \int_{u(0)}^{u(t)} (b-c) e^{a\tau \text{sign}(\dot{u}(t))} d\tau. \end{aligned} \quad (23)$$

When $\gamma_1 = 1.1$, $\gamma_3 = 3.22$, $\gamma_2 = 0.44$, $u(t) = 5.1 \sin(2t)$ and $v(0) = 0$, the behavior of the backlash-like hysteresis is depicted in Figure 1.

The objective of this paper is to construct an adaptive fuzzy controller such that the slave system (21) synchronizes the master system (19). To proceed, the following assumption is needed.

Assumption 8. The external disturbance is bounded, i.e., $|d_i(t)| \leq \bar{d}_i$, $i = 1, 2, \dots, n$ where \bar{d}_i is an unknown positive constant.

3.2. Synchronization Controller Implement. In this part, we will give the detailed procedure of the adaptive fuzzy controller design as well as the stability analysis. Let the synchronization error be $e(t) = x(t) - y(t)$. It follows from (19), (21), and (23) that

$$\begin{aligned} \mathbb{D}^q e(t) &= Ae(t) + A(f(x(t)) - f(y(t))) - \gamma_3 Gu(t) \\ &\quad - G\hbar(t) - d(t). \end{aligned} \quad (24)$$

Denote $\Xi = (1/\gamma_3)G^{-1}$; (24) implies that

$$\Xi \mathbb{D}^q e(t) = \omega(e(t)) - u(t), \quad (25)$$

where $\omega(e(t)) = \Xi(Ae(t) + A(f(x(t)) - f(y(t))) - G\hbar(t) - d(t))$ is an unknown nonlinear function.

Remark 9. In fact, it is easy to know that ω is a function of $x(t)$, $y(t)$, $e(t)$, and t . In this paper, the synchronization

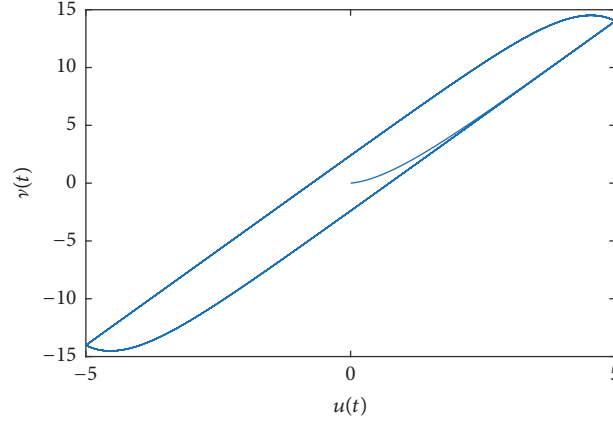


FIGURE 1: Hysteresis curve.

error will be used as the input of the fuzzy logic systems. In addition, the synchronization error $e(t)$ can be seen as a bridge between the signals $x(t)$ and $y(t)$. Consequently, we will use the denotation $\widehat{\omega}(e(t))$ for convenience.

Firstly, let us consider an ideal condition. Suppose that $\widehat{\omega}(e(t))$ is known (i.e., $d(t)$, $f(x(t))$, and $f(y(t))$ are all known in advance). Thus, the ideal controller can be given by

$$u_{eq} = \widehat{\omega}(e(t)) + Ke(t), \quad (26)$$

where $K = \text{diag}(k_1, \dots, k_n)$ with $k_i > 0$, $i = 1, 2, \dots, n$. Then, we can give the following theorem.

Theorem 10. *If the models of the master and slave systems are known, and the synchronization controller is given by (26), then we have that the synchronization error converges to zero asymptotically.*

Proof. Substituting (26) into (25), one has

$$\Xi \mathbb{D}^q e(t) = -Ke(t). \quad (27)$$

Define the following Lyapunov function:

$$\mathbb{V}(t) = \frac{1}{2} e^T(t) \Xi e(t). \quad (28)$$

According to Lemma 7, the q th derivative of $\mathbb{V}(t)$ is bounded by

$$\begin{aligned} \mathbb{D}^\alpha \mathbb{V}(t) &= \frac{1}{2} \mathbb{D}^q e^T(t) \Xi e(t) \leq e^T(t) \Xi \mathbb{D}^q e(t) \\ &\leq -\underline{k}(t), \end{aligned} \quad (29)$$

where $\underline{k} = \min\{k_1, k_2, \dots, k_n\}$. Thus, according to Lemma 5 and (29) that the synchronization error will converge to zero asymptotically. \square

Since $\widehat{\omega}(e(t))$ is an unknown function, the above controller (26) may be inapplicable. In such a case, by using the fuzzy logic system, let us approximate $\widehat{\omega}(e(t))$ (16) as

$$\widehat{\omega}_i(\vartheta_i(t), e(t)) = \vartheta_i^T(t) \varphi_i(e(t)), \quad (30)$$

where $\varphi_i(x(t))$ is a fuzzy basis function, and $\vartheta_i(t)$ is an adjustable parameter of the fuzzy system which drive $\sup\{|\widehat{\omega}_i(e(t)) - \widehat{\omega}_i(\vartheta_i^*, e(t))|\}$ small enough. Let the parameter estimation error with respect to ϑ_i be

$$\bar{\vartheta}_i(t) = \vartheta_i(t) - \vartheta_i^*, \quad (31)$$

and the fuzzy approximation error with respect to ϑ_i^* be

$$\varepsilon_i(e(t)) = \widehat{\omega}_i(e(t)) - \widehat{\omega}_i(\vartheta_i^*, e(t)). \quad (32)$$

According to the universal approximation theorem, one can know that the fuzzy systems do not violate the universal approximator property. Consequently, one can make the following assumption.

Assumption 11. There exists an unknown constant $\varepsilon^* > 0$ such that

$$\sup\{|\varepsilon_i(e(t))|\} \leq \varepsilon^*. \quad (33)$$

Based on the above analysis, one has

$$\begin{aligned} &\widehat{\omega}_i(\vartheta_i(t), e(t)) - \widehat{\omega}_i(e(t)) \\ &= \widehat{\omega}_i(\vartheta_i(t), e(t)) - \widehat{\omega}_i(\vartheta_i^*, e(t)) + \widehat{\omega}_i(\vartheta_i^*, e(t)) \\ &\quad - \widehat{\omega}_i(e(t)) \\ &= \widehat{\omega}_i(\vartheta_i(t), e(t)) - \widehat{\omega}_i(\vartheta_i^*, e(t)) - \varepsilon_i(e(t)) \\ &= \bar{\vartheta}_i^T(t) \varphi_i(e(t)) - \varepsilon_i(e(t)). \end{aligned} \quad (34)$$

Denote $\vartheta(t)\varphi(e(t)) = [\vartheta_1^T(t)\varphi_1(e(t)), \vartheta_2^T(t)\varphi_2(e(t)), \dots, \vartheta_n^T(t)\varphi_n(e(t))]^T$ and $\bar{\vartheta}(t)\varphi(e(t)) = [\bar{\vartheta}_1^T(t)\varphi_1(e(t)), \bar{\vartheta}_2^T(t)\varphi_2(e(t)), \dots, \bar{\vartheta}_n^T(t)\varphi_n(e(t))]^T$, then one can rewrite (34) as

$$\widehat{\omega}(\vartheta(t), e(t)) - \widehat{\omega}(e(t)) = \bar{\vartheta}^T(t) \varphi(e(t)) - \varepsilon(e(t)), \quad (35)$$

where $\vartheta(t) = [\vartheta_1^T(t), \vartheta_2^T(t), \dots, \vartheta_n^T(t)]^T \in \mathbb{R}^{N \times n}$ (N represents the amount of the fuzzy rules).

To simplify the stability analysis, we give the following results first.

Theorem 12. Suppose that $h(t) \in \mathbb{R}$ is a positive definite smooth function. $\delta_1 > 0$, $\delta_2 \in \mathbb{R}$ are two adjustable parameters. If it holds that

$$\mathbb{D}^q h(t) \leq -\delta_1 h(t) + \delta_2, \quad (36)$$

then $h(t)$ will be small enough eventually if proper parameters are chosen.

Proof. According to (36), one can find a function $\zeta(t)$ satisfying $\zeta(t) \geq 0$ and

$$\mathbb{D}^q h(t) + \zeta(t) = -\delta_1 h(t) + \delta_2. \quad (37)$$

It follows from (37) that

$$H(s) = \frac{s^{q-1}}{s^q + \delta_1} h(0) + \frac{s^{q-(1+q)} \delta_2}{(s^q + \delta_1)} - \frac{Z(s)}{s^q + \delta_1}, \quad (38)$$

where $H(s) = \mathcal{L}\{h(t)\}$ and $Z(s) = \mathcal{L}\{\zeta(t)\}$. One solves (38) according to (5) as

$$\begin{aligned} h(t) &= h(0) E_{q,1}(-\delta_1 t^q) + \delta_2 t^q E_{q,1+q}(-\delta_1 t^q) - \zeta(t) \\ &\quad * t^{-1} E_{q,0}(-\delta_1 t^q), \end{aligned} \quad (39)$$

where $*$ represents the convolution operator. Since that $t^{-1} E_{q,0}(-\delta_1 t^q)$ and $\zeta(t)$ are all nonnegative, one has $\zeta(t) * t^{-1} E_{q,0}(-\delta_1 t^q) \geq 0$. Consequently, one has

$$h(t) \leq h(0) E_{q,1}(-\delta_1 t^q) + \delta_2 t^q E_{q,1+q}(-\delta_1 t^q). \quad (40)$$

It is easy to know that $\arg(-\delta_1 t^q) = -\pi$, $|\delta_1 t^q| \geq 0$ and $q \in (0, 2)$; thus, by using Lemma 4, one obtains that

$$\left| E_{q,1}(-\delta_1 t^q) \right| \leq \frac{\kappa}{1 + \delta_1 t^q}, \quad (41)$$

where $\kappa > 0$, i.e.,

$$\lim_{t \rightarrow \infty} h(0) E_{q,1}(-\delta_1 t^q) = 0. \quad (42)$$

Thus, by using Lemma 3, one has for every $\varepsilon > 0$ and large enough time t that

$$t^\alpha E_{\alpha, \alpha+1}(-At^\alpha) \leq \frac{B}{A} + \frac{\varepsilon}{3}. \quad (43)$$

That is to say, if the design parameters are chosen as $\delta_2/\delta_1 \leq \varepsilon$, then according to (40) and (43) one has

$$h(t) < \varepsilon. \quad (44)$$

This completes the proof of Theorem 12. \square

Then, one can obtain the following theorem.

Theorem 13. Under Assumptions 8 and 11 and proper control parameters, if $\tilde{\varepsilon}^*(t)$ is the estimation of ε^* , $u(t)$ is implemented as

$$u(t) = Ke(t) + \mathcal{G}^T(t) \varphi(e(t)) + \tilde{\varepsilon}^*(t) \text{sign}(e(t)), \quad (45)$$

and $\vartheta_i(t)$ and $\tilde{\varepsilon}^*(t)$ are, respectively, updated by

$$\mathbb{D}^q \vartheta_i(t) = \varsigma_{1i} e_i(t) \varphi_i(e(t)) - \varsigma_{1i} \varsigma_{2i} \vartheta_i(t), \quad (46)$$

$$\mathbb{D}^q \tilde{\varepsilon}^*(t) = \varsigma_3 \sum_{i=1}^n |e_i(t)| - \varsigma_3 \varsigma_4 \tilde{\varepsilon}^*(t), \quad (47)$$

with ς_{1i} , ς_{2i} , ς_3 , ς_4 being positive design parameters, then one has that the synchronization error eventually converges to an arbitrary small region of zero.

Proof. It follows from (25), (35), and (45) that

$$\begin{aligned} \Xi \mathbb{D}^q e(t) &= \omega(e(t)) - u(t) \\ &= \omega(e(t)) - Ke(t) - \mathcal{G}^T(t) \varphi(e(t)) \\ &\quad - \tilde{\varepsilon}^*(t) \text{sign}(e(t)) \\ &= -Ke(t) - \tilde{\mathcal{G}}^T(t) \varphi(e(t)) \\ &\quad - \tilde{\varepsilon}^*(t) \text{sign}(e(t)) + \varepsilon(e(t)). \end{aligned} \quad (48)$$

Multiplying $e^T(t)$ to both sides of (48) gives

$$\begin{aligned} e^T(t) \Xi \mathbb{D}^q e(t) &= -e^T(t) Ke(t) - e^T(t) \tilde{\mathcal{G}}^T(t) \varphi(e(t)) \\ &\quad + e^T(t) \varepsilon(e(t)) \\ &\quad - e^T(t) \tilde{\varepsilon}^*(t) \text{sign}(e(t)) \\ &\leq -\underline{\kappa} e^T(t) e(t) \\ &\quad - \sum_{i=1}^n e_i(t) \tilde{\vartheta}_i^T(t) \varphi_i(e(t)) \\ &\quad + \varepsilon^* \sum_{i=1}^n |e_i(t)| - \tilde{\varepsilon}^*(t) \sum_{i=1}^n |e_i(t)| \\ &= -\underline{\kappa} e^T(t) e(t) \\ &\quad - \sum_{i=1}^n e_i(t) \tilde{\vartheta}_i^T(t) \varphi_i(e(t)) \\ &\quad - \tilde{\varepsilon}^*(t) \sum_{i=1}^n |e_i(t)|, \end{aligned} \quad (49)$$

where

$$\tilde{\varepsilon}^*(t) = \tilde{\varepsilon}^*(t) - \varepsilon^* \quad (50)$$

is the estimation error of ε^* .

It is known that the $\mathbb{D}^q C = 0$ where C is an arbitrary constant. Thus, it follows from (31) and (50) that $\mathbb{D}^q \tilde{\vartheta}_i(t) = \mathbb{D}^q \vartheta_i(t)$ and $\mathbb{D}^q \tilde{\varepsilon}^*(t) = \mathbb{D}^q \tilde{\varepsilon}^*(t)$.

Define the Lyapunov function as

$$\begin{aligned} \mathcal{V}(t) &= \frac{1}{2} e^T(t) \Xi e(t) + \sum_{i=1}^n \frac{1}{2\varsigma_{1i}} \tilde{\vartheta}_i^T(t) \tilde{\vartheta}_i(t) \\ &\quad + \frac{1}{2\varsigma_3} \tilde{\varepsilon}^{*2}(t). \end{aligned} \quad (51)$$

Using (46), (47), (49), and Lemma 6 one has

$$\begin{aligned}
& \mathbb{D}^q \mathcal{V}(t) \\
& \leq e^T(t) \Xi \mathbb{D}^q e(t) + \sum_{i=1}^n \frac{1}{\varsigma_{1i}} \tilde{\vartheta}_i^T(t) \mathbb{D}^q \tilde{\vartheta}_i(t) \\
& \quad + \frac{1}{\varsigma_3} \tilde{\varepsilon}^*(t) \mathbb{D}^q \tilde{\varepsilon}^*(t) \\
& = -\underline{k} e^T(t) e(t) - \sum_{i=1}^n e_i(t) \tilde{\vartheta}_i^T(t) \varphi_i(e(t)) \\
& \quad - \tilde{\varepsilon}^*(t) \sum_{i=1}^n |e_i(t)| + \sum_{i=1}^n \frac{1}{\varsigma_{1i}} \tilde{\vartheta}_i^T(t) \mathbb{D}^q \vartheta_i(t) \\
& \quad + \frac{1}{\varsigma_3} \tilde{\varepsilon}^*(t) \mathbb{D}^q \tilde{\varepsilon}^*(t) \\
& = -\underline{k} e^T(t) e(t) - \sum_{i=1}^n e_i(t) \tilde{\vartheta}_i^T(t) \varphi_i(e(t)) \\
& \quad + \frac{1}{\varsigma_3} \tilde{\varepsilon}^*(t) \left(\varsigma_3 \sum_{i=1}^n |e_i(t)| - \varsigma_3 \varsigma_4 \tilde{\varepsilon}^*(t) \right) \\
& \quad - \tilde{\varepsilon}^*(t) \sum_{i=1}^n |e_i(t)| \\
& \quad + \sum_{i=1}^n \frac{1}{\varsigma_{1i}} \tilde{\vartheta}_i^T(t) (\varsigma_{1i} e_i(t) \varphi_i(e(t)) - \varsigma_{1i} \varsigma_{2i} \vartheta_i(t)) \\
& = -\underline{k} e^T(t) e(t) - \sum_{i=1}^n \varsigma_{2i} \tilde{\vartheta}_i^T(t) \vartheta_i(t) - \varsigma_4 \tilde{\varepsilon}^*(t) \tilde{\varepsilon}^*(t) \\
& = -\underline{k} e^T(t) e(t) - \sum_{i=1}^n \varsigma_{2i} \tilde{\vartheta}_i^T(t) \tilde{\vartheta}_i(t) - \varsigma_4 \tilde{\varepsilon}^*(t) \tilde{\varepsilon}^*(t) \\
& \quad - \varsigma_4 \tilde{\varepsilon}^*(t) \varepsilon^*(t) - \sum_{i=1}^n \varsigma_{2i} \tilde{\vartheta}_i^T(t) \vartheta_i^* \\
& \leq -\underline{k} e^T(t) e(t) - \sum_{i=1}^n \frac{\varsigma_{2i}}{2} \tilde{\vartheta}_i^T(t) \tilde{\vartheta}_i(t) - \frac{\varsigma_4}{2} \tilde{\varepsilon}^{*2}(t) \\
& \quad + \sum_{i=1}^n \frac{\varsigma_{2i}}{2} \vartheta_i^{*T} \vartheta_i^* + \frac{\varsigma_4}{2} \varepsilon^{*2} \leq -\delta_1 \mathcal{V}(t) + \delta_2
\end{aligned} \tag{52}$$

with $\delta_1 = \min\{2\underline{k}, \varsigma_{1i}\varsigma_{2i}, \varsigma_2\varsigma_4\}$ and $\delta_2 = \sum_{i=1}^n (\varsigma_{2i}/2) \vartheta_i^{*T} \vartheta_i^* + (\varsigma_4/2) \varepsilon^{*2}$ being two positive constants.

Thus, based on (52) and Theorem 12, one knows that the synchronization error eventually converges to an arbitrary small region of zero if proper control parameters are chosen. This completes the proof of Theorem 13. \square

Remark 14. It should be pointed out that the fractional-order adaptation law was also introduced in [3, 5, 49, 50]. However, the above adaptation laws only contain a positive term (i.e., the adaptation law is designed as $\mathbb{D}^q \vartheta(t) = \sigma e_i(t) \varphi_i(t)$). Despite using this kind of adaptation law, the

asymptotical stability of the system can be guaranteed. Yet, the boundedness of the control parameters cannot be ensured. The proposed adaptation law contains a negative term (for example, $-\varsigma_{1i}\varsigma_{2i}\vartheta_i(t)$ in (46)) which will drive the updated parameter tends to a small neighborhood of the origin eventually (see the proof of Theorem 13).

Remark 15. To enforce the synchronization error tending to a region as small as possible, one must make δ_2/δ_1 small enough. To meet this objective, one should choose large k_i , ς_{1i} , ς_3 and choose small ς_{2i} , ς_4 .

Remark 16. It is worth mentioning that, in [51], to discuss the stability of the fractional-order nonlinear systems, a very complicated boundary condition

$$\left\| \sum_{k=1}^{\infty} \frac{\Gamma(1+\alpha)}{\Gamma(1+k)\Gamma(1-k+\alpha)} \mathbb{D}^k x(t) \mathbb{D}^{\alpha-k} x(t) \right\| \leq a \|x\| \tag{53}$$

is assumed to be known. The above condition was proven in [51]. Yet, how to get the exact value of a is a challenging work. But in our paper, by using the quadratic Lyapunov functions, the aforementioned problem is solved.

Remark 17. It should be pointed out that the proposed control method does not need the prior knowledge of systems models. Therefore, the control method can be easily extended to the following domains: control of fractional-order nonlinear systems, synchronization of fractional-order chaotic system, and secret communication, and so on. And relating out control method to a potential application is one of our future research directions.

4. Simulation Studies

In (19), letting $x(t) \in \mathbb{R}^3$, $x(0) = [-0.301, 0.400, 0.299]^T$, $q = 0.96$, $f_i(x_i(t)) = \tanh(x_i(t))$, $a_i = 1$, $I_i = 0$, $u(t) \equiv 0$, and

$$B = \begin{bmatrix} 2.001 & -1.201 & 0 \\ 2.000 & 1.713 & 1.154 \\ -4.751 & 0 & 1.101 \end{bmatrix}, \tag{54}$$

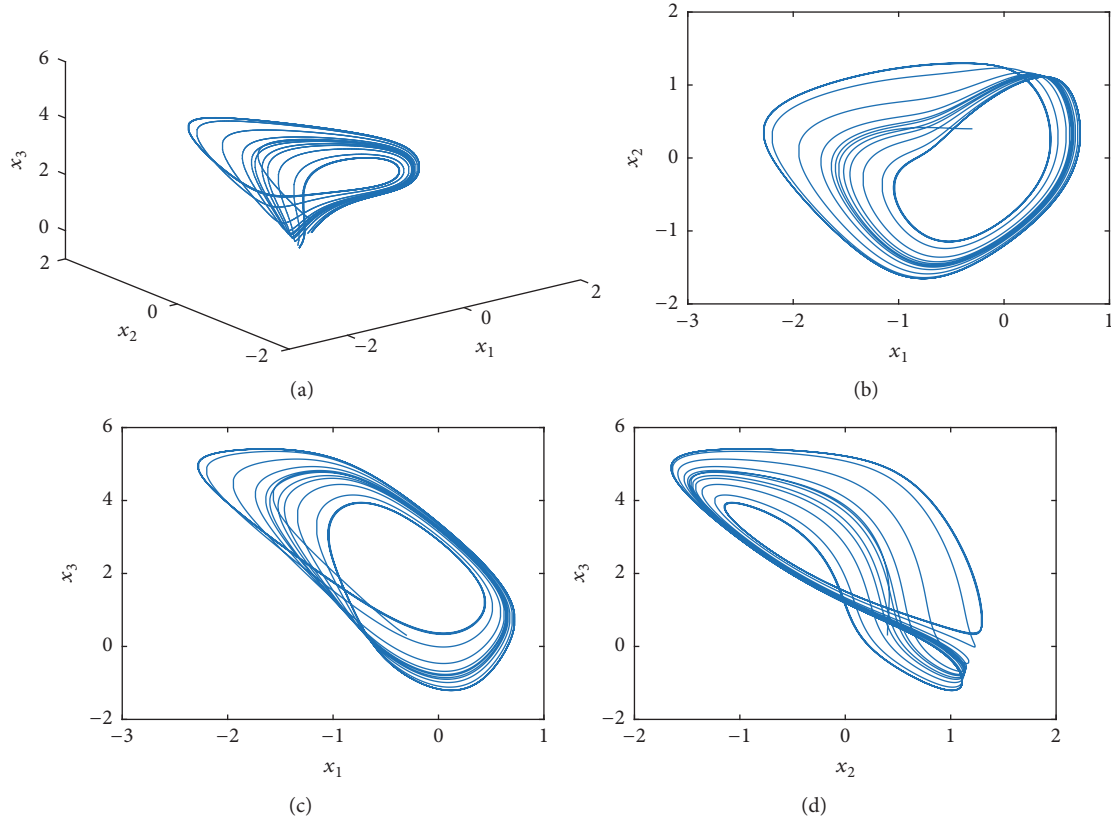
the FONN (19) shows chaotic behavior, which is depicted in Figure 2.

4.1. Synchronization of FONN with Constant System Parameters. Let the initial condition of the slave FONN (21) be $y(0) = [4.2, -3.1, -1.9]$, and $G = I_{3 \times 3}$. The external disturbance is defined as $d(t) = [\sin t, \cos t, \sin t + \cos t]^T$. The control design parameters are given as $k_1 = k_2 = k_3 = 0.5$. $\varsigma_{11} = \varsigma_{12} = \varsigma_{13} = 1.1$, $\varsigma_{21} = \varsigma_{22} = \varsigma_{23} = 0.05$, $\varsigma_3 = 1.55$, $\varsigma_4 = 0.02$. In the simulation, the noncontinuous sign function in (45) is replaced with $\arctan(10 \cdot)$.

With respect to the fuzzy logic systems, its input variable is chosen as the synchronization error $e_i(t)$. For each input, we give seven Gaussian membership functions on $[-5 \ 5]$. The parameters of the proposed membership functions, which are

TABLE I: Fuzzy parameters.

Membership functions	Parameter b	Parameter a
Membership function 1	1	-5
Membership function 2	0.8	-2
Membership function 3	0.2	-0.3
Membership function 4	0.09	0
Membership function 5	0.2	0.3
Membership function 6	0.8	2
Membership function 7	1	5

FIGURE 2: Chaotic dynamic of the FONN (19) in (a) 3D space; (b) x_1 - x_2 plane; (c) x_1 - x_3 plane; (d) x_2 - x_3 plane.

defined as $e^{-(e_i(t)-a)^2/2b^2}$, are given in Table 1. These functions are depicted in Figure 3. The initial conditions of the fuzzy parameters are given as $\vartheta_1(0) = \vartheta_2(0) = \vartheta_3(0) = \underline{0} \in \mathcal{R}^{3 \times 3}$.

The simulation results are depicted in Figures 4–6. The results that the signals $x_1(t)$, $x_2(t)$, and $x_3(t)$, respectively, track $y_1(t)$, $y_2(t)$, and $y_3(t)$, as well as the time response of the synchronization errors are presented in Figure 4. The smoothness and the boundedness of the control inputs are given in Figure 5. The fuzzy parameters, which can be concluded to be bounded according to the proposed adaptation law (46), are shown in Figure 6. From these figures one knows that the proposed controller works well and has good synchronization performance.

It is well known that the conventional systems usually suffer from discontented performance resulting from modeled

errors, parametric uncertainties, input nonlinearities, and external disturbances, because it is impossible to provide accurate mathematical models of practical systems. These system uncertainties can damage the control performance or even lead to unstable of the controlled system if they are not well handled. To show the robust of the proposed method, let us consider the condition that the master system (19) suffers from time-varying system parameters and uncertainties. Suppose that the model of the master FONN (19) is replaced with

$$\mathbb{D}^q x(t) = \Delta A x(t) + B f(x(t)) + \Delta C \xi(t) + I, \quad (55)$$

where $\Delta A = A + \bar{A} \in \mathbb{R}^{n \times n}$, $\Delta C \in \mathbb{R}^{n \times m}$, and $\xi \in \mathbb{R}^{m \times n}$ is an unknown external input signal. \bar{A} and \bar{C} are two

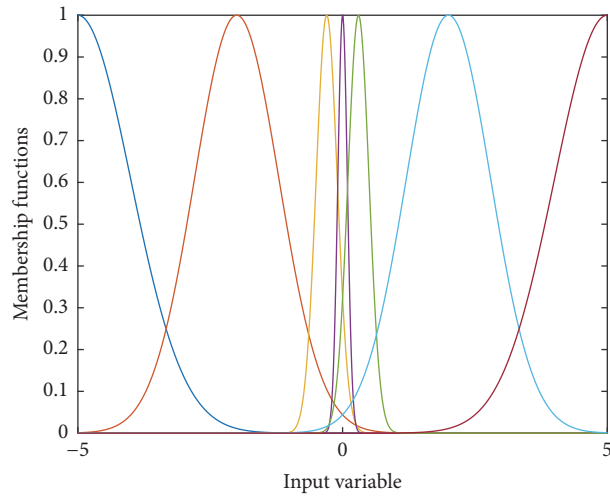


FIGURE 3: Membership functions.

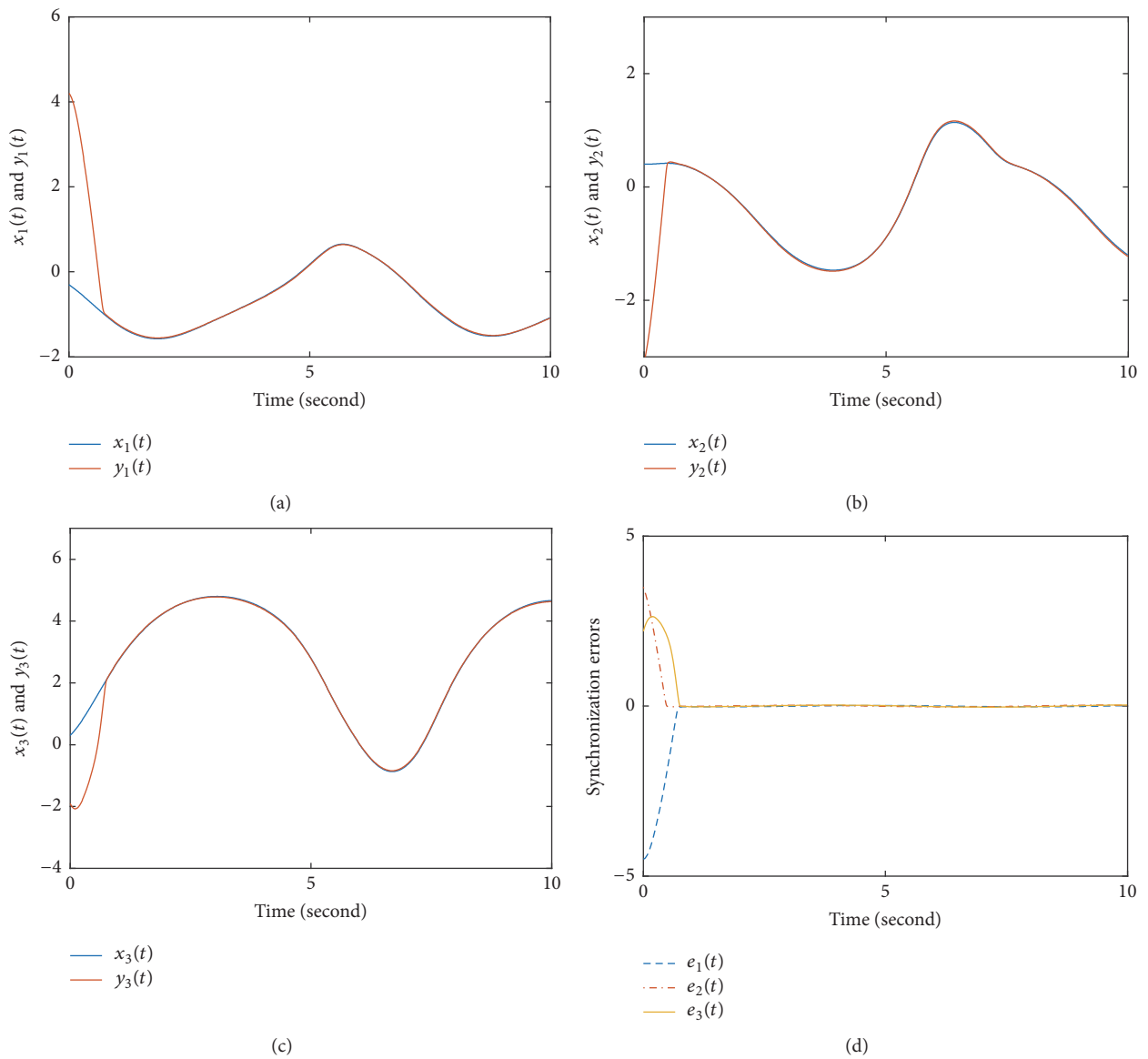


FIGURE 4: Simulation results in (a) $x_1(t)$ and $y_1(t)$; (b) $x_2(t)$ and $y_2(t)$; (c) $x_3(t)$ and $y_3(t)$; (d) synchronization errors.

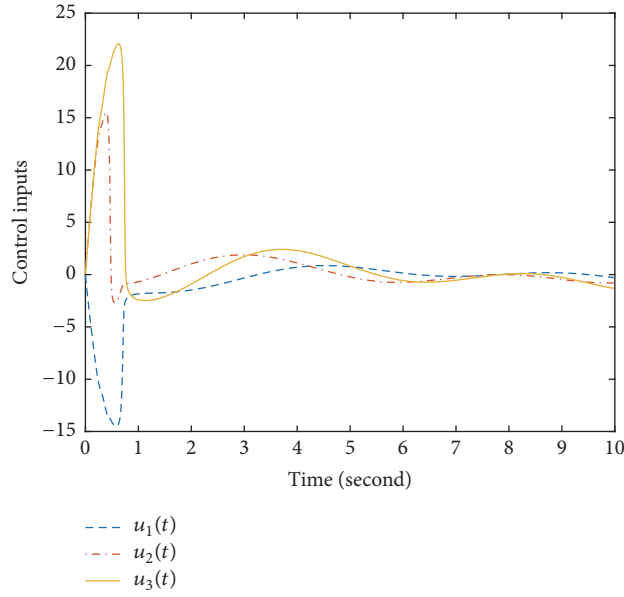


FIGURE 5: Control inputs.

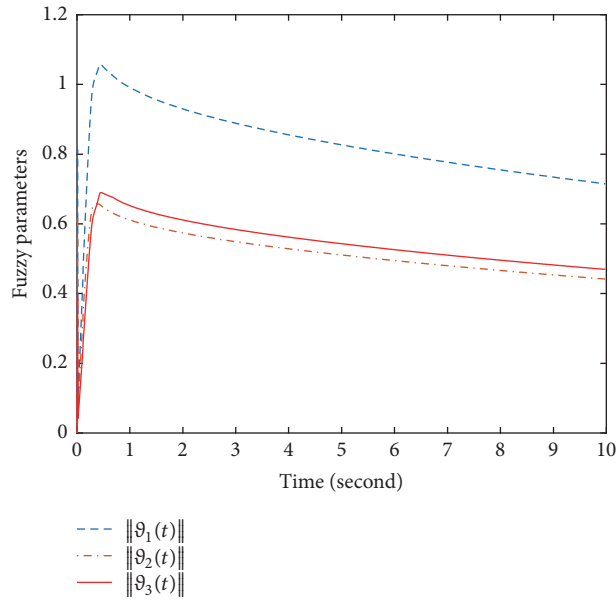


FIGURE 6: Fuzzy parameters.

unknown matrices. That is, \bar{A} represents unknown system parameter perturbations, and $\Delta C\xi(t)$ denotes unknown input nonlinearities.

For convenience, let us suppose that $[\bar{A}, \bar{C}] = N_1 D(t) [N_2, N_3]$, where $N_1 \in \mathbb{R}^{n \times g}$, $N_2 \in \mathbb{R}^{g \times n}$ and $N_3 \in \mathbb{R}^{g \times m}$ are known matrices, and $D(t) \in \mathbb{R}^{g \times g}$ is an unknown matrix.

In the simulation, let $N_1 = \begin{bmatrix} 0.1 & 0 \\ 0 & 0.1 \end{bmatrix}$, $N_2 = \begin{bmatrix} 0.1 & 0.1 & 0 \\ 0.1 & 0.2 & 0.1 \end{bmatrix}$, $N_3 = \begin{bmatrix} 0.1 & 0 & 0.1 \\ 0.1 & 0.1 & 0 \end{bmatrix}$, and $D(t) = \begin{bmatrix} 0.2 \sin t & 0 \\ 0 & 0.2 \cos t \end{bmatrix}$. It is easy to know that \bar{A} and $\Delta C\xi(t)$ are time-varying matrices.

The simulations are presented in Figure 7. It should be pointed out that, in the simulation, the slave system and the controller are chosen to be the same as those in Section 4.1. From the simulation results we can see that good synchronization performance has been achieved even the master system suffers from time-varying parameters and input nonlinearities. That is, the proposed method has good robustness.

To indicate the effectiveness of our methods, the simulation results when $\xi(t) = -[2\sin(10t) + 15\text{rand}(t), 2 \cos(10t) +$

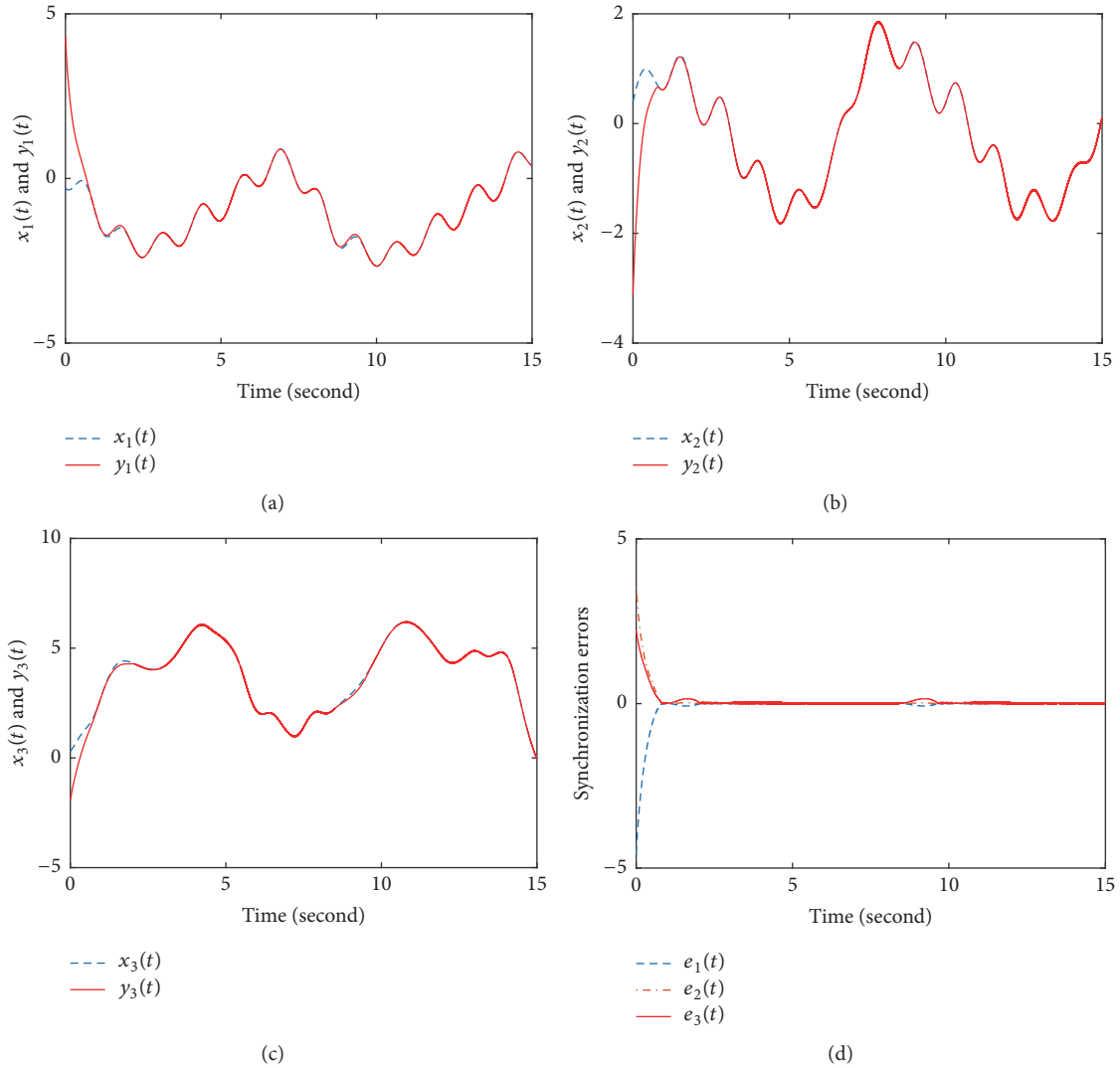


FIGURE 7: Simulation results when $u(t) = [5 \sin(20t), 3 \cos(20t), 4 \sin(10t)]^T$ in (a) $x_1(t)$ and $\hat{x}_1(t)$; (b) $x_2(t)$ and $\hat{x}_2(t)$; (c) $x_3(t)$ and $\hat{x}_3(t)$; (d) synchronization errors.

$20\text{rand}(t), 2 \sin(5t)+18\text{rand}(t)]^T$ where $\text{rand}(\cdot)$ represents the random function produced in MATLAB software are shown in Figure 8.

5. Conclusions

In this paper, an synchronization method was proposed for a class of FONNs subject to backlash-like hysteresis by means of adaptive fuzzy control. We showed that fuzzy logic systems can be employed to estimate nonlinear functions in fractional-order nonlinear systems. Based on the fractional stability theorems, an adaptive fuzzy synchronization controller, which can guarantee the synchronization error tends to an arbitrary small region of zero, was constructed. How to combine the proposed method with other control method, such as fractional-order sliding mode control, is one of our future research directions.

Data Availability

The data used to support the findings of this study are available from the corresponding author upon request.

Conflicts of Interest

The authors do not have a direct financial relation with any commercial identity mentioned in their paper that might lead to conflicts of interest for any of the authors.

Acknowledgments

This work is supported by the National Natural Science Foundation of China under Grant 11771263 and the Natural Science Foundation of Anhui Province of China under Grant 1808085MF181.

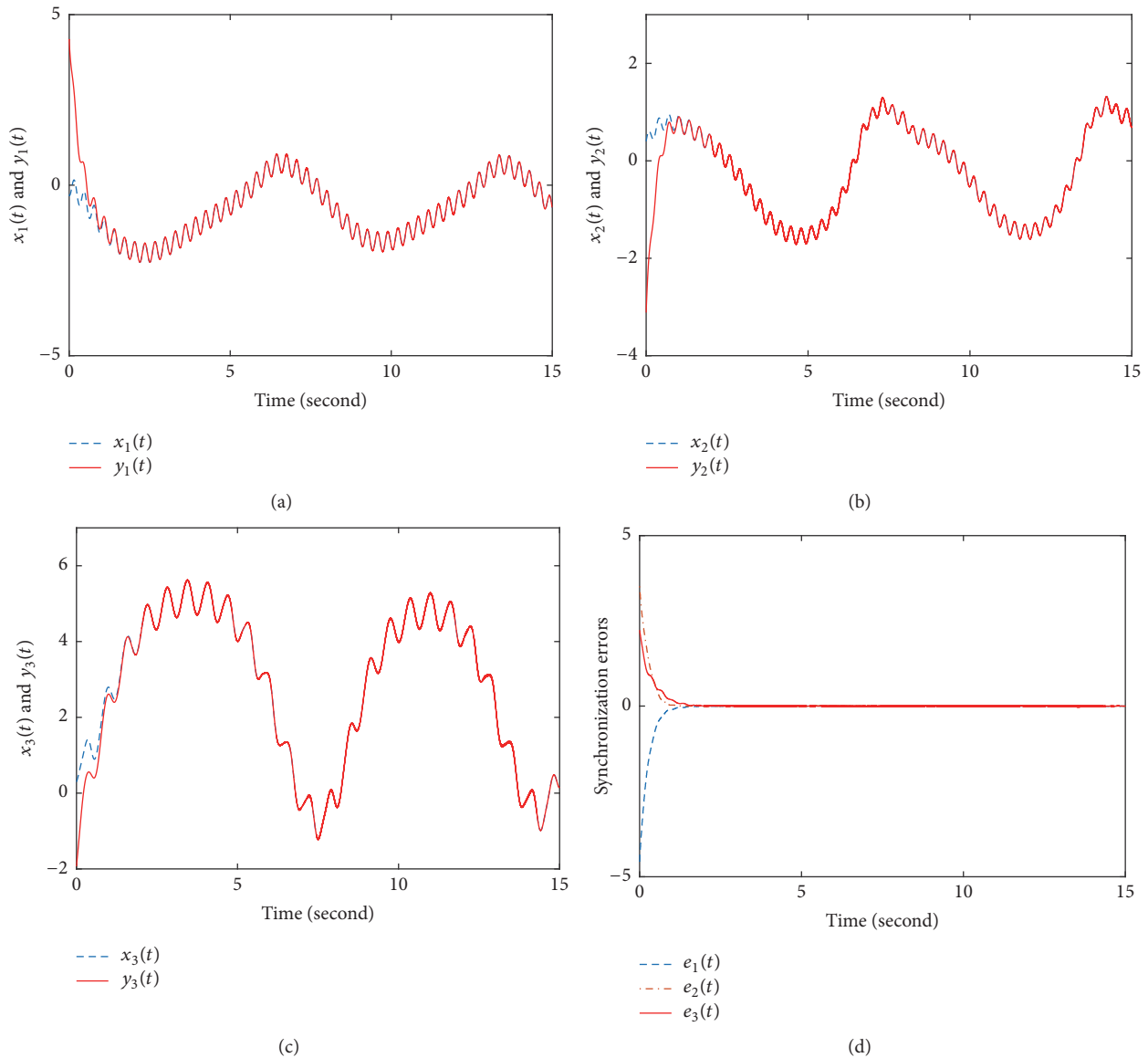


FIGURE 8: Simulation results when $\xi(t) = -[2 \sin(10t) + 15\text{rand}(t); 2 \cos(10t) + 20\text{rand}(t); 2 \sin(5t) + 18\text{rand}(t)]^T$ in (a) $x_1(t)$ and $y_1(t)$; (b) $x_2(t)$ and $y_2(t)$; (c) $x_3(t)$ and $y_3(t)$; (d) synchronization errors.

References

[1] I. Podlubny, *Fractional Differential Equations*, vol. 198 of *Mathematics in Science and Engineering*, Academic Press, San Diego, Calif, USA, 1999.

[2] Y. Li, Y. Chen, and I. Podlubny, "Mittag-Leffler stability of fractional order nonlinear dynamic systems," *Automatica*, vol. 45, no. 8, pp. 1965–1969, 2009.

[3] H. Liu, S. Li, Y. Sun, and H. Wang, "Adaptive fuzzy synchronization for uncertain fractional-order chaotic systems with unknown non-symmetrical control gain," *Acta Physica Sinica*, vol. 64, no. 7, Article ID 070503, 2015.

[4] N. Aguila-Camacho, M. A. Duarte-Mermoud, and J. A. Gallego, "Lyapunov functions for fractional order systems," *Communications in Nonlinear Science and Numerical Simulation*, vol. 19, no. 9, pp. 2951–2957, 2014.

[5] H. Liu, S. Li, H. Wang, Y. Huo, and J. Luo, "Adaptive synchronization for a class of uncertain fractional-order neural networks," *Entropy. An International and Interdisciplinary Journal of Entropy and Information Studies*, vol. 17, no. 10, pp. 7185–7200, 2015.

[6] Y. Wu and H. Lv, "Adaptive neural network backstepping control for a class of uncertain fractional-order chaotic systems with unknown backlash-like hysteresis," *AIP Advances*, vol. 6, no. 8, Article ID 085121, 2016.

[7] K. Nakkeeran, "Mathematical description of differential equation solving electrical circuits," *Journal of Circuits, Systems and Computers*, vol. 18, no. 5, pp. 985–991, 2009.

[8] H. Liu, S. Li, J. D. Cao, A. G. Alsaedi, and F. E. Alsaedi, "Adaptive fuzzy prescribed performance controller design for a class of uncertain fractional-order nonlinear systems with external disturbances," *Neurocomputing*, vol. 219, pp. 422–430, 2017.

- [9] C. Volos, V.-T. Pham, E. Zambrano-Serrano, J. M. Munoz-Pacheco, S. Vaidyanathan, and E. Tlelo-Cuautle, "Analysis of a 4-D hyperchaotic fractional-order memristive system with hidden attractors," in *Advances in Memristors, Memristive Devices and Systems*, vol. 701, pp. 207–235, Springer, 2017.
- [10] Z.-Y. Sun, P. G. Kevrekidis, X. Yu, and K. Nakkeeran, "Theoretical and computational advances in nonlinear dynamical systems," *Advances in Mathematical Physics*, Article ID 3925964, Art. ID 3925964, 3 pages, 2017.
- [11] I. Petráš, "A note on the fractional-order cellular neural networks," in *Proceedings of the International Joint Conference on Neural Networks (IJCNN '06)*, pp. 1021–1024, can, July 2006.
- [12] I. Stamova, "Global Mittag-Leffler stability and synchronization of impulsive fractional-order neural networks with time-varying delays," *Nonlinear Dynamics*, vol. 77, no. 4, pp. 1251–1260, 2014.
- [13] H.-B. Bao and J.-D. Cao, "Projective synchronization of fractional-order memristor-based neural networks," *Neural Networks*, vol. 63, pp. 1–9, 2015.
- [14] L. P. Chen, R. C. Wu, J. Cao, and J.-B. Liu, "Stability and synchronization of memristor-based fractional-order delayed neural networks," *Neural Networks*, vol. 71, pp. 37–44, 2015.
- [15] R. Rakkiyappan, R. Sivarajan, G. Velmurugan, and J. Cao, "Analysis of global $O(t^{-\alpha})$ stability and global asymptotical periodicity for a class of fractional-order complex-valued neural networks with time varying delays," *Neural Networks*, vol. 77, pp. 51–69, 2016.
- [16] G. Velmurugan and R. Rakkiyappan, "Hybrid projective synchronization of fractional-order memristor-based neural networks with time delays," *Nonlinear Dynamics*, vol. 83, no. 1-2, pp. 419–432, 2016.
- [17] H. Liu, Y. Pan, S. Li, and Y. Chen, "Synchronization for fractional-order neural networks with full/under-actuation using fractional-order sliding mode control," *International Journal of Machine Learning & Cybernetics*, pp. 1–14, 2017.
- [18] H. Liu, S. Li, H. Wang, and Y. Sun, "Adaptive fuzzy control for a class of unknown fractional-order neural networks subject to input nonlinearities and dead-zones," *Information Sciences*, vol. 454-455, pp. 30–45, 2018.
- [19] R. Wu, Y. Lu, and L. Chen, "Finite-time stability of fractional delayed neural networks," *Neurocomputing*, vol. 149, pp. 700–707, 2015.
- [20] G. Velmurugan, R. Rakkiyappan, V. Vembarasan, J. Cao, and A. Alsaedi, "Dissipativity and stability analysis of fractional-order complex-valued neural networks with time delay," *Neural Networks*, vol. 86, pp. 42–53, 2017.
- [21] A. Wu, L. Liu, T. Huang, and Z. Zeng, "Mittag-Leffler stability of fractional-order neural networks in the presence of generalized piecewise constant arguments," *Neural Networks*, vol. 85, pp. 118–127, 2017.
- [22] E. Kaslik and I. R. Rădulescu, "Dynamics of complex-valued fractional-order neural networks," *Neural Networks*, vol. 89, pp. 39–49, 2017.
- [23] X. Zhang and Y. Lin, "An adaptive output feedback dynamic surface control for a class of nonlinear systems with unknown backlash-like hysteresis," *Asian Journal of Control*, vol. 15, no. 2, pp. 489–500, 2013.
- [24] H. Wang, B. Chen, K. Liu, X. Liu, and C. Lin, "Adaptive neural tracking control for a class of nonstrict-feedback stochastic nonlinear systems with unknown backlash-like hysteresis," *IEEE Transactions on Neural Networks and Learning Systems*, vol. 25, no. 5, pp. 947–958, 2014.
- [25] K. Chen, J. Wang, Y. Zhang, and Z. Liu, "Adaptive consensus of nonlinear multi-agent systems with unknown backlash-like hysteresis," *Neurocomputing*, vol. 175, pp. 698–703, 2015.
- [26] L. Liu, Z. Wang, and H. Zhang, "Adaptive dynamic surface error constrained control for MIMO systems with backlash-like hysteresis via prediction error technique," *Nonlinear Dynamics*, vol. 84, no. 4, pp. 1989–2002, 2016.
- [27] J. Zhou, C. Wen, and T. Li, "Adaptive output feedback control of uncertain nonlinear systems with hysteresis nonlinearity," *Institute of Electrical and Electronics Engineers Transactions on Automatic Control*, vol. 57, no. 10, pp. 2627–2633, 2012.
- [28] S. Liu, C.-Y. Su, and Z. Li, "Robust adaptive inverse control of a class of nonlinear systems with Prandtl-Ishlinskii hysteresis model," *Institute of Electrical and Electronics Engineers Transactions on Automatic Control*, vol. 59, no. 8, pp. 2170–2175, 2014.
- [29] R. Dong, Y. Tan, and K. Janschek, "Nonsmooth Predictive Control for Wiener Systems with Backlash-Like Hysteresis," *IEEE/ASME Transactions on Mechatronics*, vol. 21, no. 1, pp. 17–28, 2016.
- [30] L. Bai, Q. Zhou, L. Wang, Z. Yu, and H. Li, "Observer-based adaptive control for stochastic nonstrict-feedback systems with unknown backlash-like hysteresis," *International Journal of Adaptive Control and Signal Processing*, vol. 31, no. 10, pp. 1481–1490, 2017.
- [31] G. Cui, S. Xu, B. Zhang, J. Lu, Z. Li, and Z. Zhang, "Adaptive tracking control for uncertain switched stochastic nonlinear pure-feedback systems with unknown backlash-like hysteresis," *Journal of The Franklin Institute*, vol. 354, no. 4, pp. 1801–1818, 2017.
- [32] H. A. Yousef, M. Hamdy, and K. Nashed, "Adaptive fuzzy controller for a class of nonlinear systems with unknown backlash-like hysteresis," *International Journal of Systems Science*, pp. 1–12, 2017.
- [33] H. Wang, P. X. Liu, and S. Liu, "Adaptive neural synchronization control for bilateral teleoperation systems with time delay and backlash-like hysteresis," *IEEE Transactions on Cybernetics*, 2017.
- [34] A. Boulkroune, A. Bouzeriba, T. Bouden, and A. T. Azar, "Fuzzy adaptive synchronization of uncertain fractional-order chaotic systems," in *Advances in chaos theory and intelligent control*, vol. 337, pp. 681–697, Springer, 2016.
- [35] Y. Li, S. Sui, and S. Tong, "Adaptive fuzzy control design for stochastic nonlinear switched systems with arbitrary switchings and unmodeled dynamics," *IEEE Transactions on Cybernetics*, vol. 47, no. 2, pp. 403–414, 2017.
- [36] S. Yin, P. Shi, and H. Yang, "Adaptive fuzzy control of strict-feedback nonlinear time-delay systems with unmodeled dynamics," *IEEE Transactions on Cybernetics*, vol. 46, no. 8, pp. 1926–1938, 2016.
- [37] H. Li, L. Wang, and H. Du, "Adaptive fuzzy backstepping tracking control for strict-feedback systems with input delay," *IEEE Transactions on Fuzzy Systems*, vol. 25, no. 3, pp. 642–652, 2017.
- [38] H. Li, J. Wang, and P. Shi, "Output-feedback based sliding mode control for fuzzy systems with actuator saturation," *IEEE Transactions on Fuzzy Systems*, vol. 24, no. 6, pp. 1282–1293, 2016.
- [39] X. Ma, J. Zhan, M. I. Ali, and N. Mehmood, "A survey of decision making methods based on two classes of hybrid soft set models," *Artificial Intelligence Review*, vol. 49, no. 4, pp. 511–529, 2018.
- [40] Y.-J. Liu and S. Tong, "Barrier Lyapunov functions-based adaptive control for a class of nonlinear pure-feedback systems with full state constraints," *Automatica*, vol. 64, pp. 70–75, 2016.

- [41] Y. Pan and H. Yu, "Composite learning from adaptive dynamic surface control," *Institute of Electrical and Electronics Engineers Transactions on Automatic Control*, vol. 61, no. 9, pp. 2603–2609, 2016.
- [42] Y. Pan, Y. Liu, B. Xu, and H. Yu, "Hybrid feedback feedforward: An efficient design of adaptive neural network control," *Neural Networks*, vol. 76, pp. 122–134, 2016.
- [43] Y. Liu, C. Li, T. Huang, and X. Wang, "Robust adaptive lag synchronization of uncertain fuzzy memristive neural networks with time-varying delays," *Neurocomputing*, vol. 190, pp. 188–196, 2016.
- [44] S. Wen, Z. Zeng, T. Huang, and Y. Zhang, "Exponential adaptive lag synchronization of memristive neural networks via fuzzy method and applications in pseudo random number generators," *IEEE Transactions on Fuzzy Systems*, vol. 22, no. 6, pp. 1704–1713, 2014.
- [45] J. Zhan and J. C. R. Alcantud, "A novel type of soft rough covering and its application to multicriteria group decision making," *Artificial Intelligence Review*, pp. 1–30, 2018.
- [46] H. Liu, Y. Pan, S. Li, and Y. Chen, "Adaptive Fuzzy Backstepping Control of Fractional-Order Nonlinear Systems," *IEEE Transactions on Systems, Man, and Cybernetics: Systems*, vol. 47, no. 8, pp. 2209–2217, 2017.
- [47] Y. Pan and H. Yu, "Biomimetic hybrid feedback feedforward neural-network learning control," *IEEE Transactions on Neural Networks and Learning Systems*, vol. 28, no. 6, pp. 1481–1487, 2017.
- [48] Y. Pan, M. J. Er, D. Huang, and Q. Wang, "Adaptive fuzzy control with guaranteed convergence of optimal approximation error," *IEEE Transactions on Fuzzy Systems*, vol. 19, no. 5, pp. 807–818, 2011.
- [49] H. Liu, S. Li, G. Li, and H. Wang, "Adaptive controller design for a class of uncertain fractional-order nonlinear systems: an adaptive fuzzy approach," *International Journal of Fuzzy Systems*, vol. 20, no. 2, pp. 366–379, 2018.
- [50] H. Liu, Y. Chen, G. Li, W. Xiang, and G. Xu, "Adaptive fuzzy synchronization of fractional-order chaotic (hyperchaotic) systems with input saturation and unknown parameters," *Complexity*, vol. 2017, 16 pages, 2017.
- [51] F. Zhong, H. Li, and S. Zhong, "State estimation based on fractional order sliding mode observer method for a class of uncertain fractional-order nonlinear systems," *Signal Processing*, vol. 127, pp. 168–184, 2016.

Research Article

Motion of a Spot in a Reaction Diffusion System under the Influence of Chemotaxis

Satoshi Kawaguchi 

Department of Complex and Intelligent Systems, School of Systems Information Science, Future University Hakodate,
Hakodate 041-8655, Japan

Correspondence should be addressed to Satoshi Kawaguchi; satoshi@fun.ac.jp

Received 7 December 2017; Accepted 29 March 2018; Published 21 May 2018

Academic Editor: Christos Volos

Copyright © 2018 Satoshi Kawaguchi. This is an open access article distributed under the Creative Commons Attribution License, which permits unrestricted use, distribution, and reproduction in any medium, provided the original work is properly cited.

We consider the motion of a spot under the influence of chemotaxis. We propose a two-component reaction diffusion system with a global coupling term and a Keller-Segel type chemotaxis term. For the system, we derive the equation of motion of the spot and the time evolution equation of the tensors. We show the existence of an upper limit for the velocity and a critical intensity for the chemotaxis, over which there is no circular motion. The chemotaxis suppresses the range of velocity for the circular motion. This braking effect on velocity originates from the refractory period behind the rear interface of the spot and the negative chemotactic velocity. The physical interpretation of the results and its plausibility are discussed.

1. Introduction

The behaviors of artificial and biological microswimmers such as oil droplets, bimetallic nanorods, catalytic Janus colloids, liposomes, flagellated bacteria, and *Volvox* have attracted widespread attention [1]. Under certain circumstances, some of these microswimmers are self-propelled particles, the mobility mechanism of which has been intensively studied [2, 3]. The motion of oil droplets, especially, has been studied in well-controlled experimental facilities with sufficient reproducibility. Although symmetric droplets cannot move in the absence of external force, the Marangoni effect can cause motion in the presence of an inhomogeneous chemical substance outside the droplet or a temperature gradient along the surface [4–6]. Numerical simulations and theoretical results support this mechanism and the existence of straight, circular, and complicated motions of droplets [7, 8], and experimental results qualitatively agree with the numerical results [9–12]. Droplet motion has also been the subject of a review article [13, 14].

In a two-dimensional reaction diffusion (RD) system, the droplet is often referred to as a spot solution. In order to

systematically describe the motion of spots in an RD system, the time evolution equation of the spot was derived and the mechanism of elastic collision of moving spots was clarified in a previous study [15]. This study was extended by studies on the drift and rotation bifurcations of spot solutions in RD systems [16, 17]. In order to describe the deformations of the spot, tensors were introduced. The bifurcation diagram of the spot suggested that, with increasing velocity of the spot, rotation bifurcation occurred causing the straight motion to become destabilized into circular motion.

In addition to the Marangoni effect, which plays an important role in the motion of oil droplets, chemotaxis is an important property of cell migration; it is important in mass transfer and immunological response in biology. In inflammatory response, the neutrophils among blood cells have a remarkable migration potency (chemotaxis) and can change their form by generating pseudopods toward the antigen. In biophylaxis, several chemokines (chemoattractants) are released from the macrophages and mast cells. Then other immunocompetent cells (neutrophils) respond to the gradient of the chemoattractant. Consequently, the immunocompetent cells move unidirectionally to the source point of the antigen [18].

The mathematical model for chemotaxis was first proposed by Keller and Segel [19], wherein the gradient of the chemoattractant was taken into consideration for the flow of amoeba. Neutrophil migration was considered with a Keller-Segel type chemotaxis term in [20, 21]. In these studies, the Cahn-Hilliard (CH) equation was employed, and the kinematic properties and morphological changes of the crawling cell distribution were shown. In addition to the chemotaxis of the neutrophil, cancer cell invasion under haptotaxis was modeled by the CH equation [22, 23]. The haptotactic response of cancer cells is described by the gradient of the haptoattractant. However, in the above studies, the gradients of chemoattractant and haptoattractant are assumed to be constant; there is no feedback between the cells and these chemical substances.

As described above, with the recent increase in importance of chemotaxis in biology, medicine, and cytoengineering [24–27], many experimental and theoretical studies have been performed. Although there are model systems for the cell density and concentration of chemotactic substances, no mathematical analysis has been reported on the motion of the cell. Inspired by these points, we first propose an RD system including a naive Keller-Segel type chemotaxis term. The system is autonomous, the spot secretes a chemotactic substance, and the motion of the spot is influenced by it. For the proposed RD system, we apply the method reported in [16] to derive the equation of motion of the spot and time evolution equation of the tensors. Based on these equations, we study the bifurcation from straight motion to circular motion as well as the upper limit of the velocity of circular motion. In order to verify the theoretical result, we perform numerical simulations for the tensor model. The physical meaning and validity of the results are discussed.

2. Model Equation

We first consider the following three-component RD system with an activator u , a chemotactic substance v , and an inhibitor w :

$$\tau\epsilon \frac{\partial u}{\partial t} = \epsilon^2 \nabla^2 u - \epsilon \nabla \cdot (u \nabla \chi(v)) \quad (1)$$

$$+ H(u - p(w)) - u - v,$$

$$\frac{\partial v}{\partial t} = \nabla^2 v + u - \mu v, \quad (2)$$

$$T \frac{\partial w}{\partial t} = D \nabla^2 w + u + v - w - W, \quad (3)$$

where $p(w) = p_0 + \alpha w$, $p_0, \alpha, \tau, \epsilon, \mu, T, D$, and W are positive constants, and $H(z)$ is a step function satisfying $H = 0$ for $z < 0$ and $H = 1$ for $z > 0$. Throughout this study, we consider the system in a two-dimensional space, with $\nabla = (\partial_x, \partial_y)$ and $\epsilon \ll 1$. We choose μ such that the system is monostable. Here, we fix $\mu = 0.3$. In the above excitable system, there are two stationary states: a rest state and an excited state. The rest state is $(u, v, w) = (0, 0, -W)$, and the excited state has spatially nonuniform values of u, v , and w . Between the

rest and excited states, there appear boundary layers with thickness $O(\epsilon)$, connecting the two different states.

When the second term on the right hand side of (1) is absent, (1)–(3) describe an RD system with one activator and two inhibitors, which was studied in [28]. In that system, when τ is large, the localized domain (motionless spot solution) of an activator appears. With decreasing τ , the motionless spot is destabilized through static bifurcation or oscillatory bifurcation; however, when T is small and D and α are large, these bifurcations are suppressed by w . When τ is small, the motionless spot is primarily destabilized through translational bifurcation, causing the spot to move.

In the presence of the second term on the right hand side of (1), the moving spot is influenced by the chemotaxis. A system similar to that described by (1)–(3), but with bistability, was studied in [29]. In that system, the nonlinear term in (1) was replaced by $H(u - p(w)) - u$, and a front solution was obtained. Furthermore, maze patterns and branching from a front solution were observed. The stability analyses of the spot and front solutions were conducted by applying the singular perturbation method [30].

The time evolution equation for u is obtained using the conservation equation. The diffusion term is derived from $-\nabla \cdot \mathbf{J}$, where the flux \mathbf{J} is the sum of the normal diffusion (random motility) term \mathbf{J}_d and the chemotaxis term \mathbf{J}_c . That is, $\mathbf{J} = \mathbf{J}_d + \mathbf{J}_c$, where $\mathbf{J}_d = -\epsilon^2 \nabla u$ and $\mathbf{J}_c = \epsilon u \nabla \chi(v)$. It should be noted that the signs of these fluxes are different. The sign of \mathbf{J}_c suggests that the chemotaxis term provides a negative diffusion effect, which suppresses the expansion of u . The second term on the right hand side of (1) is the Keller-Segel type chemotaxis term; we express the chemotactic sensitivity function χ as $\chi(v) = k_c \chi_0(v)$, where $\chi_0(v) = f_0 \theta v^2 / (v^2 + \theta^2)$ with $\theta = 1.0$. In order to satisfy the condition $\max |d\chi_0/dv| = 1$, we choose $f_0 = 8\sqrt{3}/9$. We call k_c the intensity of chemotaxis [31].

In (3), T and D represent the relaxation time and diffusion constant of w , respectively. Let us consider a situation in which w plays the role of feedback to suppress the static bifurcation and oscillatory bifurcation. For the rapid feedback mechanism, T and D must be small and large, respectively. In the limits $T \rightarrow 0$ and $D \rightarrow \infty$, w becomes a time-dependent but spatially independent variable, which is denoted by $\langle w(t) \rangle$:

$$\langle w(t) \rangle = \frac{1}{\Omega_0} \int d\mathbf{r} w = \frac{1}{\Omega_0} \int d\mathbf{r} (u + v) - W, \quad (4)$$

where Ω_0 is the area of the entire system. Replacing w in $p(w)$ by $\langle w(t) \rangle$, $p(w)$ becomes a global coupling term. In the case where T is very small and D is very large, we reduce the three-component RD system to the following two-component RD system with a global coupling term:

$$\tau\epsilon \frac{\partial u}{\partial t} = \epsilon^2 \nabla^2 u - \epsilon \nabla \cdot (u \nabla \chi(v)) + f\{u, v\} - v, \quad (5)$$

$$\frac{\partial v}{\partial t} = \nabla^2 v + u - \mu v, \quad (6)$$

where

$$f\{u, v\} = -u + H(u - p\{u, v\}). \quad (7)$$

The functional $p\{u, v\}$ represents a global coupling term given by

$$p\{u, v\} = p_0 + \alpha \left[\int d\mathbf{r} (u + v) - W \right], \quad (8)$$

where the integral is over the entire domain, and α and W are rescaled to absorb Ω_0 : $\alpha' = \alpha/\Omega_0$ and $W' = W\Omega_0$, and the primes are dropped. α corresponds to the intensity of the global coupling, and the value of p_0 is chosen as $p_0 = 0.275$. Hereinafter, we consider the above two-component RD system to be described by (5) and (6).

In the absence of chemotaxis, (5) and (6) describe the same system proposed by Krischer and Mikhailov [32]. This system had an activator and an inhibitor, and, for large τ , the motionless spot (localized particle-like structure) in two dimensions was stable. With decreasing τ under a large α , it was shown that the system had a stable moving spot. In order to understand intuitively the bifurcation from the motionless spot to the moving spot, we consider the limit $\epsilon \rightarrow 0$. In the limit $\epsilon \rightarrow 0$, the boundary layer of u becomes an interface, as shown in Figure 1. The location of the interface is defined by the condition $u(\mathbf{r}, t) = p$. In this limit, u and v satisfy the relation $(u + v) = 1$ (inside the domain) and 0 (outside the domain), which is obtained from (5). In the limits of $\alpha \rightarrow \infty$ and $\epsilon \rightarrow 0$, the area of the spot is conserved; using (8), we obtain

$$\int d\mathbf{r} (u + v) = W. \quad (9)$$

This restriction prohibits the expansion and oscillation of the spot; the translational bifurcation firstly occurs with decreasing τ . Even for finite values of a large α and small ϵ , the area of the spot is approximately conserved by the feedback mechanism. This supports the existence of a moving spot for small τ with large α . In contrast, for small α , the static bifurcation or oscillatory bifurcation firstly occurs with decreasing τ , and the motionless spot is destabilized to form an expanding wave or is disintegrated by unstable oscillation.

Although the bifurcation from a motionless spot to a straight moving spot and the collision of two moving spots were studied in [32], other types of moving spot were not studied. Recently, the bifurcation of the spot from straight motion to circular motion was theoretically analyzed for the system described by (5) and (6) without the chemotaxis term [16]. The result suggested that there was a critical value τ_c for the bifurcation of stationary straight motion. Although the straight motion was stable for $\tau > \tau_c$, it was destabilized by rotation (straight-circular-motion) bifurcation for $\tau \leq \tau_c$. In other words, the straight motion was destabilized into circular motion with increasing velocity.

In this study, we assume that the localized domain (spot) of an activator exists under global feedback in the system described by (5) and (6). In the system, the chemotactic substance is secreted from inside the spot, and the motion of the spot is influenced by the chemotaxis. In order to study the

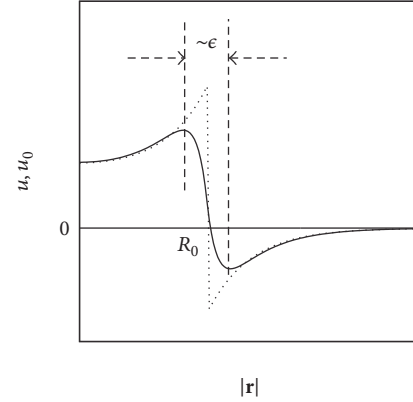


FIGURE 1: Boundary layer and interface. The solid and dotted curves correspond to $u(\mathbf{r}, t)$ and $u_0(\mathbf{r}, t) = \lim_{\epsilon \rightarrow 0} u(\mathbf{r}, t)$ along a radial direction, respectively, that is, $u(|\mathbf{r}|, t)$ and $u_0(|\mathbf{r}|, t)$. In the finite ϵ , $u(|\mathbf{r}|, t)$ has a boundary layer around $|\mathbf{r}| \sim R_0$ with the thickness of ϵ , where R_0 is determined by the condition $u(|\mathbf{r}| = R_0) = p$. $u_0(|\mathbf{r}|, t)$ does not have a boundary layer but has a sharp interface at $|\mathbf{r}| = R_0$.

influence of chemotaxis on the motion of a spot, we apply the technique reported in [16] to the system described by (5) and (6). For this purpose, we first derive the radially symmetric equilibrium solution of (5) and (6) in the limit $\epsilon \rightarrow 0$. In this limit, (6) becomes

$$\frac{\partial v}{\partial t} = \nabla^2 v + H(u - p) - \beta v, \quad (10)$$

where $\beta = 1 + \mu$. Setting $\partial v / \partial t = 0$ in (10), (10) becomes

$$\left(\frac{d^2}{dr^2} + \frac{1}{r} \frac{d}{dr} \right) v - \beta v + H(R_0 - r) = 0, \quad (11)$$

where $r = |\mathbf{r}|$ and R_0 is the equilibrium radius of the symmetric spot. We impose the boundary conditions on $v(r)$ as

$$\begin{aligned} \frac{dv(0)}{dr} &= 0, \\ v(R_0+) &= v(R_0-), \\ \frac{dv(R_0+)}{dr} &= \frac{dv(R_0-)}{dr}, \\ v(\infty) &= 0. \end{aligned} \quad (12)$$

The radially symmetric equilibrium solution of (10) in two dimensions is given by

$$\begin{aligned} \bar{v}(r) &= \begin{cases} \frac{1}{\beta} - \frac{R_0}{\sqrt{\beta}} K_1(\sqrt{\beta} R_0) I_0(\sqrt{\beta} r), & 0 < r < R_0, \\ \frac{R_0}{\sqrt{\beta}} I_1(\sqrt{\beta} R_0) K_0(\sqrt{\beta} r), & R_0 < r < \infty, \end{cases} \end{aligned} \quad (13)$$

where I_n and K_n are the modified Bessel functions of the first and second kinds of order n , respectively. The corresponding

solution of $u(r)$ is given by $\bar{u}(r) = H(R_0 - r) - \bar{v}(r)$. The above equilibrium solution is employed to study the motion of the spot in the following sections.

3. Equation of Motion of the Interface

As ϵ is small, the width of the boundary layer is small, and, therefore, the value of u changes sharply while that of v changes smoothly around the boundary layer. The velocity of the flat interface is a function of the value of v on the interface. In order to consider the dynamics of the spot in the system, we derive the equation of motion of the interface. The time evolution equation of the interface is described [16, 30, 33] by

$$\tau V = \tau C(h) + \epsilon \kappa + L, \quad (14)$$

where $C(h)$ is the velocity of a flat interface; κ is the curvature of the interface, the sign of which is chosen such that it is positive when the center of the curvature is outside of the excited domain; and h is the value of v on the interface. V is the normal component of the velocity, and L is the Lagrange multiplier for the constraint of domain area conservation (9). For the moving spot, this condition corresponds to

$$\int d\omega V(\omega) = 0, \quad (15)$$

where $d\omega$ is the infinitesimal length of the interface and the integral is carried over the entire interface.

We first consider the velocity of the interface in one dimension in (5) and (6). With the detailed derivations given in Appendix A, the velocity $\tau C(h)$ is obtained as

$$\begin{aligned} \tau C(h) = & \frac{2(1/2 - h - p)}{[(h + p)(1 - h - p)]^{1/2}} \\ & + \left(\frac{d\chi}{dv} \right) \Big|_i \left(\frac{dv}{dx} \right) \Big|_i, \end{aligned} \quad (16)$$

where p is a global coupling term (8). $\tau C(h)$ consists of two components: the velocity of the traveling front solution in one dimension and the chemotactic velocity.

In two dimensions, the velocity of a flat interface directed along \mathbf{n} is given by

$$\begin{aligned} \tau C(h) = & \frac{2(1/2 - h - p)}{[(h + p)(1 - h - p)]^{1/2}} + k_c \chi'_0(v) \left(\frac{dv}{d\mathbf{n}} \right) \Big|_i \\ \equiv & P(h) + Q(h) (\mathbf{n} \cdot \nabla) v|_i, \end{aligned} \quad (17)$$

where $\chi'_0(v) = d\chi_0(v)/dv$ and $A|_i$ represents the value of function A evaluated on the interface. \mathbf{n} is a unit normal vector on the interface, and $(dv/d\mathbf{n})$ is a normal derivative.

When the motion of the interface of the spot is slow compared with the relaxation rate of the chemotactic substance, the left hand side of (10), $(\partial v/\partial t)$, is small. In this case, we deal with the time derivative of v in (10) as a perturbation.

The asymptotic solution of (10) is written by perturbation expansion using the Green function G as

$$\begin{aligned} v(\mathbf{r}, t) = & GH - GG \frac{\partial H}{\partial t} + GGG \frac{\partial^2 H}{\partial t^2} - GGGG \frac{\partial^3 H}{\partial t^3} \\ & + \dots, \end{aligned} \quad (18)$$

where G is Green's function satisfying the equation

$$(\nabla^2 - \beta) G(\mathbf{r} - \mathbf{r}') = -\delta(\mathbf{r} - \mathbf{r}'). \quad (19)$$

In (18), GH represents the integral

$$GH = \int d\mathbf{r}_1 G(\mathbf{r} - \mathbf{r}_1) H(\mathbf{r}_1, t),$$

$$\begin{aligned} GG \frac{\partial H}{\partial t} = & \int d\mathbf{r}_1 d\mathbf{r}_2 G(\mathbf{r} - \mathbf{r}_1) G(\mathbf{r}_1 - \mathbf{r}_2) \frac{\partial H(\mathbf{r}_2, t)}{\partial t}, \\ \dots = & \dots, \end{aligned} \quad (20)$$

for brevity. In this study, we consider the situation in which the motionless spot is destabilized supercritically and the spot moves with an arbitrarily small velocity. Then, we can safely apply the perturbative expansion of v in terms of G as in (18).

4. Deformed Spot Dynamics

In this section, we derive the equation of motion of the spot. In order to describe the deformations of the spot, tensors are introduced. The tensors depend on time, and the time evolution equation of the tensors are derived following [16].

4.1. Description of Deformed Spot. We firstly describe the position and velocity of a deformed spot. The motion of the spot consists of two components: the motion of the center of gravity and the motion of the interface relative to the center of gravity. The center of gravity is denoted by $\boldsymbol{\rho}$, and the velocity of the center of gravity is given by

$$\frac{d\boldsymbol{\rho}}{dt} = \frac{1}{\Omega} \int d\omega V(\omega) \mathbf{R}(\omega) \equiv \mathbf{v}, \quad (21)$$

where Ω is the area of the spot and $\mathbf{R}(\omega)$ is a position vector measured from the center of gravity. We consider the case that $\mathbf{R}(\omega)$ is a single valued function of ϕ_r , which is given as

$$\mathbf{R}(\omega) = R(\phi_r) \mathbf{e}_r, \quad (22)$$

where \mathbf{e}_r is a radial unit vector and $R(\phi_r)$ is the distance between the center of gravity and a point on the interface, which is directed to an angle ϕ_r with respect to the x axis. Using the definition of $\mathbf{R}(\omega)$, $d\omega$ is given by

$$d\omega = \left| \frac{d\mathbf{R}}{d\phi_r} \right| d\phi_r = \sqrt{R^2 + R'^2} d\phi_r, \quad (23)$$

where $R' = dR(\phi_r)/d\phi_r$. For the deformed spot, the radius is given by

$$R(\phi_r) = R_0 + \delta R(\phi_r, t) \quad (24)$$

with

$$\delta R(\phi_r, t) = \sum_{n=-\infty}^{\infty} c_n(t) e^{in\phi_r}, \quad (25)$$

where $i = \sqrt{-1}$, R_0 is the equilibrium radius of the symmetric spot, and δR corresponds to the deviation. In the expansion of δR , $c_{\pm n}$ corresponds to a $(2\pi/n)$ -periodic deformation. According to the area conservation equation (9), $c_0 = 0$. In addition, we exclude the terms of $n = \pm 1$ because the translational motion of the spot is incorporated in $\boldsymbol{\rho}$. Thus, we set $c_{\pm 1} = 0$. Using (24), the curvature κ and the normal component of the velocity V are given up to the first order of the deviations as

$$\kappa(\phi_r, t) = -\frac{1}{R_0} - \frac{1}{R_0^2} \sum_{n=-\infty}^{\infty} (n^2 - 1) c_n(t) e^{in\phi_r}, \quad (26)$$

$$V(\phi_r, t) = \mathbf{v} \cdot \mathbf{n} + \sum_{n=-\infty}^{\infty} \dot{c}_n(t) e^{in\phi_r}, \quad (27)$$

respectively, where the overdot denotes the time derivative.

For a general function $A(\mathbf{r}, t)$, the Fourier transformation and its reverse transformation in two dimensions are defined as

$$A_{\mathbf{q}}(t) = \int d\mathbf{r} A(\mathbf{r}, t) e^{-i\mathbf{q}\cdot\mathbf{r}}, \quad (28)$$

$$A(\mathbf{r}, t) = \frac{1}{(2\pi)^2} \int d\mathbf{q} A_{\mathbf{q}}(t) e^{i\mathbf{q}\cdot\mathbf{r}} \equiv \int_{\mathbf{q}} A_{\mathbf{q}}(t) e^{i\mathbf{q}\cdot\mathbf{r}}, \quad (29)$$

respectively, where $\int_{\mathbf{q}} = \int d\mathbf{q}/(2\pi)^2$ for brevity. For an isolated domain that forms a single loop without crossing, the step function $H(u-p) = H(R-|\mathbf{r}-\boldsymbol{\rho}|)$ is transformed by the Fourier transformation as

$$H_{\mathbf{q}} = \int d\mathbf{r} H(u-p) e^{-i\mathbf{q}\cdot\mathbf{r}} = \int_{|\mathbf{r}-\boldsymbol{\rho}| < R} d\mathbf{r} e^{-i\mathbf{q}\cdot\mathbf{r}}. \quad (30)$$

Substituting (24) into (30), we obtain the expansion of $H_{\mathbf{q}}$ up to the first order of δR as

$$\begin{aligned} H_{\mathbf{q}} &= H_{\mathbf{q}}^{(0)} + H_{\mathbf{q}}^{(1)}, \\ H_{\mathbf{q}}^{(0)} &= \frac{2\pi R_0}{q} J_1(qR_0), \\ H_{\mathbf{q}}^{(1)} &= 2\pi R_0 \sum_n c_n(t) i^{-n} e^{in\phi_q} J_n(qR_0), \end{aligned} \quad (31)$$

where $q = |\mathbf{q}|$, ϕ_q is the angle between \mathbf{q} and the x -axis, and J_n is a Bessel function of the first kind of order n .

4.2. Equation of Motion of a Spot. We derive the equation of motion of a spot from (14). τC is given as functions of h and \tilde{h} by (17), in which we used the notation $\tilde{h} = (d\mathbf{v}/d\mathbf{n})_i = (\mathbf{n} \cdot \nabla)v|_i$. When the velocity of the spot is small, the deformation of the circle is small. For this situation, we derive the deviations of h and \tilde{h} from their stationary values

as a power series of τC . Using (18), we first expand h and \tilde{h} up to the fourth-order time derivatives as

$$h = h_0 + h_1 + h_2 + h_3 + h_4, \quad (32)$$

$$\tilde{h} = \tilde{h}_0 + \tilde{h}_1 + \tilde{h}_2 + \tilde{h}_3 + \tilde{h}_4, \quad (33)$$

respectively, where

$$\begin{aligned} h_0 &= \int_{\mathbf{q}} G_q H_{\mathbf{q}} e^{i\mathbf{q}\cdot\mathbf{R}(\omega)}, \\ h_1 &= h_{1,1} + h_{1,2} \\ &= i \int_{\mathbf{q}} (\mathbf{v} \cdot \mathbf{q}) G_q^2 H_{\mathbf{q}} e^{i\mathbf{q}\cdot\mathbf{R}(\omega)} - \int_{\mathbf{q}} G_q^2 \left(\frac{\partial H_{\mathbf{q}}}{\partial t} \right) e^{i\mathbf{q}\cdot\mathbf{R}(\omega)}, \\ h_2 &= h_{2,1} + h_{2,2} + h_{2,3} \\ &= -i \int_{\mathbf{q}} (\dot{\mathbf{v}} \cdot \mathbf{q}) G_q^3 H_{\mathbf{q}} e^{i\mathbf{q}\cdot\mathbf{R}(\omega)} \\ &\quad - \int_{\mathbf{q}} (\mathbf{v} \cdot \mathbf{q})^2 G_q^3 H_{\mathbf{q}} e^{i\mathbf{q}\cdot\mathbf{R}(\omega)} \\ &\quad + \int_{\mathbf{q}} G_q^3 \left(\frac{\partial^2 H_{\mathbf{q}}}{\partial t^2} \right) e^{i\mathbf{q}\cdot\mathbf{R}(\omega)}, \\ h_3 &= -i \int_{\mathbf{q}} (\mathbf{v} \cdot \mathbf{q})^3 G_q^4 H_{\mathbf{q}} e^{i\mathbf{q}\cdot\mathbf{R}(\omega)}, \\ h_4 &= \int_{\mathbf{q}} (\mathbf{v} \cdot \mathbf{q})^4 G_q^5 H_{\mathbf{q}} e^{i\mathbf{q}\cdot\mathbf{R}(\omega)}, \\ \tilde{h}_0 &= i \int_{\mathbf{q}} (\mathbf{n} \cdot \mathbf{q}) G_q H_{\mathbf{q}} e^{i\mathbf{q}\cdot\mathbf{R}(\omega)}, \\ \tilde{h}_1 &= \tilde{h}_{1,1} + \tilde{h}_{1,2} \\ &= - \int_{\mathbf{q}} (\mathbf{n} \cdot \mathbf{q}) (\mathbf{v} \cdot \mathbf{q}) G_q^2 H_{\mathbf{q}} e^{i\mathbf{q}\cdot\mathbf{R}(\omega)} \\ &\quad - i \int_{\mathbf{q}} (\mathbf{n} \cdot \mathbf{q}) G_q^2 \left(\frac{\partial H_{\mathbf{q}}}{\partial t} \right) e^{i\mathbf{q}\cdot\mathbf{R}(\omega)}, \\ \tilde{h}_2 &= \tilde{h}_{2,1} + \tilde{h}_{2,2} + \tilde{h}_{2,3} \\ &= \int_{\mathbf{q}} (\mathbf{n} \cdot \mathbf{q}) (\dot{\mathbf{v}} \cdot \mathbf{q}) G_q^3 H_{\mathbf{q}} e^{i\mathbf{q}\cdot\mathbf{R}(\omega)} \\ &\quad - i \int_{\mathbf{q}} (\mathbf{n} \cdot \mathbf{q}) (\mathbf{v} \cdot \mathbf{q})^2 G_q^3 H_{\mathbf{q}} e^{i\mathbf{q}\cdot\mathbf{R}(\omega)} \\ &\quad + i \int_{\mathbf{q}} (\mathbf{n} \cdot \mathbf{q}) G_q^3 \left(\frac{\partial^2 H_{\mathbf{q}}}{\partial t^2} \right) e^{i\mathbf{q}\cdot\mathbf{R}(\omega)}, \\ \tilde{h}_3 &= \int_{\mathbf{q}} (\mathbf{n} \cdot \mathbf{q}) (\mathbf{v} \cdot \mathbf{q})^3 G_q^4 H_{\mathbf{q}} e^{i\mathbf{q}\cdot\mathbf{R}(\omega)}, \\ \tilde{h}_4 &= i \int_{\mathbf{q}} (\mathbf{n} \cdot \mathbf{q}) (\mathbf{v} \cdot \mathbf{q})^4 G_q^5 H_{\mathbf{q}} e^{i\mathbf{q}\cdot\mathbf{R}(\omega)} \end{aligned} \quad (34)$$

(34)

(35)

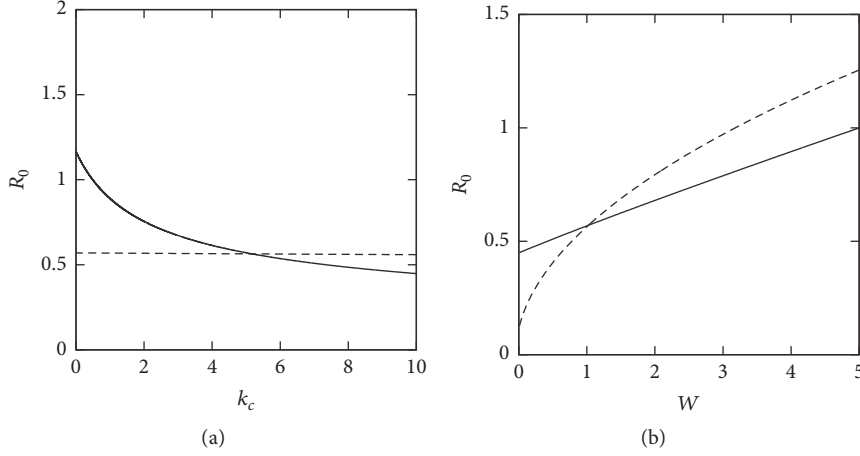


FIGURE 2: Dependence of R_0 on k_c and W in the stationary state. (a) Dependence of R_0 on k_c . $W = 1.0$. The solid and dashed curves represent the cases of $\alpha = 0$ and 5, respectively. (b) Dependence of R_0 on W . $k_c = 5.0$. The solid and dashed curves represent the cases of $\alpha = 0.1$ and 5.0, respectively.

with

$$G_q = \frac{1}{q^2 + \beta}. \quad (36)$$

In the above expansions, we omitted the term proportional to $(\mathbf{q} \cdot \mathbf{v})(\partial H_q / \partial t)$ in the expressions of h_2 and \tilde{h}_2 . In the derivation of h_3 and \tilde{h}_3 , the terms proportional to $(\partial^3 H_q / \partial t^3)$, $(\mathbf{q} \cdot \mathbf{v})(\partial^2 H_q / \partial t^2)$, $(\mathbf{q} \cdot \mathbf{v})^2(\partial H_q / \partial t)$, $(\mathbf{q} \cdot \dot{\mathbf{v}})(\partial H_q / \partial t)$, $(\mathbf{q} \cdot \dot{\mathbf{v}})H_q$, and $(\mathbf{q} \cdot \mathbf{v})(\mathbf{q} \cdot \dot{\mathbf{v}})H_q$ were omitted. In the derivation of h_4 and \tilde{h}_4 , all the terms of the derivatives of \mathbf{v} and H_q with respect to time were omitted. These terms were omitted, because they include higher order derivatives of time and are smaller than the remaining terms, or they vanish in the later integral $(1/\Omega) \int d\omega \mathbf{R}(\omega) \cdot$ due to the orthogonality relation of trigonometric functions. We remark that we include up to the third-order of \mathbf{v} : h_3 and \tilde{h}_3 , for the derivation of the equation of motion of the spot. The justification for considering terms up to this order is discussed later. On the other hand, for the derivation of equations of motion of tensors, we include up to the fourth order of \mathbf{v} : h_4 and \tilde{h}_4 . The justification for considering terms up to this order is discussed in Section 4.4.

When the spot is in a stationary motionless state, we assume that the spot is a circle with radius R_0 . The values of v and $(\mathbf{n} \cdot \nabla)v$ at the interface are denoted as $h_0^{(0)}$ and $\tilde{h}_0^{(0)}$, respectively. Using (34), $h_0^{(0)}$ is given by h_0 with the substitutions $H_q = H_q^{(0)}$ and $\mathbf{R} = \mathbf{R}^{(0)}$, where $\mathbf{R}^{(0)} = R_0 \mathbf{e}_r$. Similarly, $\tilde{h}_0^{(0)}$ is given using (35). When ϵ is small but finite, substituting $h = h_0^{(0)}$ and $\tilde{h} = \tilde{h}_0^{(0)}$ into $\tau C(h)$ with $V = 0$, (14) becomes

$$P(h_0^{(0)}) + Q(h_0^{(0)})\tilde{h}_0^{(0)} - \frac{\epsilon}{R_0} + L = 0, \quad (37)$$

where $\kappa = -1/R_0$ is used. We note that the Lagrange multiplier L in (37) can be absorbed into the constant term p_0 in $P(h_0^{(0)})$. In the limit $\epsilon \rightarrow 0$, we can calculate $h_0^{(0)}$ and

$\tilde{h}_0^{(0)}$ by using $\bar{v}(r)$, which is given by (13) (the validation is given in Appendix B). Using these expressions, (37) gives the dependence of R_0 on k_c and W . The numerical results obtained by using (13) and (17) are shown in Figure 2(a). When $\alpha = 0$, R_0 monotonically decreases with k_c . However, for large α , R_0 depends weakly on k_c and it is almost constant because of the global coupling; large global coupling suppresses variations in the area of the spot resulting in constant R_0 . The dependence of R_0 on W when k_c is large is shown in Figure 2(b). From (9), it can be seen that, for large α , R_0 approximately satisfies $\pi R_0^2 \sim W$, and, therefore, R_0 is proportional to the square root of W (see the dashed curve in Figure 2(b)).

When the spot moves with an infinitesimal velocity, h and \tilde{h} deviate from $h_0^{(0)}$ and $\tilde{h}_0^{(0)}$, respectively. By putting small deviations as $\delta h = h - h_0^{(0)}$ and $\delta \tilde{h} = \tilde{h} - \tilde{h}_0^{(0)}$, we iteratively derive δh and $\delta \tilde{h}$ in a power series of τC up to the third order. The procedure consists of two steps. We first expand τC given by (17) in a power series of δh and $\delta \tilde{h}$. Then, we solve the equation in terms of δh and expand it by τC . When the stationary motionless spot is destabilized into a moving spot, τC is expanded up to the second-order of δh and $\delta \tilde{h}$ as

$$\begin{aligned} \tau C &= \left(\frac{\partial P}{\partial h} + \frac{\partial Q}{\partial h} \tilde{h}_0^{(0)} \right)_0 \delta h + (Q)_0 \delta \tilde{h} \\ &+ \frac{1}{2} \left[\left(\frac{\partial^2 P}{\partial h^2} + \frac{\partial^2 Q}{\partial h^2} \tilde{h}_0^{(0)} \right)_0 \delta h^2 + 2 \left(\frac{\partial Q}{\partial h} \right)_0 \delta h \delta \tilde{h} \right], \end{aligned} \quad (38)$$

where, for a function $A(h)$, $(A)_0$ implies $A(h_0^{(0)})$. Up to the first order of δh and $\delta \tilde{h}$, (38) results in $\tau C = (\partial P / \partial h + \partial Q / \partial h \tilde{h}_0^{(0)})_0 \delta h + (Q)_0 \delta \tilde{h}$. For higher order corrections, a supplementary relation between δh and $\delta \tilde{h}$ is necessary. In order to relate δh with $\delta \tilde{h}$, we consider the profile of $v(\mathbf{r})$ in the radially symmetric function given by (13), where $v(\mathbf{r})$ is

a function of r ($= |\mathbf{r}|$) denoted by $\bar{v}(r)$. For this function, $(\mathbf{n} \cdot \nabla)\bar{v} = d\bar{v}/dr$. Then, $\bar{v}(R_0 + \delta r)$ and $(\mathbf{n} \cdot \nabla)\bar{v}(R_0 + \delta r)$ are expanded around $\bar{v}(R_0)$ and $d\bar{v}(R_0)/dr$ for small δr as

$$\bar{v}(R_0 + \delta r) \sim \bar{v}(R_0) + \left(\frac{d\bar{v}}{dr}\right)_{r=R_0} \delta r, \quad (39)$$

$$(\mathbf{n} \cdot \nabla)\bar{v}(R_0 + \delta r) \sim \frac{d\bar{v}(R_0)}{dr} + \left(\frac{d^2\bar{v}}{dr^2}\right)_{r=R_0} \delta r, \quad (40)$$

respectively. In (39) and (40), $(A(r))_{r=R_0}$ implies $A(R_0)$. We make an ansatz that δh and $\delta\tilde{h}$ are not independent but have a linear relation such that $\delta\tilde{h} = k\delta h$ with $k = (\bar{v}''/\bar{v}')_{r=R_0}$, where the prime corresponds to the derivative with respect to r . This assumption enables us to calculate δh as a function of τC . Substituting $\delta\tilde{h} = k\delta h$ into (38), τC becomes a quadratic equation of δh as

$$\tau C = (a + kb)\delta h + m_1\delta h^2, \quad (41)$$

where

$$a = \left(\frac{\partial P}{\partial h} + \frac{\partial Q}{\partial h}\tilde{h}_0^{(0)}\right)_0, \quad (42)$$

$$b = (Q)_0,$$

$$m_1 = \frac{1}{2} \left[\left(\frac{\partial^2 P}{\partial h^2} + \frac{\partial^2 Q}{\partial h^2}\tilde{h}_0^{(0)} \right)_0 + 2k \left(\frac{\partial Q}{\partial h} \right)_0 \right].$$

As a result of numerical calculations, we remark that $b > 0$ and $a < 0$ for small $h_0^{(0)}$, but $a > 0$ for large $h_0^{(0)}$. By solving (41) in terms of δh for small τC , the solution is expanded up to the second order of τC as

$$\delta h = \left(\frac{\tau C}{a + kb}\right) - \frac{m_1}{a + kb} \left(\frac{\tau C}{a + kb}\right)^2. \quad (43)$$

Here, it should be noted that although there are two solutions for (41), we chose one solution such that $\delta h \rightarrow \tau C/(a + kb)$ when the second-order term $(\tau C)^2$ is neglected.

In order to obtain δh up to the third order of τC , τC given by (17) is expanded up to the third order of δh and $\delta\tilde{h}$. Using $\delta\tilde{h} = k\delta h$, τC becomes a cubic equation of δh as

$$\tau C = (a + kb)\delta h + m_1\delta h^2 + m_2\delta h^3, \quad (44)$$

where m_2 is given by

$$m_2 = \frac{1}{6} \left[\left(\frac{\partial^3 P}{\partial h^3} + \frac{\partial^3 Q}{\partial h^3}\tilde{h}_0^{(0)} \right)_0 + 3k \left(\frac{\partial^2 Q}{\partial h^2} \right)_0 \right]. \quad (45)$$

In order to obtain the third-order term of τC in δh , we add a correction Δ ($\sim O(\tau C)^3$) to δh given by (43) and substitute it into (44). On solving this equation in terms of Δ , δh up to the third order of τC is obtained as

$$\delta h = \left(\frac{\tau C}{a + kb}\right) - \frac{m_1}{a + kb} \left(\frac{\tau C}{a + kb}\right)^2 + \frac{1}{a + kb} \left[\frac{2m_1^2}{a + kb} - m_2 \right] \left(\frac{\tau C}{a + kb}\right)^3. \quad (46)$$

We remark that (46) is obtained by another method; by applying Cardano's formula to (44) and expanding the solution up to the third order of τC , we obtain the same result as that of (46).

In the above process, we iteratively derived δh up to the third order of τC . We replace $k\delta h \sim \delta\tilde{h}$ in (46), and finally the power series expansion of $a\delta h + b\delta\tilde{h}$ in terms of τC is obtained as

$$a\delta h + b\delta\tilde{h} = M_1(\tau C) + M_2(\tau C)^2 + M_3(\tau C)^3, \quad (47)$$

where M_i ($i = 1, 2, 3$) is defined by

$$M_1 = 1, \quad (48)$$

$$M_2 = -\frac{m_1}{(a + bk)^2},$$

$$M_3 = \frac{1}{(a + bk)^3} \left[\frac{2m_1^2}{a + bk} - m_2 \right].$$

In the absence of chemotaxis ($Q = 0$), (47) reproduces the result that was obtained in [16].

Using (14) and (47), we derive the equation of motion of the spot by operating both sides of (47) with $(1/\Omega) \int d\omega \mathbf{R}(\omega)$. For the left hand side, we put

$$\frac{1}{\Omega} \int d\omega \mathbf{R}(\omega) \delta h = \delta \mathbf{h} = \mathbf{h}_1 + \mathbf{h}_2 + \mathbf{h}_3, \quad (49)$$

$$\frac{1}{\Omega} \int d\omega \mathbf{R}(\omega) \delta\tilde{h} = \delta \tilde{\mathbf{h}} = \tilde{\mathbf{h}}_1 + \tilde{\mathbf{h}}_2 + \tilde{\mathbf{h}}_3,$$

where \mathbf{h}_4 and $\tilde{\mathbf{h}}_4$ are neglected because these terms are higher than or equal to $O(\mathbf{v}^4)$. For the calculation of the right hand side of (47), we use (14). The magnitudes of $\epsilon\kappa$ and L were discussed in [16]; L is independent of ϕ_r , and, owing to the periodicity of the function, $\int d\omega \mathbf{R}(\omega)L = \int d\omega \mathbf{R}(\omega)L^3 = \int d\omega \mathbf{R}(\omega)V^2L = 0$. In addition, $L \sim O(\mathbf{v}^2)$, and, therefore, $\int d\omega \mathbf{R}(\omega)VL^3$ can be neglected up to the third order of \mathbf{v} . As the translational motion of the spot is incorporated in $\boldsymbol{\rho}$, we chose $c_{\pm 1} = 0$ in the expansion of $\delta R(\phi_r)$. This results in $\epsilon \int d\omega \mathbf{R}(\omega)\kappa = 0$ up to the first order of the deformation. The terms $\epsilon \int d\omega \mathbf{R}(\omega)\kappa VL^2$ and $\epsilon \int d\omega \mathbf{R}(\omega)\kappa L^2$, and the higher order terms of ϵ were small; therefore, they were neglected. Following the above discussion, we neglect the term $(\epsilon\kappa + L)$ in (14).

By carrying the integral over ϕ_r , the following equation is obtained:

$$a\delta \mathbf{h} + b\delta \tilde{\mathbf{h}} = \tau \mathbf{v} + \frac{3}{4}M_3\tau^3\mathbf{v}|\mathbf{v}|^2, \quad (50)$$

where

$$\delta \mathbf{h} = \mathbf{h}_{1,1} + \mathbf{h}_{2,1} + \mathbf{h}_3, \quad (51)$$

$$\delta \tilde{\mathbf{h}} = \tilde{\mathbf{h}}_{1,1} + \tilde{\mathbf{h}}_{2,1} + \tilde{\mathbf{h}}_3.$$

Here, $\mathbf{h}_{1,1} = (1/\Omega) \int d\omega \mathbf{R}(\omega)h_{1,1}$. The other terms on the right hand side of (51) are defined similarly. In the expansion

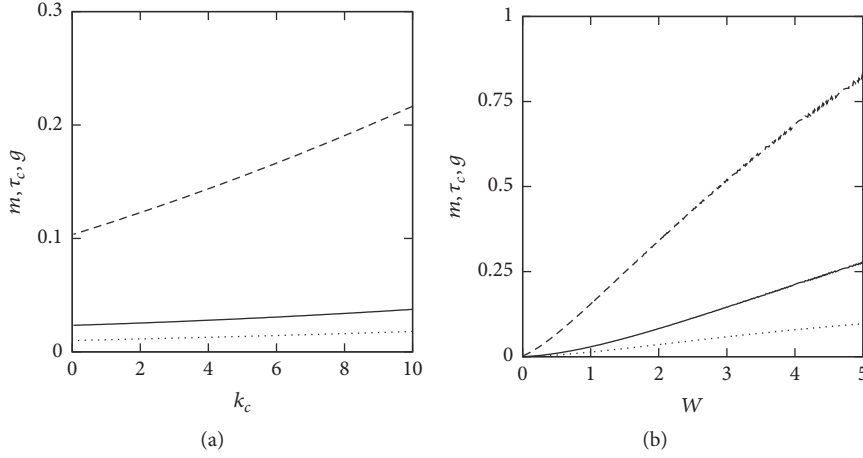


FIGURE 3: Dependence of m , τ_c , and g on k_c and W . The solid, dashed, and dotted curves represent m , τ_c , and g , respectively. (a) Dependence of m , τ_c , and g on k_c . $\alpha = 5.0$ and $W = 1.0$. In the calculation of g , τ is chosen as $\tau = \tau_c$. As M_3 is positive, g for the case $\tau < (>) \tau_c$ is smaller (larger) than this curve. (b) Dependence of m , τ_c , and g on W . $\alpha = 5.0$ and $k_c = 5.0$. In the calculation of g , τ is chosen as $\tau = \tau_c$.

(51), we neglected the terms $\mathbf{h}_{1,2}$ and $\mathbf{h}_{2,3}$, because these terms yielded only the terms $\dot{c}_{\pm 1}$ and $\ddot{c}_{\pm 1}$, respectively; however, these terms are set to zero. $\mathbf{h}_{2,2}$ disappeared in the integral over ϕ_r owing to the orthogonality relation of trigonometric functions [15]. Owing to the same reasons, the terms $\tilde{\mathbf{h}}_{1,2}$, $\tilde{\mathbf{h}}_{2,3}$, and $\tilde{\mathbf{h}}_{2,2}$ did not exist. In the integral over ϕ_r , there is no contribution from the second-order term of τC owing to the orthogonality relation of trigonometric function. This supports the justification to include terms up to the third order of τC in (47) for the minimal equation of motion of a spot. For the balance of order, it is sufficient to include terms up to the third order of \mathbf{v} in $\delta \mathbf{h}$ and $\delta \tilde{\mathbf{h}}$.

After practical calculations of $\delta \mathbf{h}$ and $\delta \tilde{\mathbf{h}}$, we finally obtain the equation of motion of the spot as

$$m\dot{\mathbf{v}} + (\tau - \tau_c)\mathbf{v} + g\mathbf{v}|\mathbf{v}|^2 = a\delta\mathbf{h}_{1,1}^{(0)} + b\delta\tilde{\mathbf{h}}_{1,1}^{(0)}, \quad (52)$$

where $\delta\mathbf{h}_{1,1}^{(0)}$ is defined as $\delta\mathbf{h}_{1,1}^{(0)} = \mathbf{h}_{1,1} - \mathbf{h}_{1,1}^{(0)}$. Here, $\mathbf{h}_{1,1}^{(0)}$ is given by $\mathbf{h}_{1,1}$ with the substitutions $H_{\mathbf{q}} = H_{\mathbf{q}}^{(0)}$ and $\mathbf{R} = \mathbf{R}^{(0)}$. $\delta\tilde{\mathbf{h}}_{1,1}^{(0)}$ is similarly defined with $\delta\mathbf{h}_{1,1}^{(0)}$. The coefficients m , τ_c , and g on the left hand side of (52) are given by

$$m = -aR_0F(1, 3, 1, 1) - bR_0F_d(2, 3, 1, 1), \quad (53)$$

$$\tau_c = -aR_0F(1, 2, 1, 1) - bR_0F_d(2, 2, 1, 1), \quad (54)$$

$$g = \frac{3}{4}M_3\tau^3 - \frac{3}{4}aR_0F(3, 4, 1, 1) - \frac{3}{4}bR_0F_d(4, 4, 1, 1), \quad (55)$$

respectively, where we defined $F(i, j, k, l)$ and $F_d(i, j, k, l)$ as

$$F(i, j, k, l) = \int_0^\infty dq q^i G_q^j J_k J_l, \quad (56)$$

$$F_d(i, j, k, l) = \int_0^\infty dq q^i G_q^j J_k \frac{\partial}{\partial(qR_0)} J_l, \quad (57)$$

respectively, where i, j, k , and l are integers and $J_n(qR_0)$ is written as J_n for brevity.

Equation (52) has the same form as the one in the absence of chemotaxis [16]. It is a Newtonian equation of the spot; the effective mass m , damping coefficient τ_c , intensity of the cubic nonlinear term g , and the right hand side of (52) form the coupling term between deformation and velocity in the following subsection. When $(\tau - \tau_c) > 0$, the motionless spot is stable; however, the motionless spot is destabilized into a moving spot for $(\tau - \tau_c) < 0$. When g is positive, the third-order nonlinear coupling term $g\mathbf{v}|\mathbf{v}|^2$ suppresses the divergence for large $|\mathbf{v}|$. It is necessary that m , τ_c , and g are positive for the existence of a stable moving spot. The dependence of m , τ_c , and g on k_c and W is shown in Figure 3. We see that these parameters are positive and monotonically increase with k_c and W .

In the derivation of (47), we made an ansatz for the relation between δh and $\delta \tilde{h}$ such that $\delta \tilde{h} = k\delta h$ with $k = (\bar{v}''/\bar{v}')_{r=R_0}$. Equation (55) suggests that g depends explicitly on k through M_3 . Through preliminary research, it is found that if k is chosen as a positive constant, the property that g is a positive and monotonically increasing function of k_c and W holds. From the above, it is seen that m , τ_c , and g are positive for any value of k_c and W , and, therefore, we fix W and examine the motion of the spot in the range $k_c \geq 0$.

4.3. Definitions of Tensors. In order to express the deformation of the spot, we introduce tensors. We rewrite the vector form (52) of each component, and, by denoting $\mathbf{v} = (v_1, v_2)$, the α component ($\alpha = 1, 2$) of (52) becomes

$$m\dot{v}_\alpha + (\tau - \tau_c)v_\alpha + g v_\alpha |\mathbf{v}|^2 = a\delta h_{1,1(\alpha)}^{(0)} + b\delta \tilde{h}_{1,1(\alpha)}^{(0)}, \quad (58)$$

where $\delta h_{1,1(\alpha)}^{(0)}$ and $\delta \tilde{h}_{1,1(\alpha)}^{(0)}$ correspond to the α component of $\delta\mathbf{h}_{1,1}^{(0)}$ and $\delta\tilde{\mathbf{h}}_{1,1}^{(0)}$, respectively. Using the tensors, the right hand side of (58) is expressed in a simple form. The second rank tensor \mathbf{S} and the third rank tensor \mathbf{U} represent the elliptical deformation and the head-tail asymmetric deformation

($2\pi/3$ -periodic deformation in the radial direction) of the spot, respectively. These tensors are traceless and symmetric. The detailed definitions are given in [16]. The deformation $\delta R(\phi_r)$ is expanded using the coefficients c_n as given by (25); $c_{\pm n}$ corresponds to a ($2\pi/n$)-periodic deformation.

We first introduce a second-rank tensor $S_{\alpha\beta}$ ($\alpha, \beta = 1, 2$) using $c_{\pm 2}$ as follows:

$$\begin{aligned} S_{11} = -S_{22} = c_2 + c_{-2} &= \frac{\delta_2}{2} \cos 2\phi_2, \\ S_{12} = S_{21} = i(c_2 - c_{-2}) &= \frac{\delta_2}{2} \sin 2\phi_2, \end{aligned} \quad (59)$$

where δ_2 is a positive constant, which represents the radial deviation of the spot from R_0 , and ϕ_2 is the angle between the long axis of the ellipse and the x -axis. The tensor elements (59) are represented by using a normal vector $\mathbf{N} = (\cos \phi_2, \sin \phi_2)$ along the long axis as

$$S_{\alpha\beta} = \delta_2 \left(N_\alpha N_\beta - \frac{\delta_{\alpha\beta}}{2} \mathbf{N}^2 \right). \quad (60)$$

The tensor \mathbf{S} is the same as the nematic order parameter tensor in liquid crystals [34]. For an elliptical spot, $R(\phi_r)$ is represented as

$$R(\phi_r) = R_0 + \frac{\delta_2}{2} \cos 2(\phi_r - \phi_2). \quad (61)$$

Next, in order to describe the head-tail asymmetric deformation, we first define T_1 and T_2 using $c_{\pm 3}$ as

$$T_1 = c_3 + c_{-3} = \delta_3 \cos 3\phi_3, \quad (62)$$

$$T_2 = i(c_3 - c_{-3}) = \delta_3 \sin 3\phi_3, \quad (63)$$

respectively, where δ_3 is a positive constant and ϕ_3 is the angle between one of the long axes of the deformed spot and the x -axis. In order to relate T_1 and T_2 with a tensor, we introduce the third-rank tensor $U_{\alpha\beta\gamma}$ (α, β , and $\gamma = 1$ or 2). The tensor elements $U_{\alpha\beta\gamma}$ are represented by using vectors $\mathbf{N}^{(m)}$ ($m = 1, 2$, and 3) as

$$U_{\alpha\beta\gamma} = \frac{4\delta_3}{3} \sum_m N_\alpha^{(m)} N_\beta^{(m)} N_\gamma^{(m)}, \quad (64)$$

where the normal vectors $\mathbf{N}^{(m)}$ are defined by

$$\begin{aligned} \mathbf{N}^{(1)} &= (\cos \phi_3, \sin \phi_3), \\ \mathbf{N}^{(2)} &= \left(\cos \left(\phi_3 + \frac{2\pi}{3} \right), \sin \left(\phi_3 + \frac{2\pi}{3} \right) \right), \\ \mathbf{N}^{(3)} &= \left(\cos \left(\phi_3 - \frac{2\pi}{3} \right), \sin \left(\phi_3 - \frac{2\pi}{3} \right) \right). \end{aligned} \quad (65)$$

The tensor \mathbf{U} is the same as the order parameter for banana (tetrahedral nematic) liquid crystals in two dimensions [35, 36]. We obtain the relations between the tensor elements $U_{\alpha\beta\gamma}$ and T_1 and T_2 as $U_{111} = T_1$, $U_{222} = -T_2$, and

$$\begin{aligned} U_{111} = -U_{122} = -U_{212} = -U_{221}, \\ U_{222} = -U_{112} = -U_{121} = -U_{211}. \end{aligned} \quad (66)$$

The spot with head-tail asymmetric deformation is represented as

$$R(\phi_r) = R_0 + \delta_3 \cos 3(\phi_r - \phi_3). \quad (67)$$

The terms $\delta h_{1,1(\alpha)}^{(0)}$ and $\delta \tilde{h}_{1,1(\alpha)}^{(0)}$ in (58) are expressed using tensors. The detailed calculations are given in Appendix C. The final form is as follows:

$$\begin{aligned} \delta h_{1,1(\alpha)}^{(0)} &= -a^* \sum_\beta S_{\alpha\beta} v_\beta, \\ \delta \tilde{h}_{1,1(\alpha)}^{(0)} &= -\bar{a}^* \sum_\beta S_{\alpha\beta} v_\beta, \end{aligned} \quad (68)$$

where

$$a^* = a_1^* + a_2^*, \quad (69)$$

$$a_1^* = -\frac{R_0}{2} F(2, 2, 1, 2),$$

$$a_2^* = -\frac{1}{2} [R_0 F(2, 2, 1, 2) - 3F(1, 2, 1, 1)], \quad (70)$$

$$\bar{a}^* = \bar{a}_1^* + \bar{a}_2^*,$$

$$\bar{a}_1^* = -\frac{R_0}{8} [-F(3, 2, 1, 2) + 3F(3, 2, 1, 1)] \quad (71)$$

$$- \frac{3}{4} F(2, 2, 0, 1),$$

$$\bar{a}_2^* = -2 \left[\frac{R_0}{4} F_d(2, 2, 2, 1) - F_d(1, 2, 1, 1) \right]. \quad (72)$$

Thus, (58) is written using $S_{\alpha\beta}$ in the form

$$m\dot{v}_\alpha + (\tau - \tau_c) v_\alpha + g v_\alpha |\mathbf{v}|^2 = -\bar{a} \sum_\beta S_{\alpha\beta} v_\beta, \quad (73)$$

where $\bar{a} = (aa^* + b\bar{a}^*)$. $\delta h_{1,1(\alpha)}^{(0)}$ and $\delta \tilde{h}_{1,1(\alpha)}^{(0)}$ yield the \mathbf{Sv} term. This is due to the periodicity of the function in the integral over ϕ_r ; in the expansion of $\delta \mathbf{R}(\phi_r)$ and $H_q^{(1)}(\phi_r)$, only $c_{\pm 2}$ terms contribute to the nonzero integral, resulting in the \mathbf{Sv} term. Equation (73) suggests that the motionless spot is destabilized into a moving spot for $\tau_c > \tau$, and the velocity of the spot is approximately given by $|\mathbf{v}|^2 \sim (\tau_c - \tau)/g$. The deformation and velocity coupling term \mathbf{Sv} modifies the straight motion of the spot.

4.4. Time Evolution Equations of Tensors. In the previous subsection, we defined the tensors and described the equation of motion of the spot by using tensors, including the time-dependent tensor $S_{\alpha\beta}$. In this subsection, we derive the time evolution equations of the tensors up to $\sim O(\mathbf{v}^4)$. We first discuss the order of \mathbf{v} , $S_{\alpha\beta}$, and $U_{\alpha\beta\gamma}$, following [16]. From (73), the motionless spot is critical at $\tau = \tau_c$, and the moving spot occurs supercritically with increasing $(\tau_c - \tau)$. We put $\delta = \tau_c - \tau$ for the smallness parameter. The time is scaled by $\hat{t} = t\delta$, and all the terms in (73) are of the order $O(\delta^{3/2})$.

Here $\mathbf{v} \sim O(\delta^{1/2})$ and $\mathbf{S} \sim O(\delta)$; therefore $S_{\alpha\beta} \sim O(\mathbf{v}^2)$. In the later calculations, we can confirm that $S_{\alpha\beta} \sim O(\mathbf{v}^2)$ and $U_{\alpha\beta\gamma} \sim O(\mathbf{v}^3)$. In the derivation of (73), we omitted the terms that include higher order derivatives of time. We estimate these terms, for example, $d^2\mathbf{v}/dt^2 \sim O(\delta^{5/2})$, $\mathbf{S}\mathbf{S}\mathbf{v} \sim O(\delta^{5/2})$, $(\mathbf{q}\cdot\mathbf{v})\partial H_{\mathbf{q}}/\partial t \sim O(\delta^{5/2})$, $\partial^3 H_{\mathbf{q}}/\partial t^3 \sim O(\delta^4)$, $(\mathbf{q}\cdot\mathbf{v})\partial^2 H_{\mathbf{q}}/\partial t^2 \sim O(\delta^{7/2})$, $(\mathbf{q}\cdot\mathbf{v})^2\partial H_{\mathbf{q}}/\partial t \sim O(\delta^3)$, and $(\mathbf{q}\cdot\dot{\mathbf{v}})\partial H_{\mathbf{q}}/\partial t \sim O(\delta^{7/2})$ in the expansion of h and \tilde{h} . From these estimates, the omission of those terms is justified.

\mathbf{S} and \mathbf{U} are composed of $c_{\pm 2}$ and $c_{\pm 3}$, respectively, so that $c_{\pm 2} \sim O(\mathbf{v}^2)$ and $c_{\pm 3} \sim O(\mathbf{v}^3)$. The coupling terms such as $c_n c_m$ ($|n|, |m| \geq 2$) are much smaller. Therefore, we linearize (14) in terms of the deformation δR . Then, the time evolution equation of δR becomes

$$\tau \frac{\partial \delta R}{\partial t} = \frac{\epsilon}{R_0^2} \left(\frac{\partial^2 \delta R}{\partial \phi_r^2} + \delta R \right) + a\delta h + b\delta \tilde{h} + L. \quad (74)$$

We consider terms up to the fourth order of \mathbf{v} , where δh and $\delta \tilde{h}$ are given by

$$\delta h = h - h_0^{(0)} = \delta h_0 + \delta h_1 + \delta h_2 + \delta h_3 + \delta h_4, \quad (75)$$

$$\delta \tilde{h} = \tilde{h} - \tilde{h}_0^{(0)} = \delta \tilde{h}_0 + \delta \tilde{h}_1 + \delta \tilde{h}_2 + \delta \tilde{h}_3 + \delta \tilde{h}_4, \quad (76)$$

respectively. Here, δh_l and δh_l ($l = 1, 2, \dots, 4$) are defined by (34) as $\delta h_0 = h_0 - h_0^{(0)}$ and $\delta h_l = h_l$, respectively. $\delta \tilde{h}_l$ is similarly defined by (35). We expand δh_1 , δh_2 , $\delta \tilde{h}_1$, and $\delta \tilde{h}_2$ as $\delta h_1 = \delta h_{1,1} + \delta h_{1,2}$, $\delta h_2 = \delta h_{2,2}$, $\delta \tilde{h}_1 = \delta \tilde{h}_{1,1} + \delta \tilde{h}_{1,2}$, and $\delta \tilde{h}_2 = \delta \tilde{h}_{2,2}$, respectively.

In order to derive the equation of motion of tensors, we calculate the first-order time derivative of c_n . The linear combination of \dot{c}_n results in the equation of motion of tensors. In this process, $\dot{\mathbf{v}}$ terms in $\delta h_{2,1}$ and $\delta \tilde{h}_{2,1}$ are neglected because these terms cause small order terms; $\sum_{\gamma} U_{\alpha\beta\gamma} \dot{v}_{\gamma}$ and $S_{\alpha\beta} \dot{v}_{\gamma}$ appear in the time evolution equation of $S_{\alpha\beta}$ and $U_{\alpha\beta\gamma}$, respectively. These terms are $\sum_{\gamma} U_{\alpha\beta\gamma} \dot{v}_{\gamma} \sim O(\mathbf{v}^6)$ and $S_{\alpha\beta} \dot{v}_{\gamma} \sim O(\mathbf{v}^5)$ so that they do not contribute to the equation of motion of tensors. In addition, $(\partial^2 H_{\mathbf{q}}/\partial t^2)$ terms in $\delta h_{2,3}$ and $\delta \tilde{h}_{2,3}$ are neglected because these terms result in the second-order time derivative of c_n ; these terms are $\dot{c}_{\pm 2} \sim O(\mathbf{v}^6)$ and $\dot{c}_{\pm 3} \sim O(\mathbf{v}^7)$ and they are small enough to be neglected.

We first derive the equation of motion of $S_{\alpha\beta}$. Using (74), we can obtain the time evolution equation of $c_{\pm 2}$, and we derive the time evolution equation of $S_{\alpha\beta}$. The detailed derivation is given in Appendices D and E. The time evolution equation of $S_{\alpha\beta}$ up to $O(\mathbf{v}^4)$ is

$$\begin{aligned} \Gamma_2 \frac{dS_{\alpha\beta}}{dt} &= -K_2 S_{\alpha\beta} + \bar{b} \left[v_{\alpha} v_{\beta} - \frac{\delta_{\alpha\beta}}{2} |\mathbf{v}|^2 \right] \\ &+ \bar{b}_s \left[v_{\alpha} v_{\beta} - \frac{\delta_{\alpha\beta}}{2} |\mathbf{v}|^2 \right] |\mathbf{v}|^2 + \bar{b}_1 \sum_{\gamma} U_{\alpha\beta\gamma} v_{\gamma} \\ &+ \bar{c} |\mathbf{v}|^2 S_{\alpha\beta}, \end{aligned} \quad (77)$$

where $\Gamma_2 = \tau + aE_2 + b\tilde{E}_2$, $K_2 = 3\epsilon/R_0^2 + aD_2 + b\tilde{D}_2$, $\bar{b} = aG_1 + b\tilde{G}_1$, $\bar{b}_s = -aG_1^s - b\tilde{G}_1^s$, $\bar{b}_1 = -aB_3/2 + b(3\tilde{A}^* - \tilde{B}_3)/2$, and $\bar{c} = -a(2T_{2,2} - V_2) - b(2\tilde{T}_{2,2} - \tilde{V}_2)$. All the parameters in these expressions are given in Appendix E. The second term in (77) originates from δh_2 and $\delta \tilde{h}_2$, the third term from δh_4 and $\delta \tilde{h}_4$, the fourth term from δh_1 and $\delta \tilde{h}_1$, and the fifth term from δh_2 and $\delta \tilde{h}_2$. Thus, in order to consider the terms up to $O(\mathbf{v}^4)$, δh_4 and $\delta \tilde{h}_4$ are necessary in the expansion equations (75) and (76). From the first and second terms in (77), we note that $S_{\alpha\beta} \sim O(\mathbf{v}^2)$.

Next, we consider the time evolution equation of $U_{\alpha\beta\gamma}$. Following procedures similar to those for $S_{\alpha\beta}$, the time evolution equation of $U_{\alpha\beta\gamma}$ up to $O(\mathbf{v}^4)$ is

$$\begin{aligned} \Gamma_3 \frac{dU_{\alpha\beta\gamma}}{dt} &= -K_3 U_{\alpha\beta\gamma} + 4d_1 \left[v_{\alpha} v_{\beta} v_{\gamma} \right. \\ &\quad \left. - \frac{|\mathbf{v}|^2}{4} (\delta_{\alpha\beta} v_{\gamma} + \delta_{\beta\gamma} v_{\alpha} + \delta_{\gamma\alpha} v_{\beta}) \right] \\ &+ \frac{2d_2}{3} \left[S_{\alpha\beta} v_{\gamma} + S_{\beta\gamma} v_{\alpha} + S_{\gamma\alpha} v_{\beta} \right. \\ &\quad \left. - \sum_{\eta} \frac{v_{\eta}}{2} (\delta_{\alpha\beta} S_{\gamma\eta} + \delta_{\beta\gamma} S_{\alpha\eta} + \delta_{\gamma\alpha} S_{\beta\eta}) \right], \end{aligned} \quad (78)$$

where $\Gamma_3 = \tau + aE_3 + b\tilde{E}_3$ and $K_3 = 8\epsilon/R_0^2 + aD_3 + b\tilde{D}_3$. d_1 and d_2 are defined as

$$\begin{aligned} d_1 &= -\frac{R_0}{4} [aF(3, 4, 1, 3) + bF_d(4, 4, 1, 3)], \quad (79) \\ d_2 &= -a\frac{R_0}{2} [F(2, 2, 2, 3) + F_d(2, 2, 1, 1)] \\ &\quad - b\frac{R_0}{2} [F_d(3, 2, 2, 3) \\ &\quad + \frac{1}{4} (F(3, 2, 1, 3) - 3F(3, 2, 1, 1))] \\ &\quad - \frac{b}{2} [F(2, 2, 0, 1) + F(2, 2, 1, 2)], \end{aligned} \quad (80)$$

respectively. In the above equation, all the terms are $\sim O(\mathbf{v}^3)$. The terms of $O(\mathbf{v}^4)$ disappeared because of the orthogonality relation of trigonometric functions. The next higher order term is $O(\mathbf{v}^5)$, which is not included in expansions δh and $\delta \tilde{h}$ in (75) and (76). The second term in (78) originates from δh_3 and $\delta \tilde{h}_3$, and the third term from δh_1 and $\delta \tilde{h}_1$. From the first and second terms in (78), we note that $U_{\alpha\beta\gamma} \sim O(\mathbf{v}^3)$.

5. Tensor Model

Using (73), (77), and (78), we discuss the stationary solution, the stability conditions of straight motion, and the critical

velocity of circular motion. For the sake of convenience, we rescale (73), (77), and (78) into

$$\frac{dv_\alpha}{dt} = \gamma v_\alpha - v_\alpha |\mathbf{v}|^2 - \bar{a}' \sum_\beta S_{\alpha\beta} v_\beta, \quad (81)$$

$$\begin{aligned} \frac{dS_{\alpha\beta}}{dt} = & -\kappa S_{\alpha\beta} + \bar{b}' \left[v_\alpha v_\beta - \frac{1}{2} |\mathbf{v}|^2 \delta_{\alpha\beta} \right] \\ & + \bar{b}'_s \left[v_\alpha v_\beta - \frac{1}{2} |\mathbf{v}|^2 \delta_{\alpha\beta} \right] |\mathbf{v}|^2 \\ & + \bar{b}'_1 \sum_\gamma U_{\alpha\beta\gamma} v_\gamma + \bar{c}' |\mathbf{v}|^2 S_{\alpha\beta}, \end{aligned} \quad (82)$$

$$\begin{aligned} \frac{dU_{\alpha\beta\gamma}}{dt} = & -KU_{\alpha\beta\gamma} \\ & + d'_1 \left[v_\alpha v_\beta v_\gamma - \frac{|\mathbf{v}|^2}{4} (\delta_{\alpha\beta} v_\gamma + \delta_{\beta\gamma} v_\alpha + \delta_{\gamma\alpha} v_\beta) \right] \\ & + \frac{d'_2}{3} \left[S_{\alpha\beta} v_\gamma + S_{\beta\gamma} v_\alpha + S_{\gamma\alpha} v_\beta \right. \\ & \left. - \sum_\eta \frac{v_\eta}{2} (\delta_{\alpha\beta} S_{\gamma\eta} + \delta_{\beta\gamma} S_{\alpha\eta} + \delta_{\gamma\alpha} S_{\beta\eta}) \right], \end{aligned} \quad (83)$$

respectively. We name (81)–(83) as the full tensor model [37]. In the above full tensor model, we chose parameters such that $g/m = 1$ and put $\gamma = (\tau_c - \tau)/m$ and $\bar{a}' = \bar{a}/m$ in (81). The other rescaled parameters in (82) and (83) were $\kappa = K_2/\Gamma_2$, $\bar{b}' = \bar{b}/\Gamma_2$, $\bar{b}'_s = \bar{b}_s/\Gamma_2$, $\bar{b}'_1 = \bar{b}_1/\Gamma_2$, $\bar{c}' = \bar{c}/\Gamma_2$, $K = K_3/\Gamma_3$, $d'_1 = 2d_1/\Gamma_3$, and $d'_2 = d_2/\Gamma_3$.

We summarize the coefficients in (81)–(83) as follows. γ is a damping coefficient in the time evolution equation of v_α ; although the motionless spot is stable for $\gamma < 0$, the motionless spot is destabilized for $\gamma > 0$ and there appears a moving spot. κ and K are damping coefficients in the time evolution equations of $S_{\alpha\beta}$ and $U_{\alpha\beta\gamma}$, respectively. In this study, we fix K as a positive constant and consider κ in the range $\kappa > 0$. \bar{b}' and \bar{b}'_s are coefficients of the quadratic and fourth order of \mathbf{v} , respectively, in the time evolution equation of $S_{\alpha\beta}$. The term \bar{b}'_s can be absorbed into \bar{b}' with the replacement $\bar{b}' \rightarrow (\bar{b}' + \bar{b}'_s |\mathbf{v}|^2)$. From the results, it can be seen that the term \bar{b}' is enhanced (suppressed) when the sign of \bar{b}'_s is the same as (different from) that of \bar{b}' . d'_1 is the coefficient of the cubic term of \mathbf{v} in the time evolution equation of $U_{\alpha\beta\gamma}$. These terms cause deformations with increasing velocity. The other parameters are coupling coefficients of deformation and velocity. \bar{a}' and d'_2 are the coupling coefficients of $S_{\alpha\beta} v_\beta$ and $S_{\alpha\beta} v_\gamma$, respectively, and these terms influence the time evolution of v_α and $U_{\alpha\beta\gamma}$, respectively. \bar{b}'_1 and \bar{c}' are the coupling coefficients of $U_{\alpha\beta\gamma} v_\gamma$ and $|\mathbf{v}|^2 S_{\alpha\beta}$, respectively. When $\bar{b}'_1 = 0$, $U_{\alpha\beta\gamma}$ is decoupled from v_α and $S_{\alpha\beta}$. $\bar{c}' |\mathbf{v}|^2 S_{\alpha\beta}$ can be absorbed into $-\kappa S_{\alpha\beta}$ with the

replacement $\kappa \rightarrow (\kappa - \bar{c}' |\mathbf{v}|^2)$. Then, the term κ is suppressed (enhanced) when \bar{c}' is positive (negative), with $|\mathbf{v}|^2 \neq 0$.

The dependence of \bar{a}' , \bar{b}' , \bar{b}'_s , \bar{c}' , \bar{b}'_1 , d'_1 , and d'_2 on k_c is shown in Figure 4. In each figure, these parameters (shown on the vertical axis) are scaled by R_0^2 . We see that both \bar{a}' and \bar{b}' are negative, and \bar{b}'_1 , $\bar{c}' \neq 0$ even at $k_c = 0$. Although \bar{b}'_1 is a monotonically increasing function of k_c , \bar{c}' is a monotonically decreasing function of k_c . d'_1 and d'_2 are positive but d'_1 is much smaller than d'_2 .

Henceforth, we drop the primes on the parameters in the full tensor model (81)–(83). In the full tensor model, when K is large and \mathbf{v} is small, the effect of $U_{\alpha\beta\gamma}$ on $S_{\alpha\beta}$ is small in (82). In this case, we put $\bar{b}'_1 = 0$, and the v_α , $S_{\alpha\beta}$, and $U_{\alpha\beta\gamma}$ system described by (81)–(83) is reduced to a v_α and $S_{\alpha\beta}$ system. We call this system the reduced tensor model.

6. Stationary Solution and Phase Diagrams

In the following subsections, we consider the stationary solution and phase diagrams. For this, we rewrite v_α , $S_{\alpha\beta}$, and $U_{\alpha\beta\gamma}$ by introducing the following variables:

$$\begin{aligned} v_1 &= v \cos \phi, \\ v_2 &= v \sin \phi, \\ S_{11} &= \frac{s}{2} \cos 2\theta, \\ S_{12} &= \frac{s}{2} \sin 2\theta, \\ U_{111} &= c_3 + c_{-3}, \\ U_{222} &= -i(c_3 - c_{-3}), \\ c_{\pm 3} &= \frac{\delta_3}{2} e^{\mp i3\phi_3} \equiv \frac{z}{4} e^{\mp i3\phi}, \end{aligned} \quad (84)$$

where we choose $v, s, z > 0$. From (81), we obtain the time evolution equations of v and ϕ as

$$\frac{d}{dt} v = v(\gamma - v^2) - \frac{1}{2} \bar{a}' s v \cos 2(\theta - \phi), \quad (85)$$

$$\frac{d}{dt} \phi = -\frac{1}{2} \bar{a}' s \sin 2(\theta - \phi), \quad (86)$$

respectively. From (82), we obtain the time evolution equations of s and θ as

$$\frac{d}{dt} s = -\kappa s + \bar{b}' v^2 \cos 2(\theta - \phi) + \bar{b}'_s v^4 \cos 2(\theta - \phi) \quad (87)$$

$$+ \bar{b}'_1 z v \cos(2\theta + \phi - 3\phi) + \bar{c}' v^2 s,$$

$$\frac{d}{dt} \theta = -\frac{\bar{b}' v^2}{2s} \sin 2(\theta - \phi) - \frac{\bar{b}'_s v^4}{2s} \sin 2(\theta - \phi) \quad (88)$$

$$+ \frac{\bar{b}'_1 z v}{2s} \sin(3\phi - \phi - 2\theta),$$

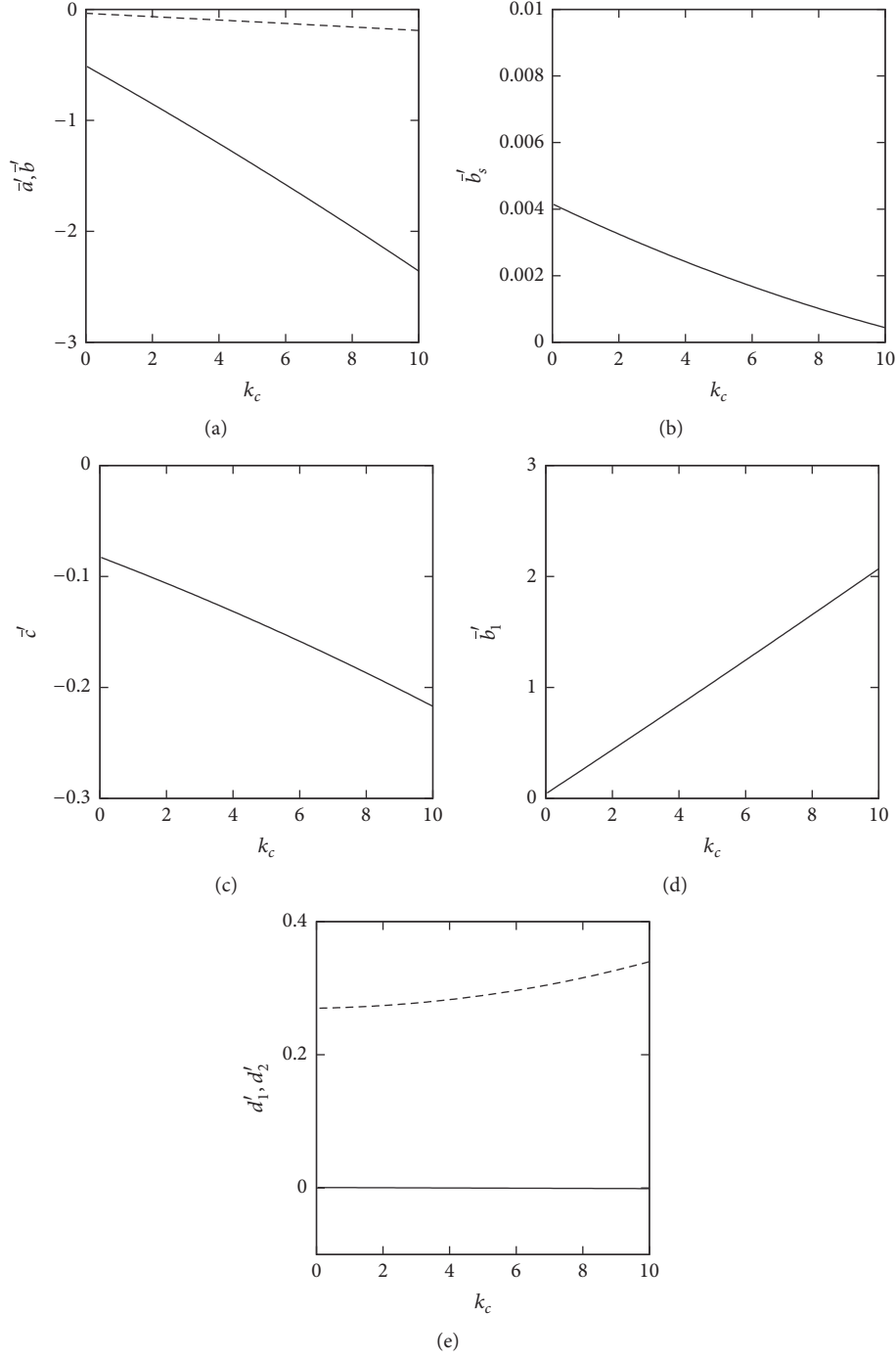


FIGURE 4: Dependence of \bar{a}' , \bar{b}' , \bar{b}'_s , \bar{c}' , \bar{b}'_1 , d'_1 , and d'_2 on k_c . $\alpha = 5.0$ and $W = 1.0$. All the parameters in the vertical axis are scaled by R_0^2 . (a) \bar{a}' and \bar{b}' . The solid and dashed curves represent \bar{a}' and \bar{b}' , respectively. (b) \bar{b}'_s . (c) \bar{c}' . (d) \bar{b}'_1 . (e) d'_1 and d'_2 . The solid and dashed curves represent d'_1 and d'_2 , respectively.

respectively. From (83), we obtain the time evolution equations of z and φ as

$$\begin{aligned} \frac{d}{dt}z &= -Kz + d_1 v^3 \cos 3(\varphi - \phi) \\ &+ d_2 sv \cos(3\varphi - 2\theta - \phi), \end{aligned} \quad (89)$$

$$\begin{aligned} \frac{d}{dt}\varphi &= -\frac{d_1}{3z}v^3 \sin 3(\varphi - \phi) \\ &- \frac{d_2}{3z}sv \sin(3\varphi - 2\theta - \phi). \end{aligned} \quad (90)$$

Using (85)–(90), we theoretically derive the stationary solution and phase diagrams. In order to verify the theoretical

result, we perform simulations of the reduced tensor model. For the numerical calculations, we employ the fourth-order Runge-Kutta algorithm with the time increment $\Delta t = 1.0 \times 10^{-4}$ and fix the parameters as $\bar{a} = \bar{b} = -1$, $K = 0.3$, $d_1 = 0.1$, and $d_2 = 0.5$.

6.1. Stationary Solution. For the reduced and full tensor models, we consider the stationary solution of the moving spot, which moves straight in the x direction. This situation corresponds to $\phi = 0$. In the case of $\bar{b}_1 = \bar{b}_s = \bar{c} = 0$, the stationary solution of (85) and (86) becomes $v_0^2 = \gamma/(1+B)$ with $B = \bar{a}\bar{b}/2\kappa$. In order to avoid the divergence of v_0^2 , we assume that $\bar{a}\bar{b} > 0$. For $\bar{c} \neq 0$, we consider the dependence of the stationary solution of s , z , θ , and φ on the signs of \bar{a} and \bar{b} . In the stationary state of (86) with $\phi = 0$, there are two stationary solutions of θ depending on the sign of \bar{a} and \bar{b} : (I) \bar{a} and \bar{b} are positive with $\theta_0 = l\pi$ and (II) \bar{a} and \bar{b} are negative with $\theta_0 = (l + 1/2)\pi$, where l is an integer. Using (87)–(90), the stationary solution of case (I) is

$$\begin{aligned} s_0 &= \left[\frac{(\bar{b} + \bar{b}_s v_0^2) K + \bar{b}_1 d_1 v_0^2}{K(\kappa - \bar{c} v_0^2) - d_2 \bar{b}_1 v_0^2} \right] v_0^2, \\ z_0 &= \cos 3\varphi_0 \left[\frac{d_1(\kappa - \bar{c} v_0^2) + d_2(\bar{b} + \bar{b}_s v_0^2)}{K(\kappa - \bar{c} v_0^2) - d_2 \bar{b}_1 v_0^2} \right] v_0^3, \end{aligned} \quad (91)$$

where φ_0 satisfies $\sin 3\varphi_0 = 0$ and v_0 is a stationary solution of v , which is determined later. On the other hand, for case (II), the stationary solution is

$$v_{0,\pm}^2 = \frac{1}{f_1} \left[f_2 \pm \sqrt{f_3} \right]$$

$$\text{with } f_1 = 2 \left[K\bar{c} + d_2 \bar{b}_1 - \frac{1}{2} \bar{a} (\bar{b}_1 d_1 + K \bar{b}_s) \right],$$

$$f_2 = \left(\frac{1}{2} \bar{a} \bar{b} + \kappa + \gamma \bar{c} \right) K + \gamma d_2 \bar{b}_1,$$

$$f_3 = \left[\left(\frac{1}{2} \bar{a} \bar{b} - \kappa + \gamma \bar{c} \right) K + \gamma d_2 \bar{b}_1 \right]^2 + 2 \bar{a} \kappa \left[(\bar{b} + \bar{b}_s \gamma) K^2 + \gamma \bar{b}_1 d_1 K \right].$$

In order to satisfy the condition that $v_{0,\pm}^2 \rightarrow \gamma/(1+B)$ in the limits $\bar{b}_1, \bar{b}_s,$ and $\bar{c} \rightarrow 0$, only $v_{0,-}^2$ exists. In the physical images of the moving spot in cases (I) and (II) with $\varphi_0 = 0$, the long axes of the elliptical domain are parallel and perpendicular to the moving direction, respectively [16].

6.2. Stability of Straight Motion in the Reduced Tensor Model. When K is large in (89), z is rapidly damped to zero. In addition, when v is small, the influences of z on s and θ in (87) and (88) are small. For this case, we discuss the stability of the straight motion of the spot by setting $\bar{b}_1 = 0$ in (87) and

$$\begin{aligned} s_0 &= - \left[\frac{(\bar{b} + \bar{b}_s v_0^2) K + \bar{b}_1 d_1 v_0^2}{K(\kappa - \bar{c} v_0^2) - d_2 \bar{b}_1 v_0^2} \right] v_0^2, \\ z_0 &= \cos 3\varphi_0 \left[\frac{d_1(\kappa - \bar{c} v_0^2) + d_2(\bar{b} + \bar{b}_s v_0^2)}{K(\kappa - \bar{c} v_0^2) - d_2 \bar{b}_1 v_0^2} \right] v_0^3. \end{aligned} \quad (92)$$

From these results, it is seen that z_0 has the same expression irrespective of the signs of \bar{a} and \bar{b} . As z_0 is positive, φ_0 satisfying $\sin 3\varphi_0 = 0$ is chosen as

$$\begin{aligned} \text{(i)} \quad \varphi_0 &= \frac{2m}{3} \pi, \\ &\text{if } \left[\frac{d_1(\kappa - \bar{c} v_0^2) + d_2(\bar{b} + \bar{b}_s v_0^2)}{K(\kappa - \bar{c} v_0^2) - v_0^2 d_2 \bar{b}_1} \right] > 0, \\ \text{(ii)} \quad \varphi_0 &= \frac{(2m+1)}{3} \pi, \\ &\text{if } \left[\frac{d_1(\kappa - \bar{c} v_0^2) + d_2(\bar{b} + \bar{b}_s v_0^2)}{K(\kappa - \bar{c} v_0^2) - v_0^2 d_2 \bar{b}_1} \right] < 0. \end{aligned} \quad (93)$$

For both cases ((I) and (II)), the stationary solution of z_0 is given by

$$z_0 = \left| \frac{d_1(\kappa - \bar{c} v_0^2) + d_2(\bar{b} + \bar{b}_s v_0^2)}{K(\kappa - \bar{c} v_0^2) - d_2 \bar{b}_1 v_0^2} \right| v_0^3. \quad (94)$$

In both cases ((I) and (II)), by substituting s_0 into (85) in the stationary state, we obtain two stationary solutions $v_{0,\pm}$ as

(88). Using (86) and (88), we can derive the time evolution equation of $\psi = \theta - \phi$ as

$$\frac{d\psi}{dt} = -\frac{1}{2} \left(-\bar{a}s + \frac{\bar{b}v^2}{s} + \frac{\bar{b}_s v^4}{s} \right) \sin 2\psi. \quad (96)$$

For the stationary states $v = v_{0,-}$, $s = s_0$, we discuss the stability condition of the straight motion. From (96), the stationary solution ψ_0 satisfies $2\psi_0 = 2l\pi$ or $(2l+1)\pi$, and their corresponding stability conditions are $(-\bar{a}s_0 + \bar{b}v_{0,-}^2/s_0 + \bar{b}_s v_{0,-}^4/s_0) > 0$ or $(-\bar{a}s_0 + \bar{b}v_{0,-}^2/s_0 + \bar{b}_s v_{0,-}^4/s_0) < 0$, respectively. Since \bar{a} and \bar{b} are negative in our RD system, as shown in Figure 4(a), we consider the case of $\psi_0 = \pi/2$ as follows.

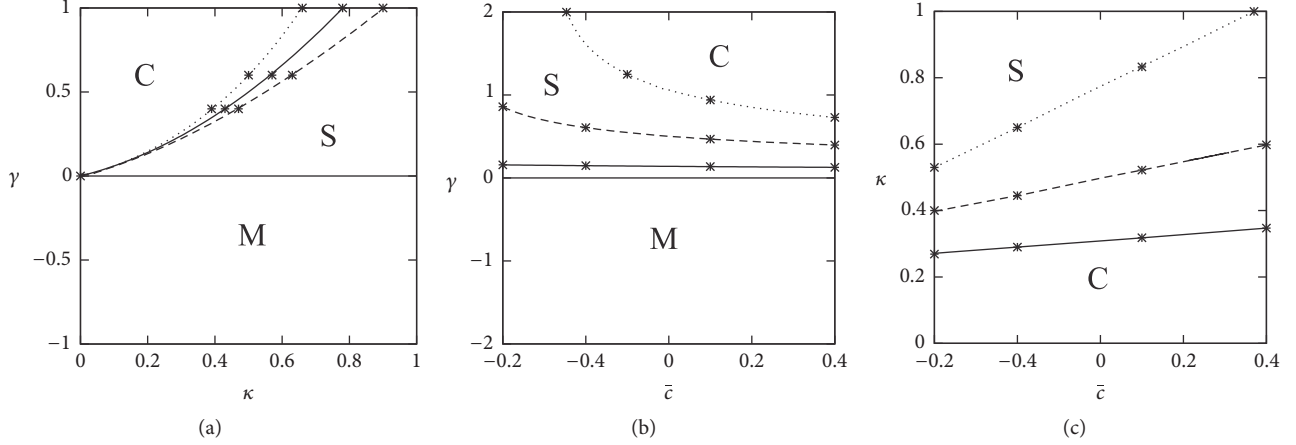


FIGURE 5: Phase diagram of spot motion. $\bar{a} = \bar{b} = -1$ and $\bar{b}_s = 0.05$. Data are obtained by the analysis of (96). M, S, and C in the figure represent regions of no motion, straight motion, and circular motion, respectively. The mark * represents the data obtained by the simulation of the reduced tensor model. (a) Phase diagram in the κ - γ plane. The solid, dashed, and dotted curves correspond to the cases of $\bar{c} = 0, 0.2,$ and $-0.2,$ respectively. The upper (lower) region of each curve corresponds to the region of circular (straight) motion, and the region $\gamma \leq 0$ corresponds to the region of no motion. (b) Phase diagram in the \bar{c} - γ plane. The solid, dashed, and dotted curves correspond to cases of $\kappa = 0.2, 0.5,$ and $0.8,$ respectively. The region across each curve is the same as in (a). (c) Phase diagram in the \bar{c} - κ plane. The solid, dashed, and dotted curves correspond to the cases of $\gamma = 0.25, 0.5,$ and $1.0,$ respectively. The upper (lower) region of each curve corresponds to the region of straight (circular) motion.

In this case, the stability condition is calculated using the s_0 given by (92). The bifurcation of straight-circular motion, when $\bar{b}_s = \bar{c} = 0$, was already studied in [16], and the critical value for the straight motion is expressed as

$$\gamma_c = \frac{\kappa^2}{\bar{a}\bar{b}} + \frac{\kappa}{2}. \quad (97)$$

The phase diagram in the κ - γ plane is shown by the solid curve in Figure 5(a). When $\gamma \leq 0$, the motionless spot is stable. When γ is in the range $0 < \gamma \leq \gamma_c$, the spot moves straight. However, when $\gamma > \gamma_c$, the straight motion become unstable and changes into circular motion. On the other hand, when $\bar{b}_s \neq 0$ and $\bar{c} \neq 0$, the stability condition for straight motion is

$$\bar{a} \left[\frac{\bar{b}v_{0,-}^2 + \bar{b}_s v_{0,-}^4}{\kappa - \bar{c}v_{0,-}^2} \right] < \kappa - \bar{c}v_{0,-}^2. \quad (98)$$

The phase diagram is a curved surface in κ - γ - \bar{c} space; the boundary of different motions of spot is obtained by using (98). The phase diagram in the κ - γ plane is shown in Figure 5(a) with dashed and dotted curves. Comparing the curves with that for the case when $\bar{b}_s = \bar{c} = 0$ (the solid curve), it can be seen that when $\bar{c} > 0$, the parameter region for the circular motion is larger. However, when $\bar{c} < 0$, the parameter region for the circular motion is smaller. We can explain this result using (87); the term $\bar{c}v^2s$ essentially reduces the parameter κ of the damping term $-\kappa s$ such that the damping term becomes $-(\kappa - \bar{c}v^2)s$. When \bar{c} is positive (negative), the term $\bar{c}v^2s$ effectively reduces (increases) κ so that the deformation s becomes large (small). This leads to positive (negative) \bar{c} results in the larger parameter region

of the circular motion. In our RD system, \bar{c} is negative and $|\bar{c}|$ monotonically increases with k_c (see Figure 4(c)), and the parameter region for circular motion becomes smaller as the intensity of chemotaxis increases. The phase diagrams in the \bar{c} - γ plane and \bar{c} - κ plane are shown in Figures 5(b) and 5(c), respectively. Figure 5(b) suggests that the parameter region for the circular motion is smaller for a larger value of κ . Equation (87) suggests that a larger value of κ damps s strongly such that the deformation is small, resulting in a smaller region of the circular motion. On the other hand, Figure 5(c) suggests that the parameter region for the circular motion is larger for a larger value of γ . Equation (85) suggests that a large positive value of γ enhances v such that the deformation becomes large, resulting in a larger region of circular motion. In each figure, the simulation results for the reduced tensor model are shown; they agree well with the theoretical results.

6.3. Dependence of Critical Velocity on Parameters. In the previous subsection, we showed that a spot appears in the circular motion when $\gamma > \gamma_c$. In this parameter region, we examine the stationary circular motion of the spot with a constant angular frequency ω and velocity v_r . For this, we set $\bar{b}_1 = 0$ and substitute $v = v_r, s = s_r, \theta = \omega t + \zeta/2$, and $\phi = \omega t$ into (85)–(88), and obtain the relations among ζ, s_r, v_r , and ω . The calculation is straightforward; the final expressions are shown.

We first consider the case when $\bar{b}_s = \bar{c} = 0$, where up to $O(v^3)$ terms are considered, and obtain the relations $\cos \zeta = \kappa/\bar{a}s_r, s_r^2 = \bar{b}v_r^2/\bar{a}, v_r^2 = (\gamma - \kappa/2), \omega^2 = (\bar{a}\bar{b}/4)(v_r^2 - v_c^2)$, and $v_c^2 = \kappa^2/\bar{a}\bar{b}$. When the spot rotates with an angular frequency ω , ω satisfies $\omega^2 \geq 0$, and this condition leads to $v_r \geq v_c$ [16]. The dependence of the critical velocity v_c for the stable angular

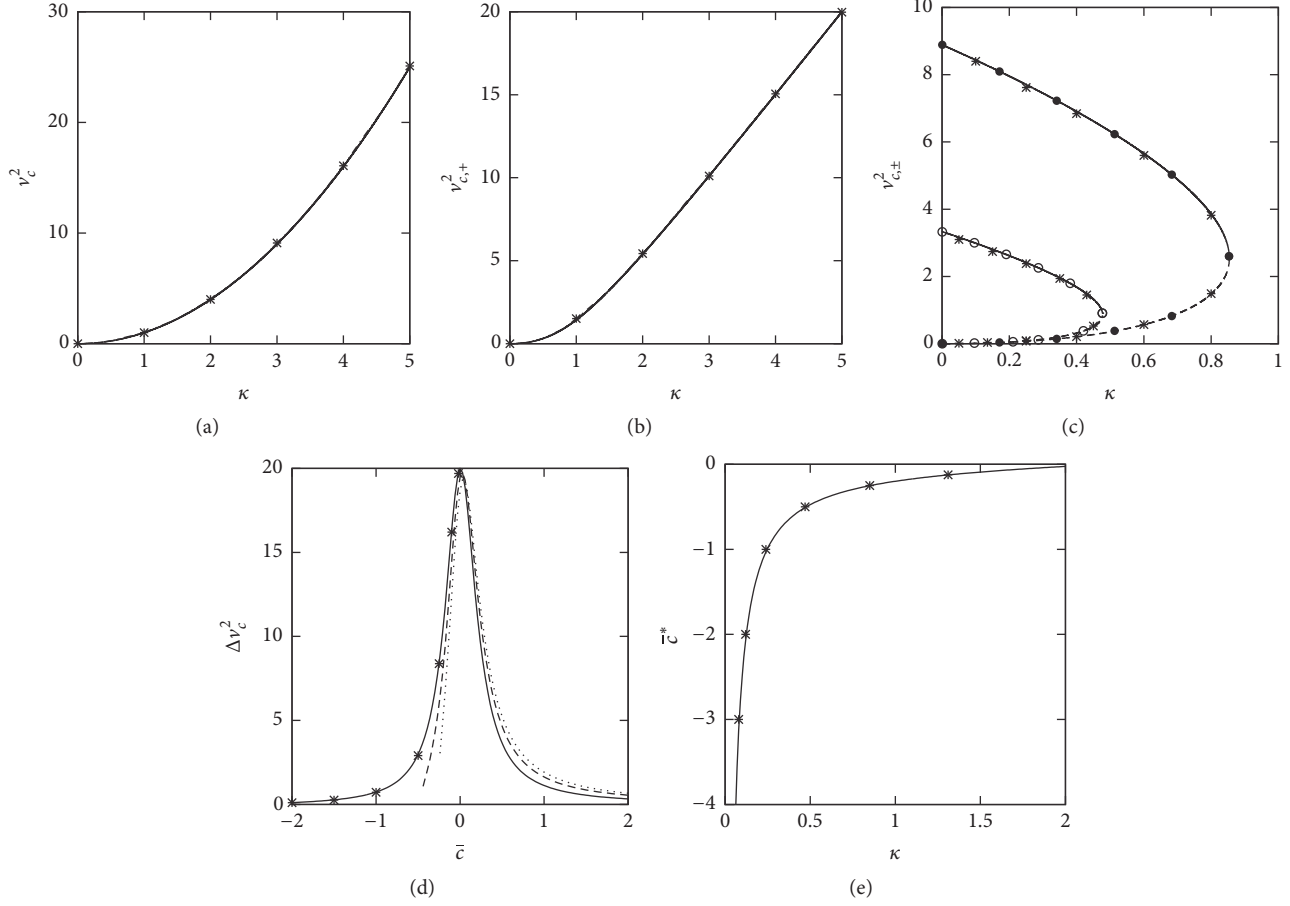


FIGURE 6: Dependence of the critical velocity v_c , $v_{c,\pm}$, Δv_c^2 , and \bar{c}^* on κ and \bar{c} . $\bar{a} = \bar{b} = -1$. The mark * represents data obtained by the simulation of the reduced tensor model. (a) Dependence of v_c^2 on κ . $\bar{b}_s = \bar{c} = 0$. (b) Dependence of $v_{c,+}^2$ on κ . $\bar{b}_s = -0.2$ and $\bar{c} = -0.25$. (c) Dependence of $v_{c,\pm}^2$ on κ . $\bar{b}_s = 0.05$. The curves with filled (\bullet) and open (\circ) circles correspond to the cases of $\bar{c} = -0.25$ and $\bar{c} = -0.5$, respectively. The solid and dashed curves represent $v_{c,-}^2$ and $v_{c,+}^2$, respectively. (d) Dependence of Δv_c^2 on \bar{c} . $\bar{b}_s = 0.05$. The solid, dashed, and dotted curves correspond to $\kappa = 0.1, 0.5$, and 0.8 , respectively. (e) Dependence of \bar{c}^* on κ . $\bar{b}_s = 0.05$.

frequency on κ (≥ 0) is shown in Figure 6(a). In this case, there is a lower limit of velocity v_c for the circular motion but no upper limit of velocity for the same.

Next, we consider the case when $\bar{b}_s \neq 0$ and $\bar{c} \neq 0$, where up to $O(v^4)$ terms are considered. After similar calculations to the case of $\bar{b}_s = \bar{c} = 0$, we obtain the relations $\cos \zeta = (\kappa - \bar{c}v_r^2)/\bar{a}s_r$, $s_r^2 = (\bar{b}v_r^2 + \bar{b}_s v_r^4)/\bar{a}$, $v_r^2 = (\gamma - \kappa/2)/(1 - \bar{c}/2)$, and $\omega^2 = (\bar{a}\bar{b}_s - \bar{c}^2)v_r^4/4 + (\bar{a}\bar{b} + 2\kappa\bar{c})v_r^2/4 - \kappa^2/4$. In this case, ω^2 is a quartic function of v_r . For the condition $\omega^2 \geq 0$, there are two cases depending on the sign of $(\bar{a}\bar{b}_s - \bar{c}^2)$. When $(\bar{a}\bar{b}_s - \bar{c}^2) > 0$, ω^2 exists for $v_r^2 \geq v_{c,+}^2$, where $v_{c,\pm}^2$ are the solutions of $\omega^2 = 0$, which are given by $v_{c,\pm}^2 = [-(\bar{a}\bar{b} + 2\kappa\bar{c}) \pm \sqrt{D_r}]/[2(\bar{a}\bar{b}_s - \bar{c}^2)]$ with $D_r = (\bar{a}\bar{b} + 2\kappa\bar{c})^2 + 4\kappa^2(\bar{a}\bar{b}_s - \bar{c}^2)$. The dependence of $v_{c,+}^2$ on κ is shown in Figure 6(b); there is only a lower limit of velocity $v_{c,+}$. This property is the same with the case when $\bar{b}_c = \bar{c} = 0$. On the other hand, when $(\bar{a}\bar{b}_s - \bar{c}^2) < 0$, ω^2 exists in a certain range of v_r^2 ; $v_{c,+}^2 \leq v_r^2 \leq v_{c,-}^2$ under the condition $D_r \geq 0$. In this case, there is a lower limit and an upper limit of

velocity, $v_{c,+}$ and $v_{c,-}$, respectively. The gap between $v_{c,-}^2$ and $v_{c,+}^2$ is defined by $\Delta v_c^2 = v_{c,-}^2 - v_{c,+}^2 = \sqrt{D_r}/(\bar{c}^2 - \bar{a}\bar{b}_s)$. Let us consider two limiting cases. In the limit $|\bar{c}| \rightarrow \infty$, $v_{c,\pm}^2$ and $\Delta v_c^2 \rightarrow 0$. That is, the circular motion cannot exist. On the other hand, for small $|\bar{c}|$ and $|\bar{b}_s| \ll 1$, we expand $v_{c,\pm}^2$ in terms of \bar{c} and \bar{b}_s and obtain $v_{c,+}^2 \sim \kappa^2/(\bar{a}\bar{b} + 2\kappa\bar{c})$ and $v_{c,-}^2 \sim (\bar{a}\bar{b} + 2\kappa\bar{c})/(\bar{c}^2 - \bar{a}\bar{b}_s)$. Thus, in the limits \bar{b}_s and $\bar{c} \rightarrow 0$, $v_{c,+}^2 \rightarrow \kappa^2/\bar{a}\bar{b}$, $v_{c,-}^2 \rightarrow \infty$, and $\Delta v_c^2 \rightarrow \infty$. This suggests that $v_{c,+} \rightarrow v_c$ and there is no upper limit of velocity, which are the same with the case when $\bar{b}_s = \bar{c} = 0$. From the numerical results shown in Figures 4(a), 4(b), and 4(c), $(\bar{a}\bar{b}_s - \bar{c}^2) < 0$ in our RD system; therefore, it turns out that v_r^2 exists only in a finite range, $v_{c,+}^2 \leq v_r^2 \leq v_{c,-}^2$. For larger $|\bar{c}|$, the gap $\Delta v_{c,\pm}^2$ is smaller, as shown in Figure 6(c). The dependence of Δv_c^2 on \bar{c} is shown in Figure 6(d), which suggests that Δv_c^2 monotonically decreases with increasing $|\bar{c}|$. Since $|\bar{c}|$ increases monotonically as k_c increases (Figure 4(c)), Δv_c^2

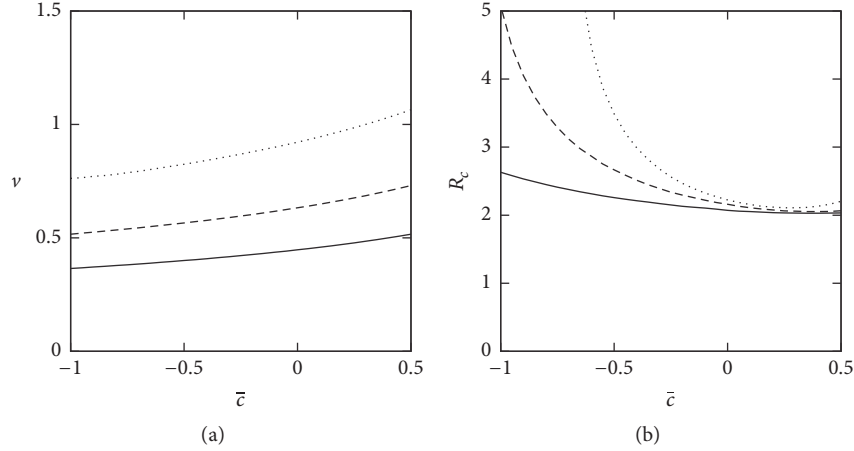


FIGURE 7: Dependence of velocity and radius on \bar{c} in the stationary circular motion. Data are obtained by the simulation of the reduced tensor model. $\bar{b}_s = 0.1$. The solid, dashed, and dotted curves correspond to $(\gamma, \kappa) = (0.25, 0.1)$, $(0.5, 0.2)$, and $(1.0, 0.3)$, respectively. (a) Dependence of v on \bar{c} . (b) Dependence of R_c on \bar{c} .

decreases as the chemotaxis increases. When the condition $D_r = 0$ is satisfied, $v_{c,-} = v_{c,+}$ and $\Delta v_c^2 = 0$, which yields the critical value \bar{c}^* as

$$\bar{c}^* = -\frac{(\bar{a}\bar{b})^2 + 4\kappa^2(\bar{a}\bar{b}_s)}{4\kappa\bar{a}\bar{b}}. \quad (99)$$

When $|\bar{c}| > |\bar{c}^*|$, $D_r < 0$, and, therefore, $v_{c,\pm}^2$ does not exist. There is no parameter region of γ for a positive value of κ ; the circular motion does not occur for any values of γ . The dependence of \bar{c}^* on κ is shown in Figure 6(e). Equation (99) can be positive for large κ . However, when \bar{c} is chosen as a positive value, the velocities v and s increase monotonically with increasing γ , and, therefore, the system diverges in the simulation. For this reason, \bar{c}^* is shown in the range $\bar{c}^* \leq 0$.

In order to verify the above theoretical results, the simulation results for the reduced tensor model are shown in each figure. The results obtained via simulation agree well with the theoretical results. In Figures 6(a) and 6(b), for given κ and \bar{c} , there is only a lower limit of γ for the circular motion of the spot, resulting in v_c and $v_{c,+}$, respectively. On the other hand, in Figure 6(c), for given κ and \bar{c} , there is not only a lower limit of γ but also an upper limit of γ for the circular motion of the spot, resulting in $v_{c,+}$ and $v_{c,-}$, respectively. However, in Figure 6(e), for given κ and \bar{c}^* , there is no parameter region of γ for the circular motion of the spot.

The dependence of the stationary velocity and radius of the circular motion on \bar{c} are shown in Figure 7. The velocity v increases monotonically with increasing \bar{c} , as shown in Figure 7(a). The corresponding radius of the spot motion R_c is shown in Figure 7(b). For fixed values of γ and κ , v decreases and R_c increases as $|\bar{c}|$ increases in the range $\bar{c} \leq 0$. The effect of chemotaxis is incorporated in \bar{c} , and \bar{c} is negative; $|\bar{c}|$ increases as the intensity of chemotaxis k_c increases in our RD system (Figure 4(c)). Thus, it is seen that the chemotaxis reduces v and increases R_c .

From the above analyses on (85)–(88) with $\bar{b}_1 = 0$, we conclude four points on the properties of stationary circular motion. (i) There is a lower limit of velocity. (ii) Although there is no upper limit for the velocity when up to $O(v^3)$ terms are considered, there will be an upper limit for the velocity if up to $O(v^4)$ terms are considered. (iii) The range of velocity decreases as the chemotaxis increases. (iv) There is a critical value \bar{c}^* (corresponding critical intensity of the chemotaxis is denoted by k_c^*) such that when $|\bar{c}| > |\bar{c}^*|$ ($k_c > k_c^*$), the circular motion does not occur for any values of γ .

6.4. Simulation of the Full Tensor Model. In this subsection, we examine the effect of $U_{\alpha\beta\gamma}$ on v_α and $S_{\alpha\beta}$. For this, we consider the case of $\bar{b}_1 \neq 0$. The data are obtained by the simulation of the full tensor model.

The phase diagrams of the spot motion are shown in Figure 8. The phase diagrams in the \bar{c} - γ plane and \bar{c} - κ plane are shown in Figures 8(a) and 8(b), respectively. We note that the behaviors in the full tensor model are similar to that in the reduced model (Figures 5(b) and 5(c)). For positive (negative) \bar{b}_1 , the region of the circular motion is larger (smaller). The phase diagrams in the \bar{b}_1 - γ plane and \bar{b}_1 - κ plane are shown in Figures 8(c) and 8(d), respectively. The behaviors are similar to the phase diagrams in the \bar{c} - γ plane and \bar{c} - κ plane. This result suggests that the effect of $\sum_\gamma U_{\alpha\beta\gamma} v_\gamma$ on the time evolution equation of $S_{\alpha\beta}$ is similar to that of $|\mathbf{v}|^2 S_{\alpha\beta}$.

The phase diagram of spot motion in the \bar{c} - \bar{b}_1 plane is shown in Figure 9. It can be seen that the circular motion occurs in the parameter region of positive and large values of \bar{c} and \bar{b}_1 . $S_{\alpha\beta}$ and $U_{\alpha\beta\gamma}$ measure the elliptical deformation and head-tail asymmetric deformation of the spot, respectively; these deformations lead to the circular motion.

The effects of \bar{c} and \bar{b}_1 on the stationary velocity v and the corresponding radius of circular motion R_c are shown in Figure 10. On comparing these figures, it can

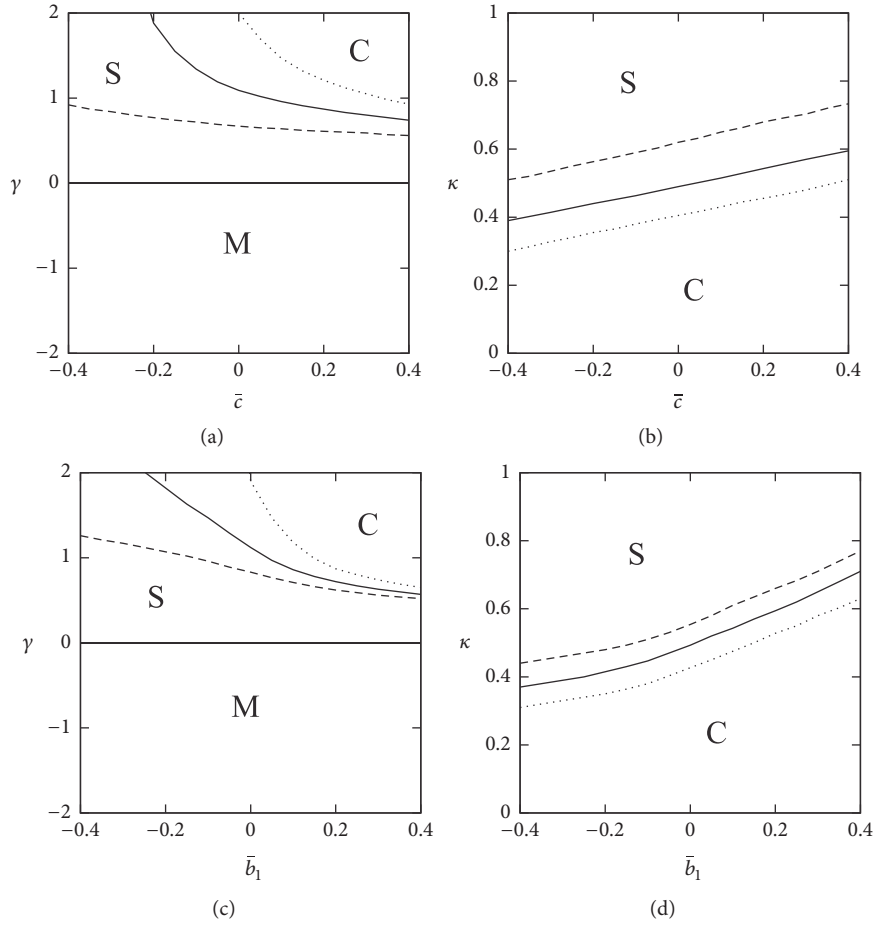


FIGURE 8: Phase diagram of spot motion. Data are obtained by the simulation of the full tensor model. $\bar{b}_s = 0.1$. M, S, and C in the figure represent regions of no motion, straight motion, and circular motion, respectively. (a) Phase diagram in the \bar{c} - γ plane. $\kappa = 0.8$. The solid, dashed, and dotted curves correspond to the cases of $\bar{b}_1 = 0, 0.25$, and -0.25 , respectively. The upper (lower) region of each curve corresponds to the region of circular (straight) motion, and the region $\gamma \leq 0$ corresponds to the region of no motion. (b) Phase diagram in the \bar{c} - κ plane. $\gamma = 0.5$. The solid, dashed, and dotted curves correspond to the cases of $\bar{b}_1 = 0, 0.25$, and -0.25 , respectively. The upper (lower) region of each curve corresponds to the region of straight (circular) motion. (c) Phase diagram in the \bar{b}_1 - γ plane. $\kappa = 0.8$. The solid, dashed, and dotted curves correspond to the cases of $\bar{c} = 0, 0.25$, and -0.25 , respectively. The region across each curve is the same as in (a). (d) Phase diagram in the \bar{b}_1 - κ plane. $\gamma = 0.5$. The solid, dashed, and dotted curves correspond to the cases of $\bar{c} = 0, 0.25$, and -0.25 , respectively. The region across each curve is the same as in (b).

be seen that although v and R_c depend on \bar{c} and \bar{b}_1 , the influences of \bar{b}_1 on v and R_c are much smaller than those of \bar{c} .

The dependence of the critical velocity $v_{c,\pm}$ and \bar{c}^* on κ is shown in Figure 11. There exists a critical velocity $v_{c,\pm}$ for $\bar{b}_1 \neq 0$ as shown in Figure 11(a). For larger \bar{b}_1 , the gap Δv_c^2 is larger. This suggests that $\bar{b}_1 \sum_\gamma U_{\alpha\beta\gamma} v_\gamma$ enhances the circular motion, which is consistent with the results shown in Figure 8. For positive \bar{b}_1 , $|\bar{c}^*|$ becomes larger than that in the reduced tensor model (solid curve) as shown in Figure 11(b). On the other hand, for negative \bar{b}_1 , there is no \bar{c}^* . In our system, \bar{b}_1 is positive and increases as the intensity of chemotaxis k_c increases as shown in Figure 4(d). Thus, \bar{c}^* still exists in the full tensor model, and $|\bar{c}^*|$ is larger than that in the reduced model.

7. Discussions

In this section, we discuss the physical origins of the braking effect observed in the previous section. For our RD system, we derived the time evolution equation of $S_{\alpha\beta}$ up to $O(\mathbf{v}^4)$ (see (77)). There were three terms of $O(\mathbf{v}^4)$: $\bar{b}_s(v_\alpha v_\beta - \delta_{\alpha\beta}|\mathbf{v}|^2/2)|\mathbf{v}|^2$, $\bar{b}_1 \sum_\gamma U_{\alpha\beta\gamma} v_\gamma$, and $\bar{c}|\mathbf{v}|^2 S_{\alpha\beta}$. The \bar{b}_s term can be absorbed into the $\bar{b}(v_\alpha v_\beta - \delta_{\alpha\beta}|\mathbf{v}|^2/2)$ term by replacing \bar{b} with $(\bar{b} + \bar{b}_s|\mathbf{v}|^2)$. Then, with increasing velocity, the \bar{b}_s term changes the value of only \bar{b} . In our theoretical analysis, considering that the influence of $U_{\alpha\beta\gamma}$ is small, we set $\bar{b}_1 = 0$ and examined the effect of $\bar{c}|\mathbf{v}|^2 S_{\alpha\beta}$ on the stationary solution in Sections 6.2 and 6.3. When up to $O(\mathbf{v}^3)$ terms were considered, there was no upper limit of velocity for

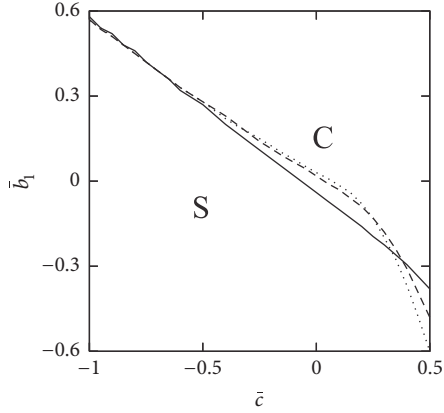


FIGURE 9: Phase diagram of spot motion in the \bar{c} - \bar{b}_1 plane. Data are obtained by the simulation of the full tensor model. $\bar{b}_s = 0.1$. The marks S and C in the figure represent regions of straight motion and circular motion, respectively. The solid, dashed, and dotted curves correspond to the cases of $(\gamma, \kappa) = (0.25, 0.3)$, $(0.5, 0.5)$, and $(1.0, 0.8)$, respectively.

the circular motion of the spot, as shown in Figure 6(a). However, on including the $O(\mathbf{v}^4)$ terms, even in the absence of chemotaxis ($k_c = 0$), $\bar{c} \neq 0$. The term $\bar{c}|\mathbf{v}|^2 S_{\alpha\beta}$ influenced the upper limit of velocity of the circular motion, as shown in Figure 6(c). One of the physical origins of the upper limit of velocity is the refractory period behind the rear interface. When $k_c = 0$, the RD system described by (5) and (6) is considered to have an activator and an inhibitor, as reported by Krischer and Mikhailov [32]. When τ is large, the motionless pulse (localized domain) in one dimension is stable. With decreasing τ , the motionless pulse is destabilized into a traveling pulse in one dimension. For a traveling pulse in one dimension, there is a refractory period behind the rear interface. A repulsive interaction occurs between pulses in the wave train; the repulsion results from the refractory period imposed on the leading interface of a traveling pulse by the tail of the preceding pulse [38]. In two dimensions, when a spot moves along a circle, there is an upper limit of velocity due to the refractory period behind the rear interface; the refractory period causes a braking effect on the velocity of the spot traveling along a circle.

In the absence of chemotaxis, that is, $k_c = 0$, we estimate the upper limit of velocity. Let us consider the traveling pulse with velocity c in one dimension of the system described by (5) and (6) in the limit $\epsilon \rightarrow 0$. The spatial dependence of the inhibitor before the leading interface and that behind the rear interface are given by $v_{\text{lead}}(z) = C_{\text{lead}} \exp(\lambda_- z)$ ($z > 0$) and $v_{\text{rear}}(z) = C_{\text{rear}} \exp(\lambda_+ z)$ ($z < 0$), respectively, where $z = x - ct$, $\lambda_{\pm} = [-c \pm \sqrt{c^2 + 4\beta}]/2$, and $C_{\text{lead(rear)}}$ is a coefficient. Using these expressions, we estimate the relaxation length (refractory period) of the inhibitor behind the rear interface by the linear approximation of $1/\lambda_+ \sim c/\beta$ for large c . For the spot moving along a circle with a given radius r_0 , the upper limit of velocity c_{max} will approximately satisfy the relation $2\pi r_0 \gg 1/\lambda_+ \sim c_{\text{max}}/\beta$: $c_{\text{max}} \ll 2\pi r_0 \beta$. This suggests that, for large c , the refractory period is proportional to c . As the

velocity of the spot increases, the inhibitor at the leading interfaces becomes large due to the overlap, and, therefore, the velocity becomes small (because of the first term in (16)). These effects on velocity are manifested when the spot moves rapidly along a circle with a small radius.

In the presence of chemotaxis, that is, $k_c > 0$, we discuss another physical origin of the braking effect. The chemotaxis is caused by the gradient of the chemotactic substance at the interface. In our RD system, the chemotactic substance is autosecretion; it is produced inside the spot and diffuses outward. The chemotactic substance is distributed around the center of the spot and monotonically decreases away from the center. For the traveling pulse, the chemotactic substance at the rear interface is larger than that at the leading interface. The gradient of the chemotactic substance at the leading (rear) interface is negative (positive). The absolute value of the gradient of the chemotactic substance at the leading interface is larger than that at the rear interface. In addition, $(d\chi/dv)$ at the leading and rear interfaces are positive. Overall, the chemotactic velocity is negative (because of the second term in (16)). Thus, the chemotaxis in our system essentially reduces velocity.

8. Conclusions

In this study, we considered the motion of a spot solution in two dimensions under the influence of chemotaxis. Starting from a three-component RD system, we proposed a two-component (an activator and a chemotactic substance) RD system with a global coupling term. We remark that, in our model system, the spot secretes the chemotactic substance from the inside and the motion of the spot is influenced by the chemotaxis. Thus, the model is an autonomous system. The chemotaxis term is of the Keller-Segel type, and the chemotactic velocity is opposite to the traveling direction. The reason for the opposite direction is that the system involves autosecretion, and the gradient of the chemotactic substance at the leading interface is negative. Although there have been several studies on the motion of spots under the influence of chemotaxis, the chemoattractant was supplied from the outside [20–23]. The spot in these models is driven toward the source (higher concentration) point of the chemoattractant. These models are nonautonomous systems, and, therefore, different from our model.

For the RD system, by employing the method proposed in [16], we derived the equation of motion of the spot and the time evolution equations of the tensors. Terms up to the fourth order of \mathbf{v} were considered, and we found that the terms $|\mathbf{v}|^2 S_{\alpha\beta}$ and $\sum_{\gamma} U_{\alpha\beta\gamma} v_{\gamma}$ played an important role in the motion of the spot. Our numerical results suggested the existence of an upper limit of velocity for the circular motion of the spot due to the braking effect. There are two physical origins for the braking effect: the refractory period behind the rear interface and the chemotactic velocity opposite to the moving direction. The former is unique to the circular motion and is not applicable for a spot in straight motion. On the other hand, the latter is general in our autonomous chemotactic system and is applicable

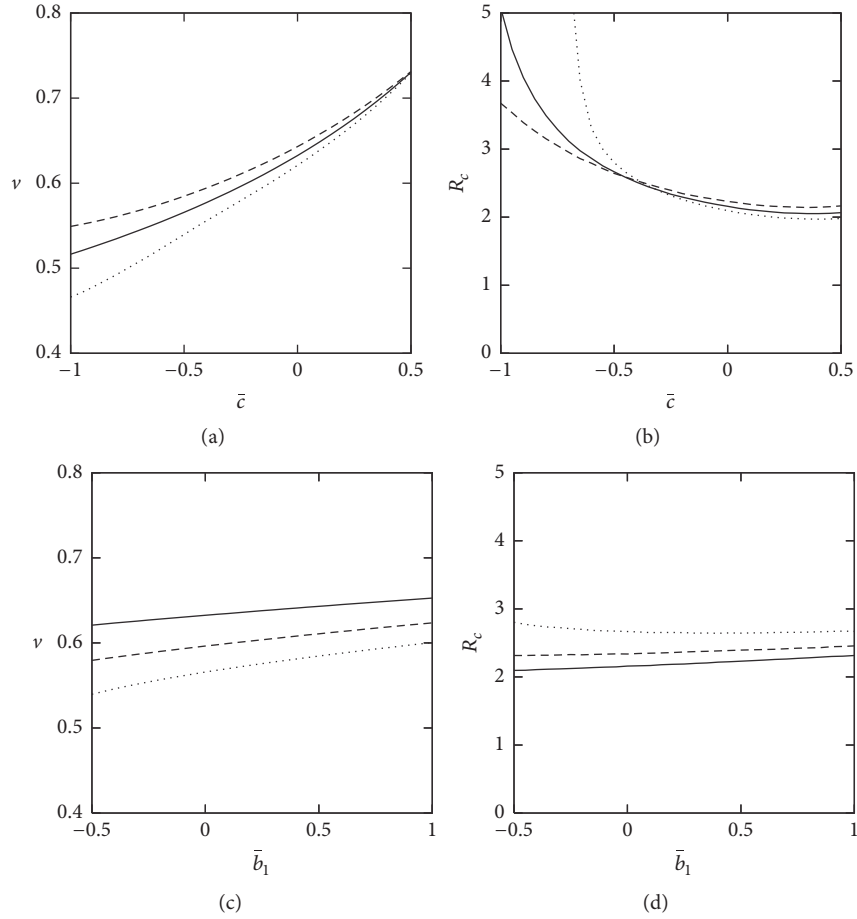


FIGURE 10: Dependence of velocity and radius on \bar{c} and \bar{b}_1 in the stationary circular motion. Data are obtained by the simulation of the full tensor model. $\bar{b}_s = 0.1$, $\gamma = 0.5$, and $\kappa = 0.2$. (a) Dependence of v on \bar{c} . (b) Dependence of R_c on \bar{c} , where, in (a) and (b), the solid, dashed, and dotted curves correspond to $\bar{b}_1 = 0, 0.5$, and -0.5 , respectively. (c) Dependence of v on \bar{b}_1 . (d) Dependence of R_c on \bar{b}_1 , where, in (c) and (d), the solid, dashed, and dotted curves correspond to $\bar{c} = 0, -0.25$, and -0.5 , respectively.

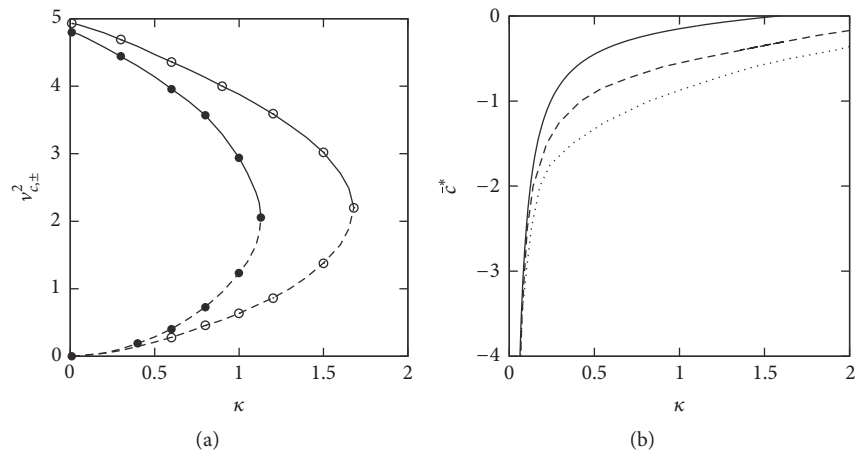


FIGURE 11: Dependence of the critical velocity $v_{c,\pm}$ and \bar{c}^* on κ . Data are obtained by the simulation of the full tensor model. $\bar{b}_s = 0.1$. (a) Dependence of $v_{c,\pm}^2$ on κ . $\bar{c} = -0.5$. The curves with filled (\bullet) and open (\circ) circles correspond to the cases of $\bar{b}_1 = 0.25$ and $\bar{b}_1 = 0.5$, respectively. The solid and dashed curves represent $v_{c,-}^2$ and $v_{c,+}^2$, respectively. (b) Dependence of \bar{c}^* on κ . $\bar{b}_s = 0.1$. The solid, dashed, and dotted curves correspond to the cases of $\bar{b}_1 = 0, 0.25$, and 0.5 , respectively.

for all moving directions. Owing to the former reason, an upper limit of velocity for the spot moving in a circle exists even in the absence of chemotaxis. Based on the results of our chemotaxis system, we conclude three points. (i) A spot moving on a straight line is destabilized to circular motion with increasing velocity. (ii) The velocity of a spot moving along a circle is restricted to a certain range, which is narrower than that in the absence of the chemotaxis. (iii) There is a critical intensity of chemotaxis k_c^* , and the spot does not undergo circular motion for $k_c > k_c^*$.

In practical experiments, the candidates of autonomous systems including chemotaxis are *E. coli* and macrophage [39, 40]. However, there is an essential difference between these biological systems and our model system; *E. coli* is a rod-shaped cell with a flagellum and macrophage has an amoeba-like shape with pseudopods, and the shape of the motionless state of these cells is not described by a circle. *E. coli* swims by rotating the flagellum, and macrophage crawls by changing its size and shape. In contrast, in our model system, the spot was a solution of an RD system and the shape of the motionless state was assumed to be a circle. The motionless spot was primarily destabilized through drift bifurcation, and it changed into a moving spot with straight motion. The straight moving spot was secondly destabilized through rotation bifurcation, and it changed into a moving spot with circular motion. Due to these differences, the bifurcation points of the straight and circular motions and the critical velocity for the circular motion in these biological systems must be different from those of our model system. However, the collective motions of bacteria and amoebas are modeled by RD systems, and many spatiotemporal patterns are shown [41, 42]: the diffusion-limited aggregation, Eden-like, uniform disk, branched, target, spiral patterns, and so on. This suggests that the behavior of individual cell in these biological systems can be described by RD systems. From these considerations, the above biological systems are promising candidates of autonomous systems including chemotaxis, and experimental observations of moving cell with circular motion are expected.

Appendix

A. Velocity of the Interface in One Dimension

Here, we derive the velocity of the interface in one dimension, given by (16), by following [43]. We denote h as the value of v at the interface $x = x_0$ at time $t = t_0$. Applying the stretching transformations $\eta = (t - t_0)/\epsilon$ and $\xi = (x - x_0)/\epsilon$ to (5), we obtain

$$\begin{aligned} \tau u_\eta = u_{\xi\xi} - \left(\frac{d\chi}{dv} \right) \Big|_i \left(\frac{dv}{dx} \right) \Big|_i u_\xi - u \\ + H(u - p) - h, \end{aligned} \quad (\text{A.1})$$

where $(A)|_i$ denotes the function A evaluated at $x = x_0$, and the position of the interface in the stretching coordinate is $\xi = 0$. In order to consider the traveling front solution of (A.1),

we introduce the moving coordinate $z = \xi - c\eta$. Then, (A.1) becomes

$$\begin{aligned} \tau u_\eta = u_{zz} + \left(\tau c - \left(\frac{d\chi}{dv} \right) \Big|_i \left(\frac{dv}{dx} \right) \Big|_i \right) u_z - u \\ + H(u - p) - h \\ \equiv u_{zz} + c' u_z - u + H(u - p) - h, \end{aligned} \quad (\text{A.2})$$

where c is the velocity of the front and $c' = (\tau c - (d\chi/dv)|_i (dv/dx)|_i)$. The boundary conditions at $z = \pm\infty$ are

$$\begin{aligned} u(-\infty, \eta) = 1 - h, \\ u(+\infty, \eta) = -h, \end{aligned} \quad (\text{A.3})$$

and the boundary conditions at $z = 0$ are

$$\begin{aligned} u(0+, \eta) = u(0-, \eta) = p, \\ u_z(0+, \eta) = u_z(0-, \eta). \end{aligned} \quad (\text{A.4})$$

The stationary solution of (A.2) is

$$u(z) = \begin{cases} C_- e^{\lambda_+ z} + (1 - h) & (z < 0), \\ C_+ e^{\lambda_- z} - h & (z \geq 0), \end{cases} \quad (\text{A.5})$$

where C_\pm is a coefficient and $\lambda_\pm = (1/2)[-c' \pm \sqrt{c'^2 + 4}]$. Under the boundary conditions (A.4), we get $C_+ = \lambda_+ / (\lambda_+ - \lambda_-) = p + h$ and $C_- = \lambda_- / (\lambda_+ - \lambda_-) = p + h - 1$. Using these relations, we obtain

$$\begin{aligned} c' = \tau c - \left(\frac{d\chi}{dv} \right) \Big|_i \left(\frac{dv}{dx} \right) \Big|_i \\ = \frac{2(1/2 - p - h)}{[(p + h)(1 - p - h)]^{1/2}}. \end{aligned} \quad (\text{A.6})$$

In the main text, τc in (A.6) is denoted as $\tau C(h)$, which is explicitly expressed as (16).

B. Explicit Expressions of $h_0^{(0)}$ and $\tilde{h}_0^{(0)}$ in the Limit $\epsilon \rightarrow 0$

We show that in the limit $\epsilon \rightarrow 0$, $h_0^{(0)}$ and $\tilde{h}_0^{(0)}$ calculated using (13) agree with the ones calculated using (34) and (35) with the substitutions $H_{\mathbf{q}} = H_{\mathbf{q}}^{(0)}$ and $\mathbf{R} = \mathbf{R}^{(0)}$, where $\mathbf{R}^{(0)} = R_0 \mathbf{e}_r$, respectively.

$h_0^{(0)}$ and $\tilde{h}_0^{(0)}$ obtained directly from (13) are

$$h_0^{(0)} = \bar{v}(R_0) = \frac{1}{\beta} - \frac{R_0}{\sqrt{\beta}} K_1 \left(\sqrt{\beta} R_0 \right) I_0 \left(\sqrt{\beta} R_0 \right), \quad (\text{B.1})$$

$$\tilde{h}_0^{(0)} = \frac{d\bar{v}(R_0)}{dr} = -R_0 I_1 \left(\sqrt{\beta} R_0 \right) K_1 \left(\sqrt{\beta} R_0 \right), \quad (\text{B.2})$$

respectively.

We first derive $h_0^{(0)}$ from the definition (34). Substituting $H_{\mathbf{q}} = H_{\mathbf{q}}^{(0)}$ and $\mathbf{R} = \mathbf{R}^{(0)}$ into (34), we obtain

$$\begin{aligned} h_0^{(0)} &= \int_{\mathbf{q}} G_{\mathbf{q}} H_{\mathbf{q}}^{(0)} e^{i\mathbf{q}\cdot\mathbf{R}^{(0)}} \\ &= R_0 \int_0^{\infty} dq \left(\frac{1}{q^2 + \beta} \right) J_0(qR_0) J_1(qR_0). \end{aligned} \quad (\text{B.3})$$

We apply the formulas of the integrals ([44])

$$\begin{aligned} \int_0^{\infty} dx \frac{x^{\mu+1}}{(x^2 + t^2)(x^2 + y^2)^{\nu/2}} J_{\nu} \left(a\sqrt{x^2 + y^2} \right) J_{\mu}(bx) \\ = \frac{t^{\mu} J_{\nu} \left(a\sqrt{y^2 - t^2} \right)}{(y^2 - t^2)^{\nu/2}} K_{\mu}(bt) \end{aligned} \quad (\text{B.4})$$

$(b \geq a > 0, |\text{Re}(\mu)| < \text{Re}(\nu) + 2),$

$$\int_0^{\infty} dx J_0(ax) J_1(bx) = \begin{cases} \frac{1}{b} & (b > a > 0), \\ \frac{1}{2b} & (b = a > 0), \\ 0 & (a > b > 0) \end{cases} \quad (\text{B.5})$$

to (B.3); we can confirm that (B.3) agrees with (B.1).

Next, we derive $\tilde{h}_0^{(0)}$ from the definition (35). Substituting $H_{\mathbf{q}} = H_{\mathbf{q}}^{(0)}$ and $\mathbf{R} = \mathbf{R}^{(0)}$ into (35), we obtain

$$\begin{aligned} \tilde{h}_0^{(0)} &= i \int_{\mathbf{q}} (\mathbf{n} \cdot \mathbf{q}) G_{\mathbf{q}} H_{\mathbf{q}}^{(0)} e^{i\mathbf{q}\cdot\mathbf{R}^{(0)}} \\ &= -R_0 \int_0^{\infty} dq \left(\frac{q}{q^2 + \beta} \right) J_1^2(qR_0). \end{aligned} \quad (\text{B.6})$$

Applying formula (B.4) to (B.6), we can confirm that (B.6) agrees with (B.2).

C. Derivation of (68)

Here, we give the detailed derivation of (68). We first derive $\delta\mathbf{h}_{1,1}^{(0)}$. Up to the first order of the deviations, $\delta\mathbf{h}_{1,1}^{(0)}$ is decomposed as

$$\begin{aligned} \delta\mathbf{h}_{1,1}^{(0)} &= \frac{i}{\Omega} \int_{\mathbf{q}} \int d\omega (\mathbf{v} \cdot \mathbf{q}) G_{\mathbf{q}}^2 H_{\mathbf{q}} e^{i\mathbf{q}\cdot\mathbf{R}} \\ &\quad - \frac{i}{\Omega} \int_{\mathbf{q}} \int d\omega (\mathbf{v} \cdot \mathbf{q}) G_{\mathbf{q}}^2 H_{\mathbf{q}}^{(0)} e^{i\mathbf{q}\cdot\mathbf{R}_0} \mathbf{R}_0 \\ &\sim \frac{i}{\Omega} \int_{\mathbf{q}} \int d\phi_r (\mathbf{v} \cdot \mathbf{q}) G_{\mathbf{q}}^2 H_{\mathbf{q}}^{(1)} e^{i\mathbf{q}\cdot\mathbf{R}_0} R_0^2 \mathbf{e}_r \\ &\quad - \frac{1}{\Omega} \int_{\mathbf{q}} \int d\phi_r (\mathbf{v} \cdot \mathbf{q}) (\mathbf{q} \cdot \delta\mathbf{R}(\phi_r)) \\ &\quad \quad \times G_{\mathbf{q}}^2 H_{\mathbf{q}}^{(0)} e^{i\mathbf{q}\cdot\mathbf{R}_0} R_0^2 \mathbf{e}_r \\ &\quad + \frac{2i}{\Omega} \int_{\mathbf{q}} \int d\phi_r (\mathbf{v} \cdot \mathbf{q}) G_{\mathbf{q}}^2 H_{\mathbf{q}}^{(0)} e^{i\mathbf{q}\cdot\mathbf{R}_0} \delta R(\phi_r) R_0 \mathbf{e}_r \\ &\equiv \Phi_1 + \Phi_2 + \Phi_3, \end{aligned} \quad (\text{C.1})$$

where δR and $H_{\mathbf{q}}$ are given in (25) and (31), respectively.

Substituting $H_{\mathbf{q}}^{(1)}$ into Φ_1 , the α ($\alpha = 1, 2$) component $\Phi_{1(\alpha)}$ is obtained as

$$\Phi_{1(\alpha)} = \frac{R_0}{2} \int dq q^2 G_{\mathbf{q}}^2 J_1 J_2 \sum_{\beta} S_{\alpha\beta} \nu_{\beta} \equiv -a_1^* \sum_{\beta} S_{\alpha\beta} \nu_{\beta}. \quad (\text{C.2})$$

Substituting $\delta\mathbf{R}(\phi_r)$ and $H_{\mathbf{q}}^{(0)}$ into Φ_2 , $\Phi_{2(\alpha)}$ is obtained as

$$\begin{aligned} \Phi_{2(\alpha)} \\ = \left[\frac{R_0}{4} \int dq q^2 G_{\mathbf{q}}^2 J_1 J_2 - \frac{R_0}{4} \int dq q^2 G_{\mathbf{q}}^2 J_0 J_1 \right] \sum_{\beta} S_{\alpha\beta} \nu_{\beta}. \end{aligned} \quad (\text{C.3})$$

Substituting $\delta R(\phi_r)$ and $H_{\mathbf{q}}^{(0)}$ into Φ_3 , $\Phi_{3(\alpha)}$ is obtained as

$$\Phi_{3(\alpha)} = - \int dq q G_{\mathbf{q}}^2 J_1^2 \sum_{\beta} S_{\alpha\beta} \nu_{\beta}. \quad (\text{C.4})$$

Using the formula for the Bessel function $(J_{n-1}(z) - J_{n+1}(z))/2 = J_n(z) - nJ_n(z)/z$, $(\Phi_{2(\alpha)} + \Phi_{3(\alpha)})$ becomes

$$\begin{aligned} (\Phi_{2(\alpha)} + \Phi_{3(\alpha)}) \\ = \left[\frac{R_0}{2} \int dq q^2 G_{\mathbf{q}}^2 J_1 J_2 - \frac{3}{2} \int dq q G_{\mathbf{q}}^2 J_1^2 \right] \sum_{\beta} S_{\alpha\beta} \nu_{\beta} \\ \equiv -a_2^* \sum_{\beta} S_{\alpha\beta} \nu_{\beta}. \end{aligned} \quad (\text{C.5})$$

a_1^* and a_2^* are the same as those of the result in [16].

Next, we derive $\delta\tilde{\mathbf{h}}_{1,1}^{(0)}$. Up to the first order of the deviations, $\delta\tilde{\mathbf{h}}_{1,1}^{(0)}$ is decomposed as

$$\begin{aligned}
\delta\tilde{\mathbf{h}}_{1,1}^{(0)} &= \frac{-1}{\Omega} \int_{\mathbf{q}} \int d\omega (\mathbf{n} \cdot \mathbf{q}) (\mathbf{v} \cdot \mathbf{q}) G_q^2 H_q e^{i\mathbf{q} \cdot \mathbf{R}} \mathbf{R} \\
&+ \frac{1}{\Omega} \int_{\mathbf{q}} \int d\omega (\mathbf{n} \cdot \mathbf{q}) (\mathbf{v} \cdot \mathbf{q}) G_q^2 H_q^{(0)} e^{i\mathbf{q} \cdot \mathbf{R}_0} \mathbf{R}_0 \\
&\sim \frac{-2}{\Omega} \int_{\mathbf{q}} \int d\phi_r (\mathbf{n} \cdot \mathbf{q}) (\mathbf{v} \cdot \mathbf{q}) G_q^2 H_q^{(0)} e^{i\mathbf{q} \cdot \mathbf{R}_0} R_0 \delta R(\phi_r) \mathbf{e}_r \\
&- \frac{1}{\Omega} \int_{\mathbf{q}} \int d\phi_r (\mathbf{n} \cdot \mathbf{q}) (\mathbf{v} \cdot \mathbf{q}) G_q^2 H_q^{(1)} e^{i\mathbf{q} \cdot \mathbf{R}_0} R_0^2 \mathbf{e}_r \\
&- \frac{1}{\Omega} \int_{\mathbf{q}} \int d\phi_r (\mathbf{n} \cdot \mathbf{q}) (\mathbf{v} \cdot \mathbf{q}) (i\mathbf{q} \cdot \delta \mathbf{R}(\phi_r)) \\
&\times G_q^2 H_q^{(0)} e^{i\mathbf{q} \cdot \mathbf{R}_0} R_0^2 \mathbf{e}_r \\
&+ \frac{1}{\Omega} \int_{\mathbf{q}} \int d\phi_r (\mathbf{v} \cdot \mathbf{q}) q \delta R'(\phi_r) \sin(\phi_q - \phi_r) \\
&\times G_q^2 H_q^{(0)} e^{i\mathbf{q} \cdot \mathbf{R}_0} R_0 \mathbf{e}_r \\
&\equiv \Psi_1 + \Psi_2 + \Psi_3 + \Psi_4.
\end{aligned} \tag{C.6}$$

Substituting $H_q^{(0)}$ and $\delta R(\phi_r)$ into Ψ_1 , the α ($\alpha = 1, 2$) component $\Psi_{1(\alpha)}$ is obtained as

$$\Psi_{1(\alpha)} = \int dq q G_q^2 (J_2 - J_0) J_1 \sum_{\beta} S_{\alpha\beta} v_{\beta}. \tag{C.7}$$

Substituting $H_q^{(1)}$ into Ψ_2 , $\Psi_{2(\alpha)}$ is obtained as

$$\Psi_{2(\alpha)} = -\frac{R_0}{4} \int dq q^2 G_q^2 (J_2 - J_0) J_2 \sum_{\beta} S_{\alpha\beta} v_{\beta}. \tag{C.8}$$

Substituting $H_q^{(0)}$ and $\delta \mathbf{R}$ into Ψ_3 , $\Psi_{3(\alpha)}$ is obtained as

$$\Psi_{3(\alpha)} = \frac{R_0}{8} \int dq q^3 G_q^2 (3J_1 - J_2) J_1 \sum_{\beta} S_{\alpha\beta} v_{\beta}. \tag{C.9}$$

Substituting $H_q^{(0)}$ and $\delta R'(\phi_r)$ into Ψ_4 , $\Psi_{4(\alpha)}$ is obtained as

$$\Psi_{4(\alpha)} = \frac{3}{4} \int dq q^2 G_q^2 J_0 J_1 \sum_{\beta} S_{\alpha\beta} v_{\beta}. \tag{C.10}$$

In the main text, $(\Psi_{3(\alpha)} + \Psi_{4(\alpha)})$ is expressed as

$$\begin{aligned}
&(\Psi_{3(\alpha)} + \Psi_{4(\alpha)}) \\
&= \int dq q^2 G_q^2 \left[\frac{R_0}{8} q (3J_1 - J_2) J_1 + \frac{3}{4} J_0 J_1 \right] \sum_{\beta} S_{\alpha\beta} v_{\beta} \\
&\equiv -\tilde{a}_1^* \sum_{\beta} S_{\alpha\beta} v_{\beta},
\end{aligned} \tag{C.11}$$

and $(\Psi_{1(\alpha)} + \Psi_{2(\alpha)})$ is expressed as

$$\begin{aligned}
&(\Psi_{1(\alpha)} + \Psi_{2(\alpha)}) \\
&= 2 \int dq q G_q^2 \left[\frac{1}{4} R_0 q J_2 - J_1 \right] \frac{\partial J_1}{\partial (q R_0)} \sum_{\beta} S_{\alpha\beta} v_{\beta} \\
&\equiv -\tilde{a}_2^* \sum_{\beta} S_{\alpha\beta} v_{\beta},
\end{aligned} \tag{C.12}$$

where we used $J_n'(z) = (J_{n-1} - J_{n+1})/2$ as the formula for the Bessel function.

D. Expansions of δh and $\delta\tilde{h}$ in (75) and (76)

The expansions of δh and $\delta\tilde{h}$ in (75) and (76) are

$$\begin{aligned}
\delta h_0 &= -\sum_n D_n c_n e^{in\phi_r}, \\
\delta h_{1,1} &= -\frac{v_-}{2} \sum_n A_n c_n e^{i(n+1)\phi_r} - \frac{v_+}{2} \sum_n B_n c_n e^{i(n-1)\phi_r}, \\
\delta h_{1,2} &= -\sum_n E_n \dot{c}_n e^{in\phi_r}, \\
\delta h_{2,2} &= -\frac{G_0}{2} |\mathbf{v}|^2 + \frac{G_1}{4} (v_-^2 e^{2i\phi_r} + v_+^2 e^{-2i\phi_r}) \\
&+ \sum_n c_n e^{in\phi_r} [v_-^2 e^{2i\phi_r} T_{n,1} - 2|\mathbf{v}|^2 T_{n,2} + v_+^2 e^{-2i\phi_r} T_{n,3}] \\
&+ \sum_n c_n e^{in\phi_r} [(v_-^2 e^{2i\phi_r} + v_+^2 e^{-2i\phi_r}) V_1 + |\mathbf{v}|^2 V_2], \\
&\dots = \dots, \\
\delta\tilde{h}_0 &= -\sum_n \tilde{D}_n c_n e^{in\phi_r}, \\
\delta\tilde{h}_{1,1} &= -\frac{v_-}{2} \sum_n (\tilde{A}_n + n\tilde{A}^*) c_n e^{i(n+1)\phi_r} \\
&- \frac{v_+}{2} \sum_n (\tilde{B}_n - n\tilde{A}^*) c_n e^{i(n-1)\phi_r}, \\
\delta\tilde{h}_{1,2} &= -\sum_n \tilde{E}_n \dot{c}_n e^{in\phi_r}, \\
\delta\tilde{h}_{2,2} &= \sum_n \tilde{S}^* c_n n (v_+^2 e^{-2i\phi_r} - v_-^2 e^{2i\phi_r}) e^{in\phi_r} \\
&+ \left[-\frac{\tilde{G}_0}{2} |\mathbf{v}|^2 + \frac{\tilde{G}_1}{4} (v_-^2 e^{2i\phi_r} + v_+^2 e^{-2i\phi_r}) \right] \\
&+ \sum_n c_n e^{in\phi_r} [v_-^2 e^{2i\phi_r} \tilde{T}_{n,1} - 2|\mathbf{v}|^2 \tilde{T}_{n,2} + v_+^2 e^{-2i\phi_r} \tilde{T}_{n,3}] \\
&+ \sum_n c_n e^{in\phi_r} [(v_-^2 e^{2i\phi_r} + v_+^2 e^{-2i\phi_r}) \tilde{V}_1 + |\mathbf{v}|^2 \tilde{V}_2], \\
&\dots = \dots,
\end{aligned} \tag{D.1}$$

where $v_{\pm} = v_1 \pm iv_2$ and all the coefficients in (D.1) and (D.2) are given in Appendix E. In order to calculate the time

evolution of c_n , $e^{-in\phi_r}$ is multiplied to both sides of eq. (74), and integration is performed over ϕ_r in the range $0 \leq \phi_r \leq 2\pi$. Using the periodicity of trigonometric functions, we obtain the time evolution equation of c_n . As the tensors \mathbf{S} and \mathbf{U} are linear combinations of $c_{\pm n}$, we can derive their time evolution equations.

E. Coefficients in (D.1) and (D.2)

We give the coefficients in (D.1) and (D.2) below. By using $F(i, j, k, l)$ and $F_d(i, j, k, l)$, they are expressed as

$$\begin{aligned}
A_n &= R_0 [F(2, 2, n, n+1) + F_d(2, 2, 1, 1)], \\
B_n &= R_0 [-F(2, 2, n, n-1) + F_d(2, 2, 1, 1)], \\
D_n &= R_0 [F(1, 1, 1, 1) - F(1, 1, n, n)], \\
E_n &= R_0 F(1, 2, n, n), \\
G_n &= R_0 F(2, 3, n, n+1), \\
G_1^s &= R_0 F(4, 5, 1, 2), \\
T_{n,1} &= \frac{R_0}{4} F(3, 3, n, n+2), \\
T_{n,2} &= \frac{R_0}{4} F(3, 3, n, n), \\
T_{n,3} &= \frac{R_0}{4} F(3, 3, n, n-2), \\
V_1 &= \frac{R_0}{4} F_d(3, 3, 1, 2), \\
V_2 &= \frac{R_0}{2} F(3, 3, 1, 1), \\
\tilde{A}_n &= R_0 \left[\frac{1}{4} (F(3, 2, 1, 3) - 3F(3, 2, 1, 1)) \right. \\
&\quad \left. + F_d(3, 2, n, n+1) \right], \\
\tilde{A}^* &= \frac{1}{2} [F(2, 2, 0, 1) + F(2, 2, 1, 2)], \\
\tilde{B}_n &= R_0 \left[\frac{1}{4} (F(3, 2, 1, 3) - 3F(3, 2, 1, 1)) \right. \\
&\quad \left. - F_d(3, 2, n, n-1) \right], \\
\tilde{D}_n &= R_0 [F_d(2, 1, 1, 1) - F_d(2, 1, n, n)], \\
\tilde{E}_n &= R_0 F_d(2, 2, n, n), \\
\tilde{G}_0 &= R_0 F_d(3, 3, 1, 0), \\
\tilde{G}_1 &= R_0 F_d(3, 3, 1, 2), \\
\tilde{G}_1^s &= R_0 F_d(5, 5, 1, 2), \\
\tilde{S}^* &= -\frac{1}{8} [F(3, 3, 1, 1) + F(3, 3, 1, 3)],
\end{aligned} \tag{E.1}$$

$$\begin{aligned}
\tilde{T}_{n,1} &= \frac{R_0}{4} F_d(4, 3, n, n+2), \\
\tilde{T}_{n,2} &= \frac{R_0}{4} F_d(4, 3, n, n), \\
\tilde{T}_{n,3} &= \frac{R_0}{4} F_d(4, 3, n, n-2), \\
\tilde{V}_1 &= \frac{R_0}{16} [F(4, 3, 0, 1) - 2F(4, 3, 1, 2) + F(4, 3, 1, 4)], \\
\tilde{V}_2 &= \frac{R_0}{2} F_d(4, 3, 1, 1).
\end{aligned} \tag{E.2}$$

Conflicts of Interest

The author declares that there are no conflicts of interest.

References

- [1] J. Elgeti, R. G. Winkler, and G. Gompper, "Physics of microswimmers-single particle motion and collective behavior: a review," *Reports on Progress in Physics*, vol. 78, no. 5, Article ID 056601, 2015.
- [2] K. Kroy, D. Chakraborty, and F. Cichos, "Hot microswimmers," *The European Physical Journal Special Topics*, vol. 225, no. 11-12, pp. 2207-2225, 2016.
- [3] A. Geiseler, P. Hänggi, and F. Marchesoni, "Self-Polarizing Microswimmers in Active Density Waves," *Scientific Reports*, vol. 7, Article ID 41884, 2017.
- [4] Y.-J. Chen and K. Yoshikawa, "Interface dynamics under nonequilibrium conditions: From a self-propelled droplet to dynamic pattern evolution," *European Physical Journal E*, vol. 34, no. 4, Article ID i2011-11038-3, 2011.
- [5] N. Yoshinaga, K. H. Nagai, Y. Sumino, and H. Kitahata, "Drift instability in the motion of a fluid droplet with a chemically reactive surface driven by Marangoni flow," *Physical Review E: Statistical, Nonlinear, and Soft Matter Physics*, vol. 86, no. 1, Article ID 016108, 2012.
- [6] S. Yabunaka, T. Ohta, and N. Yoshinaga, "Self-propelled motion of a fluid droplet under chemical reaction," *The Journal of Chemical Physics*, vol. 136, no. 7, Article ID 074904, 2012.
- [7] M. Tarama, A. M. Menzel, B. Ten Hagen, R. Wittkowski, T. Ohta, and H. Löwen, "Dynamics of a deformable active particle under shear flow," *The Journal of Chemical Physics*, vol. 139, no. 10, Article ID 104906, 2013.
- [8] M. Tarama, A. M. Menzel, and H. Löwen, "Deformable microswimmer in a swirl: Capturing and scattering dynamics," *Physical Review E: Statistical, Nonlinear, and Soft Matter Physics*, vol. 90, no. 3, Article ID 032907, 2014.
- [9] Y.-J. Chen, Y. Nagamine, and K. Yoshikawa, "Self-propelled motion of a droplet induced by Marangoni-driven spreading," *Physical Review E: Statistical, Nonlinear, and Soft Matter Physics*, vol. 80, no. 1, Article ID 016303, 2009.
- [10] S. Thutupalli, R. Seemann, and S. Herminghaus, "Swarming behavior of simple model squirmers," *New Journal of Physics*, vol. 13, Article ID 073021, 2011.
- [11] K. H. Nagai, F. Takabatake, Y. Sumino, H. Kitahata, M. Ichikawa, and N. Yoshinaga, "Rotational motion of a droplet induced by interfacial tension," *Physical Review E: Statistical, Nonlinear, and Soft Matter Physics*, vol. 87, no. 1, Article ID 013009, 2013.

- [12] S. Tanaka, Y. Sogabe, and S. Nakata, "Spontaneous change in trajectory patterns of a self-propelled oil droplet at the air-surfactant solution interface," *Physical Review E: Statistical, Nonlinear, and Soft Matter Physics*, vol. 91, no. 3, Article ID 032406, 2015.
- [13] M. Tarama, Y. Itino, A. M. Menzel, and T. Ohta, "Individual and collective dynamics of self-propelled soft particles," *The European Physical Journal Special Topics*, vol. 223, no. 1, pp. 121–139, 2014.
- [14] T. Ohta, "Dynamics of deformable active particles," *Journal of the Physical Society of Japan*, vol. 86, no. 7, Article ID 072001, 2017.
- [15] T. Ohta, "Pulse dynamics in a reaction-diffusion system," *Physica D: Nonlinear Phenomena*, vol. 151, no. 1, pp. 61–72, 2001.
- [16] T. Ohta, T. Ohkuma, and K. Shitara, "Deformation of a self-propelled domain in an excitable reaction-diffusion system," *Physical Review E: Statistical, Nonlinear, and Soft Matter Physics*, vol. 80, no. 5, Article ID 056203, 2009.
- [17] K. Shitara, T. Hiraiwa, and T. Ohta, "Deformable self-propelled domain in an excitable reaction-diffusion system in three dimensions," *Physical Review E: Statistical, Nonlinear, and Soft Matter Physics*, vol. 83, no. 6, Article ID 066208, 2011.
- [18] A. Nishikimi, H. Fukuhara, W. Su et al., "Sequential regulation of DOCK2 dynamics by two phospholipids during neutrophil chemotaxis," *Science*, vol. 324, no. 5925, pp. 384–387, 2009.
- [19] E. F. Keller and L. A. Segel, "Initiation of slime mold aggregation viewed as an instability," *Journal of Theoretical Biology*, vol. 26, no. 3, pp. 399–415, 1970.
- [20] J. Song and D. Kim, "Three-dimensional chemotaxis model for a crawling neutrophil," *Physical Review E: Statistical, Nonlinear, and Soft Matter Physics*, vol. 82, no. 5, Article ID 051902, 2010.
- [21] J. Song and D. Kim, "Computational kinetic study of chemotactic cell migration," *Journal of Applied Physics*, vol. 114, no. 15, Article ID 154701, 2013.
- [22] L. Zhang, J. Song, and D. Kim, "A study on the interfacial effect on cancer-cell invasion," *Journal of Applied Physics*, vol. 109, no. 7, Article ID 074702, 2011.
- [23] L. Zhang, S. Kang, and D. Kim, "Computational analysis of the effects of matrix-degrading enzymes on cancer-cell invasion," *Journal of Applied Physics*, vol. 112, no. 12, Article ID 124704, 2012.
- [24] L. M. Sander and T. S. Deisboeck, "Growth patterns of microscopic brain tumors," *Physical Review E: Statistical, Nonlinear, and Soft Matter Physics*, vol. 66, no. 5, Article ID 051901, 2002.
- [25] W. G. Tharp, R. Yadav, D. Irimia et al., "Neutrophil chemorepulsion in defined interleukin-8 gradients in vitro and in vivo," *Journal of Leukocyte Biology*, vol. 79, no. 3, pp. 539–554, 2006.
- [26] C. W. Frevert, G. Boggy, T. M. Keenan, and A. Folch, "Measurement of cell migration in response to an evolving radial chemokine gradient triggered by a microvalve," *Lab on a Chip*, vol. 6, no. 7, pp. 849–856, 2006.
- [27] T. Lämmermann, "In the eye of the neutrophil swarm-navigation signals that bring neutrophils together in inflamed and infected tissues," *Journal of Leukocyte Biology*, vol. 100, no. 1, pp. 55–63, 2016.
- [28] S. Kawaguchi and M. Mimura, "Synergistic effect of two inhibitors on one activator in a reaction-diffusion system," *Physical Review E: Statistical, Nonlinear, and Soft Matter Physics*, vol. 77, no. 4, Article ID 046201, 2008.
- [29] S. Kawaguchi, "Chemotaxis-growth under the influence of lateral inhibition in a three-component reaction-diffusion system," *Nonlinearity*, vol. 24, no. 4, pp. 1011–1031, 2011.
- [30] T. Ohta, M. Mimura, and R. Kobayashi, "Higher-dimensional localized patterns in excitable media," *Physica D: Nonlinear Phenomena*, vol. 34, no. 1-2, pp. 115–144, 1989.
- [31] M. Mimura and T. Tsujikawa, "Aggregating pattern dynamics in a chemotaxis model including growth," *Physica A: Statistical Mechanics and its Applications*, vol. 230, no. 3-4, pp. 499–543, 1996.
- [32] K. Krischer and A. Mikhailov, "Bifurcation to traveling spots in reaction-diffusion systems," *Physical Review Letters*, vol. 73, no. 23, pp. 3165–3168, 1994.
- [33] X.-Y. Chen, "Dynamics of interfaces in reaction diffusion systems," *Hiroshima Mathematical Journal*, vol. 21, no. 1, pp. 47–83, 1991.
- [34] P. G. de Gennes and J. Prost, *The Physics of Liquid Crystals*, Oxford University Press, Oxford, UK, 2nd edition, 1995.
- [35] L. G. Fel, "Tetrahedral symmetry in nematic liquid crystals," *Physical Review E: Statistical, Nonlinear, and Soft Matter Physics*, vol. 52, no. 1, pp. 702–717, 1995.
- [36] H. R. Brand, H. Pleiner, and P. E. Cladis, "Tetrahedral cross-couplings: Novel physics for banana liquid crystals," *Physica A: Statistical Mechanics and its Applications*, vol. 351, no. 2-4, pp. 189–197, 2005.
- [37] T. Hiraiwa, M. Y. Matsuo, T. Ohkuma, T. Ohta, and M. Sano, "Dynamics of a deformable self-propelled domain," *EPL (Europhysics Letters)*, vol. 91, no. 2, Article ID 20001, 2010.
- [38] E. Meron, "Pattern formation in excitable media," *Physics Reports*, vol. 218, no. 1, pp. 1–66, 1992.
- [39] E. O. Budrene and H. C. Berg, "Complex patterns formed by motile cells of *Escherichia coli*," *Nature*, vol. 349, no. 6310, pp. 630–633, 1991.
- [40] M. Kronlage, J. Song, L. Sorokin et al., "Autocrine purinergic receptor signaling is essential for macrophage chemotaxis," *Science Signaling*, vol. 3, no. 132, p. ra55, 2010.
- [41] M. Mimura, H. Sakaguchi, and M. Matsushita, "Reaction-diffusion modelling of bacterial colony patterns," *Physica A: Statistical Mechanics and its Applications*, vol. 282, no. 1, pp. 283–303, 2000.
- [42] D. A. Kessler and H. Levine, "Pattern formation in *Dicystostelium* via the dynamics of cooperative biological entities," *Physical Review E: Statistical, Nonlinear, and Soft Matter Physics*, vol. 48, no. 6, pp. 4801–4804, 1993.
- [43] J. Rinzel and D. Terman, "Propagation phenomena in a bistable reaction-diffusion system," *SIAM Journal on Applied Mathematics*, vol. 42, no. 5, pp. 1111–1137, 1982.
- [44] I. S. Gradshteyn and I. M. Ryzhik, *Table of Integrals, Series, and Products*, Academic Press, 6th edition, 2000.

Research Article

Reachable Set Bounding for a Class of Nonlinear Time-Varying Systems with Delay

Xingao Zhu,¹ Yuangong Sun ,¹ and Fanwei Meng²

¹School of Mathematical Sciences, University of Jinan, Jinan, Shandong 250022, China

²School of Mathematical Sciences, Qufu Normal University, Qufu, Shandong 273165, China

Correspondence should be addressed to Yuangong Sun; sunyuangong@163.com

Received 3 January 2018; Revised 28 February 2018; Accepted 8 March 2018; Published 11 April 2018

Academic Editor: Xin Yu

Copyright © 2018 Xingao Zhu et al. This is an open access article distributed under the Creative Commons Attribution License, which permits unrestricted use, distribution, and reproduction in any medium, provided the original work is properly cited.

We investigate the problem of reachable set bounding for a class of continuous-time and discrete-time nonlinear time-varying systems with time-varying delay. Unlike some preceding works, the involved disturbance input and time-varying delay are not assumed to be bounded. By employing an approach which does not involve the conventional Lyapunov-Krasovskii functional, new conditions are proposed such that all the state trajectories of the system converge asymptotically within a ball. Two illustrative examples are also given to show the effectiveness of the obtained results.

1. Introduction

Reachable set bounding plays an important role in ensuring safe operation in practical engineering through synthesizing controllers to avoid undesirable (or unsafe) regions in the state space [1]. Therefore, the problem of reachable set bounding with different dynamics has been investigated by many researchers in recent years in [2–7], to name a few.

Time delay has received a lot of attention due to its common presence in practical engineering and its detrimental effects on stability [8–14] and performance of systems such as oscillation [15–19]. Therefore, the problem of the reachable set bounding for systems with delay becomes very important. By using the Lyapunov-Razumikhin approach, an ellipsoid was given to bound the reachable set of linear systems with delay and bounded peak inputs in [20]. An improved condition for reachable set bounding for linear systems with delay was proposed in [21] by virtue of a Lyapunov-Krasovskii type functional and the rate of delay. Less conservative estimation results on the reachable set for delayed systems with polytopic uncertainties were established in [22, 23] by choosing pointwise maximum Lyapunov functional corresponding to a vertex of the polytope. A delay-partitioning method was applied to study the reachable set bounding problem of delayed systems in [24], which further reduced the conservatism of some existing results. By using the Lyapunov method, LMI

conditions for the existence of ellipsoid-based bounds of reachable sets of a linear uncertain discrete system were given in [25].

However, most of the aforementioned works on the reachable set bounding have been mainly focused on linear time-delay systems with constant matrices or a combination of constant matrices (polytopic uncertainties). It seems to us that little has been known about the explicit estimation of reachable set for nonlinear time-varying systems with time-varying delay. Note that it is difficult to apply the usual Lyapunov-Krasovskii functional method to time-varying systems, because it may lead to unsolvable matrix Riccati differential equations or indefinite linear matrix inequalities.

Based on a method developed in positive systems which does not involve the Lyapunov-Krasovskii functional, a delay-independent condition was derived such that all the state trajectories of linear time-varying systems converge exponentially within a ball in [26]. Recently, the result in [26] was extended to homogeneous positive systems of degree one with time-varying delays in [27]. For a class of nonlinear time-delay systems with bounded disturbances, a new approach to obtain the smallest box which bounds all reachable sets was proposed in [28]. For a switched system with nonlinear disturbance which can be bounded by a linear system, global exponential stability criteria were established in [29].

Inspired by this and motivated by the work in [30, 31], the paper will introduce a new approach which is different from the Lyapunov-Krasovskii functional method to derive new explicit conditions such that all the state trajectories of a class of continuous-time and discrete-time nonlinear time-varying systems with delay converge asymptotically within a ball. The main contribution of this paper is threefold: (1) the nonlinear term considered in this paper takes the more general form, which contains the systems studied in [26–29] as special cases; (2) the involved disturbance input and time-varying delay are not assumed to be bounded; (3) unlike some existing works, we do not need to transform the system to a time-invariant one, which leads to less conservative conditions for reachable set bounding.

The rest of this paper is briefly outlined as follows. In Section 2, we present the notation used through this paper as well as preliminaries for our results. Section 3 then focuses on deriving explicit conditions under which all the state trajectories of the system converge asymptotically within a ball. Section 4 provides two illustrative examples to show the effectiveness of the obtained results. The paper is concluded in Section 5.

2. Preliminaries

Throughout this paper, the following notation will be used. Let \mathbb{R}^n and $\mathbb{R}^{n \times n}$ denote the set of n -dimensional real vectors and the n -dimensional real Euclidean space, respectively. Denote $\mathbb{N}_0 = \{0, 1, 2, \dots\}$ and $\langle n \rangle = \{1, 2, \dots, n\}$. The matrix $A \in \mathbb{R}^{n \times n}$ is said to be *Metzler* if all its off-diagonal entries are nonnegative. For $x \in \mathbb{R}^n$, we denote by x_i the i th coordinate of x . For two vectors $x, y \in \mathbb{R}^n$, we write $x > y$ if $x_i > y_i$, $x \geq y$ if $x_i \geq y_i$, $x < y$ if $x_i < y_i$, $x \leq y$ if $x_i \leq y_i$, $i \in \langle n \rangle$. Let $\mathbb{R}_+^n = \{x \in \mathbb{R}^n : x \geq 0\}$. Given $x \in \mathbb{R}^n$, set $\|x\|_\infty = \max_{i \in \langle n \rangle} |x_i|$ and $|x| \in \mathbb{R}_+^n$ whose i th coordinate is $|x_i|$. The weighted ∞ -norm of the vector $x \in \mathbb{R}^n$ is defined by $\|x\|_\infty^v = \max_{i \in \langle n \rangle} (|x_i|/v_i)$, where $v > 0$ is an n -dimensional vector.

We first consider the continuous-time nonlinear time-varying system with delay

$$\begin{aligned} \dot{x}(t) &= F(t, x(t)) + G(t, x(t - \tau(t))) + w(t), \quad t \geq 0, \\ x(t) &= \phi(t), \quad t \in [-\tau_{\max}, 0], \end{aligned} \quad (1)$$

where $x(t) \in \mathbb{R}^n$ is the state vector, the time-varying delay $\tau(t)$ is continuous on $[0, \infty)$ and satisfies $t - \tau(t) \geq -\tau_{\max}$ with $\tau_{\max} > 0$, $w(t) : [0, \infty) \rightarrow \mathbb{R}^n$ is the continuous disturbance input, $\phi \in \mathcal{C}([-\tau_{\max}, 0], \mathbb{R}^n)$ is the continuous vector valued function specifying the initial state of the system, and the vector fields $F(t, x), G(t, x) : [0, \infty) \times \mathbb{R}^n \rightarrow \mathbb{R}^n$ are continuous and locally Lipschitz with respect to x , which ensures the existence and uniqueness of solutions of system (1) [32].

We also consider the following discrete-time nonlinear time-varying system with delay described by

$$\begin{aligned} x(k+1) &= F(k, x(k)) + G(k, x(k-d(k))) + w(k), \\ k &\in \mathbb{N}_0, \end{aligned}$$

$$x(k) = \phi(k), \quad k \in \{-d_{\max}, \dots, 0\}, \quad (2)$$

where $x(k) \in \mathbb{R}^n$ is the state vector, the time-varying delay $d(k) : \mathbb{N}_0 \rightarrow \mathbb{N}_0$ satisfies $k - d(k) \geq -d_{\max}$ with $d_{\max} > 0$, the vector fields $F, G : \mathbb{N}_0 \times \mathbb{R}^n \rightarrow \mathbb{R}^n$, $w(k) : \mathbb{N}_0 \rightarrow \mathbb{R}^n$ is the disturbance input, and $\phi : \{-d_{\max}, \dots, 0\} \rightarrow \mathbb{R}^n$ is the vector sequence specifying the initial state of the system.

We first extend some definitions given in [33] to the time variant case.

Definition 1. A continuous vector field $f(t, x) : [0, \infty) \times \mathbb{R}^n \rightarrow \mathbb{R}^n$, which is continuously differentiable with respect to x on $\mathbb{R}^n \setminus \{0\}$, is said to be cooperative if the Jacobian matrix $(\partial f / \partial x)(t, a)$ is Metzler for all $t \in [0, \infty)$ and $a \in \mathbb{R}_+^n \setminus \{0\}$.

Definition 2. $g : [0, \infty) \times \mathbb{R}^n \rightarrow \mathbb{R}^n$ is order-preserving on \mathbb{R}_+^n if $g(t, x) \geq g(t, y)$ for any $t \in [0, \infty)$ and any $x, y \in \mathbb{R}_+^n$ satisfying $x \geq y$.

Definition 3. $f : [0, \infty) \times \mathbb{R}^n \rightarrow \mathbb{R}^n$ is said to be homogeneous if, for all $t \in [0, \infty)$, all $x \in \mathbb{R}^n$, and all real $\lambda > 0$, $f(t, \lambda x) = \lambda f(t, x)$.

It can be similarly shown as in [33] that cooperative vector fields have the following property.

Proposition 4. *Let the vector field $f : [0, \infty) \times \mathbb{R}^n \rightarrow \mathbb{R}^n$ be cooperative. For any two vectors $x, y \in \mathbb{R}_+^n$, with $x_i = y_i$ and $x \geq y$, one has $f_i(t, x) \geq f_i(t, y)$ for $t \in [0, \infty)$.*

3. Main Results

We first study the reachable set bounding for the continuous-time system (1). Assume that the vector fields F and G satisfy the following assumption.

Assumption A1. (i) There exists a cooperative and homogeneous vector field $f : [0, \infty) \times \mathbb{R}^n \rightarrow \mathbb{R}^n$ such that $F_i(t, x) \text{sign}(x_i) \leq f_i(t, |x|)$ for $t \geq 0$, $x \in \mathbb{R}^n$, $x_i \neq 0$, and $i \in \langle n \rangle$.

(ii) There exists a homogeneous and order-preserving vector field $g : [0, \infty) \times \mathbb{R}^n \rightarrow \mathbb{R}^n$ such that $|G(t, x)| \leq g(t, |x|)$ for $t \geq 0$ and $x \in \mathbb{R}^n$.

Theorem 5. *Suppose that Assumption A1 holds, and there exist a vector $v > 0$ and a differential function $\mu : [-\tau_{\max}, \infty) \rightarrow (0, \infty)$ with $\mu(t) \equiv \mu(0)$ for $t \in [-\tau_{\max}, 0]$, such that $\lim_{t \rightarrow +\infty} \mu(t) = 0$,*

$$f(t, v) + g(t, v) < 0, \quad t \geq 0, \quad (3)$$

$$\frac{f_i(t, v)}{v_i} \mu(t) + \frac{g_i(t, v)}{v_i} \mu(t - \tau(t)) - \dot{\mu}(t) < 0, \quad (4)$$

$$t \geq 0, \quad i \in \langle n \rangle.$$

If there exists a positive constant ε_0 satisfying

$$\frac{-|w_i(t)|}{f_i(t, v) + g_i(t, v)} \leq \varepsilon_0, \quad t \geq 0, \quad i \in \langle n \rangle, \quad (5)$$

then each solution $x(t)$ of system (1) with the initial condition $x(t) = \phi(t)$, $t \in [-\tau_{\max}, 0]$, satisfies

$$\|x(t)\|_{\infty}^v \leq \varepsilon_0 + \bar{K}\mu(t), \quad t \geq 0, \quad (6)$$

where $\bar{K} = K/\mu(0)$, $K = \max\{0, \|\phi\| - \varepsilon_0\}$ and $\|\phi\| = \sup_{t \in [-\tau_{\max}, 0]} \|\phi(t)\|_{\infty}^v$.

Proof. Denote

$$z_i(t) = \frac{|x_i(t)|}{v_i} - \varepsilon_0 - \bar{K}\mu(t), \quad t \geq 0, \quad i \in \langle n \rangle. \quad (7)$$

Based on definitions of \bar{K} and $\|\phi\|$, we have that $z_i(t) \leq 0$ for all $i \in \langle n \rangle$ and $t \in [-\tau_{\max}, 0]$. Next we will prove that $z_i(t) \leq 0$ for all $i \in \langle n \rangle$ and $t \geq 0$. Otherwise, there exists an index $m_1 \in \langle n \rangle$ and $t_* > 0$, such that $z_i(t) \leq 0$ for $i \in \langle n \rangle$ and $t \in [-\tau_{\max}, t_*]$, $z_{m_1}(t_*) = 0$, and

$$\dot{z}_{m_1}(t_*) \geq 0. \quad (8)$$

By the definition of $z_i(t)$, we have that

$$\begin{aligned} |x(t_*)| &\leq (\varepsilon_0 + \bar{K}\mu(t_*))v, \\ |x_{m_1}(t_*)| &= (\varepsilon_0 + \bar{K}\mu(t_*))v_{m_1}. \end{aligned} \quad (9)$$

Since f is cooperative and homogeneous, we get from Proposition 4 that

$$\begin{aligned} f_{m_1}(t_*, |x(t_*)|) &\leq f_{m_1}(t_*, (\varepsilon_0 + \bar{K}\mu(t_*))v) \\ &= (\varepsilon_0 + \bar{K}\mu(t_*))f_{m_1}(t_*, v). \end{aligned} \quad (10)$$

Noting that $t_* - \tau(t_*) \in [-\tau_{\max}, t_*]$, we obtain

$$|x(t_* - \tau(t_*))| \leq (\varepsilon_0 + \bar{K}\mu(t_* - \tau(t_*)))v. \quad (11)$$

Since g is order-preserving and homogeneous, we have

$$\begin{aligned} g_{m_1}(t_*, |x(t_* - \tau(t_*))|) \\ \leq g_{m_1}(t_*, (\varepsilon_0 + \bar{K}\mu(t_* - \tau(t_*)))v) \\ = (\varepsilon_0 + \bar{K}\mu(t_* - \tau(t_*)))g_{m_1}(t_*, v). \end{aligned} \quad (12)$$

Therefore, we can get from Assumption A1, (10), and (12) that

$$\begin{aligned} \dot{z}_{m_1}(t_*) &= \frac{D_- |x_{m_1}(t_*)|}{v_{m_1}} - \bar{K}\dot{\mu}(t_*) \\ &\leq \frac{1}{v_{m_1}} [f_{m_1}(t_*, |x(t_*)|) \\ &\quad + g_{m_1}(t_*, |x(t_* - \tau(t_*))|) + |w_{m_1}(t_*)|] \\ &\quad - \bar{K}\dot{\mu}(t_*) \leq \frac{1}{v_{m_1}} [\varepsilon_0 (f_{m_1}(t_*, v) + g_{m_1}(t_*, v)) \\ &\quad + |w_{m_1}(t_*)|] + \bar{K} \left[\frac{f_{m_1}(t_*, v)}{v_{m_1}} \mu(t_*) \right. \\ &\quad \left. + \frac{g_{m_1}(t_*, v)}{v_{m_1}} \mu(t_* - \tau(t_*)) - \dot{\mu}(t_*) \right]. \end{aligned} \quad (13)$$

By using (3) and (5), we have that

$$\varepsilon_0 (f_{m_1}(t_*, v) + g_{m_1}(t_*, v)) + |w_{m_1}(t_*)| \leq 0. \quad (14)$$

This together with (4) and (13) yields $\dot{z}_{m_1}(t_*) < 0$, which is a contradiction with (8). As a result, $z_i(t) \leq 0$ for $t \geq 0$; that is,

$$\frac{|x_i(t)|}{v_i} \leq \varepsilon_0 + \bar{K}\mu(t), \quad t \geq 0, \quad i \in \langle n \rangle. \quad (15)$$

It implies that $\|x(t)\|_{\infty}^v \leq \varepsilon_0 + \bar{K}\mu(t)$ for $t \geq 0$. This completes the proof of Theorem 5. \square

Remark 6. In Theorem 5, conditions (3), (4), and (5) arisen from Assumption A1 depend on the time t . Such conditions may be less conservative for some cases since they do not require that the disturbance and the time-varying delay are bounded. If we further assume that $f(t, v) \leq f(v)$, $g(t, v) \leq g(v)$, and $|w_i(t)| \leq \varepsilon_i$ for $t \geq 0$ and $i \in \langle n \rangle$, where $f(v)$ is a time-invariant, cooperative, and homogeneous vector field, $g(v)$ is a time-invariant, homogeneous, and order-preserving vector field, and ε_i are constants, then conditions (3) and (5) are independent of time and hence become verifiable, and $\mu(t)$ can be chosen to be $e^{-\lambda t}$ for some $\lambda > 0$ in condition (4).

In the sequel, we study the reachable set bounding for the discrete-time system (2), where the vector fields F and G satisfy the following assumption.

Assumption A2. There exist homogeneous and order-preserving vector fields f and g such that $|F(k, x)| \leq f(k, |x|)$ and $|G(k, x)| \leq g(k, |x|)$ for $k \in \mathbb{N}_0$ and $x \in \mathbb{R}^n$.

Theorem 7. Assume that Assumption A2 holds, and there exist a vector $v > 0$ and a positive sequence $\gamma(k)$ with $\gamma(k) \equiv \gamma(0)$ for $k \in \{-d_{\max}, \dots, 0\}$, such that $\lim_{k \rightarrow +\infty} \gamma(k) = 0$,

$$f(k, v) + g(k, v) < v, \quad k \in \mathbb{N}_0, \quad (16)$$

$$\begin{aligned} \frac{f_i(k, v)}{v_i} \gamma(k) + \frac{g_i(k, v)}{v_i} \gamma(k - d(k)) &< \gamma(k + 1), \\ k \in \mathbb{N}_0, \quad i \in \langle n \rangle. \end{aligned} \quad (17)$$

If there exists a positive constant ε_0 satisfying

$$\frac{-|w_i(k)|}{f_i(k, v) + g_i(k, v) - v_i} \leq \varepsilon_0, \quad k \in \mathbb{N}_0, \quad i \in \langle n \rangle, \quad (18)$$

then for any sequence $\phi(k) \in \mathbb{R}^n$ defined on $\{-d_{\max}, \dots, 0\}$, the solution of system (2) satisfies

$$\|x(k)\|_{\infty}^v \leq \varepsilon_0 + \widehat{K}\gamma(k), \quad k \in \mathbb{N}_0, \quad (19)$$

where $\widehat{K} = K/\gamma(0)$, $K = \max\{0, \|\phi\| - \varepsilon_0\}$ and $\|\phi\| = \max_{k \in \{-d_{\max}, \dots, 0\}} \|\phi(k)\|_{\infty}^v$.

Proof. We first have

$$\|x(k)\|_{\infty}^v \leq \|\phi\| \leq \varepsilon_0 + \widehat{K}\gamma(k), \quad k \in \{-d_{\max}, \dots, 0\}. \quad (20)$$

Assume that

$$\|x(k)\|_{\infty}^v \leq \varepsilon_0 + \widehat{K}\gamma(k), \quad k \in \{0, 1, \dots, m\}. \quad (21)$$

That is,

$$|x(k)| \leq (\varepsilon_0 + \widehat{K}\gamma(k))v, \quad k \in \{-d_{\max}, \dots, m\}. \quad (22)$$

Since f and g are homogeneous and order-preserving, we get from Assumption A2 that

$$\begin{aligned} |F(m, x(m))| &\leq f(m, |x(m)|) \\ &\leq [\varepsilon_0 + \widehat{K}\gamma(m)] f(m, v), \\ |G(m, x(m-d(m)))| &\leq g(m, |x(m-d(m))|) \\ &\leq [\varepsilon_0 + \widehat{K}\gamma(m-d(m))] g(m, v). \end{aligned} \quad (23)$$

Therefore,

$$\begin{aligned} \frac{|x_i(m+1)|}{v_i} &\leq \frac{1}{v_i} [f_i(m, |x(m)|) \\ &\quad + g_i(m, |x(m-d(m))|) + |w_i(m)|] \\ &\leq \frac{1}{v_i} [\varepsilon_0 (f_i(m, v) + g_i(m, v)) + |w_i(m)|] \\ &\quad + \widehat{K} \left[\frac{f_i(m, v)}{v_i} \gamma(m) + \frac{g_i(m, v)}{v_i} \gamma(m-d(m)) \right], \end{aligned} \quad (24)$$

$i \in \langle n \rangle.$

Note that conditions (16) and (18) imply that

$$\varepsilon_0 (f_i(m, v) + g_i(m, v)) + |w_i(m)| \leq \varepsilon_0 v_i, \quad i \in \langle n \rangle. \quad (25)$$

This together with (17) and (24) yields that

$$\frac{|x_i(m+1)|}{v_i} \leq \varepsilon_0 + \widehat{K}\gamma(m+1). \quad (26)$$

By induction, we have that (19) holds. This completes the proof of Theorem 7 \square

Remark 8. In Theorem 7, although conditions (16), (17), and (18) arisen from Assumption A2 depend on the time t , they may be less conservative for some cases since they do not require that the disturbance and the time-varying delay are bounded. If we further assume that $f(k, v) \leq f(v)$, $g(k, v) \leq g(v)$, and $|w_i(k)| \leq \varepsilon_i$ for $k \in \mathbb{N}_0$ and $i \in \langle n \rangle$, where $f(v)$ and $g(v)$ are time-invariant, homogeneous, and order-preserving

vector fields, and ε_i are constants, then conditions (16) and (18) are independent of time and verifiable, and $\gamma(k)$ can be chosen to be η^k for some $1 > \eta > 0$ in condition (17).

4. Numerical Examples

We now present two numerical examples to illustrate the main results of this paper.

Example 1. Consider the continuous-time nonlinear time-varying system given by (1) with

$$\begin{aligned} F(t, x) &= \begin{bmatrix} -5 + \sin t & \frac{t}{1+t} \\ \cos t & -5 - \sin t \end{bmatrix} \begin{bmatrix} x_1 \\ x_2 \end{bmatrix} \\ &\quad + \sqrt{x_1^2 + x_2^2} \begin{bmatrix} \sin t \\ \frac{t}{1+t} \end{bmatrix}, \\ G(t, x) &= \frac{x_1 x_2}{\sqrt{x_1^2 + x_2^2}} \begin{bmatrix} \cos t \\ \sin t \end{bmatrix}, \\ w(t) &= 0.05 \begin{bmatrix} \sin t \\ \cos t \end{bmatrix}, \\ \tau(t) &= 2 + \sin t. \end{aligned} \quad (27)$$

It can be seen that F and G satisfy Assumption A1 with

$$\begin{aligned} f(t, x) &\equiv \begin{bmatrix} -4x_1 + x_2 + \sqrt{x_1^2 + x_2^2} \\ x_1 - 4x_2 + \sqrt{x_1^2 + x_2^2} \end{bmatrix}, \\ g(t, x) &\equiv \frac{x_1 x_2}{\sqrt{x_1^2 + x_2^2}} \begin{bmatrix} 1 \\ 1 \end{bmatrix}, \end{aligned} \quad (28)$$

$t \geq 0.$

Condition (3) reduces to

$$\begin{aligned} -4v_1 + v_2 + \sqrt{v_1^2 + v_2^2} + \frac{v_1 v_2}{\sqrt{v_1^2 + v_2^2}} &< 0, \\ v_1 - 4v_2 + \sqrt{v_1^2 + v_2^2} + \frac{v_1 v_2}{\sqrt{v_1^2 + v_2^2}} &< 0. \end{aligned} \quad (29)$$

Let $\mu(t) = e^{-\lambda t}$ for $\lambda > 0$. Then, condition (4) holds if

$$\begin{aligned} \frac{-4v_1 + v_2 + \sqrt{v_1^2 + v_2^2}}{v_1} + \frac{v_1 v_2}{v_1 \sqrt{v_1^2 + v_2^2}} e^{3\lambda} + \lambda &< 0, \\ \frac{v_1 - 4v_2 + \sqrt{v_1^2 + v_2^2}}{v_2} + \frac{v_1 v_2}{v_2 \sqrt{v_1^2 + v_2^2}} e^{3\lambda} + \lambda &< 0. \end{aligned} \quad (30)$$

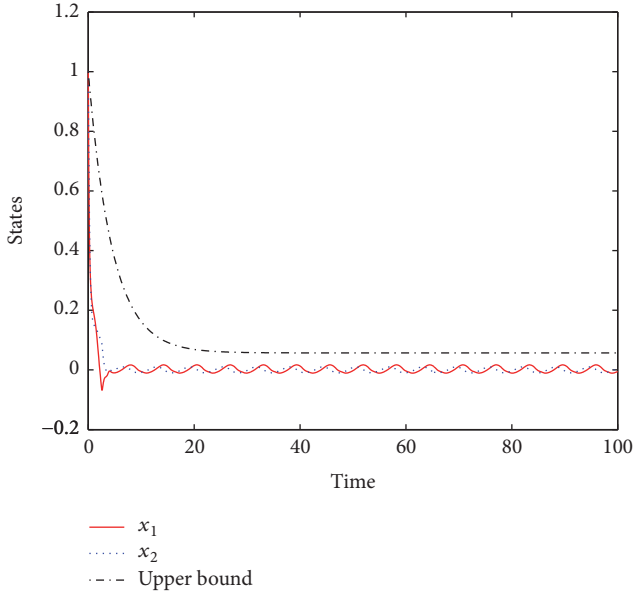


FIGURE 1: State and its upper bound of continuous-time system (1).

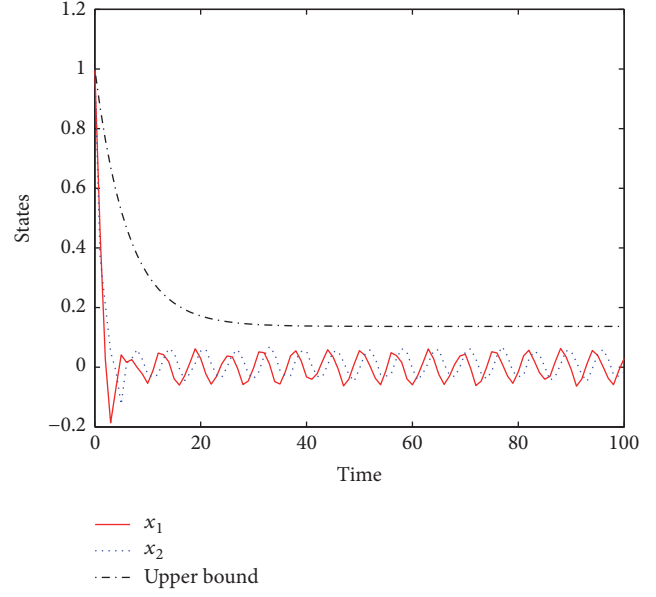


FIGURE 2: State and its upper bound of discrete-time system (2).

For given ν and λ satisfying (29) and (30), condition (5) yields that

$$\varepsilon_0 = \min \left\{ \frac{0.05}{4\nu_1 - \nu_2 - \sqrt{\nu_1^2 + \nu_2^2} - 2\nu_1\nu_2/\sqrt{\nu_1^2 + \nu_2^2}}, \frac{0.05}{-\nu_1 + 4\nu_2 - \sqrt{\nu_1^2 + \nu_2^2} - 2\nu_1\nu_2/\sqrt{\nu_1^2 + \nu_2^2}} \right\}. \quad (31)$$

Set $\nu = (1, 1)^T$ and $\lambda = 0.219$. A straightforward computation yields that conditions (29) and (30) hold, and $\varepsilon_0 = 0.057$. If we choose the initial condition $\phi(t) = (1, 1)^T$ for $t \in [-3, 0]$, then $\|\phi\| = 1$ and $\bar{K} = 0.943$. By using Theorem 5, the solution $x(t)$ of this system satisfies $\|x(t)\|_\infty^v \leq 0.057 + 0.943e^{-0.219t}$ for all $t \geq 0$. The simulation result is presented in Figure 1.

Generally speaking, the minimal parameter constant ε_0 can be determined by the following nonlinear programming problem: minimize ε_0 defined by (31) subject to $\nu > 0$, $\lambda > 0$, and (29) and (30).

Example 2. Consider the discrete-time nonlinear time-varying system given by (2) with

$$F(k, x) = 0.2\sqrt{x_1^2 + x_2^2} \begin{bmatrix} \sin k \\ k \\ 1+k \end{bmatrix},$$

$$G(k, x) = \frac{x_1 x_2}{2} \begin{bmatrix} \frac{\cos k}{\sqrt{x_1^2 + x_2^2}} \\ \sin k \\ \sqrt{2x_1^2 + 3x_2^2} \end{bmatrix},$$

$$w(k) = 0.05 \begin{bmatrix} \cos k \\ \sin k \end{bmatrix},$$

$$d(k) = 2 + \sin(0.5k\pi).$$

(32)

It is easy to see that F and G satisfy Assumption A2 with

$$f(k, x) \equiv 0.2\sqrt{x_1^2 + x_2^2} \begin{bmatrix} 1 \\ 1 \end{bmatrix},$$

$$g(k, x) \equiv \frac{x_1 x_2}{2} \begin{bmatrix} \frac{1}{\sqrt{x_1^2 + x_2^2}} \\ 1 \\ \sqrt{2x_1^2 + 3x_2^2} \end{bmatrix}, \quad (33)$$

 $k \in \mathbb{N}_0.$

By choosing the vector $\nu = (1, 1)^T$ and $\gamma(k) = \eta^k$ with $\eta = 0.852$, we have that both (16) and (17) hold. A further computation yields that $\varepsilon_0 = 0.137$. By choosing the initial condition $\phi(k) = (1, 1)^T$, we have $\|\phi\| = 1$ and $\bar{K} = 0.863$. By using Theorem 7, the solution $x(k)$ of the system satisfies $\|x(k)\|_\infty^v \leq 0.137 + 0.863(0.852)^k$ for all $k \in \mathbb{N}_0$. The simulation result is presented in Figure 2.

5. Conclusion

In this paper, the problem of reachable set bounding for a class of continuous-time and discrete-time nonlinear time-varying systems with delay has been investigated, where the involved disturbance input and time-varying delay may be unbounded. By using an approach which is different from the Lyapunov-Krasovskii functional method, we establish sufficient conditions such that all the state trajectories

of the system converge asymptotically within a ball. Two illustrative examples and simulation results are given to show the effectiveness of the obtained results.

Conflicts of Interest

The authors declare no conflicts of interest.

Acknowledgments

This paper is supported by the National Natural Science Foundation of China under Grant nos. 61473133, 11671227, and 61374074 and the Natural Science Foundation of Shandong Province under Grant no. JQ201119.

References

- [1] J. Lygeros, C. Tomlin, and S. Sastry, "Controllers for reachability specifications for hybrid systems," *Automatica*, vol. 35, no. 3, pp. 349–370, 1999.
- [2] J. Lam, B. Zhang, Y. Chen, and S. Xu, "Reachable set estimation for discrete-time linear systems with time delays," *International Journal of Robust and Nonlinear Control*, vol. 25, no. 2, pp. 269–281, 2015.
- [3] C. Shen and S. Zhong, "The ellipsoidal bound of reachable sets for linear neutral systems with disturbances," *Journal of The Franklin Institute*, vol. 348, no. 9, pp. 2570–2585, 2011.
- [4] Z. Zuo, Z. Wang, Y. Chen, and Y. Wang, "A non-ellipsoidal reachable set estimation for uncertain neural networks with time-varying delay," *Communications in Nonlinear Science and Numerical Simulation*, vol. 19, no. 4, pp. 1097–1106, 2014.
- [5] B. Zhang, J. Lam, and S. Xu, "Reachable set estimation and controller design for distributed delay systems with bounded disturbances," *Journal of The Franklin Institute*, vol. 351, no. 6, pp. 3068–3088, 2014.
- [6] Z. Zuo, D. W. Ho, and Y. Wang, "Reachable set estimation for linear systems in the presence of both discrete and distributed delays," *IET Control Theory & Applications*, vol. 5, no. 15, pp. 1808–1812, 2011.
- [7] Z. Zuo, Y. Fu, and Y. Wang, "Results on reachable set estimation for linear systems with both discrete and distributed delays," *IET Control Theory & Applications*, vol. 6, no. 14, pp. 2346–2350, 2012.
- [8] Y. Sun and J. Qi, "Note on exponential stability of certain nonlinear differential systems with time-varying delays," *Applied Mathematics Letters*, vol. 25, no. 12, pp. 2240–2245, 2012.
- [9] Y. Li, Y. Sun, and F. Meng, "New criteria for exponential stability of switched time-varying systems with delays and nonlinear disturbances," *Nonlinear Analysis: Hybrid Systems*, vol. 26, pp. 284–291, 2017.
- [10] Y. Li, Y. Sun, F. Meng, and Y. Tian, "Exponential stabilization of switched time-varying systems with delays and disturbances," *Applied Mathematics and Computation*, vol. 324, pp. 131–140, 2018.
- [11] G. Zong, H. Ren, and L. Hou, "Finite-time stability of interconnected impulsive switched systems," *IET Control Theory & Applications*, vol. 10, no. 6, pp. 648–654, 2016.
- [12] Y. Yin, G. Zong, and X. Zhao, "Improved stability criteria for switched positive linear systems with average dwell time switching," *Journal of The Franklin Institute*, vol. 354, no. 8, pp. 3472–3484, 2017.
- [13] Y. Sun, Y. Tian, and X.-J. Xie, "Stabilization of positive switched linear systems and its application in consensus of multiagent systems," *Institute of Electrical and Electronics Engineers Transactions on Automatic Control*, vol. 62, no. 12, pp. 6608–6613, 2017.
- [14] Y. Sun, Z. Wu, and F. Meng, "Common weak linear copositive Lyapunov functions for positive switched linear systems," *Complexity*, vol. 2018, 7 pages, 2018.
- [15] F. Meng and Y. Huang, "Interval oscillation criteria for a forced second-order nonlinear differential equations with damping," *Applied Mathematics and Computation*, vol. 218, no. 5, pp. 1857–1861, 2011.
- [16] H. Liu, F. Meng, and P. Liu, "Oscillation and asymptotic analysis on a new generalized Emden-Fowler equation," *Applied Mathematics and Computation*, vol. 219, no. 5, pp. 2739–2748, 2012.
- [17] J. Shao, Z. Zheng, and F. Meng, "Oscillation criteria for fractional differential equations with mixed nonlinearities," *Advances in Difference Equations*, p. 323, 2013.
- [18] J. Shao, F. Meng, and Z. Zheng, "Oscillation theorems for linear matrix Hamiltonian systems," *Applied Mathematics and Computation*, vol. 253, pp. 402–409, 2015.
- [19] H. Liu and F. Meng, "Interval oscillation criteria for second-order nonlinear forced differential equations involving variable exponent," *Advances in Difference Equations*, Paper No. 291, 14 pages, 2016.
- [20] E. Fridman and U. Shaked, "On reachable sets for linear systems with delay and bounded peak inputs," *Automatica*, vol. 39, no. 11, pp. 2005–2010, 2003.
- [21] J.-H. Kim, "Improved ellipsoidal bound of reachable sets for time-delayed linear systems with disturbances," *Automatica*, vol. 44, no. 11, pp. 2940–2943, 2008.
- [22] Z. Zuo, Y. Chen, Y. Wang, D. W. Ho, M. Z. Chen, and H. Li, "A note on reachable set bounding for delayed systems with polytopic uncertainties," *Journal of The Franklin Institute*, vol. 350, no. 7, pp. 1827–1835, 2013.
- [23] Z. Zuo, D. W. Ho, and Y. Wang, "Reachable set bounding for delayed systems with polytopic uncertainties: the maximal Lyapunov-Krasovskii functional approach," *Automatica*, vol. 46, no. 5, pp. 949–952, 2010.
- [24] P. T. Nam and P. N. Pathirana, "Further result on reachable set bounding for linear uncertain polytopic systems with interval time-varying delays," *Automatica*, vol. 47, no. 8, pp. 1838–1841, 2011.
- [25] N. D. That, P. T. Nam, and Q. P. Ha, "Reachable set bounding for linear discrete-time systems with delays and bounded disturbances," *Journal of Optimization Theory and Applications*, vol. 157, no. 1, pp. 96–107, 2013.
- [26] L. V. Hien and H. M. Trinh, "A new approach to state bounding for linear time-varying systems with delay and bounded disturbances," *Automatica*, vol. 50, no. 6, pp. 1735–1738, 2014.
- [27] N. Zhang, Y. Sun, and P. Zhao, "State bounding for homogeneous positive systems of degree one with time-varying delay and exogenous input," *Journal of The Franklin Institute*, vol. 354, no. 7, pp. 2893–2904, 2017.
- [28] P. T. Nam, P. N. Pathirana, and H. Trinh, "Reachable set bounding for nonlinear perturbed time-delay systems: the smallest bound," *Applied Mathematics Letters*, vol. 43, pp. 68–71, 2015.
- [29] J. Qi and Y. Sun, "Global exponential stability of certain switched systems with time-varying delays," *Applied Mathematics Letters*, vol. 26, no. 7, pp. 760–765, 2013.

- [30] H. R. Feyzmahdavian, T. Charalambous, and M. Johansson, "Exponential stability of homogeneous positive systems of degree one with time-varying delays," *Institute of Electrical and Electronics Engineers Transactions on Automatic Control*, vol. 59, no. 6, pp. 1594–1599, 2014.
- [31] Y. Sun and F. Meng, "Reachable set estimation for a class of nonlinear time-varying systems," *Complexity*, vol. 2017, Article ID 5876371, 6 pages, 2017.
- [32] J. K. Hale and S. M. Verduyn Lunel, *Introduction to Functional-Differential Equations*, Springer, Berlin, Germany, 1993.
- [33] H. L. Smith, *Monotone Dynamical Systems: An Introduction to the Theory of Competitive and Cooperative Systems*, American Mathematical Society, Raleigh, NC, USA, 1995.

Research Article

Traveling Wave Solutions of Two Nonlinear Wave Equations by (G'/G) -Expansion Method

Yazhou Shi,¹ Xiangpeng Li,² and Ben-gong Zhang ¹

¹School of Mathematics and Computer Science, Wuhan Textile University, Wuhan 430073, China

²Graduate Department, Wuhan Textile University, Wuhan 430073, China

Correspondence should be addressed to Ben-gong Zhang; benyan1219@126.com

Received 4 October 2017; Revised 16 January 2018; Accepted 21 January 2018; Published 22 February 2018

Academic Editor: Zhi-Yuan Sun

Copyright © 2018 Yazhou Shi et al. This is an open access article distributed under the Creative Commons Attribution License, which permits unrestricted use, distribution, and reproduction in any medium, provided the original work is properly cited.

We employ the (G'/G) -expansion method to seek exact traveling wave solutions of two nonlinear wave equations—Padé-II equation and Drinfel'd-Sokolov-Wilson (DSW) equation. As a result, hyperbolic function solution, trigonometric function solution, and rational solution with general parameters are obtained. The interesting thing is that the exact solitary wave solutions and new exact traveling wave solutions can be obtained when the special values of the parameters are taken. Comparing with other methods, the method used in this paper is very direct. The (G'/G) -expansion method presents wide applicability for handling nonlinear wave equations.

1. Introduction

With the development of computer algebra, searching exact solutions for nonlinear partial differential equations (PDEs) has become more and more attractive field for researchers. The reason is that the complicate and tedious algebraic calculation can be completed by computer symbolic system like Maple and Mathematica. As a result, a lot of numerical and exact solutions can be obtained for nonlinear PDEs, especially nonlinear wave equations in mathematical physics. These solutions will play an important role in soliton theory. In order to get exact solutions directly, many powerful methods have been introduced such as inverse scattering method [1], bilinear transformation [2], Bäcklund and Darboux transformation [3–5], tanh-sech method [6, 7], extended tanh method [8], Exp-function method [9–11], the sine-cosine method [12–14], the Jacobi elliptic function method [15], F -expansion method [16, 17], auxiliary equation method [18, 19], bifurcation method [20–22], homotopy perturbation method [23], and homogeneous balance method [24, 25]. Recently, Wang et al. [26] introduced a new approach, namely, the (G'/G) -expansion method, for a reliable treatment of the nonlinear wave equations. The useful (G'/G) -expansion method is then widely used by many authors [27–30].

In this paper, our aim is to use the (G'/G) -expansion method to study two nonlinear wave equations, namely, Padé-II equation and Drinfel'd-Sokolov-Wilson (DSW) equation.

The Padé-II equation,

$$u_t + u_x + uu_x - \frac{9}{10}u_{xxx} - \frac{19}{10}u_{xxt} = 0, \quad (1)$$

is a new nonlinear wave equation modeling unidirectional propagation of long wave in dispersive media. It is originally derived by using a padé (2, 2) approximation of the phase velocity that arises in linear water wave theory [31]. To our best knowledge, there are little works on exact solutions of this equation. Here we will use (G'/G) -expansion method to get its exact traveling wave solutions. After that the other nonlinear wave equation will be studied as

$$u_t + pvv_x = 0, \quad (2)$$

$$v_t + qv_{xxx} + ruv_x + sv_xv = 0, \quad (3)$$

where p , q , r , s are nonzero parameters. This equation was first proposed by Drinfel'd and Sokolov [32] and Wilson [33], short for DSW. Soliton structure of DSW equation was studied in [34]; the exact solutions and numerical

solutions were studied by Adomian decomposition method [35], elliptic equation method [36], and other numerical methods [37, 38]. Here the (G'/G) -expansion method will be used to get new traveling wave solutions of DSW equation.

The rest of the paper is organized as follows. In Section 2, we will shortly present a methodology of the (G'/G) -expansion method. In Section 3, the Padé-II equation and the DSW equation will be studied by the proposed method. And finally, some conclusions will be given in Section 4.

2. Description of the (G'/G) -Expansion Method

The (G'/G) -expansion method is first proposed by Wang [26]. The main steps are as follows:

Suppose that a nonlinear equation is given by

$$P(u, u_t, u_x, u_{tt}, u_{xt}, u_{xx}, \dots) = 0, \quad (4)$$

where $u = u(x, t)$ is an unknown function and P is a polynomial in $u = u(x, t)$ and its partial derivatives, in which the highest order derivatives and nonlinear terms are involved. In the following we give the main steps of the (G'/G) -expansion method.

Step 1. The traveling wave variable $u(x, t) = u(\xi)$, $\xi = x - ct$, where c is a constant, permits us to reduce (4) to an ODE for $u = u(\xi)$ in the form

$$P(u, -cu', u', c^2u'', -cu'', u'', \dots) = 0. \quad (5)$$

Step 2. Suppose that the solution of (4) can be expressed by a polynomial in (G'/G) as follows:

$$u(\xi) = \alpha_m \left(\frac{G'}{G}\right)^m + \alpha_{m-1} \left(\frac{G'}{G}\right)^{m-1} + \dots, \quad (6)$$

where $G = G(\xi)$ satisfies the second-order linear differential equation in the form

$$G'' + \lambda G' + \mu G = 0, \quad (7)$$

where $\alpha_m, \alpha_{m-1}, \dots, \alpha_0, \lambda$ and μ are constants to be determined later; $\alpha_m \neq 0$. The unwritten part in (6) is also a polynomial in (G'/G) , but the degree of which is generally equal to or less than $m - 1$. The positive integer m can be determined by considering the homogeneous balance between the highest order derivatives and nonlinear terms appearing in (5).

Step 3. Substituting (6) into (5) and using (7), collecting all terms with the same order of (G'/G) together, and then equating each coefficient of the resulting polynomial to zero yield a set of algebraic equations for $\alpha_m, \alpha_{m-1}, \dots, \alpha_0, c, \lambda$ and μ .

Step 4. Since the general solutions of (7) have been well known for us, then substituting $\alpha_m, \alpha_{m-1}, \dots, \alpha_0$ and c and the general solutions of (7) into (6), we can get the traveling wave solutions of the nonlinear differential equation (4).

3. Application of (G'/G) -Expansion Method to Padé-II Equation and DSW Equation

In this section, we will use the (G'/G) -expansion method to Padé-II equation and DSW equation to construct exact traveling wave solutions. We first study the Padé-II equation, and then the DSW equation.

3.1. Exact Traveling Wave Solutions of Padé-II Equation. In order to get traveling wave solutions of (1), we need the traveling wave transformation $u(x, t) = u(\xi)$, $\xi = x - ct$ where c is wave speed. Substituting them into (1) and integrating once, we have

$$c_1 + (1 - c)u + \frac{1}{2}u^2 + \left(\frac{19}{10}c - \frac{9}{10}\right)u'' = 0, \quad (8)$$

where c_1 is integral constant that is to be determined later.

Considering the homogeneous balance between u'' and u^2 , we have

$$m + 2 = 2m \implies m = 2. \quad (9)$$

We suppose that

$$u(\xi) = \alpha_2 \left(\frac{G'}{G}\right)^2 + \alpha_1 \left(\frac{G'}{G}\right) + \alpha_0, \quad \alpha_2 \neq 0, \quad (10)$$

where $G = G(\xi)$ satisfies the following equation

$$G'' + \lambda G' + \mu G = 0, \quad (11)$$

and $\alpha_0, \alpha_1, \alpha_2, \lambda$ and μ are constants to be determined later. By using (10) and (11), it is derived that

$$\begin{aligned} u'' &= 6\alpha_2 \left(\frac{G'}{G}\right)^4 + (2\alpha_1 + 10\lambda\alpha_2) \left(\frac{G'}{G}\right)^3 \\ &\quad + (8\alpha_2\mu + 3\lambda\alpha_1 + 4\alpha_2\lambda^2) \left(\frac{G'}{G}\right)^2 \\ &\quad + (6\lambda\mu\alpha_2 + 2\alpha_1\mu + \alpha_1\lambda^2) \left(\frac{G'}{G}\right) + 2\alpha_2\mu^2 \\ &\quad + \alpha_1\lambda\mu, \\ u^2 &= \alpha_2^2 \left(\frac{G'}{G}\right)^4 + 2\alpha_1\alpha_2 \left(\frac{G'}{G}\right)^3 \\ &\quad + (2\alpha_0\alpha_2 + \alpha_1^2) \left(\frac{G'}{G}\right)^2 + 2\alpha_0\alpha_1 \left(\frac{G'}{G}\right) \\ &\quad + \alpha_0^2. \end{aligned} \quad (12)$$

By substituting (10)–(12) into (8) and collecting all terms with the same power of G'/G together, the left-hand sides of (8) are converted into the polynomials in G'/G . Equating the coefficients of the polynomials to zero yields a set of simultaneous algebraic equations for $\alpha_0, \alpha_1, \alpha_2, \lambda, c, c_1, c_2$ and μ as follows:

$$\begin{aligned} & \frac{19c-9}{10} \times (2\alpha_2\mu^2 + \alpha_1\lambda\mu) + \frac{1}{2}\alpha_0^2 + (1-c)\alpha_0 \\ & + c_1 = 0, \\ & \frac{19c-9}{10} \times (6\lambda\mu\alpha_2 + 2\alpha_1\mu + \alpha_1\lambda^2) + \alpha_1\alpha_2 \\ & + (1-c)\alpha_1 = 0, \\ & \frac{19c-9}{10} \times (8\alpha_2\mu + 3\lambda\alpha_1 + 4\alpha_2\lambda^2) + \frac{1}{2}(2\alpha_0\alpha_2 + \alpha_1^2) \\ & + (1-c)\alpha_2 = 0, \\ & \frac{19c-9}{10} \times (2\alpha_1 + 10\lambda\alpha_2) + \alpha_1\alpha_2 = 0, \\ & \frac{19c-9}{10} \times 6\alpha_2 + \frac{1}{2}\alpha_2^2 = 0. \end{aligned} \tag{13}$$

where A_1 and A_2 are arbitrary constants.

Substituting the solution of (16) into (15), the traveling wave solutions of equation (1) can be obtained as follows.

Case 1. When $\lambda^2 - 4\mu > 0$, then we have the following exact traveling wave solution of (1):

$$\begin{aligned} u(x, t) &= u(\xi) \\ &= -\frac{3}{10}(19c-9)(\lambda^2-4\mu)A^2 + (c-1) \\ &+ \frac{2}{5}\lambda^2(19c-9) + \frac{72-152c}{10}\mu, \end{aligned} \tag{17}$$

where $A = ((A_1 \cosh((1/2)\sqrt{\lambda^2-4\mu\xi}) + A_2 \sinh((1/2)\sqrt{\lambda^2-4\mu\xi}))/ (A_1 \sinh((1/2)\sqrt{\lambda^2-4\mu\xi}) + A_2 \cosh((1/2)\sqrt{\lambda^2-4\mu\xi}))$, $\xi = x - ct$.

Case 2. When $\lambda^2 - 4\mu < 0$, then we have the following exact traveling wave solution of (1):

Solving the algebraic equations above yields

$$\begin{aligned} \alpha_2 &= -\frac{6}{5}(-9+19c), \\ \alpha_1 &= -\frac{6}{5}(-9\lambda+19c\lambda), \\ \alpha_0 &= (c-1) + \frac{19c-9}{10}\lambda^2 + \frac{72-152c}{10}\mu, \end{aligned} \tag{14}$$

$c \neq \frac{9}{19}$,

where λ and μ are constants.

Substituting system (14) into (10), we have the formulae of the solutions of (1) as follows:

$$\begin{aligned} u(x, t) &= u(\xi) \\ &= -\frac{6}{5}(-9+19c)\left(\frac{G'}{G}\right)^2 \\ &- \frac{6}{5}(-9\lambda+19c\lambda)\left(\frac{G'}{G}\right) + (c-1) \\ &+ \frac{19c-9}{10}\lambda^2 + \frac{72-152c}{10}\mu. \end{aligned} \tag{15}$$

Solving (11), we deduce after some reduction that

$$\frac{G'}{G} = \frac{1}{2}\sqrt{\lambda^2-4\mu} \left(\frac{A_1 \cosh\left(\frac{1}{2}\sqrt{\lambda^2-4\mu\xi}\right) + A_2 \sinh\left(\frac{1}{2}\sqrt{\lambda^2-4\mu\xi}\right)}{A_1 \sinh\left(\frac{1}{2}\sqrt{\lambda^2-4\mu\xi}\right) + A_2 \cosh\left(\frac{1}{2}\sqrt{\lambda^2-4\mu\xi}\right)} \right) - \frac{\lambda}{2}, \tag{16}$$

$$\begin{aligned} u(x, t) &= u(\xi) \\ &= \frac{3}{10}(19c-9)(\lambda^2-4\mu)B^2 + (c-1) \\ &+ \frac{2}{5}\lambda^2(19c-9) + \frac{72-152c}{10}\mu, \end{aligned} \tag{18}$$

where $B = ((-A_1 \sin((1/2)\sqrt{\lambda^2-4\mu\xi}) + A_2 \cos((1/2)\sqrt{\lambda^2-4\mu\xi}))/ (A_1 \cos((1/2)\sqrt{\lambda^2-4\mu\xi}) + A_2 \sin((1/2)\sqrt{\lambda^2-4\mu\xi}))$, $\xi = x - ct$.

Case 3. When $\lambda^2 - 4\mu = 0$, then we have the following exact rational solution of (1):

$$\begin{aligned} u(x, t) &= u(\xi) \\ &= -\frac{6}{5}(19c-9)\left(\frac{A_2}{A_1+A_2\xi}\right)^2 + (c-1) \\ &+ \frac{3}{5}\lambda(19c-9) + \frac{19c-9}{10}\lambda^2 + \frac{72-152c}{10}\mu, \end{aligned} \tag{19}$$

where $\xi = x - ct$, A_1, A_2, λ, μ are constants.

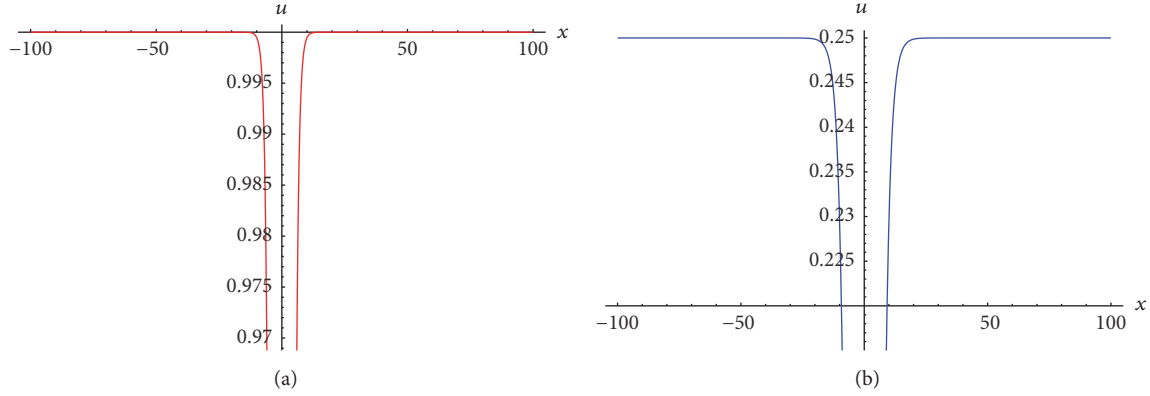


FIGURE 1: The two-dimensional profiles of the solitary wave solution (21) with $c = 1$, $t = 0$, $\lambda = 1$ ((a) red line) and $c = 1$, $t = 0$, $\lambda = 0.5$ ((b) blue line).

From the above three cases, it is not difficult to construct the solitary wave solutions and rational solutions from the general case traveling wave solutions. For example, let $A_1 = 0$, $\mu = 0$, $A_2 \neq 0$, $\lambda > 0$; then (17) yields the following solitary wave solution:

$$\begin{aligned} u(x, t) &= u(\xi) \\ &= -\frac{3}{10}(19c - 9)\lambda^2 \tanh^2\left(\frac{\lambda}{2}\xi\right) + (c - 1) \\ &\quad + \frac{2}{5}\lambda^2(19c - 9). \end{aligned} \quad (20)$$

On the other hand, if we let $A_2 = 0$, $\mu = 0$, $A_1 \neq 0$, $\lambda > 0$ then (17) yields the following solitary wave solution:

$$\begin{aligned} u(x, t) &= u(\xi) \\ &= -\frac{3}{10}(19c - 9)\lambda^2 \coth^2\left(\frac{\lambda}{2}\xi\right) + (c - 1) \\ &\quad + \frac{2}{5}\lambda^2(19c - 9), \end{aligned} \quad (21)$$

where $\xi = x - ct$.

We can see that different traveling wave solutions and rational solutions can be obtained by choosing different parameters. For example, if we choose $A_1 = 0$, $\mu = 0$, $A_2 \neq 0$, $\lambda > 0$, then substituting them into (18), (19), trigonometric function solutions and rational solutions can be obtained in the same manner.

Next we will analyze the nonlinear structure of the solitary wave solutions. We should point out that the solitary wave solution (21) possesses a singular point, while solution (18) has an infinite number of singular points. In the meaning of physics, it shows that there exists blowup phenomenon of the solutions (21) and (18). We show the blowup of solution (21) by the two-dimensional profiles in Figure 1.

3.2. Exact Traveling Wave Solutions of DSW Equation. Now we turn to study the DSW equations (2) and (3). Just as shown above, we have the following traveling wave transformation:

$$\begin{aligned} u(x, t) &= u(\xi), \\ v(x, t) &= v(\xi), \\ \xi &= x - ct. \end{aligned} \quad (22)$$

Substituting (22) into (2) and (3), respectively, we have

$$-cu' + pvv' = 0, \quad (23)$$

$$-cv' + qv''' + ruv' + su'v = 0. \quad (24)$$

Integrating (23) once and substituting it into (24) after integration, we have

$$\frac{rp + 2sp}{6c}v^3 + qv'' + \left(\frac{rc_1}{c} - c\right)v + c_2 = 0, \quad (25)$$

where c_1, c_2 are integral constants.

Considering the homogeneous balance between v'' and v^3 , we have

$$m + 2 = 3m \implies m = 1. \quad (26)$$

We suppose that

$$v(\xi) = \alpha_1 \left(\frac{G'}{G}\right) + \alpha_0, \quad \alpha_1 \neq 0, \quad (27)$$

where $G = G(\xi)$ satisfies (11) and α_0, α_1 are constants.

By using (11) and (27), it is derived that

$$\begin{aligned}
 v^3(\xi) &= \alpha_1^3 \left(\frac{G'}{G}\right)^3 + 3\alpha_0\alpha_1^2 \left(\frac{G'}{G}\right)^2 + 3\alpha_1\alpha_0^2 \left(\frac{G'}{G}\right) \\
 &\quad + \alpha_0^3, \\
 v''(\xi) &= 2\alpha_1 \left(\frac{G'}{G}\right)^3 + 3\alpha_\lambda\alpha_1 \left(\frac{G'}{G}\right)^2 \\
 &\quad + (2\alpha_1\mu + \lambda^2 + \alpha_1) \left(\frac{G'}{G}\right) + \alpha_1\lambda\mu.
 \end{aligned} \tag{28}$$

By substituting (27) and (28) into (25) and collecting all terms with the same power of G'/G together, the left-hand sides of (25) are converted into the polynomials in G'/G . Equating the coefficients of the polynomials to zero yields a set of simultaneous algebraic equations for α_0 , α_1 , λ , c , c_1 , c_2 and μ as follows:

$$\begin{aligned}
 \frac{rp + 2sp}{6c}\alpha_0^3 + q\lambda\alpha_1\mu + \left(\frac{rc_1}{c} - c\right)\alpha_0 + c_2 &= 0, \\
 \frac{rp + 2sp}{6c}\alpha_0^2\alpha_1 + 2q\alpha_1\mu + q\lambda^2\alpha_1 + \left(\frac{rc_1}{c} - c\right)\alpha_1 &= 0, \\
 \frac{rp + 2sp}{6c}\alpha_0\alpha_1^2 + 3q\alpha_1\lambda &= 0, \\
 \frac{rp + 2sp}{6c}\alpha_1^3 + 2q\alpha_1 &= 0.
 \end{aligned} \tag{29}$$

Solving the algebraic equations above yields

$$\begin{aligned}
 \alpha_1 &= \pm q \sqrt{\frac{6(\lambda^2 - 4\mu)}{p(r + 2s)}}, \\
 \alpha_0 &= \mp \lambda q \sqrt{\frac{3(\lambda^2 - 4\mu)}{2p(r + 2s)}}, \\
 c &= \frac{1}{2}(-q\lambda^2 + 4q\mu), \\
 c_1 &= 0, \\
 c_2 &= 0,
 \end{aligned} \tag{30}$$

or

$$\begin{aligned}
 \alpha_1 &= \frac{2\alpha_0}{\lambda}, \\
 c &= \frac{-rp\alpha_0^2 - 2sp\alpha_0^2}{3q\lambda^2}, \\
 c_1 &= \frac{c(2c - q\lambda^2 - 4q\mu)}{2r}, \\
 c_2 &= 0,
 \end{aligned} \tag{31}$$

where λ , α_0 are nonzero constants.

Substituting system (30) or (31) into (27), we have the formulae of the solutions of (25) as follows:

$$\begin{aligned}
 v(x, t) &= v(\xi) \\
 &= \pm q \sqrt{\frac{6(\lambda^2 - 4\mu)}{p(r + 2s)}} \left(\frac{G'}{G}\right) \\
 &\quad \mp \lambda q \sqrt{\frac{3(\lambda^2 - 4\mu)}{2p(r + 2s)}}, \\
 \xi &= x - \frac{1}{2}(-q\lambda^2 + 4q\mu)t,
 \end{aligned} \tag{32}$$

or

$$\begin{aligned}
 v(x, t) &= v(\xi) = \frac{2\alpha_0}{\lambda} \left(\frac{G'}{G}\right) + \alpha_0, \\
 \xi &= x - \frac{-rp\alpha_0^2 - 2sp\alpha_0^2}{3q\lambda^2}t,
 \end{aligned} \tag{33}$$

where α_0 , λ are nonzero constants.

Substituting the solution of (16) into (32) or (33), we can get the exact solutions of $v(x, t)$. Then substituting $v(x, t)$ into (23), we will get the solutions of $u(x, t)$. From the expression of (32) and (33), we conclude that the only difference of the exact solution $v(x, t)$ between these two cases are their coefficients. Without loss of generality, we calculate the case (33). Now substituting solution (16) into (33), the traveling wave solutions of DSW equation can be obtained as follows.

Case 1. When $\lambda^2 - 4\mu > 0$, then we have the following exact traveling wave solution of DSW equation:

$$\begin{aligned}
 v(x, t) &= v(\xi) = \frac{\alpha_0}{\lambda} \sqrt{\lambda^2 - 4\mu} \left(\frac{A_1 \cosh\left(\frac{1}{2}\sqrt{\lambda^2 - 4\mu}\xi\right) + A_2 \sinh\left(\frac{1}{2}\sqrt{\lambda^2 - 4\mu}\xi\right)}{A_1 \sinh\left(\frac{1}{2}\sqrt{\lambda^2 - 4\mu}\xi\right) + A_2 \cosh\left(\frac{1}{2}\sqrt{\lambda^2 - 4\mu}\xi\right)} \right), \\
 u(x, t) &= u(\xi) = \frac{P}{2c}v^2(\xi) + \frac{c_1}{c},
 \end{aligned} \tag{34}$$

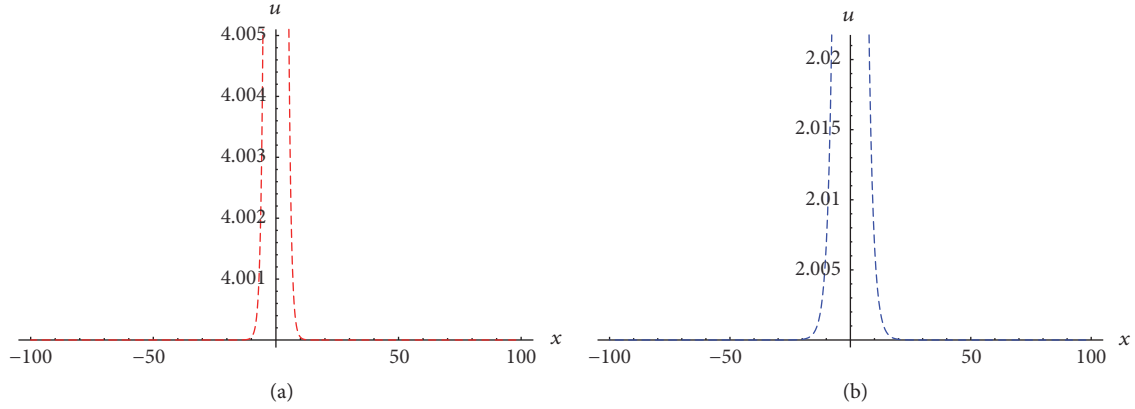


FIGURE 2: The two-dimensional profiles of the solitary wave solution (39) with $c = 1$, $t = 0$, $\lambda = 1$, $r = 0.5$, $p = q = 1$, $\alpha = 0.5$ ((a) red dashed line) and $c = 1$, $t = 0$, $\lambda = 0.5$, $r = 0.5$, $p = q = 1$, $\alpha = 0.5$ ((b) blue dashed line).

where $c = (-rp\alpha_0^2 - 2sp\alpha_0^2)/3q\lambda^2$, $c_1 = c(2c - q\lambda^2 - 4q\mu)/2r$, $\xi = x - ((-rp\alpha_0^2 - 2sp\alpha_0^2)/3q\lambda^2)t$, λ , μ , α_0 , A_1 and A_2 are constants.

Case 2. When $\lambda^2 - 4\mu < 0$, then we have the following exact traveling wave solution of DSW equation:

$$v(x, t) = v(\xi) = \frac{\alpha_0}{\lambda} \sqrt{\lambda^2 - 4\mu} \left(\frac{-A_1 \sin\left(\frac{1}{2}\sqrt{\lambda^2 - 4\mu}\xi\right) + A_2 \cos\left(\frac{1}{2}\sqrt{\lambda^2 - 4\mu}\xi\right)}{A_1 \cos\left(\frac{1}{2}\sqrt{\lambda^2 - 4\mu}\xi\right) + A_2 \sin\left(\frac{1}{2}\sqrt{\lambda^2 - 4\mu}\xi\right)} \right), \quad (35)$$

$$u(x, t) = u(\xi) = \frac{p}{2c} v^2(\xi) + \frac{c_1}{c},$$

where $c = (-rp\alpha_0^2 - 2sp\alpha_0^2)/3q\lambda^2$, $c_1 = c(2c - q\lambda^2 - 4q\mu)/2r$, $\xi = x - ((-rp\alpha_0^2 - 2sp\alpha_0^2)/3q\lambda^2)t$, λ , μ , α_0 , A_1 and A_2 are constants.

Case 3. When $\lambda^2 - 4\mu = 0$, then we have the following exact traveling wave solution of DSW equation:

$$v(x, t) = v(\xi) = \frac{2\alpha_0 A_2}{\lambda(A_1 + A_2 \xi)}, \quad (36)$$

$$u(x, t) = u(\xi) = \frac{p}{2c} v^2(\xi) + \frac{c_1}{c},$$

where $c = (-rp\alpha_0^2 - 2sp\alpha_0^2)/3q\lambda^2$, $c_1 = c(2c - q\lambda^2 - 4q\mu)/2r$, $\xi = x - ((-rp\alpha_0^2 - 2sp\alpha_0^2)/3q\lambda^2)t$, λ , μ , α_0 , A_1 and A_2 are constants.

From the above three general cases, it is not difficult to get the exact solitary wave solutions of DSW equation. For example, let $A_1 = 0$, $\mu = 0$, $A_2 \neq 0$, $\lambda > 0$; then (34) yield the following solitary wave solution:

$$v(x, t) = v(\xi) = \alpha_0 \tanh\left(\frac{\lambda}{2}\xi\right), \quad (37)$$

$$u(x, t) = u(\xi) = \frac{p\alpha_0^2}{2r} \tanh^2\left(\frac{\lambda}{2}\xi\right) + \frac{2c - q\lambda^2}{2r}.$$

On the other hand, if we let $A_2 = 0$, $\mu = 0$, $A_1 \neq 0$, $\lambda > 0$; then (17) yields the following solitary wave solution:

$$v(x, t) = v(\xi) = \alpha_0 \coth\left(\frac{\lambda}{2}\xi\right), \quad (38)$$

$$u(x, t) = u(\xi) = \frac{p\alpha_0^2}{2r} \coth^2\left(\frac{\lambda}{2}\xi\right) + \frac{2c - q\lambda^2}{2r}, \quad (39)$$

where $c = (-rp\alpha_0^2 - 2sp\alpha_0^2)/3q\lambda^2$, $c_1 = c(2c - q\lambda^2)/2r$, $\xi = x - ((-rp\alpha_0^2 - 2sp\alpha_0^2)/3q\lambda^2)t$, λ and α_0 are nonzero constants.

We can see that a number of traveling wave solutions and rational solutions can be obtained by choosing different parameters. For example, if we choose $A_1 = 0$, $\mu = 0$, $A_2 \neq 0$, $\lambda > 0$ then substituting them into (34)–(36), trigonometric function solutions and rational solutions can be obtained. To our best knowledge, the rational solutions appear the first time; they are new exact solutions of DSW equation. These new exact solutions will enrich the previous results.

We should also point out that the solitary wave solutions (38) and (39) possess a singular point, while solutions (35) have an infinite number of singular points. In the meaning of physics, it shows there exists blowup of these solutions. We also show the two-dimensional profiles of solutions (39) in Figure 2.

4. Conclusion and Discussion

In this paper, we investigate two nonlinear water wave equations which have important applications in several areas of physics and engineering by using the (G'/G) -expansion method. As a result, several pairs of exact traveling wave solutions are given directly. The most important thing is that we can get new explicit solitary wave solutions when choosing different parameters. These new exact solitary wave solutions not only enrich the previous results but also are helpful to further study these two nonlinear wave equations. Especially, for the Padé-II equation, it is a new nonlinear wave equation modeling unidirectional propagation of long wave in dispersive media. It is worth further studying. At the same time, we analyze the nonlinear structure of the solitary wave solutions. We show the blowup of the solutions (21) and (39) by plotting their two-dimensional profiles. There should be much more interesting structures of these two nonlinear wave equations. We will further study them in the near future. However, according to our study, we can conclude that the method used in this paper is a powerful mathematical tool for solving nonlinear wave equations in mathematical physics and engineering fields. It is direct and concise. Much tedious algebraic calculations can be finished by computer programmes like Mathematica, Maple, and so on. Many well known nonlinear wave equations can be handled by this method.

Conflicts of Interest

The authors declare that there are no conflicts of interest regarding the publication of this paper.

Acknowledgments

Thanks are due for Professor Chen Zeng's invitation to the George Washington University, Washington DC, USA. This research is partially supported by NSFC with nos. 11401448 and 11605125. And this work is also supported by China Scholarship Council (CSC) with no. 201608420043.

References

- [1] M. J. Ablowitz and P. A. Clarkson, *Solitons, Nonlinear Evolution Equations and Inverse Scattering*, Cambridge University Press, New York, NY, USA, 1991.
- [2] O. Pashaev and G. Tanoğlu, "Vector shock soliton and the Hirota bilinear method," *Chaos, Solitons & Fractals*, vol. 26, no. 1, pp. 95–105, 2005.
- [3] C. H. Gu, *Darboux Transformation in soliton Theory and its Gemetric Application*, Shanghai scientific and Technical Publishers, Shanghai, China, 1999.
- [4] V. B. Matveev and M. A. Salle, *Darboux Transformations and Solitons*, Springer, Berlin, Gemany, 1991.
- [5] A. Coely, *Baklund and Darboux Transform*, American Mathematical Society, Providence, RI, USA, 2001.
- [6] A.-M. Wazwaz, "The Camassa-Holm-KP equations with compact and noncompact travelling wave solutions," *Applied Mathematics and Computation*, vol. 170, no. 1, pp. 347–360, 2005.
- [7] H. A. Abdusalam, "On an improved complex tanh-function method," *International Journal of Nonlinear Sciences and Numerical Simulation*, vol. 6, no. 2, pp. 99–106, 2005.
- [8] E. Fan, "Extended tanh-function method and its applications to nonlinear equations," *Physics Letters A*, vol. 277, no. 4-5, pp. 212–218, 2000.
- [9] J. H. He, "Exp-function method for nonlinear wave equations, Chaos," *Solitons & Fractals*, vol. 30, no. 2, pp. 506–511, 2006.
- [10] J. He and M. A. Abdou, "New periodic solutions for nonlinear evolution equations using Exp-function method," *Chaos, Solitons & Fractals*, vol. 34, no. 5, pp. 1421–1429, 2007.
- [11] J. H. He and X. H. Wu, "Exp-function method and its application to nonlinear equations," *Chaos, Solitons & Fractals*, vol. 38, no. 3, pp. 903–910, 2008.
- [12] A.-M. Wazwaz, "The sine-cosine method for obtaining solutions with compact and noncompact structures," *Applied Mathematics and Computation*, vol. 159, no. 2, pp. 559–576, 2004.
- [13] A.-M. Wazwaz, "A sine-cosine method for handling nonlinear wave equations," *Mathematical and Computer Modelling*, vol. 40, no. 5-6, pp. 499–508, 2004.
- [14] A. Wazwaz and M. A. Helal, "Nonlinear variants of the BBM equation with compact and noncompact physical structures," *Chaos, Solitons & Fractals*, vol. 26, no. 3, pp. 767–776, 2005.
- [15] S. Liu, Z. Fu, S. Liu, and Q. Zhao, "Jacobi elliptic function expansion method and periodic wave solutions of nonlinear wave equations," *Physics Letters A*, vol. 289, no. 1-2, pp. 69–74, 2001.
- [16] Y. Zhou, M. Wang, and T. Miao, "The periodic wave solutions and solitary wave solutions for a class of nonlinear partial differential equations," *Physics Letters A*, vol. 323, no. 1-2, pp. 77–88, 2004.
- [17] M. Wang and X. Li, "Applications of F -expansion to periodic wave solutions for a new Hamiltonian amplitude equation," *Chaos, Solitons & Fractals*, vol. 24, no. 5, pp. 1257–1268, 2005.
- [18] B.-g. Zhang, Z.-r. Liu, and J.-f. Mao, "New exact solutions for mCH and mDP equations by auxiliary equation method," *Applied Mathematics and Computation*, vol. 217, no. 4, pp. 1306–1314, 2010.
- [19] B.-G. Zhang, W. Li, and X. Li, "Peakons and new exact solitary wave solutions of extended quantum Zakharov-Kuznetsov equation," *Physics of Plasmas*, vol. 24, no. 6, Article ID 062113, 2017.
- [20] Z. Wen, "Bifurcations and nonlinear wave solutions for the generalized two-component integrable Dullin-Gottwald-Holm system," *Nonlinear Dynamics*, vol. 82, no. 1-2, pp. 767–781, 2015.
- [21] Z. Wen, "Bifurcations and exact traveling wave solutions of a new two-component system," *Nonlinear Dynamics*, vol. 87, no. 3, pp. 1917–1922, 2017.
- [22] S. Li, Y. Li, and B.-G. Zhang, "Some singular solutions and their limit forms for generalized Calogero-Bogoyavlenskii-Schiff equation," *Nonlinear Dynamics*, vol. 85, no. 3, pp. 1665–1677, 2016.
- [23] B.-g. Zhang, S.-y. Li, and Z.-r. Liu, "Homotopy perturbation method for modified Camassa-Holm and Degasperis-Procesi equations," *Physics Letters A*, vol. 372, no. 11, pp. 1867–1872, 2008.
- [24] M. L. Wang, "Solitary wave solutions for variant Boussinesq equations," *Physics Letters A*, vol. 199, no. 3-4, pp. 169–172, 1995.
- [25] M. Wang, Y. Zhou, and Z. Li, "Application of a homogeneous balance method to exact solutions of nonlinear equations in mathematical physics," *Physics Letters A*, vol. 216, no. 1-5, pp. 67–75, 1996.

- [26] M. L. Wang, X. Z. Li, and J. L. Zhang, "The G'/G -expansion method and travelling wave solutions of nonlinear evolution equations in mathematical physics," *Phys Lett A*, pp. 417–423, 2008.
- [27] M. Wang, J. Zhang, and X. Li, "Application of the G'/G -expansion to travelling wave solutions of the Broer-Kaup and the approximate long water wave equations," *Applied Mathematics and Computation*, vol. 206, no. 1, pp. 321–326, 2008.
- [28] B.-G. Zhang, "Analytical and multishaped solitary wave solutions for extended reduced ostrovsky equation," *Abstract and Applied Analysis*, vol. 2013, Article ID 670847, 2013.
- [29] Y.-B. Zhou and C. Li, "Application of modified G'/G -expansion method to traveling wave solutions for Whitham-Broer-Kaup-like equations," *Communications in Theoretical Physics*, vol. 51, no. 4, pp. 664–670, 2009.
- [30] M. Mirzazadeh, M. Eslami, and A. Biswas, "Soliton solutions of the generalized Klein-Gordon equation by using (G'/G) -expansion method," *Computational & Applied Mathematics*, vol. 33, no. 3, pp. 831–839, 2014.
- [31] R. Fetecau and D. Levy, "Approximate model equations for water waves," *Communications in Mathematical Sciences*, vol. 3, no. 2, pp. 159–170, 2005.
- [32] V. G. Drinfeld and V. V. Sokolov, "Equations of Korteweg-de Vries type, and simple Lie algebras," *Doklady Akademii Nauk SSSR*, vol. 258, no. 1, pp. 11–16, 1981.
- [33] G. Wilson, "The affine Lie algebra $C_2(1)$ and an equation of Hirota and Satsuma," *Physics Letters A*, vol. 89, no. 7, pp. 332–334, 1982.
- [34] R. Hirota, B. Grammaticos, and A. Ramani, "Soliton structure of the Drinfeld-Sokolov-Wilson equation," *Journal of Mathematical Physics*, vol. 27, no. 6, pp. 1499–1505, 1986.
- [35] M. Inc, "On numerical doubly periodic wave solutions of the coupled Drinfeld-Sokolov-Wilson equation by the decomposition method," *Applied Mathematics and Computation*, vol. 172, no. 1, pp. 421–430, 2006.
- [36] H. T. Chen, "New Double Periodic Solutions of the Classical Drinfeld-Sokolov-Wilson Equation," *Numerical Analysis and Applied Mathematics*, vol. 1048, pp. 138–142, 2008.
- [37] C. Liu and X. Liu, "Exact solutions of the classical Drinfeld-Sokolov-Wilson equations and the relations among the solutions," *Physics Letters A*, vol. 303, no. 2-3, pp. 197–203, 2002.
- [38] Y. Yao, "Abundant families of new traveling wave solutions for the coupled Drinfeld-Sokolov-Wilson equation," *Chaos, Solitons & Fractals*, vol. 24, no. 1, pp. 301–307, 2005.

Research Article

Chaos in a System with an Absolute Nonlinearity and Chaos Synchronization

Victor Kamdoun Tamba,¹ Karthikeyan Rajagopal ²,
Viet-Thanh Pham ³, and Duy Vo Hoang³

¹Department of Telecommunication and Network Engineering, IUT-Fotso Victor of Bandjoun, University of Dschang, P.O. Box 134, Bandjoun, Cameroon

²Department of Electrical and Communication Engineering, The PNG University of Technology, Lae, Morobe, Papua New Guinea

³Modeling Evolutionary Algorithms Simulation and Artificial Intelligent, Faculty of Electrical & Electronics Engineering, Ton Duc Thang University, Ho Chi Minh City, Vietnam

Correspondence should be addressed to Viet-Thanh Pham; phamvietthanh@tdt.edu.vn

Received 21 October 2017; Revised 21 December 2017; Accepted 2 January 2018; Published 30 January 2018

Academic Editor: Zhi-Yuan Sun

Copyright © 2018 Victor Kamdoun Tamba et al. This is an open access article distributed under the Creative Commons Attribution License, which permits unrestricted use, distribution, and reproduction in any medium, provided the original work is properly cited.

A system with an absolute nonlinearity is studied in this work. It is noted that the system is chaotic and has an adjustable amplitude variable, which is suitable for practical uses. Circuit design of such a system has been realized without any multiplier and experimental measurements have been reported. In addition, an adaptive control has been applied to get the synchronization of the system.

1. Introduction

Although chaos in dynamic systems has been investigated for many years [1–4], new systems with chaos still attract the attention of numerous researches [5–11]. Finding new chaotic systems and investigating chaos control and chaos synchronization methodologies are attractive topics [12–15] due to the applications of chaos in various areas such as waveforms of chaotic radar [16], image encryption [17], secure image transmission [18], video encryption design [19], and S-box construction [20].

Previous studies suggest that absolute function is effective to design chaotic systems [21, 22]. It is worth noting that an absolute term is not a quadratic nonlinearity and can be implemented with diodes and operational amplifiers [22]. By using an absolute term, one of the most elementary chaotic systems was introduced by Linz and Sprott [21]. Such a system was also realized by a circuit [22]. Jerk systems with absolute nonlinearities were presented in [23]. Authors investigated the synchronization of a chaotic system, which includes only four terms and an absolute-value nonlinearity [24]. In addition, absolute-value term was explored to propose

a hyperchaotic circuit without any multiplier [25]. Huang and Liu introduced a fractional-order chaotic system with the presence of an absolute term [26]. Bao et al. designed a memristor-based system with four line equilibria by implementing three absolute terms [27]. It is interesting that adjustable amplitude of chaotic attractor was obtained with absolute terms [28].

The aim of this work is to study a simple system with chaos. There is only one nonlinear term, an absolute nonlinearity, in such system. It is noted that the system exhibits variable chaotic attractors, which have been rarely investigated in Sprott's systems with absolute-value nonlinearity and six terms. Dynamics, circuit, and synchronization of such a system with an absolute nonlinearity are presented in the next sections.

2. The System with an Absolute Term and Its Dynamics

Absolute function has been applied to construct different systems with chaotic behavior [27, 28]. In this work, by

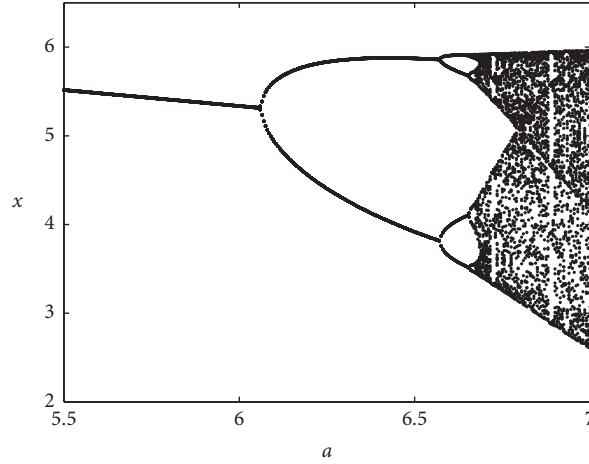


FIGURE 1: Presentation of the bifurcation diagram for $a \in [5.5, 7]$, while $b = 4$ and $c = 1$.

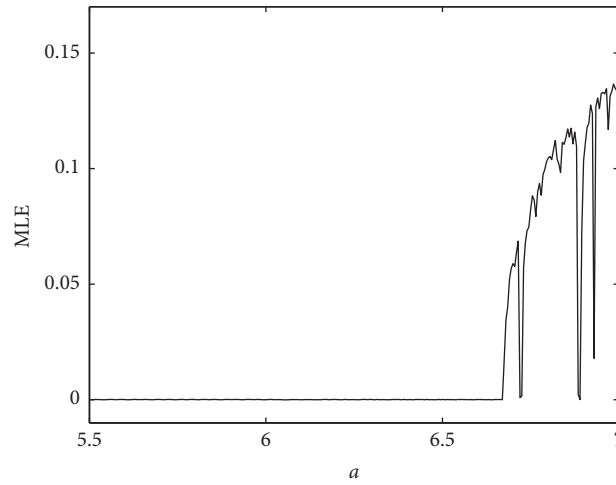


FIGURE 2: Presentation of maximum Lyapunov exponents for $a \in [5.5, 7]$, while $b = 4$ and $c = 1$.

using an absolute nonlinearity, we study a six-term system described by

$$\begin{aligned} \dot{x} &= a|y| + bz, \\ \dot{y} &= 1 + z, \\ \dot{z} &= -cx - z. \end{aligned} \quad (1)$$

System (1) has three positive parameters ($a, b, c > 0$). We have found that system (1) displays different behavior when varying the parameter a .

We have changed the parameter a for plotting the bifurcation diagram and the maximum Lyapunov exponents (presented in Figures 1 and 2). As shown in Figures 1 and 2, system (1) is periodic for $a < 6.67$. From Figures 1 and 2, we also observe a period doubling route to chaos, which is illustrated further in Figure 3. For $a > 6.67$, chaotic dynamics can be seen. For $a = 6.8$, $b = 4$, and $c = 1$, chaos in system (1) is presented in Figure 4. Chaos in this case is verified by the Lyapunov exponents of the system $L_1 = 0.1046 > 0$, $L_2 = 0$, and $L_3 = -1.1048$.

Interestingly, we can change the amplitude of the variable x easily by adding a control parameter (k_x) into system (1):

$$\begin{aligned} \dot{x} &= a|y| + bz, \\ \dot{y} &= 1 + z, \\ \dot{z} &= -cx - z + k_x. \end{aligned} \quad (2)$$

As shown in Figure 5, chaotic attractors are adjusted by using the control parameter k_x . When increasing k_x , the average value of the variable x is increased (see Figure 6).

Moreover, the amplitudes of three variables (x, y, z) are changed simultaneously by introducing a control parameter (k_{xyz}) into system (1) as follows:

$$\begin{aligned} \dot{x} &= a|y| + bz, \\ \dot{y} &= k_{xyz} + z, \\ \dot{z} &= -cx - z. \end{aligned} \quad (3)$$

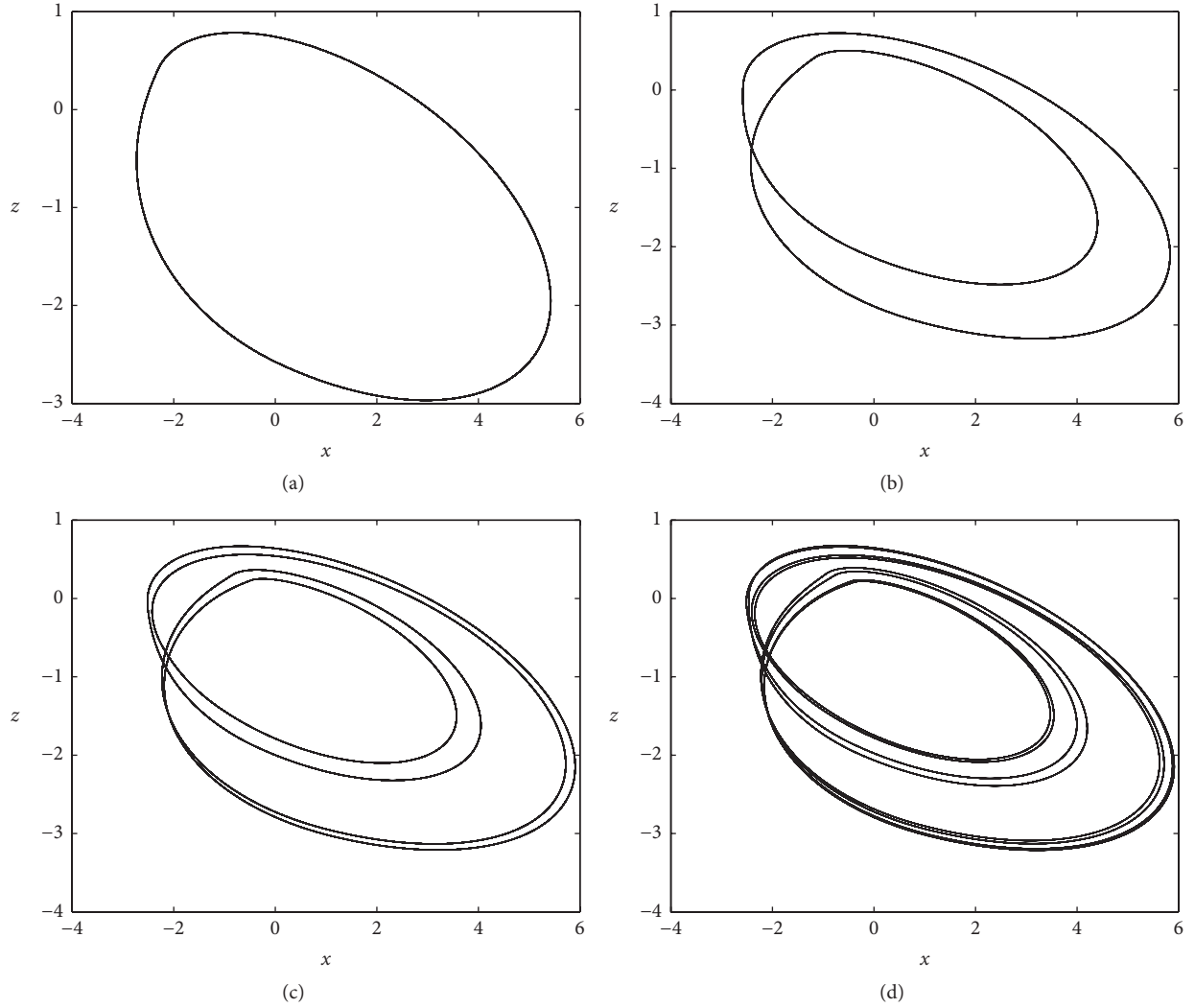


FIGURE 3: Different periodical dynamics observed in x - z plane for $b = 4$ and $c = 1$; initial conditions $(x(0), y(0), z(0)) = (0, 0, 0)$ when (a) $a = 5.75$, (b) $a = 6.25$, (c) $a = 6.625$, and (d) $a = 6.665$.

As illustrated in Figure 7, chaotic attractors are reduced and enlarged when varying the control parameter k_{xyz} . It is worth noting that Sprott has discovered various systems with absolute-value nonlinearity and six terms [3]. However, there are few systems displaying controllable chaotic attractors, which have received significant attention recently [29–31].

3. Circuit Design for the System

The numerical approach is vital for investigation of the dynamics of theoretical chaotic models [32–35]. By using this method, the dynamical behaviors of such models can be characterized in terms of their parameters. However, to explore their feasibilities, the electronic circuit implementation of these theoretical models is needed [36–39]. Moreover, the physical realization of theoretical chaotic models is relevant in many engineering applications [40–42]. In this section, we design and implement an electronic circuit to illustrate the

feasibility of system (1). The electronic circuit diagram for system (1) is depicted in Figure 8.

The circuit diagram of Figure 8 consists of operational amplifiers associated with resistors and capacitors exploited to implement the basic operations such as integration, addition, and subtraction. The nonlinear term of the model is implemented by absolute-value circuit of Figure 8(b). The bias is provided by a 15 Volts DC symmetry source. By applying Kirchhoff's laws into the circuit of Figure 8, we obtain the following state equations:

$$\begin{aligned} \frac{dV_x}{dt} &= \frac{|V_y|}{R_a C} + \frac{V_z}{R_b C} \\ \frac{dV_y}{dt} &= \frac{V_{DC}}{RC} + \frac{V_z}{RC} \\ \frac{dV_z}{dt} &= -\frac{V_x}{R_c C} - \frac{V_z}{RC}, \end{aligned} \quad (4)$$

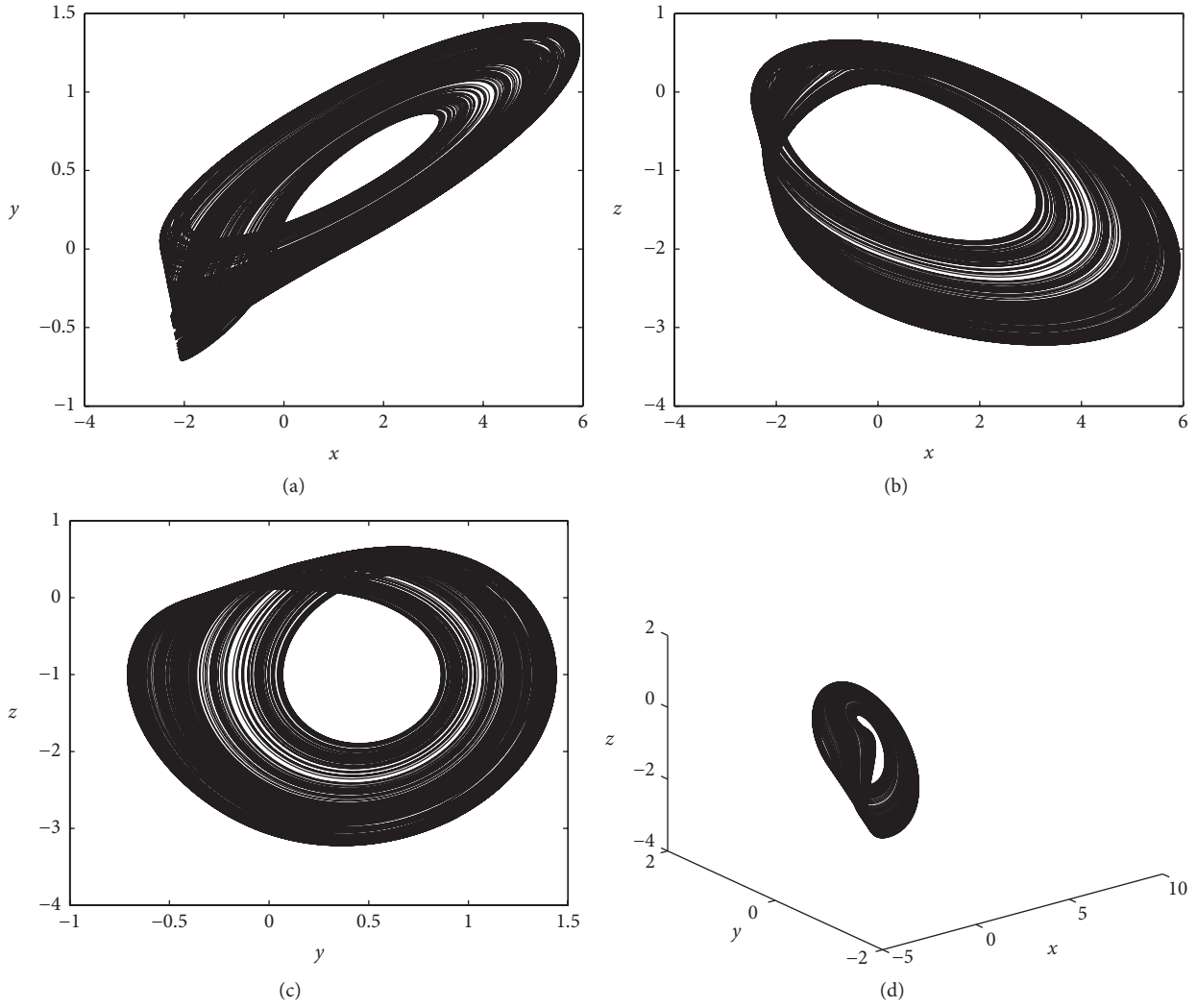


FIGURE 4: Phase portrait observed in (a) x - y plane, (b) x - z plane, (c) y - z plane, and (d) x - y - z space for $a = 6.8$, $b = 4$, and $c = 1$ and initial conditions $(x(0), y(0), z(0)) = (0, 0, 0)$.

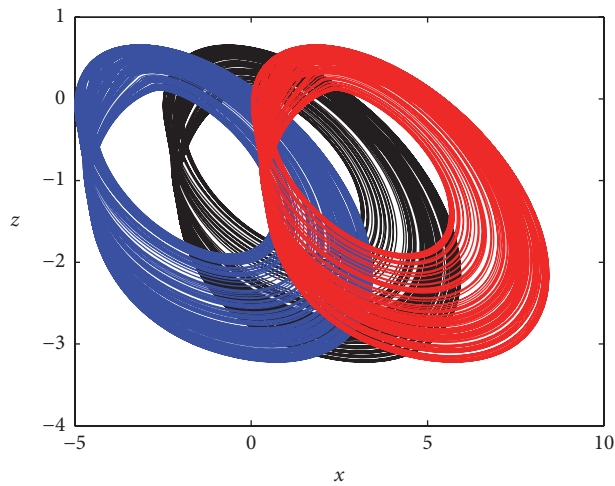


FIGURE 5: Variable chaotic attractor when varying the control parameter k_x : black color for $k_x = 0$, blue color for $k_x = -2$, and red color for $k_x = 2$.

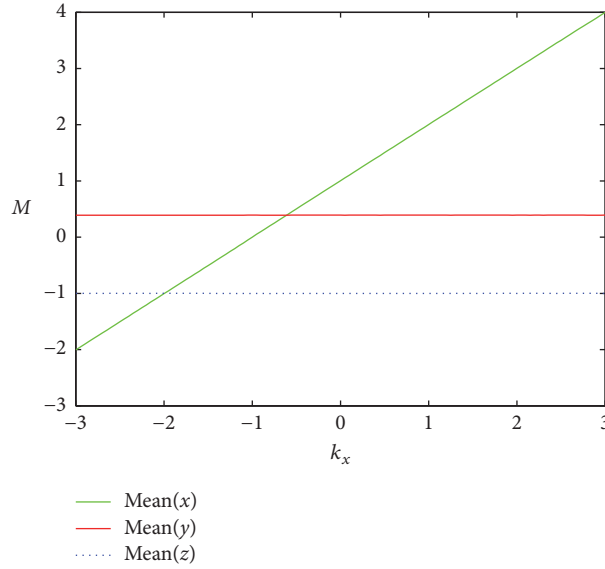


FIGURE 6: Average values of three variables (x, y, z) for $k_x \in [-3, 3]$.

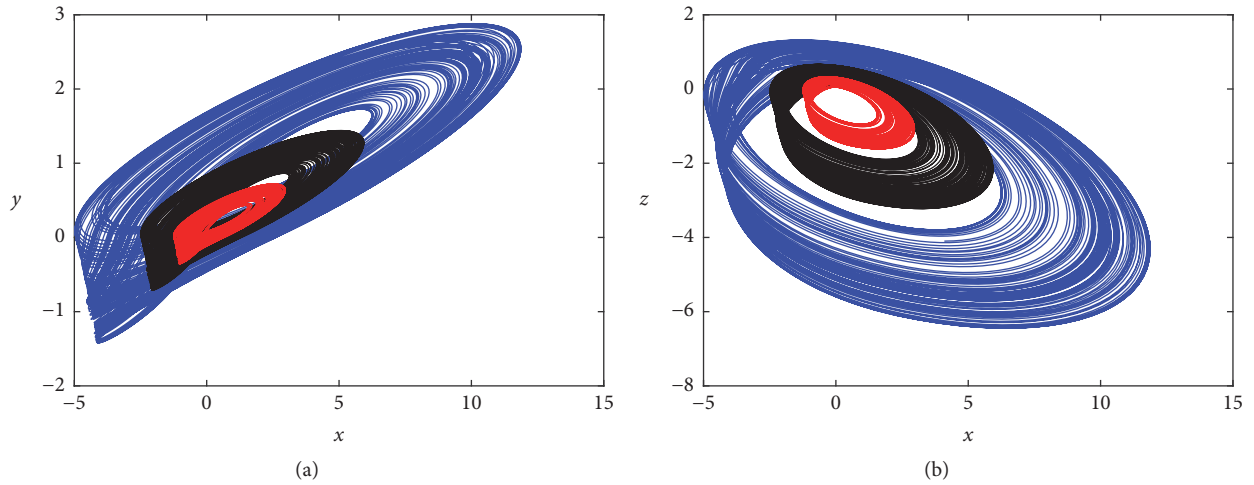


FIGURE 7: Controllable chaotic attractors in (a) x - y plane and (b) x - z plane when varying the control parameter k_{xyz} : black color for $k_{xyz} = 1$, blue color for $k_{xyz} = 2$, and red color for $k_{xyz} = 0.5$.

where $V_x, V_y,$ and V_z are the output voltages of the operational amplifiers OP_1, OP_2, and OP_3, respectively. In order to compare system (4) with theoretical model (1), the following settings of variables and parameters, $V_x = x \times 1V, V_y = y \times 1V, V_z = z \times 1V, t = \tau RC, a = R/R_a, b = R/R_b,$ and $c = R/R_c,$ are adopted. With the following values of parameters, $a = 6.8, b = 4,$ and $c = 1$ (for which system (1) displays chaotic behavior), the values of circuit components are selected as follows: $C = 10 \text{ nF}, R = 10 \text{ k}\Omega, R_a = 1.47 \text{ k}\Omega, R_b = 2.5 \text{ k}\Omega,$ and $R_c = 10 \text{ k}\Omega.$

As shown in Figure 9, the circuit has been implemented and experimental measurements have been recorded. Details of the real circuit are presented in Figure 10. The experimental phase portraits of the circuit in $(V_x, V_y), (V_x, V_z),$ and (V_y, V_z) planes obtained with an oscilloscope are shown in Figure 11.

From Figure 11, one can see that the experimental chaotic phase portraits agree with those obtained from the numerical simulations. This means that the proposed electronic circuit emulates well the dynamics of theoretical model (1).

4. Synchronization for the System with Unknown Parameters

It is well known that, in practical situations, some or all of the system parameters cannot be exactly known in advance. Also, most parameters values are characterized by uncertainties related to the modeling errors or experimental conditions (temperature, external electric and magnetic fields, etc.) that can destroy or even break the synchronization [43–45].

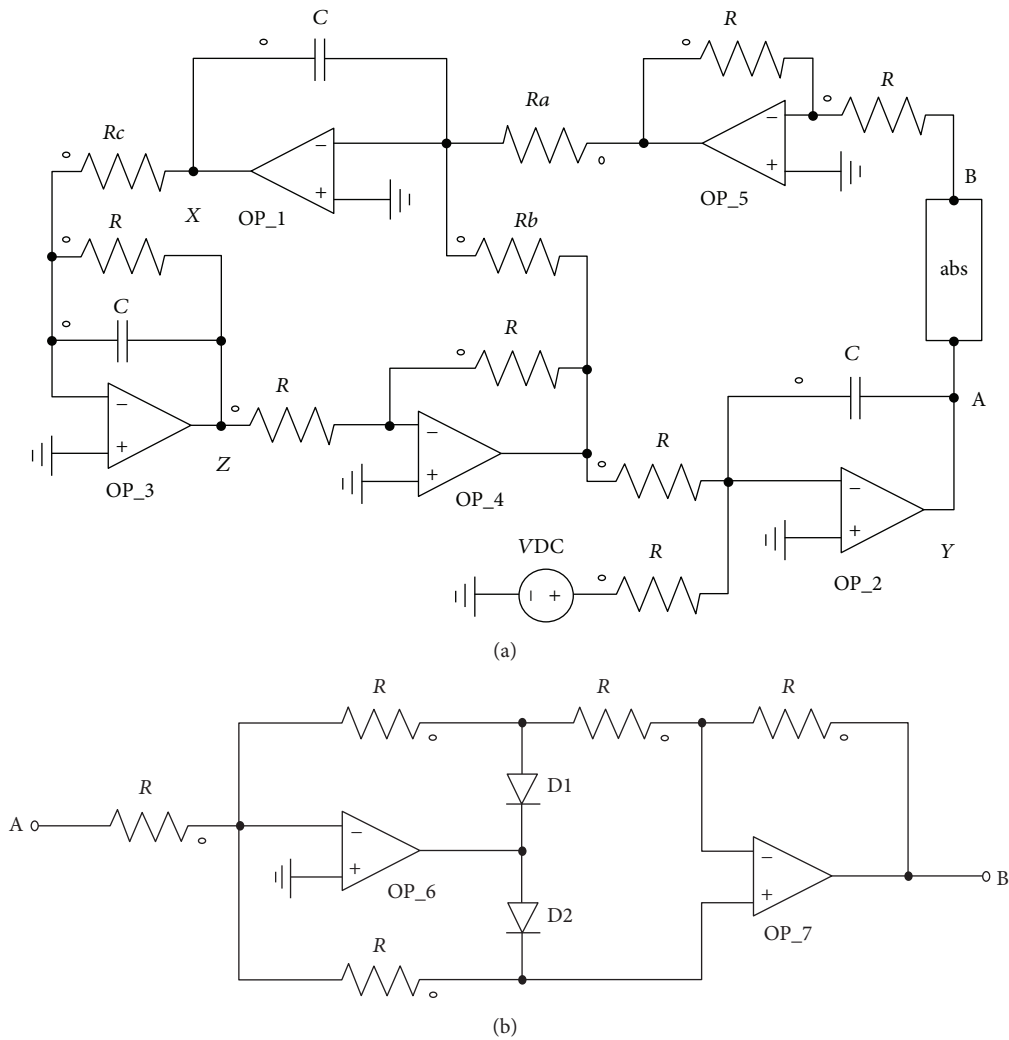


FIGURE 8: Electronic circuit design of system (1) (a) and the circuit realization of the absolute value function (b).

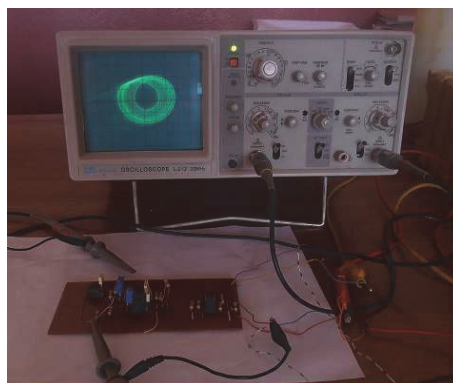


FIGURE 9: Implemented circuit was measured by using an oscilloscope.

Therefore, it is essential to consider the synchronization problem of chaotic systems in the presence of unknown system parameters. In this section, we design an adaptive control scheme [43] to synchronize two identical structures of system (1) with unknown parameters.

4.1. Design of the Slave System. We will assume that all the state variables and parameters of the master system (1) are accessible to measurements and those of slave system are unknown. Based on the concept of adaptive method, the following theorem is formulated.

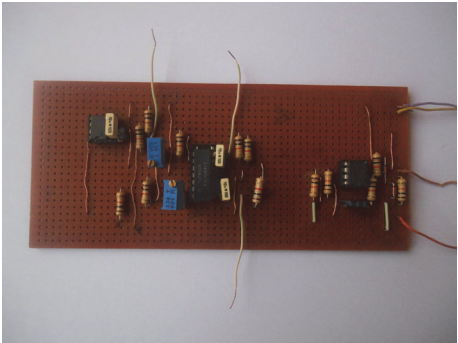
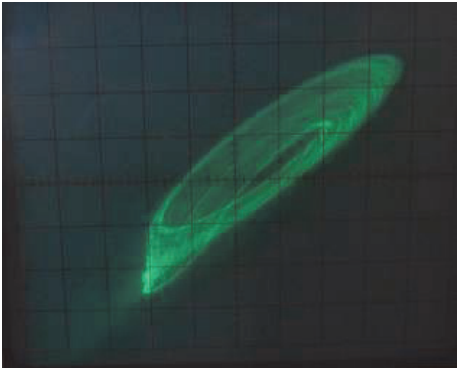
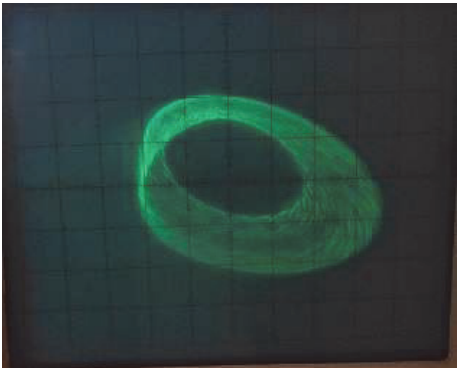


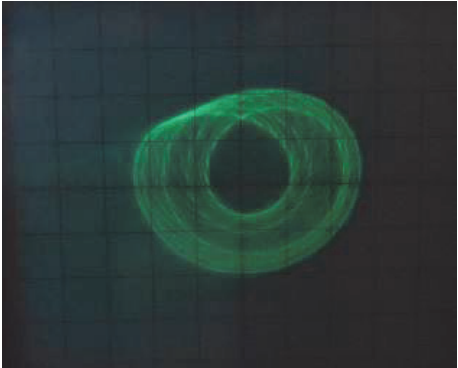
FIGURE 10: Real circuit implemented by using electronic components.



(a)



(b)



(c)

FIGURE 11: Experimental phase portraits of the real circuit in (a) (V_x, V_y) plane, (b) (V_x, V_z) plane, and (c) (V_y, V_z) plane with $R_a = 1.47 \text{ k}\Omega$, $R_b = 2.5 \text{ k}\Omega$, and $R_c = 10 \text{ k}\Omega$.

Theorem 1. Let system (1) be the master system rewritten in the following form:

$$\dot{X}_m = f(X_m) + F(X_m)\theta, \quad (5)$$

where

$$\begin{aligned} X_m &= (x_m, y_m, z_m)^T, \\ f(X_m) &= (0, 1 + z_m, -z_m)^T, \\ F(X_m) &= \begin{pmatrix} |y_m| & z_m & 0 \\ 0 & 0 & 0 \\ 0 & 0 & -x_m \end{pmatrix}, \\ \theta &= (a, b, c)^T; \end{aligned} \quad (6)$$

then the slave system

$$\dot{X}_s = f(X_s) + F(X_s)\hat{\theta}(t) + u \quad (7)$$

can synchronize with the master system (5), with the control function u designed as

$$\begin{aligned} u &= -\{e + f(X_s) - f(X_m) + [F(X_s) - F(X_m)]\hat{\theta}(t)\} \end{aligned} \quad (8)$$

and the update law of the estimations of the unknown parameters determined by

$$\dot{\hat{\theta}}(t) = -F^T(X_m)e, \quad (9)$$

where $e = X_s - X_m$ is the error system and $\hat{\theta} = (\hat{a}, \hat{b}, \hat{c})^T$ are the estimations of the corresponding parameters of the slave system (7).

Proof. The error dynamical system can be expressed as

$$\dot{e} = \dot{X}_s - \dot{X}_m = -e + F(X_m)(\hat{\theta}(t) - \theta). \quad (10)$$

Choose the storage Lyapunov function as

$$V(e, \theta(t)) = \frac{1}{2}e^T e + \frac{1}{2}(\hat{\theta}(t) - \theta)^T (\hat{\theta}(t) - \theta). \quad (11)$$

Then, the time derivative of $V(e, \theta(t))$ along the trajectory is

$$\begin{aligned} \dot{V} &= \frac{1}{2}(\dot{e}^T e + e^T \dot{e}) + \frac{1}{2}\left\{\left(\dot{\hat{\theta}}(t)\right)^T (\hat{\theta}(t) - \theta) \right. \\ &+ (\hat{\theta}(t) - \theta)^T \dot{\hat{\theta}}(t)\left.\right\} = \frac{1}{2}\{-e^T e \\ &+ (\hat{\theta}(t) - \theta)^T F^T(X_m)e - e^T e \\ &+ e^T F(X_m)(\hat{\theta}(t) - \theta)\} + \frac{1}{2}\left\{\left(\dot{\hat{\theta}}(t)\right)^T (\hat{\theta}(t) - \theta) \right. \\ &+ (\hat{\theta}(t) - \theta)^T \dot{\hat{\theta}}(t)\left.\right\} = -e^T e. \end{aligned} \quad (12)$$

So \dot{V} is negative semidefinite, and since V is positive definite, it follows that $e \in L_\infty$ and $\theta \in L_\infty$. Thus $\dot{e} \in L_\infty$, and, according to (10), it can be obtained that

$$\begin{aligned} \int_0^t \|e\|^2 dt &= \int_0^t e^T e dt \leq -\frac{1}{l} \int_0^t \dot{V} dt \\ &= \frac{1}{l} [V(0) - V(t)] \leq \frac{1}{l} V(0). \end{aligned} \quad (13)$$

Since $V(0) \leq \infty$ and $e \in L_2$, according to Barbalat's lemma, we have $\|e(t)\| \rightarrow 0$ as $t \rightarrow \infty$; that is, the error dynamical system (10) will be stabilized at the zero equilibrium asymptotically. Thus, according to the Lyapunov stability theorem, the adaptive synchronization with unknown parameters between the drive system (5) and the response system (7) is achieved under the controller defined in (8) and parameters update law determined by (9). This completes the proof. \square

4.2. Numerical Verifications. For numerical verification, the master system is defined as in (5) with parameters a, b , and c . According to Theorem 1, the slave system is described as follows:

$$\begin{aligned} \dot{x}_s &= \hat{a}|y_m| + \hat{b}z_m - (x_s - x_m), \\ \dot{y}_s &= 1 + z_m - (y_s - y_m), \\ \dot{z}_s &= -\hat{c}x_m - z_m - (z_s - z_m), \end{aligned} \quad (14)$$

where

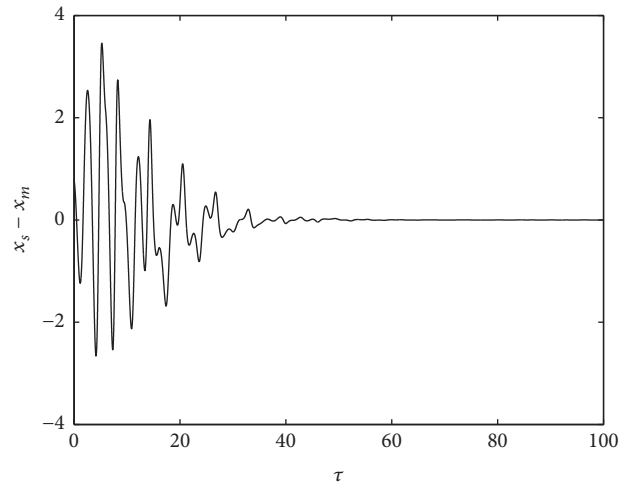
$$\begin{aligned} \hat{a} &= -|y_m|(x_s - x_m), \\ \hat{b} &= -z_m(y_s - y_m), \\ \hat{c} &= x_m(z_s - z_m). \end{aligned} \quad (15)$$

The numerical computations are obtained using the standard fourth-order Runge-Kutta integration algorithm with a time step $\Delta t = 0.001$; initial conditions on parameters are being selected randomly as follows: $\hat{a}(0) = 1.20$, $\hat{b}(0) = 0.80$, and $\hat{c}(0) = 0.25$. The master system's parameters are chosen as $a = 6.8$, $b = 4$, and $c = 1$ in order to ensure the chaotic behavior. The synchronization errors and the graph of parameters estimations are shown in Figures 12 and 13, respectively.

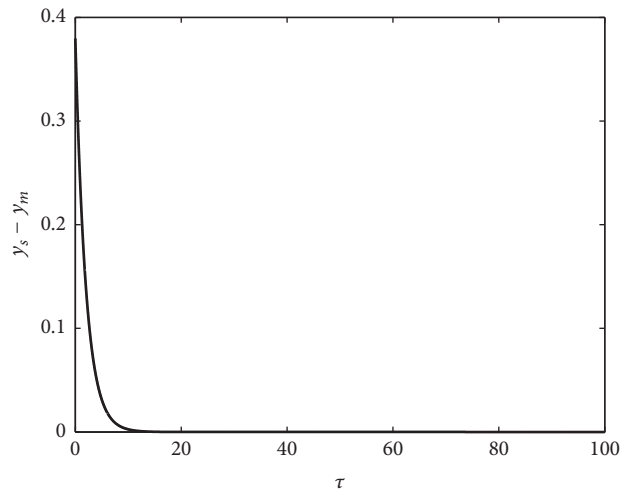
Numerical simulations (see Figures 12 and 13) show that the adaptive synchronization between master system (5) and slave system (7) with unknown parameters is achieved successfully and the error signals approach asymptotically zero. Obviously, these results may be exploited in engineering applications such as communication, image processing, physics, and mechatronics.

5. Conclusions

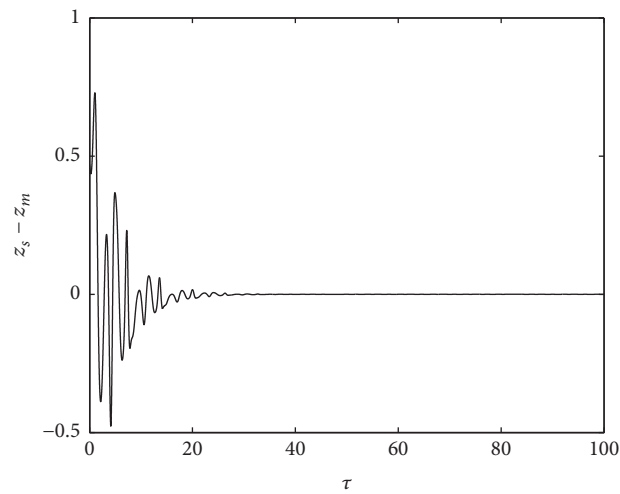
By using an absolute nonlinearity, we have introduced a six-term system with chaos. Dynamics of the system with



(a)

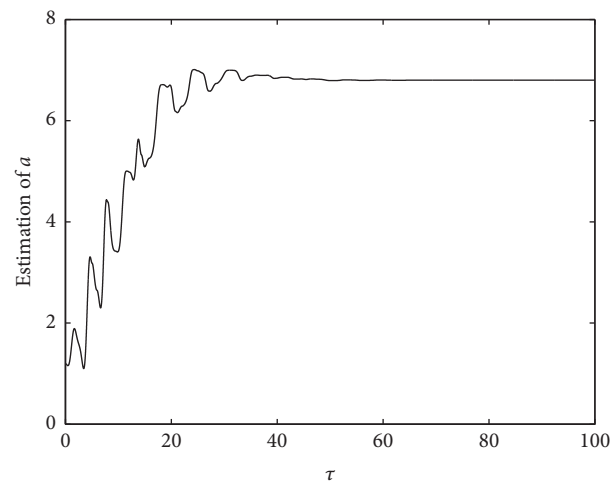


(b)

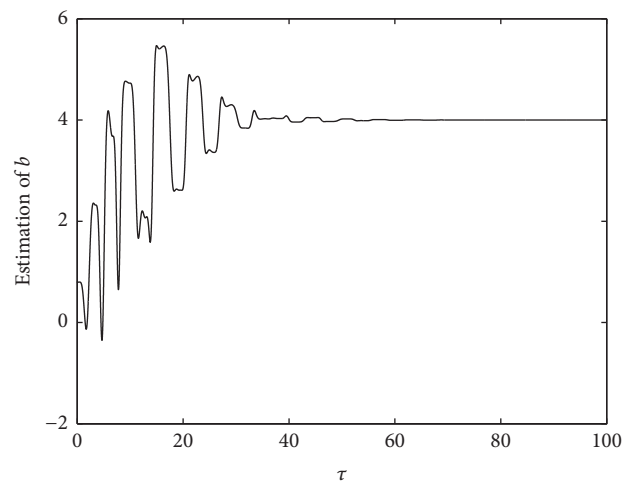


(c)

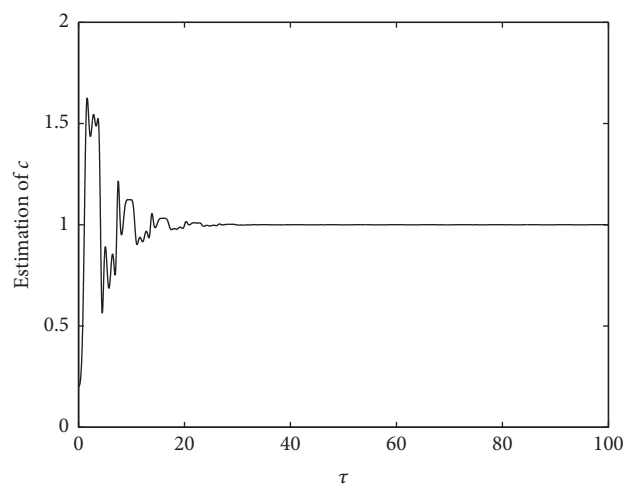
FIGURE 12: Error dynamics showing transition to synchronized states of the system and its observer. (a) $e_x = x_s - x_m$, (b) $e_y = y_s - y_m$, and (c) $e_z = z_s - z_m$. The initial conditions are chosen randomly as $x_m(0) = 0.01$, $y_m(0) = 0.02$, and $z_m(0) = 0.03$ and $x_s(0) = 0.8$, $y_s(0) = 0.4$, and $z_s(0) = 0.5$, respectively, for the drive and response systems. The master system parameters are $a = 6.8$, $b = 4$, and $c = 1$ to ensure the chaotic behavior.



(a)



(b)



(c)

FIGURE 13: Graphs of estimation of unknown parameters of slave system. (a) \hat{a} , (b) \hat{b} , and (c) \hat{c} . The initial conditions are selected randomly as $\hat{a}(0) = 1.2$, $\hat{b}(0) = 0.8$, and $\hat{c}(0) = 0.25$.

only one absolute nonlinearity have been investigated. One interesting finding is that the x variable can be adjusted with a control parameter. In addition, it is simple to implement this chaotic system because we do not need any analog multiplier. Adaptive synchronization between such two chaotic systems has been reported and these results should be exploited further for practical applications.

Conflicts of Interest

The authors declare that there are no conflicts of interest regarding the publication of this paper.

Acknowledgments

The authors thank Dr. Sifeu Takougang Kingni, Department of Mechanical and Electrical Engineering, Institute of Mines and Petroleum Industries, University of Maroua, for suggesting many helpful references.

References

- [1] E. N. Lorenz, "Deterministic nonperiodic flow," *Journal of the Atmospheric Sciences*, vol. 20, pp. 130–141, 1963.
- [2] O. E. RöSSLer, "An equation for continuous chaos," *Physics Letters A*, vol. 57, no. 5, pp. 397–398, 1976.
- [3] J. C. Sprott, *Elegant Chaos Algebraically Simple Chaotic Flows*, World Scientific, Singapore, 2010.
- [4] G. Chen and T. Ueta, "Yet another chaotic attractor," *International Journal of Bifurcation and Chaos*, vol. 9, no. 7, pp. 1465–1466, 1999.
- [5] M. Nategh, D. Baleanu, E. Taghizadeh, and Z. G. Gilani, "Almost local stability in discrete delayed chaotic systems," *Nonlinear Dynamics*, vol. 89, no. 4, pp. 2393–2402, 2017.
- [6] W. Liu, K. Sun, and S. He, "SF-SIMM high-dimensional hyperchaotic map and its performance analysis," *Nonlinear Dynamics*, vol. 89, no. 4, pp. 2521–2532, 2017.
- [7] C. Li, I. Pehlivan, J. Sprott, and A. Akgul, "A novel four-wing strange attractor born in bistability," *IEICE Electronics Express*, vol. 12, no. 4, pp. 1–12, 2015.
- [8] B. C. Bao, Q. Xu, H. Bao, and M. Chen, "Extreme multistability in a memristive circuit," *Electronics Letters*, vol. 52, pp. 1008–1010, 2016.
- [9] M. Chen, Q. Xu, Y. Lin, and B. Bao, "Multistability induced by two symmetric stable node-foci in modified canonical Chua's circuit," *Nonlinear Dynamics*, vol. 87, no. 2, pp. 789–802, 2017.
- [10] T. Gotthans and J. Petrzela, "New class of chaotic systems with circular equilibrium," *Nonlinear Dynamics*, vol. 73, pp. 429–436, 2015.
- [11] T. Gotthans, J. C. Sprott, and J. Petrzela, "Simple Chaotic Flow with Circle and Square Equilibrium," *International Journal of Bifurcation and Chaos*, vol. 26, no. 8, Article ID 1650137, 2016.
- [12] B. Bao, T. Jiang, G. Wang, P. Jin, H. Bao, and M. Chen, "Two-memristor-based Chua's hyperchaotic circuit with plane equilibrium and its extreme multistability," *Nonlinear Dynamics*, vol. 89, pp. 1157–1171, 2017.
- [13] M. P. Aghababa, "Stabilization of a class of fractional-order chaotic systems using a non-smooth control methodology," *Nonlinear Dynamics*, vol. 89, no. 2, pp. 1357–1370, 2017.
- [14] K. Rajagopal, A. Karthikeyan, and A. K. Srinivasan, "FPGA implementation of novel fractional-order chaotic systems with two equilibriums and no equilibrium and its adaptive sliding mode synchronization," *Nonlinear Dynamics*, vol. 87, no. 4, pp. 2281–2304, 2017.
- [15] S. Shao, M. Chen, and X. Yan, "Adaptive sliding mode synchronization for a class of fractional-order chaotic systems with disturbance," *Nonlinear Dynamics*, vol. 83, no. 4, pp. 1855–1866, 2016.
- [16] F. Lin and J. Liu, "Chaotic radar using nonlinear laser dynamics," *IEEE Journal of Quantum Electronics*, vol. 40, no. 6, pp. 815–820, 2004.
- [17] Y. Wang, K.-W. Wong, X. Liao, and G. Chen, "A new chaos-based fast image encryption algorithm," *Applied Soft Computing*, vol. 11, no. 1, pp. 514–522, 2011.
- [18] S. Sadoudi, C. Tanougast, M. S. Azzaz, and A. Dandache, "Design and FPGA implementation of a wireless hyperchaotic communication system for secure real-time image transmission," *Eurasip Journal on Image and Video Processing*, vol. 2013, article 43, pp. 1–18, 2013.
- [19] A. Akgul, H. Calgan, I. Koyuncu, I. Pehlivan, and A. Istanbulu, "Chaos-based engineering applications with a 3D chaotic system without equilibrium points," *Nonlinear Dynamics*, vol. 84, no. 2, pp. 481–495, 2016.
- [20] F. Ozkaynak and S. Yavuz, "Designing chaotic S-boxes based on time-delay chaotic system," *Nonlinear Dynamics*, vol. 74, no. 3, pp. 551–557, 2013.
- [21] S. J. Linz and J. C. Sprott, "Elementary chaotic flow," *Physics Letters A*, vol. 259, no. 3–4, pp. 240–245, 1999.
- [22] J. C. Sprott, "A new class of chaotic circuit," *Physics Letters A*, vol. 266, no. 1, pp. 19–23, 2000.
- [23] J. C. Sprott, "Simple chaotic systems and circuits," *American Journal of Physics*, vol. 68, no. 8, pp. 758–763, 2000.
- [24] P. H. Chang and D. Kim, "Introduction and synchronization of a five-term chaotic system with an absolute-value term," *Nonlinear Dynamics*, vol. 73, pp. 311–323, 2013.
- [25] C. Li, J. C. Sprott, W. Thio, and H. Zhu, "A new piecewise linear hyperchaotic circuit," *IEEE Transactions on Circuits and Systems II: Express Briefs*, vol. 61, no. 12, pp. 977–981, 2014.
- [26] L. Huang and A. Liu, "Analysis and synchronization for a new fractional-order chaotic system with absolute value term," *Nonlinear Dynamics*, vol. 70, no. 1, pp. 601–608, 2012.
- [27] H. Bao, N. Wang, B. Bao, M. Chen, P. Jin, and G. Wang, "Initial condition-dependent dynamics and transient period in memristor-based hypogenetic jerk system with four line equilibria," *Communications in Nonlinear Science and Numerical Simulation*, vol. 57, pp. 264–275, 2018.
- [28] C. Li, J. Wang, and W. Hu, "Absolute term introduced to rebuild the chaotic attractor with constant Lyapunov exponent spectrum," *Nonlinear Dynamics*, vol. 68, no. 4, pp. 575–587, 2012.
- [29] C. Li, J. C. Sprott, Z. Yuan, and H. Li, "Constructing chaotic systems with total amplitude control," *International Journal of Bifurcation and Chaos*, vol. 25, no. 10, Article ID 1530025, 2015.
- [30] C. Li and J. C. Sprott, "Variable-boostable chaotic flows," *Optik - International Journal for Light and Electron Optics*, vol. 127, no. 22, pp. 10389–10398, 2016.
- [31] C. Li, J. C. Sprott, A. Akgul, H. H. C. Iu, and Y. Zhao, "A new chaotic oscillator with free control," *Chaos: An Interdisciplinary Journal of Nonlinear Science*, vol. 27, no. 8, Article ID 083101, 2017.

- [32] Z. Wei and Q. Yang, "Dynamical analysis of a new autonomous 3-D chaotic system only with stable equilibria," *Nonlinear Analysis: Real World Applications*, vol. 12, no. 1, pp. 106–118, 2011.
- [33] Z. Wei, "Dynamical behaviors of a chaotic system with no equilibria," *Physics Letters A*, vol. 376, no. 2, pp. 102–108, 2011.
- [34] X. Wang and G. Chen, "A chaotic system with only one stable equilibrium," *Communications in Nonlinear Science and Numerical Simulation*, vol. 17, no. 3, pp. 1264–1272, 2012.
- [35] X. Wang and G. Chen, "Constructing a chaotic system with any number of equilibria," *Nonlinear Dynamics*, vol. 71, no. 3, pp. 429–436, 2013.
- [36] S. Bouali, A. Buscarino, L. Fortuna, M. Frasca, and L. V. Gambuzza, "Emulating complex business cycles by using an electronic analogue," *Nonlinear Analysis: Real World Applications*, vol. 13, no. 6, pp. 2459–2465, 2012.
- [37] C. Li, H. Li, and Y. Tong, "Analysis of a novel three-dimensional chaotic system," *Optik - International Journal for Light and Electron Optics*, vol. 124, no. 13, pp. 1516–1522, 2013.
- [38] Q. Lai and L. Wang, "Chaos, bifurcation, coexisting attractors and circuit design of a three-dimensional continuous autonomous system," *Optik - International Journal for Light and Electron Optics*, vol. 127, no. 13, pp. 5400–5406, 2016.
- [39] B. C. Bao, H. Bao, N. Wang, M. Chen, and Q. Xu, "Hidden extreme multistability in memristive hyperchaotic system," *Chaos Solitons Fractals*, vol. 94, pp. 102–111, 2017.
- [40] M. E. Yalcin, J. A. Suykens, and J. Vandewalle, "True random bit generation from a double-scroll attractor," *IEEE Transactions on Circuits and Systems I: Regular Papers*, vol. 51, no. 7, pp. 1395–1404, 2004.
- [41] C. K. Volos, I. M. Kyprianidis, and I. N. Stouboulos, "A chaotic path planning generator for autonomous mobile robots," *Robotics and Autonomous Systems*, vol. 60, no. 4, pp. 651–656, 2012.
- [42] C. K. Volos, I. M. Kyprianidis, and I. N. Stouboulos, "Image encryption process based on chaotic synchronization phenomena," *Signal Processing*, vol. 93, no. 5, pp. 1328–1340, 2013.
- [43] H. B. Fotsin and P. Wofo, "Adaptive synchronization of a modified and uncertain chaotic van der Pol-Duffing oscillator based on parameter identification," *Chaos Solitons Fractals*, vol. 24, no. 5, pp. 1363–1371, 2015.
- [44] Y. Xu, W. Zhou, J. Fang, and W. Sun, "Adaptive bidirectionally coupled synchronization of chaotic systems with unknown parameters," *Nonlinear Dynamics*, vol. 66, no. 1-2, pp. 67–76, 2011.
- [45] J. Kengne, J. C. Chedjou, G. Kenne, K. Kyamakya, and G. H. Kom, "Analog circuit implementation and synchronization of a system consisting of a van der Pol oscillator linearly coupled to a Duffing oscillator," *Nonlinear Dynamics*, vol. 70, no. 3, pp. 2163–2173, 2012.

Research Article

Fractional-Order Sliding Mode Synchronization for Fractional-Order Chaotic Systems

Chenhui Wang 

College of Applied Mathematics, Xiamen University of Technology, Xiamen 361024, China

Correspondence should be addressed to Chenhui Wang; chwang@xmut.edu.cn

Received 5 October 2017; Revised 19 December 2017; Accepted 20 December 2017; Published 17 January 2018

Academic Editor: Christos Volos

Copyright © 2018 Chenhui Wang. This is an open access article distributed under the Creative Commons Attribution License, which permits unrestricted use, distribution, and reproduction in any medium, provided the original work is properly cited.

Some sufficient conditions, which are valid for stability check of fractional-order nonlinear systems, are given in this paper. Based on these results, the synchronization of two fractional-order chaotic systems is investigated. A novel fractional-order sliding surface, which is composed of a synchronization error and its fractional-order integral, is introduced. The asymptotical stability of the synchronization error dynamical system can be guaranteed by the proposed fractional-order sliding mode controller. Finally, two numerical examples are given to show the feasibility of the proposed methods.

1. Introduction

In the past two decades, synchronization of chaotic systems (CSs) has received more and more attention, and a lot of interesting works have been done, which have potential application values in secret communications, signal processing, and complex systems [1–9]. Recently, control and synchronization of fractional-order chaotic systems (FOCSs), which can be seen as a generalization of the integer-order CSs, have been studied extensively. A lot of controllers have been implemented such as active control [10], feedback control [11], sliding mode control [12, 13], adaptive control, [14, 15], and adaptive fuzzy control [8, 9, 16].

It is well known that sliding mode control (SMC) is a very effective control method to cope with system uncertainties and external disturbances [17–27]. Consequently, it has been used to synchronize FOCSs. For example, a novel FOCS and its SMC have been studied in [28]; SMC of a 3D FOCS using a fractional-order switching type controller is investigated in [29]. Using a hierarchical fuzzy neural network, [30] proposed a new adaptive SMC method for the synchronization of uncertain FOCSs. On the other hand, it is well known that, in stability analysis of nonlinear systems, quadratic Lyapunov functions are most commonly used. However, [31, 32] show that it is not realistic to use quadratic

Lyapunov functions in the stability analysis of fractional-order nonlinear systems due to the complicated infinite series produced by differentiating the squared Lyapunov function with fractional order. It should be mentioned that, in most aforementioned works, the stability analysis is given based on fractional Lyapunov methods. How to establish some stability analysis methods according to the model of FOCSs is a meaningful work.

In control theory, stability analysis is an essential aspect. With respect to fractional-order linear systems, the stability condition was firstly investigated in [33]. Then, using LMI, some sufficient conditions are given in [34]. The related results on the stability analysis of fractional-order nonlinear systems can be seen in [35–41] and the references therein. It should be pointed out that the stability criterion for fractional-order nonlinear systems requires further study. Thus, proposing some new stability criterion for FOCSs is necessary. In this paper, we will give two sufficient conditions for the stability of a class of FOCSs. Based on these theorems, a fractional-order SMC will be given. The contributions of this paper are concluded as follows: (1) two sufficient conditions are proposed to check the stability of the fractional-order nonlinear system and (2) a novel fractional-order SMC is given, and the stability of the closed-loop system is proven rigorously.

2. Preliminaries

In this section, we will give some properties of fractional calculus. The q th fractional-order integral is expressed as [42]

$$\mathbb{D}^q f(t) = \frac{1}{\Gamma(q)} \int_0^t (t-\tau)^{q-1} f(\tau) d\tau. \quad (1)$$

The Caputo fractional derivative is given by

$$\mathbb{D}^q f(t) = \frac{1}{\Gamma(n-q)} \int_0^t (t-\tau)^{n-q-1} f^{(n)}(\tau) d\tau, \quad (2)$$

where q is the fractional order satisfying $n-1 \leq q < n$.

The Laplace transform of Caputo fractional derivative is given as [42]

$$\int_0^\infty e^{-st} \mathbb{D}^q x(t) dt = s^q F(s) - \sum_{k=0}^{n-1} s^{q-k-1} x^{(k)}(0), \quad (3)$$

where $F(s) = \mathcal{L}\{f(t)\}$. In the next section, we will use the following results.

The Mittag-Leffler function is given by

$$E_{\beta_1, \beta_2}(z) = \sum_{k=0}^{\infty} \frac{z^k}{\Gamma(\beta_1 k + \beta_2)}, \quad (4)$$

where $\beta_1, \beta_2 > 0$ and $z \in \mathbb{C}$. The Laplace transform of (4) is

$$\mathcal{L}\{t^{\beta_2-1} E_{\beta_1, \beta_2}(-at^{\beta_1})\} = \frac{s^{\beta_1-\beta_2}}{s^{\beta_1} + a}. \quad (5)$$

Lemma 1 (see [42]). Let $A \in \mathbb{R}^{n \times n}$, $0 < \alpha \leq 1$, β be an arbitrary real number, and $b > 0$ be a real constant; then,

$$E_{\alpha, \beta}(A) \leq \frac{b}{1 + \|A\|}, \quad (6)$$

where $\mu \leq |\arg(\text{eig}(A))| \leq \pi$ with $\mu \in \mathbb{R}$ satisfying $\pi\alpha/2 < \mu < \min\{\pi, \pi\alpha\}$.

Lemma 2 (see [43]). Let $t \in [0, T]$ and

$$x(t) \leq h(t) + \int_0^t k(\tau) x(\tau) d\tau, \quad (7)$$

where $k(t) \geq 0$. Then, one has

$$x(t) \leq h(t) + \int_0^t k(\tau) h(\tau) \exp\left[\int_\tau^t k(u) du\right] d\tau. \quad (8)$$

Lemma 3 (see [42, 44]). Let $0 < \alpha < 2$. β is a complex number, and μ is a real number. If

$$\frac{\pi\alpha}{2} < \mu < \min\{\pi, \pi\alpha\}, \quad (9)$$

then, for an arbitrary integer $n \geq 1$, the following expansion holds:

$$E_{\alpha, \beta}(z) = -\sum_{j=1}^n \frac{1}{\Gamma(\beta - \alpha j) z^j} + o\left(\frac{1}{|z|^{n+1}}\right). \quad (10)$$

3. Main Results

3.1. Some Sufficient Conditions for the Stability Analysis of Fractional-Order Systems. Consider a class of fractional-order systems described by

$$\mathbb{D}^q x_j(t) = c_j x_j(t) + \sum_{i=1}^n a_{ij} f_i(x_i(t)), \quad (11)$$

or equivalently

$$\mathbb{D}^q x(t) = Cx(t) + Af(x(t)), \quad (12)$$

where $j = 1, 2, \dots, n$, $0 < q < 1$, and $x(t) = [x_1(t), x_2(t), \dots, x_n(t)]^T \in \mathbb{R}^n$ is the state vector; $f(x(t)) = [f_1(x_1(t)), f_2(x_2(t)), \dots, f_n(x_n(t))]^T \in \mathbb{R}^n$ represents a smooth nonlinear function, $A = \{a_{ij}\}$, $i = 1, 2, \dots, n$, $j = 1, 2, \dots, n$, and $C = \text{diag}(c_i)$ are two matrices. Then, we have the following results.

Theorem 4. If $c_i < 0$ and the nonlinear function is bounded, that is, there exists a constant $m_i > 0$ such that

$$|f_i(x_i(t))| \leq m_i, \quad (13)$$

then there exist two positive constants t_0 and M such that

$$|x_i(t)| \leq M \quad (14)$$

for all $t > t_0$.

Proof. It follows from (11) that

$$X_i(s) = \frac{s^{q-1}}{s^q - c_i} x_i(0) + \frac{1}{s^q - c_i} \sum_{j=1}^n a_{ij} \mathcal{L}(f_j(x_j(t))). \quad (15)$$

Using (5), one solves (15) as

$$x_i(t) = x_i(0) E_{q,1}(c_i t^q) + \sum_{j=1}^n a_{ij} \int_0^t (t-\tau)^{q-1} E_{q,q}(c_i(t-\tau)^q) f_j(x_j(\tau)) d\tau. \quad (16)$$

Thus, according to (13), one has

$$\begin{aligned} |x_i(t)| &\leq |x_i(0)| E_{q,1}(c_i t^q) \\ &\quad + \sum_{j=1}^n |a_{ij}| m_j \int_0^t (t-\tau)^{q-1} E_{q,q}(c_i(t-\tau)^q) d\tau. \end{aligned} \quad (17)$$

Noting that the Laplace transform of a Mittag-Leffler function is

$$\int_0^t \tau^{\beta-1} E_{\beta_1, \beta_2}(-k\tau^{\beta_1}) d\tau = t^{\beta_2} E_{\beta_1, \beta_2+1}(-kt^{\beta_1}), \quad (18)$$

then one has

$$|x_i(t)| \leq |x_i(0)| E_{q,1}(c_i t^q) + A_i t^q E_{q,q+1}(c_i t^q), \quad (19)$$

where $A_i = \sum_{j=1}^n |a_{ij}| m_j$ is a positive constant.

It follows from Lemma 3 that

$$A_i t^q E_{q,q+1}(-c_i t^q) \leq \frac{A_i}{-c_i}. \quad (20)$$

Consequently, for large enough time t , one has

$$\lim_{t \rightarrow \infty} |x_i(t)| \leq M, \quad (21)$$

where $M = \max_{1 \leq i \leq n} \{A_i/c_i\}$. This ends the proof of Theorem 4. \square

It should be pointed out that Theorem 4 can only drive $x_i(t)$ to a small region of zero. To discuss the asymptotic stability, one needs the following assumptions.

Assumption 5. The equilibrium point of system (11) is the origin.

Assumption 6. $f(x(t))$ is a Lipschitz continuous function; that is, the following inequality holds:

$$\|f(x(t)) - f(y(t))\| \leq l \|x(t) - y(t)\|, \quad (22)$$

where $l > 0$ is a Lipschitz constant.

Remark 7. It should be mentioned that Assumptions 5 and 6 are reasonable. In fact, every equilibrium point of system (11) can be moved to the origin by some linear transformations. In many FOCSS, the nonlinear functions are smooth and Lipschitz continuous, for example, fractional-order Lorenz system, fractional-order Chen system, fractional-order Lü system, fractional-order financial system, and fractional Volta system [45].

Theorem 8. Consider system (12). Under Assumption 6, if $(lb/c)\|A\| < q$, where $c = \max_{1 \leq i \leq n} -c_i$, then the asymptotical stability of system (12) can be guaranteed.

Proof. Suppose that $x(t), y(t) \in R^n$ are two arbitrary solutions of (12). Denote $e(t) = x(t) - y(t)$; then, one has

$$\mathbb{D}^q e(t) = C e(t) + A(f(x(t)) - f(y(t))). \quad (23)$$

It follows from (23) that

$$s^q E(s) = s^{q-1} e(0) + C E(s) + A \mathcal{L}\{f(x(t)) - f(y(t))\}, \quad (24)$$

where $E(s) = \mathcal{L}\{e(t)\}$.

After some straightforward manipulators, one has

$$E(s) = (Is^q - C)^{-1} \cdot (s^{q-1} e(0) + A \mathcal{L}\{f(x(t)) - f(y(t))\}). \quad (25)$$

Solving (25) yields

$$e(t) = E_{q,1}(Ct^q) e(0) + A \int_0^t (t-\tau)^{q-1} \cdot E_{q,q}(C(t-\tau)^q) \mathcal{L}\{f(x(t)) - f(y(t))\} d\tau. \quad (26)$$

According to Assumption 6 and Lemma 1, one can find a constant $b > 0$ such that

$$\|e(t)\| \leq \frac{b \|e(0)\|}{1 + \|C\| t^q} + lb \|A\| \int_0^t \frac{(t-\tau)^{q-1}}{1 + \|C\| (t-\tau)^q} \|e(\tau)\| d\tau. \quad (27)$$

Using Lemma 2, one has

$$\begin{aligned} \|x(t)\| &\leq \frac{b \|e(0)\|}{1 + \|C\| t^q} + \int_0^t \frac{lb \|A\| (t-\tau)^{q-1} \|e(0)\|}{(1 + \|C\| (t-\tau)^q) (1 + \|C\| \tau^q)} \exp\left(\int_\tau^t \frac{lb \|A\| (t-u)^{q-1}}{1 + \|C\| (t-u)^q} du\right) d\tau \\ &= \frac{b \|e(0)\|}{1 + \|C\| t^q} + \int_0^t \frac{bl \|A\| (t-\tau)^{q-1} \|e(0)\|}{(1 + \|C\| \tau^q) (1 + \|C\| (t-\tau)^q)^{1-b/q\|C\|}} d\tau \\ &\leq \frac{b \|e(0)\|}{1 + \|C\| t^q} + lb \|A\| \|e(0)\| \|C\|^{lb\|A\|/q\|C\|-2} \int_0^t (t-\tau)^{lb\|A\|/\|C\|-1} \tau^{-q} d\tau \\ &= \frac{b \|e(0)\|}{1 + \|C\| t^q} + lb \|A\| \|e(0)\| \|C\|^{lb\|A\|/q\|C\|-2} \frac{\Gamma(lb\|A\|/\|C\|) \Gamma(1-q)}{\Gamma(1+lb\|A\|/\|C\|-q)} t^{lb\|A\|/\|C\|-q}. \end{aligned} \quad (28)$$

Noting that $(lb/c)\|A\| < q$, where $c = \|C\| = \max_{1 \leq i \leq n} -c_i$, then according to (28) one has

$$\lim_{t \rightarrow \infty} \|e(t)\| = 0, \quad (29)$$

which completes the proof. \square

3.2. Synchronization Controller Design. The master and slave FOCSS are defined, respectively, as

$$\mathbb{D}^q \zeta(t) = P \zeta(t) + Q \tilde{h}(\zeta(t)), \quad (30)$$

$$\mathbb{D}^q \tilde{\zeta}(t) = P \tilde{\zeta}(t) + Q \tilde{h}(\tilde{\zeta}(t)) + Gu(t), \quad (31)$$

where $\zeta(t), \hat{\zeta}(t) \in \mathbb{R}^n$ are the state vectors of the master FOCS and slave FOCS, respectively, $P, Q, G \in \mathbb{R}^{n \times n}$ are three constant matrices, G is a positive definite control gain matrix, and $u(t) \in \mathbb{R}^n$ represents the control input.

Define the synchronization error $\varepsilon(t) = \zeta(t) - \hat{\zeta}(t)$. The objective of this section is to design a proper control input $u(t)$ such that $\varepsilon(t)$ converges to zero eventually. To proceed, let us give the following assumption first.

Assumption 9. \hbar is a Lipschitz continuous function; that is, the following inequality holds:

$$\|\hbar(\zeta(t)) - \hbar(\hat{\zeta}(t))\| \leq a_0 \|\zeta(t) - \hat{\zeta}(t)\|, \quad (32)$$

where $a_0 > 0$ is a constant.

To meet the synchronization object, let us construct the following fractional-order sliding mode surface:

$$s(t) = \Lambda \varepsilon(t) - \frac{1}{\Gamma(q)} \Lambda (P + K) \int_0^t (t - \tau)^{(q-1)} \varepsilon(\tau) d\tau, \quad (33)$$

where $\Lambda, K \in \mathbb{R}^{n \times n}$ are two design matrices. Then, it follows from (30), (31), and (33) that

$$\begin{aligned} \mathbb{D}^q s(t) &= \Lambda P \varepsilon(t) + \Lambda Q (\hbar(\zeta(t)) - \hbar(\hat{\zeta}(t))) - Gu(t) \\ &\quad - \Lambda (P + K) \varepsilon(t) \\ &= \Lambda Q (\hbar(\zeta(t)) - \hbar(\hat{\zeta}(t))) - Gu(t) \\ &\quad - \Lambda K \varepsilon(t). \end{aligned} \quad (34)$$

Consequently, let $\mathbb{D}^q s(t) = 0$; the control input can be given as

$$u(t) = G^{-1} \Lambda Q (\hbar(\zeta(t)) - \hbar(\hat{\zeta}(t))) - G^{-1} \Lambda K \varepsilon(t). \quad (35)$$

Now, we can give the following results.

Theorem 10. *Consider the master FOCS (30) and the slave FOCS (31) under Assumption 9. Suppose that the sliding surface is given by (33) and the control input is designed as (35). If the design matrices satisfy $P - \Lambda K < 0$ and $a_0 \|Q - \Lambda Q\| \leq \underline{\lambda} q$, where $\underline{\lambda}$ is the smallest eigenvalue of $\Lambda K - P$, then one can conclude that the synchronization error converges to the origin asymptotically.*

Proof. It follows from (30) and (31) that

$$\mathbb{D}^q \varepsilon(t) = P \varepsilon(t) + Q \hbar(\zeta(t)) - \hbar(\hat{\zeta}(t)) - Gu(t). \quad (36)$$

Substituting (35) into (36) yields

$$\begin{aligned} \mathbb{D}^q \varepsilon(t) &= (P - \Lambda K) \varepsilon(t) \\ &\quad + (Q - \Lambda Q) \hbar(\zeta(t)) - \hbar(\hat{\zeta}(t)). \end{aligned} \quad (37)$$

Noting that $P - \Lambda K < 0$ and $a_0 \|Q - \Lambda Q\| \leq \underline{\lambda} q$, it follows from (37), Assumption 9, and Theorem 8 that $\lim_{t \rightarrow \infty} \varepsilon(t) = 0$. This completes the proof of Theorem 10. \square

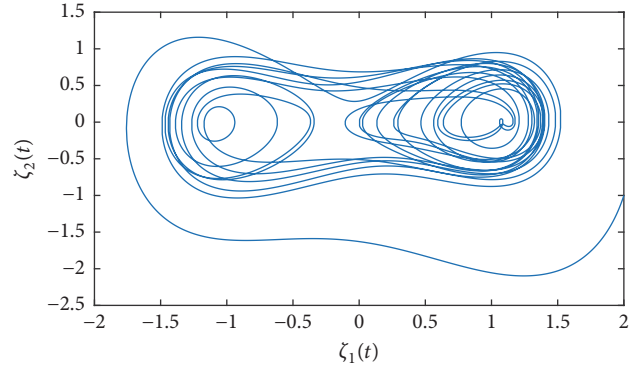


FIGURE 1: Phase attractor of FOCS (38).

4. Simulation Results

In this section, two examples will be given to show the effectiveness of the proposed method.

4.1. Synchronizing Two 2D Fractional-Order Duffing Systems. The fractional-order Duffing system is described by [46]

$$\begin{aligned} \mathbb{D}^q \zeta_1(t) &= \zeta_2(t), \\ \mathbb{D}^q \zeta_2(t) &= \zeta_1(t) - \zeta_1^3(t) - 0.15 \zeta_2(t) + 0.3 \cos(t). \end{aligned} \quad (38)$$

The Jacobian matrix of system (38) for the equilibrium point $E_1^* = (\zeta_1^*, \zeta_2^*)$ is

$$J_{E_1^*} = \begin{bmatrix} 0 & 1 \\ 1 - 3\zeta_1^{*2} & -0.15 \end{bmatrix}. \quad (39)$$

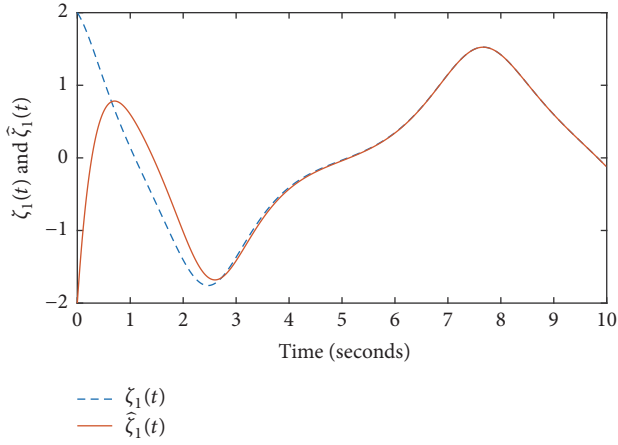
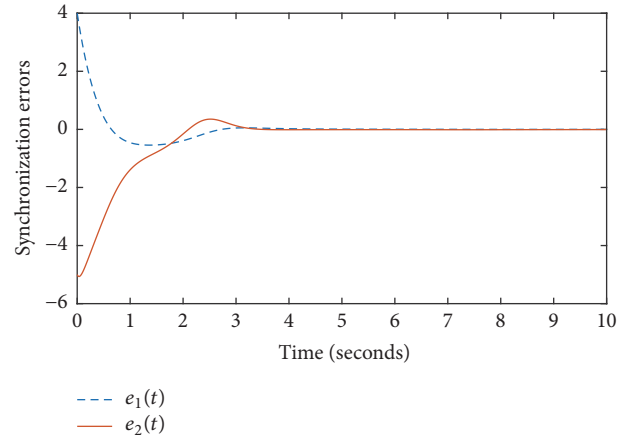
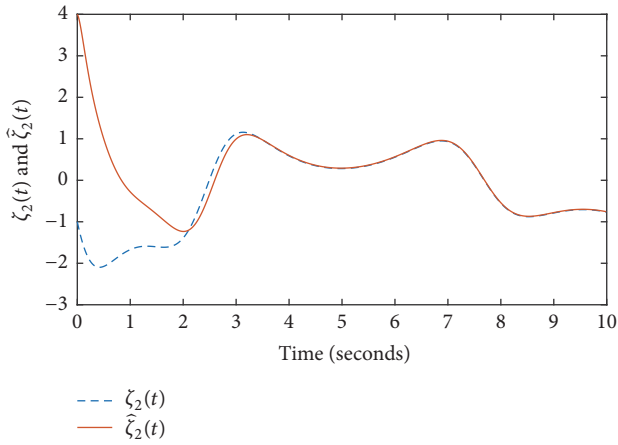
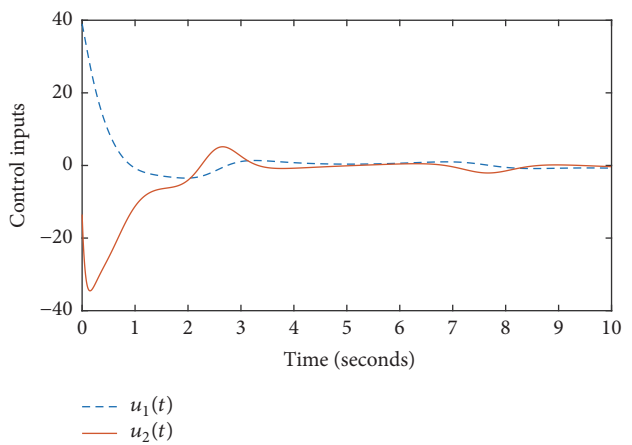
It is easy to know that system (38) has three equilibria: $E_1 = (1.0729, 0)$, $E_2 = (-0.9062, 0)$, and $E_3 = (-0.1667, 0)$. For equilibrium E_1 , we get the eigenvalues $\lambda_1 \approx -0.0750 + 1.4876i$ and $\lambda_2 \approx -0.0750 - 1.4876i$. For equilibrium E_2 , the eigenvalues are $\lambda_1 \approx 1.8548$ and $\lambda_2 \approx -2.0048$. For equilibrium E_3 , we obtain the eigenvalues $\lambda_1 \approx 1.1521$ and $\lambda_2 \approx -1.3021$. According to these eigenvalues, we can conclude that a minimal commensurate order to obtain the chaotic behavior of system (38) is [45]

$$q > \frac{2}{\pi} \arctan\left(\frac{1.4876}{0.0750}\right) = 0.9679. \quad (40)$$

Under the initial conditions $\zeta_1(0) = 2$ and $\zeta_2(0) = -1$ and the fractional order $q = 0.98$, FOCS (38) shows a chaotic behavior, which is depicted in Figure 1.

According to (30) and (38), it is easy to know that

$$\begin{aligned} P &= \begin{bmatrix} 0 & 1 \\ 1 & 0 \end{bmatrix}, \\ Q &= \begin{bmatrix} 0 & 0 \\ 0 & 1 \end{bmatrix}, \\ \hbar(t) &= \begin{bmatrix} 0 \\ -\zeta_1^3(t) - 0.15 \zeta_2(t) + 0.3 \cos(t) \end{bmatrix}. \end{aligned} \quad (41)$$


 FIGURE 2: Synchronization between $\zeta_1(t)$ and $\tilde{\zeta}_1(t)$.

 FIGURE 4: Time response of synchronization errors $e_1(t)$ and $e_2(t)$.

 FIGURE 3: Synchronization between $\zeta_2(t)$ and $\tilde{\zeta}_2(t)$.

 FIGURE 5: Time response of control inputs $u_1(t)$ and $u_2(t)$.

Since system (38) is a chaotic system, then we know that both signals $\zeta_1(t)$ and $\zeta_2(t)$ are bounded (from Figure 1, one knows that $|\zeta_1(t)| < 2$ and $|\zeta_2(t)| < 2$). Thus, Assumption 9 is satisfied with $a_0 = 3$.

In the simulation, the initial condition for the slave FOCS is $\tilde{\zeta}_1(0) = -2$ and $\tilde{\zeta}_2(0) = 4$. Suppose that $G = \text{diag}(1, 1)$. The design matrices are chosen as

$$K = \begin{bmatrix} -73 & 34 \\ 52 & -12 \end{bmatrix}, \quad (42)$$

$$\Lambda = \begin{bmatrix} 0.1 & 0.2 \\ 0.2 & 0.3 \end{bmatrix}.$$

Thus, we have that $\|Q - \Lambda Q\| = 0.728$, $\underline{\lambda} = 3.1$, and the two conditions $P - \Lambda K < 0$ and $a_0\|Q - \Lambda Q\| \leq \underline{\lambda}q$ in Theorem 10 are satisfied.

The simulation results are presented in Figures 2–5. The results where the state variables of the slave FOCS track the master system's states are presented in Figures 2 and 3. The time response of the synchronization errors is depicted in Figure 4. From these pictures, we can see that the synchronization controller works well, and the synchronization

errors converge to the origin fast. From (35), we know that the synchronization control input is a continuous function. The smoothness of the control input is given in Figure 5, from which we can see that the proposed controller has small fluctuation.

4.2. Synchronizing Two 3D Fractional-Order Chaotic Neural Networks. Let us consider the following fractional-order chaotic neural networks expressed by [15]

$$\begin{aligned} \mathbb{D}^q \zeta_1(t) &= -\zeta_1(t) + 2 \tanh(\zeta_1(t)) - 1.2 \tanh(\zeta_2(t)), \\ \mathbb{D}^q \zeta_2(t) &= -\zeta_2(t) + 2 \tanh(\zeta_1(t)) + 1.71 \tanh(\zeta_2(t)) \\ &\quad + 1.15 \tanh(\zeta_3(t)), \\ \mathbb{D}^q \zeta_3(t) &= -\zeta_3(t) - 4.75 \tanh(\zeta_1(t)) \\ &\quad + 1.10 \tanh(\zeta_3(t)). \end{aligned} \quad (43)$$

Suppose that $q = 0.95$ and the initial condition is $\zeta_1(0) = -0.3$, $\zeta_2(0) = 0.4$, and $\zeta_3(0) = 0.3$. The dynamical behavior of FOCS (43) is given in Figure 6.

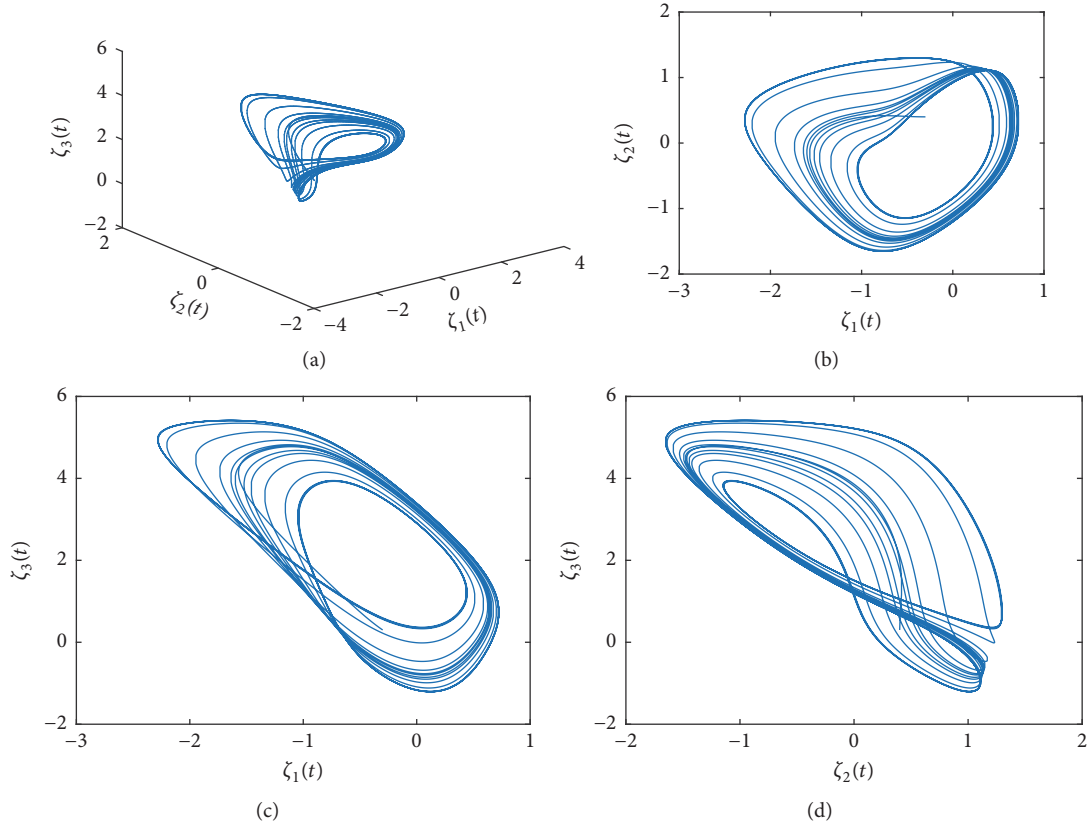


FIGURE 6: Dynamical behavior of system (43) in (a) 3D space, (b) $\zeta_1(t) - \zeta_2(t)$ plane, (c) $\zeta_1(t) - \zeta_3(t)$ plane, and (d) $\zeta_2(t) - \zeta_3(t)$ plane.

It is easy to know in the master chaotic system (43) that $P = \text{diag}(-1, -1, -1)$, $\tilde{h}(t) = [\tanh(\zeta_1(t)), \tanh(\zeta_2(t)), \tanh(\zeta_3(t))]^T$,

$$Q = \begin{bmatrix} 2.00 & -1.20 & 0.00 \\ 2.00 & 1.71 & 1.15 \\ -4.75 & 0.00 & 1.10 \end{bmatrix}. \quad (44)$$

Thus, we have $\|Q\| = 1.235$ and $\tilde{h}(t)$ satisfy the Lipschitz condition. The Lipschitz constant a_0 can be chosen as 1.

The initial condition of the slave FOCS is $\hat{\zeta}_1(0) = 3.2$, $\hat{\zeta}_2(0) = -4$, and $\hat{\zeta}_3(0) = -3.5$. Let $G = \text{diag}(1, 1, 1)$. The design matrices are chosen as

$$K = \begin{bmatrix} 1.2484 & -0.1401 & 0.0127 \\ 0.0127 & 1.1210 & -1.1019 \\ -0.1146 & -0.0892 & 0.9172 \end{bmatrix}, \quad (45)$$

$$\Lambda = \begin{bmatrix} 0.8 & 0.1 & 0 \\ 0 & 0.9 & 0.1 \\ 0.1 & 0.1 & 1.1 \end{bmatrix}.$$

Thus, we know that $\|Q - \Lambda Q\| = 0.7115$, $\underline{\lambda} = 2$, and the two conditions $P - \Lambda K < 0$ and $a_0 \|Q - \Lambda Q\| \leq \underline{\lambda} q$ in Theorem 10 are satisfied.

The simulation results are given in Figures 7 and 8. Just like the results in Figures 2–5, we know that good synchronization performance has been obtained.

5. Conclusion

In this paper, two stability criteria for fractional-order nonlinear systems are given. Based on these theorems, the synchronization of two identical FOCSs is addressed. A fractional-order sliding surface, which contains a fractional-order integral of the synchronization errors, is given. The proposed controller can guarantee the asymptotical stability of the closed-loop systems. However, in the controller design, we need to know the exact value of the Lipschitz constant. How to reduce this condition is one of our future research directions.

Conflicts of Interest

The author does not have a direct financial relation with any commercial identity mentioned in this paper that might lead to conflicts of interest.

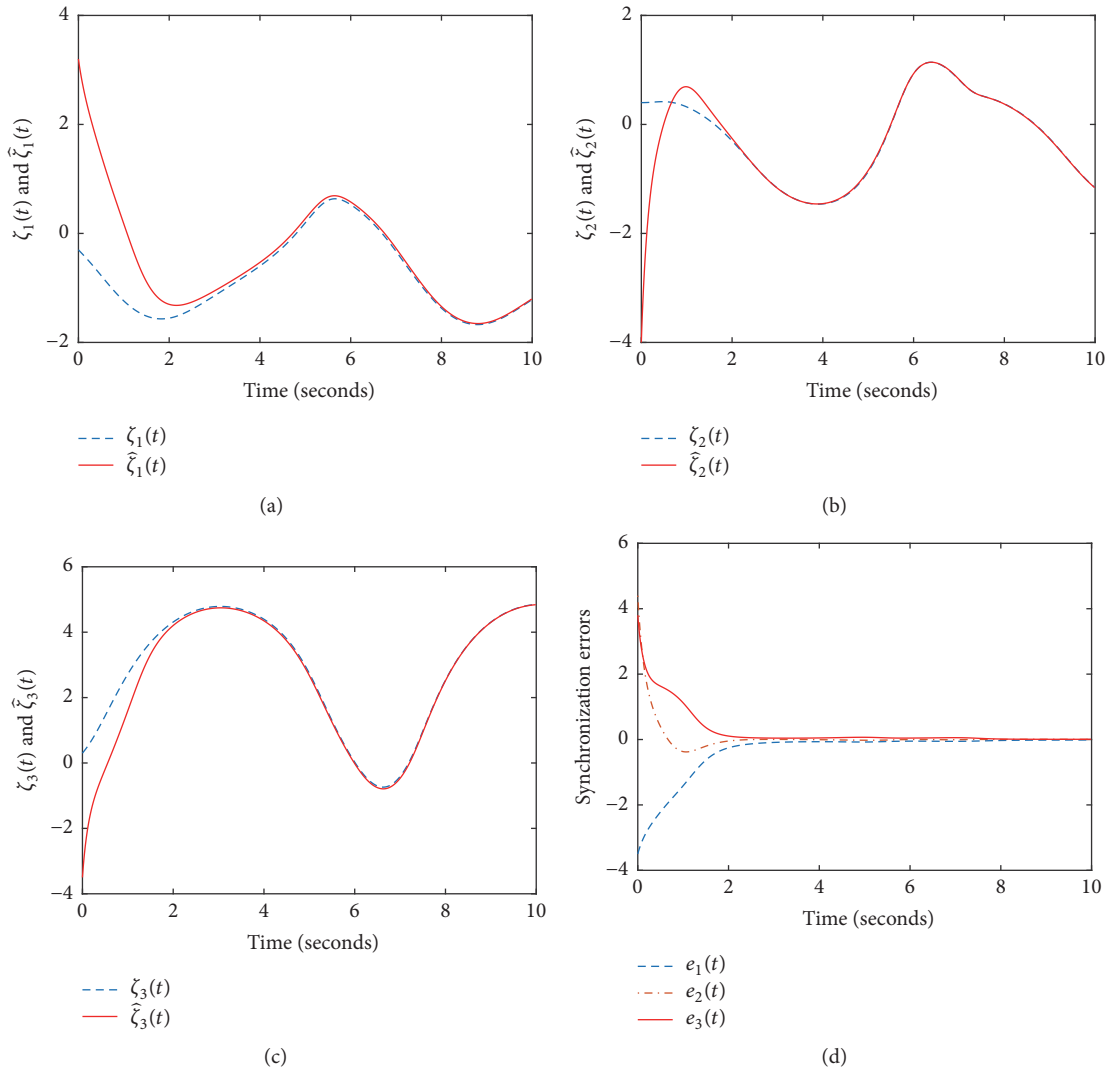


FIGURE 7: Simulation results in (a) synchronization between $\zeta_1(t)$ and $\tilde{\zeta}_1(t)$, (b) synchronization between $\zeta_2(t)$ and $\tilde{\zeta}_2(t)$, (c) synchronization between $\zeta_3(t)$ and $\tilde{\zeta}_3(t)$, and (d) synchronization errors $e_1(t)$, $e_2(t)$, and $e_3(t)$.

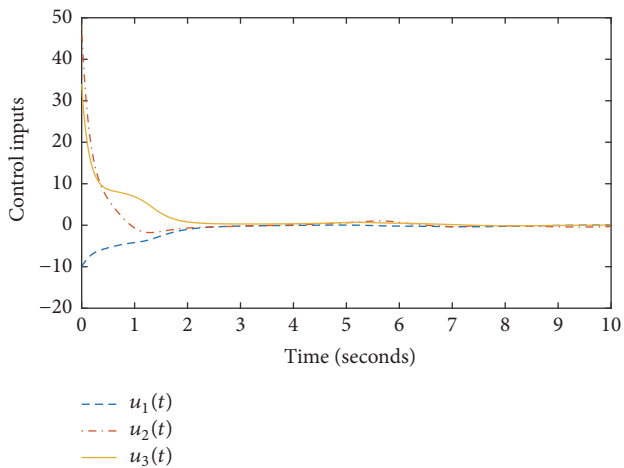


FIGURE 8: Time response of control inputs $u_1(t)$, $u_2(t)$, and $u_3(t)$.

Acknowledgments

This work is supported by the National Natural Science Foundation of China (Grant no. 11302184) and the Young and Middle-Aged Teacher Education and Science Research Foundation of Fujian Province of China (Grant no. JAT170423).

References

- [1] H. Liu, S.-G. Li, Y.-G. Sun, and H.-X. Wang, "Adaptive fuzzy synchronization for uncertain fractional-order chaotic systems with unknown non-symmetrical control gain," *Wuli Xuebao/Acta Physica Sinica*, vol. 64, no. 7, Article ID 070503, 2015.
- [2] H. Liu, S. Li, Y. Sun, and H. Wang, "Prescribed performance synchronization for fractional-order chaotic systems," *Chinese Physics B*, vol. 24, no. 9, Article ID 090505, 2015.
- [3] S. Vaidyanathan and S. Pakiriswamy, "A five-term 3-D novel conservative chaotic system and its generalized projective

- synchronization via adaptive control method,” *Control Theory and Technology*, vol. 9, no. 1, pp. 61–78, 2016.
- [4] C. Volos, V.-T. Pham, E. Zambrano-Serrano, J. M. Munoz-Pacheco, S. Vaidyanathan, and E. Tlelo-Cuautle, “Analysis of a 4-D hyperchaotic fractional-order memristive system with hidden attractors,” in *Advances in Memristors, Memristive Devices and Systems*, vol. 701, pp. 207–235, Springer, 2017.
 - [5] C. Volos, S. Vaidyanathan, V.-T. Pham et al., “Adaptive control and synchronization of a memristor-based Shinriki’s system,” in *Advances in Memristors, Memristive Devices and Systems*, vol. 701, pp. 237–261, Springer, 2017.
 - [6] A. Ouannas, Z. Odibat, N. Shawagfeh, A. Alsaedi, and B. Ahmad, “Universal chaos synchronization control laws for general quadratic discrete systems,” *Applied Mathematical Modelling: Simulation and Computation for Engineering and Environmental Systems*, vol. 45, pp. 636–641, 2017.
 - [7] A. Ouannas and Z. Odibat, “On inverse generalized synchronization of continuous chaotic dynamical systems,” *International Journal of Applied and Computational Mathematics*, vol. 2, no. 1, pp. 1–11, 2016.
 - [8] A. Boulkroune, A. Bouzeriba, T. Bouden, and A. T. Azar, “Fuzzy adaptive synchronization of uncertain fractional-order chaotic systems,” in *Advances in chaos theory and intelligent control*, vol. 337, pp. 681–697, Springer, 2016.
 - [9] A. Boulkroune, A. Bouzeriba, and T. Bouden, “Fuzzy generalized projective synchronization of incommensurate fractional-order chaotic systems,” *Neurocomputing*, vol. 173, pp. 606–614, 2016.
 - [10] S. Çiçek, A. Ferikoglu, and I. Pehlivan, “A new 3D chaotic system: dynamical analysis, electronic circuit design, active control synchronization and chaotic masking communication application,” *Optik - International Journal for Light and Electron Optics*, vol. 127, no. 8, pp. 4024–4030, 2016.
 - [11] S. Vaidyanathan and A. T. Azar, “Dynamic analysis, adaptive feedback control and synchronization of an eight-term 3-D novel chaotic system with three quadratic nonlinearities,” in *Advances in Chaos Theory and Intelligent Control*, vol. 337, pp. 155–178, Springer, 2016.
 - [12] S. Sampath and S. Vaidyanathan, “Hybrid synchronization of identical chaotic systems via novel sliding control method with application to Sampath four-scroll chaotic system,” *Control Theory and Technology*, vol. 9, no. 1, pp. 221–235, 2016.
 - [13] P. Muthukumar, P. Balasubramaniam, and K. Ratnavelu, “Sliding mode control design for synchronization of fractional order chaotic systems and its application to a new cryptosystem,” *International Journal of Dynamics and Control*, vol. 5, no. 1, pp. 115–123, 2017.
 - [14] H. Liu, S. Li, H. Wang, Y. Huo, and J. Luo, “Adaptive synchronization for a class of uncertain fractional-order neural networks,” *Entropy*, vol. 17, no. 10, pp. 7185–7200, 2015.
 - [15] H. Liu, Y. Pan, S. Li, and Y. Chen, “Synchronization for fractional-order neural networks with full/under-actuation using fractional-order sliding mode control,” *International Journal of Machine Learning and Cybernetics*, pp. 1–14, 2017.
 - [16] H. Liu, S.-G. Li, H.-X. Wang, and G.-J. Li, “Adaptive fuzzy synchronization for a class of fractional-order neural networks,” *Chinese Physics B*, vol. 26, no. 3, Article ID 030504, 2017.
 - [17] H. Li, J. Yu, C. Hilton, and H. Liu, “Adaptive sliding-mode control for nonlinear active suspension vehicle systems using T-S fuzzy approach,” *IEEE Transactions on Industrial Electronics*, vol. 60, no. 8, pp. 3328–3338, 2013.
 - [18] Y. Pan and H. Yu, “Composite learning from adaptive dynamic surface control,” *Institute of Electrical and Electronics Engineers Transactions on Automatic Control*, vol. 61, no. 9, pp. 2603–2609, 2016.
 - [19] H. Li, P. Shi, and D. Yao, “Adaptive sliding mode control of markov jump nonlinear systems with actuator faults,” *IEEE Transactions on Automatic Control*, vol. 62, no. 4, pp. 1933–1939, 2016.
 - [20] H. Wang, “Core-EP decomposition and its applications,” *Linear Algebra and Its Applications*, vol. 508, pp. 289–300, 2016.
 - [21] H. Wang and X. Liu, “A partial order on the set of complex matrices with index one,” *Linear and Multilinear Algebra*, pp. 1–11, 2017.
 - [22] J. Liu, S. Vazquez, L. Wu, A. Marquez, H. Gao, and L. G. Franquelo, “Extended State Observer-Based Sliding-Mode Control for Three-Phase Power Converters,” *IEEE Transactions on Industrial Electronics*, vol. 64, no. 1, pp. 22–31, 2017.
 - [23] Y. Pan, C. Yang, L. Pan, and H. Yu, “Integral Sliding Mode Control: Performance, Modification and Improvement,” *IEEE Transactions on Industrial Informatics*, 2017.
 - [24] H. Wang and W. Guo, “The minimal rank of matrix expressions with respect to Hermitian matrix-revised,” *Journal of The Franklin Institute*, vol. 353, no. 5, pp. 1206–1219, 2016.
 - [25] H. Komurcugil and S. Biricik, “Time-Varying and Constant Switching Frequency-Based Sliding-Mode Control Methods for Transformerless DVR Employing Half-Bridge VSI,” *IEEE Transactions on Industrial Electronics*, vol. 64, no. 4, pp. 2570–2579, 2017.
 - [26] Y. Pan, H. Wang, X. Li, and H. Yu, “Adaptive Command-Filtered Backstepping Control of Robot Arms With Compliant Actuators,” *IEEE Transactions on Control Systems Technology*, pp. 1–8, 2017.
 - [27] Y. Pan, Z. Guo, X. Li, and H. Yu, “Output-feedback adaptive neural control of a compliant differential SMA actuator,” *IEEE Transactions on Control Systems Technology*, vol. 25, no. 6, pp. 2202–2210, 2017.
 - [28] C. Yin, S. Dadras, S.-M. Zhong, and Y. Chen, “Control of a novel class of fractional-order chaotic systems via adaptive sliding mode control approach,” *Applied Mathematical Modelling*, vol. 37, no. 4, pp. 2469–2483, 2013.
 - [29] C. Yin, Y. Cheng, S.-M. Zhong, and Z. Bai, “Fractional-order switching type control law design for adaptive sliding mode technique of 3D fractional-order nonlinear systems,” *Complexity*, vol. 21, no. 6, pp. 363–373, 2016.
 - [30] A. Mohammadzadeh and S. Ghaemi, “A modified sliding mode approach for synchronization of fractional-order chaotic/hyperchaotic systems by using new self-structuring hierarchical type-2 fuzzy neural network,” *Neurocomputing*, vol. 191, pp. 200–213, 2016.
 - [31] J. Shen and J. Lam, “Non-existence of finite-time stable equilibria in fractional-order nonlinear systems,” *Automatica*, vol. 50, no. 2, pp. 547–551, 2014.
 - [32] J. C. Trigeassou, N. Maamri, J. Sabatier, and A. Oustaloup, “A Lyapunov approach to the stability of fractional differential equations,” *Signal Processing*, vol. 91, no. 3, pp. 437–445, 2011.
 - [33] D. Matignon, “Stability result for fractional differential equations with applications to control processing,” in *Computational Engineering in Systems Applications*, pp. 963–968, IMACS, IEEE-SMC, Lille, France, 1997.
 - [34] J.-G. Lu and G. Chen, “Robust stability and stabilization of fractional-order interval systems: an LMI approach,” *IEEE*

- Transactions on Automatic Control*, vol. 54, no. 6, pp. 1294–1299, 2009.
- [35] Y. Li, Y. Chen, and I. Podlubny, “Mittag-Leffler stability of fractional order nonlinear dynamic systems,” *Automatica*, vol. 45, no. 8, pp. 1965–1969, 2009.
- [36] H. Delavari, D. Baleanu, and J. Sadati, “Stability analysis of Caputo fractional-order nonlinear systems revisited,” *Nonlinear Dynamics*, vol. 67, no. 4, pp. 2433–2439, 2012.
- [37] X.-J. Wen, Z.-M. Wu, and J.-G. Lu, “Stability analysis of a class of nonlinear fractional-order systems,” *IEEE Transactions on Circuits and Systems II: Express Briefs*, vol. 55, no. 11, pp. 1178–1182, 2008.
- [38] S. Liu, W. Jiang, X. Li, and X.-F. Zhou, “Lyapunov stability analysis of fractional nonlinear systems,” *Applied Mathematics Letters*, vol. 51, pp. 13–19, 2016.
- [39] X. Yang, C. Li, T. Huang, and Q. Song, “Mittag-Leffler stability analysis of nonlinear fractional-order systems with impulses,” *Applied Mathematics and Computation*, vol. 293, pp. 416–422, 2017.
- [40] H. Liu, S. Li, J. D. Cao, A. G. Alsaedi, and F. E. Alsaadi, “Adaptive fuzzy prescribed performance controller design for a class of uncertain fractional-order nonlinear systems with external disturbances,” *Neurocomputing*, vol. 219, pp. 422–430, 2017.
- [41] H. Liu, Y. Pan, S. Li, and Y. Chen, “Adaptive Fuzzy Backstepping Control of Fractional-Order Nonlinear Systems,” *IEEE Transactions on Systems, Man, and Cybernetics: Systems*, vol. 47, no. 8, pp. 2209–2217, 2017.
- [42] I. Podlubny, *Fractional Differential Equations*, vol. 198 of *Mathematics in Science and Engineering*, Academic Press, San Diego, Calif, USA, 1999.
- [43] L. Chen, Y. Chai, R. Wu, and J. Yang, “Stability and stabilization of a class of nonlinear fractional-order systems with caputo derivative,” *IEEE Transactions on Circuits and Systems II: Express Briefs*, vol. 59, no. 9, pp. 602–606, 2012.
- [44] H. Liu, S. Li, G. Li, and H. Wang, “Adaptive Controller Design for a Class of Uncertain Fractional-Order Nonlinear Systems: An Adaptive Fuzzy Approach,” *International Journal of Fuzzy Systems*, pp. 1–14, 2017.
- [45] I. Petráš, *Fractional-Order Nonlinear Systems: Modeling, Analysis and Simulation*, Springer Science & Business Media, 2011.
- [46] Z. M. Ge and C. Y. Ou, “Chaos in a fractional order modified Duffing system,” *Chaos, Solitons & Fractals*, vol. 34, no. 2, pp. 262–291, 2007.